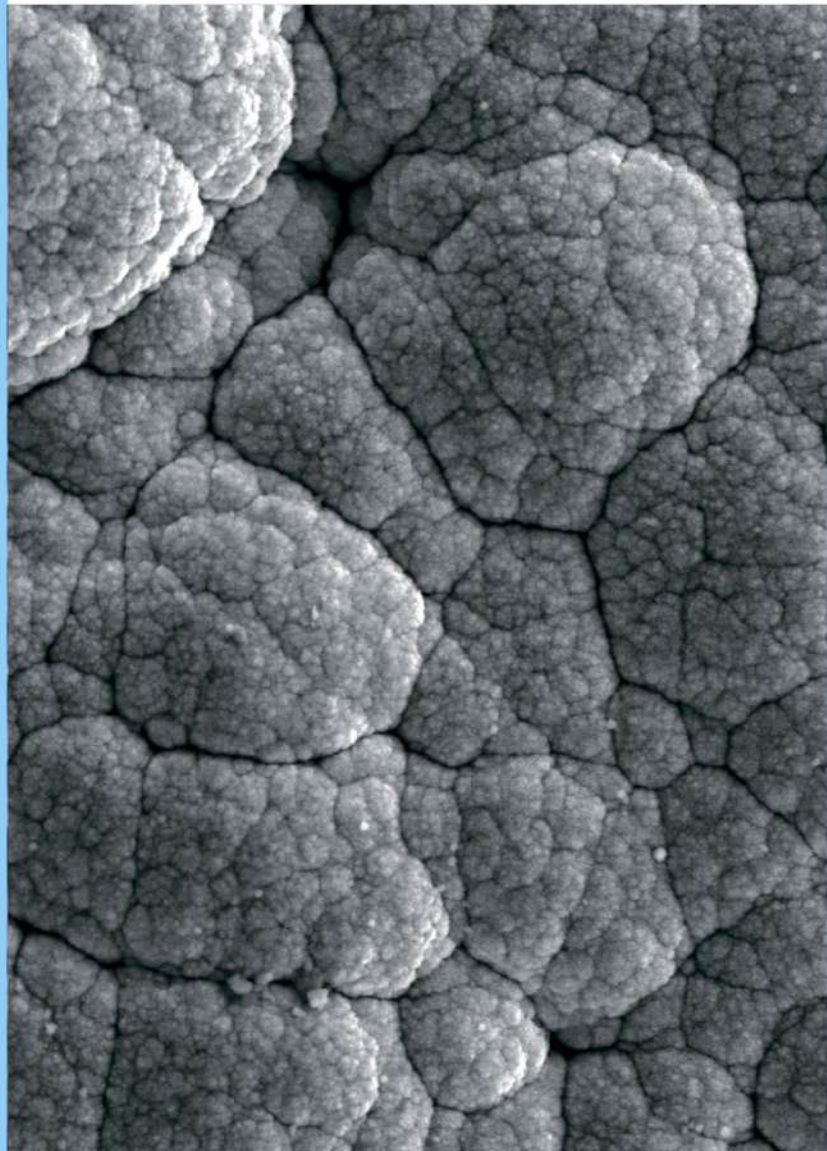


ISSN 2782-4039 (Print)
ISSN 2782-6074 (Online)

Frontier Materials & Technologies



2024
Nº 4

Frontier Materials & Technologies

Founded in 2008

№ 4

2024

16+

Quarterly
Scientific Journal

The Founder is
Togliatti State University

Editor-in-Chief

Mikhail M. Krishtal, DSc (Physics and Mathematics), Professor

Deputy Editor-in-Chief

for Metallurgy and Materials Science

Dmitry L. Merson, DSc (Physics and Mathematics), Professor

Deputy Editor-in-Chief

for Mechanical Engineering and Machine Science

Aleksandr P. Shaikin, DSc (Engineering), Professor

Deputy Editor-in-Chief

for Welding and Allied Processes and Technologies

Aleksandr I. Kovtunov, DSc (Engineering), Associate Professor

Editors:

Petr Yu. Bochkarev, DSc (Engineering), Professor

Boris M. Brzhozovskiy, DSc (Engineering), Professor

Aleksandr F. Denisenko, DSc (Engineering), Professor

Yuri Z. Estrin, DSc (Physics and Mathematics), Professor

Sergey S. Gavryushin, DSc (Engineering), Professor

Gregory Gerstein, DSc (Engineering)

Fedor V. Grechnikov, Academician of the Russian Academy of Sciences, DSc (Engineering), Professor

Mikhail I. Karpov, Corresponding Member of the Russian Academy of Sciences, DSc (Engineering), Professor

Aleksandr V. Katsman, PhD (Physics and Mathematics)

Aleksandr A. Kazakov, DSc (Engineering), Professor

Aleksandr V. Kudrya, DSc (Engineering), Professor

Sergey V. Kuzmin, Corresponding Member of the Russian Academy of Sciences, DSc (Engineering), Professor

Aleksey V. Makarov, Corresponding Member of the Russian Academy of Sciences, DSc (Engineering)

Radik R. Mulyukov, Corresponding Member of the Russian Academy of Sciences,

DSc (Physics and Mathematics), Professor

Oleg B. Naimark, DSc (Physics and Mathematics), Professor

Nikolay V. Nosov, DSc (Engineering), Professor

Aleksandr V. Pilinsky, PhD (Engineering), Associate Professor

Aleksey E. Romanov, DSc (Physics and Mathematics), Professor

Vasili V. Rubanik, Corresponding Member of the National Academy of Sciences of Belarus, DSc (Engineering)

Vladimir A. Shishkov, DSc (Engineering)

Tushar Madhukar Sonar, PhD (Engineering)

Ramasubbu Sunder, Fellow of the Indian Academy of Sciences, PhD (Engineering)

Vladimir P. Tabakov, DSc (Engineering), Professor

Alexey Yu. Vinogradov, DSc (Engineering), PhD (Physics and Mathematics), Professor

Until December 2021,
the journal was published under
the title
**“Science Vector
of Togliatti State University”**.

Indexed in Scopus.
Included in the List of HAC,
RSCI core, DOAJ,
“White List”.
Available in Crossref,
Google Scholar.

Registered by the Federal
Service for Supervision
of Communications,
Information Technology
and Mass Media
(Registration Certificate
ПИ No. ФС77-83040
dated March 31, 2022).

Subscription index
in the Russian Press catalogue:
13088.

Desktop publishing:

Natalya A. Nikitenko

*Responsible/technical
editor:*

Natalya A. Nikitenko

Mailing Address:

14, Belorusskaya St.,

Togliatti,

Russia, 445020

Phone: **(8482) 44-91-74**

E-mail:

vektornaukitgu@yandex.ru

Website:

<https://vektornaukitech.ru>

Passed for printing
23.12.2024.
Published 28.12.2024.
Format 60×84 1/8.
Digital printing.
Conventional printed sheets 15.1.
Circulation is 30 copies.
Order 3-485-24.
The price is free.

EDITORIAL BOARD INFORMATION

Editor-in-Chief

Mikhail M. Krishtal, Doctor of Sciences (Physics and Mathematics), Professor, Rector (Togliatti State University, Togliatti, Russia).
Scopus AuthorID: [14634063100](#)
ResearcherID: [AAD-7707-2019](#)
ORCID: <https://orcid.org/0000-0001-7189-0002>

Deputy Editor-in-Chief for Metallurgy and Materials Science

Dmitry L. Merson, Doctor of Sciences (Physics and Mathematics), Professor, Director of the Research and Development Institute of Advanced Technologies (Togliatti State University, Togliatti, Russia).
Scopus AuthorID: [6603449333](#)
ResearcherID: [M-7210-2016](#)
ORCID: <https://orcid.org/0000-0001-5006-4115>

Deputy Editor-in-Chief for Mechanical Engineering and Machine Science

Aleksandr P. Shaikin, Doctor of Sciences (Engineering), Professor, Professor of Chair “Energy-Converting Machines and Control Systems” (Togliatti State University, Togliatti, Russia).
Scopus AuthorID: [6602779899](#)
ORCID: <https://orcid.org/0000-0002-9832-4753>

Deputy Editor-in-Chief for Welding and Allied Processes and Technologies

Aleksandr I. Kovtunov, Doctor of Sciences (Engineering), Associate Professor, Professor of Chair “Welding, Pressure Treatment of Materials and Allied Processes” (Togliatti State University, Togliatti, Russia).
Scopus AuthorID: [36761987000](#)
ResearcherID: [B-4545-2016](#)
ORCID: <https://orcid.org/0000-0002-7705-7377>

Editorial board:

Petr Yu. Bochkarev, Doctor of Sciences (Engineering), Professor, Professor of Chair “Mechanical Engineering Technology and Applied Mechanics” (Kamyshin Technological Institute (Branch) of Volgograd State Technical University, Kamyshin, Russia), Professor of Chair “Technical Support of Agro-Industrial Complex” (Saratov State Vavilov Agrarian University, Saratov, Russia).
Scopus AuthorID: [57189893110](#)

Boris M. Brzhozovskiy, Doctor of Sciences (Engineering), Professor, chief researcher of Laboratory of Theory of Mechanisms and Machine Structure (Institute of Machines Science named after A.A. Blagonravov of the Russian Academy of Sciences, Moscow, Russia).
Scopus AuthorID: [55683317200](#)

Alexander F. Denisenko, Doctor of Sciences (Engineering), Professor, Professor of Chair “Technology of Mechanical Engineering, Machines and Tools” (Samara State Technical University, Samara, Russia).

Scopus AuthorID: [36131150100](#)

Yuri Z. Estrin, Doctor of Sciences (Physics and Mathematics), Professor, Professor of Chair of Engineering Materials (Monash University, Melbourne, Australia).

Scopus AuthorID: [7005031984](#)

Sergey S. Gavryushin, Doctor of Sciences (Engineering), Professor, Head of Chair “Computer Systems of Production Automation”, Head of the Theory & Machines Structure Laboratory (Bauman Moscow State Technical University, Moscow, Russia; Mechanical Engineering Research Institute of the Russian Academy of Sciences, Moscow, Russia).

Scopus AuthorID: [6507067486](#)

ResearcherID: [AAT-8610-2020](#)

ORCID: <https://orcid.org/0000-0002-6547-1351>

Gregory Gerstein, Doctor of Sciences (Engineering), Laboratory Head (Leibniz University Hannover, Hanover, Germany).

Scopus AuthorID: [55001912200](#)

Fedor V. Grechnikov, Academician of the Russian Academy of Sciences, Doctor of Sciences (Engineering), Professor, Head of the Chair of Forming Processes (Samara National Research University, Samara, Russia).

Scopus AuthorID: [6506174877](#)

ResearcherID: [P-2319-2016](#)

ORCID: <https://orcid.org/0000-0002-3767-4004>

Mikhail I. Karpov, Corresponding Member of the Russian Academy of Sciences, Doctor of Sciences (Engineering), Professor, Head of the Laboratory of Materials Science (Institute of Solid State Physics of the Russian Academy of Sciences, Chernogolovka, Russia).

Scopus AuthorID: [7004130343](#)

ResearcherID: [Q-9288-2016](#)

Aleksandr V. Katsman, PhD (Physics and Mathematics), Senior Research Associate (Technion – Israel Institute of Technology, Haifa, Israel).

Scopus AuthorID: [7004225554](#)

Aleksandr A. Kazakov, Doctor of Sciences (Engineering), Professor, Professor of Chair “Metallurgy and Casting Technologies”, Head of the Metallurgy Expertise Laboratory (Peter the Great Saint-Petersburg Polytechnic University, St. Petersburg, Russia).

Scopus AuthorID: [56037035400](#)

ResearcherID: [E-6090-2014](#)

ORCID: <https://orcid.org/0000-0001-6511-1228>

Aleksandr V. Kudrya, Doctor of Sciences (Engineering), Professor, Professor of Chair of Physical Metallurgy and Physics of Strength (National University of Science and Technology MISiS, Moscow, Russia).

Scopus AuthorID: [6603628218](#)

Sergey V. Kuzmin, Corresponding Member of the Russian Academy of Sciences, Doctor of Sciences (Engineering), Professor, First Prorector, Professor of Chair “Equipment and Technology of Welding Production” (Volgograd State Technical University, Volgograd, Russia).

Scopus AuthorID: [57217278342](#)

ResearcherID: [I-7424-2012](#)

ORCID: <https://orcid.org/0000-0003-2802-8497>

Aleksey V. Makarov, Corresponding Member of the Russian Academy of Sciences, Doctor of Sciences (Engineering), Chief Research Associate, Head of Chair of Materials Science, Head of the Laboratory of Mechanical Properties (M.N. Mikheev Institute of Metal Physics of Ural Branch of Russian Academy of Sciences, Ekaterinburg, Russia).

Scopus AuthorID: [57195590138](#)

ResearcherID: [D-5663-2016](#)

ORCID: <https://orcid.org/0000-0002-2228-0643>

Radik R. Mulyukov, Corresponding Member of the Russian Academy of Sciences, Doctor of Sciences (Physics and Mathematics), Professor, Director (Institute for Metals Superplasticity Problems of the Russian Academy of Sciences, Ufa, Russia).

Scopus AuthorID: [7003520439](#)

ResearcherID: [B-3800-2016](#)

ORCID: <https://orcid.org/0000-0002-0452-3816>

Oleg B. Naimark, Doctor of Sciences (Physics and Mathematics), Professor, Head of the Laboratory of Physical Foundations of Strength (Institute of Continuous Media Mechanics of Ural Branch of Russian Academy of Sciences, Perm, Russia).

Scopus AuthorID: [6701720806](#)

Nikolay V. Nosov, Doctor of Sciences (Engineering), Professor, Professor of Chair “Technology of Mechanical Engineering, Machines and Tools” (Samara State Technical University, Samara, Russia).

Scopus AuthorID: [6602506825](#)

Aleksandr V. Pilinsky, PhD (Engineering), Associate Professor, MSME (Master of Science in Mechanical Engineering), Los Angeles, USA.

ORCID: <https://orcid.org/0009-0009-8933-195X>

Aleksey E. Romanov, Doctor of Sciences (Physics and Mathematics), Professor, Professor of the Institute of Advanced Data Transfer Systems (ITMO University, St. Petersburg, Russia).

Scopus AuthorID: [7202768874](#)

Vasili V. Rubanik, Corresponding Member of the National Academy of Sciences of Belarus, Doctor of Sciences (Engineering), Head of the Laboratory of Metal Physics (Institute of Technical Acoustics of the National Academy of Sciences of Belarus, Vitebsk, Belarus).

Scopus AuthorID: [57215218253](#)

Vladimir A. Shishkov, Doctor of Sciences (Engineering), Head of the Technical Department (Palladio LLC, Togliatti, Russia).

RSCI AuthorID: [596086](#)

SPIN-code: [9504-4454](#)

Tushar Madhukar Sonar, PhD (Engineering), Senior Research Scientist of Chair “Welding Engineering”

(South Ural State University, Chelyabinsk, Russia).

Scopus AuthorID: [57200800257](#)

ResearcherID: [AAS-6037-2021](#)

ORCID: <https://orcid.org/0000-0002-3997-5337>

Ramasubbu Sunder, Fellow of the Indian Academy of Sciences, PhD (Engineering), Director (BISS (P) Ltd, Bangalore, India).

Scopus AuthorID: [7003530245](#)

ResearcherID: [H-6740-2016](#)

ORCID: <https://orcid.org/0000-0001-6143-0723>

Vladimir P. Tabakov, Doctor of Sciences (Engineering), Professor, Head of Chair “Innovative Technologies in Mechanical Engineering” (Ulyanovsk State Technical University, Ulyanovsk, Russia).

Scopus AuthorID: [6701501345](#)

ResearcherID: [E-1832-2017](#)

ORCID: <https://orcid.org/0000-0002-2568-9401>

Alexey Yu. Vinogradov, Doctor of Sciences (Engineering), PhD (Physics and Mathematics), Professor, Professor of Faculty of Mechanical and Industrial Engineering (Norwegian University of Science and Technology, Trondheim, Norway).

Scopus AuthorID: [7402889776](#)

ResearcherID: [A-7175-2009](#)

ORCID: <https://orcid.org/0000-0001-9585-2801>

СВЕДЕНИЯ О ЧЛЕНАХ РЕДКОЛЛЕГИИ

Главный редактор

Криштал Михаил Михайлович, доктор физико-математических наук, профессор, ректор (Тольяттинский государственный университет, Тольятти, Россия).

Scopus AuthorID: [14634063100](#)

ResearcherID: [AAD-7707-2019](#)

ORCID: <https://orcid.org/0000-0001-7189-0002>

Заместитель главного редактора по направлению «Металлургия и материаловедение»

Мерсон Дмитрий Львович, доктор физико-математических наук, профессор, директор Научно-исследовательского института перспективных технологий (Тольяттинский государственный университет, Тольятти, Россия).

Scopus AuthorID: [6603449333](#)

ResearcherID: [M-7210-2016](#)

ORCID: <https://orcid.org/0000-0001-5006-4115>

Заместитель главного редактора по направлению «Машиностроение и машиноведение»

Шайкин Александр Петрович, доктор технических наук, профессор, профессор кафедры «Энергетические машины и системы управления» (Тольяттинский государственный университет, Тольятти, Россия).

Scopus AuthorID: [6602779899](#)

ORCID: <https://orcid.org/0000-0002-9832-4753>

Заместитель главного редактора по направлению «Сварка, родственные процессы и технологии»

Ковтунов Александр Иванович, доктор технических наук, доцент, профессор кафедры «Сварка, обработка материалов давлением и родственные процессы» (Тольяттинский государственный университет, Тольятти, Россия).

Scopus AuthorID: [36761987000](#)

ResearcherID: [B-4545-2016](#)

ORCID: <https://orcid.org/0000-0002-7705-7377>

Редакционная коллегия:

Бочкарев Петр Юрьевич, доктор технических наук, профессор, профессор кафедры «Технология машиностроения и прикладная механика» (Камышинский технологический институт (филиал) Волгоградского государственного технического университета, Камышин, Россия), профессор кафедры «Техническое обеспечение АПК» (Саратовский государственный аграрный университет имени Н.И. Вавилова, Саратов, Россия).

Scopus AuthorID: [57189893110](#)

Бржозовский Борис Максевич, доктор технических наук, профессор главный научный сотрудник лаборатории теории механизмов и структуры машин (Институт машиноведения им. А.А. Благонравова РАН, Москва, Россия).

Scopus AuthorID: [55683317200](#)

Виноградов Алексей Юрьевич, доктор технических наук, кандидат физико-математических наук, профессор факультета механической и промышленной инженерии (Норвежский университет науки и технологии, Тронхейм, Норвегия).

Scopus AuthorID: [7402889776](#)

ResearcherID: [A-7175-2009](#)

ORCID: <https://orcid.org/0000-0001-9585-2801>

Гаврюшин Сергей Сергеевич, доктор технических наук, профессор, заведующий кафедрой «Компьютерные системы автоматизации производства», заведующий лабораторией компьютерных систем автоматизации производства и цифровых технологий (Московский государственный технический университет имени Н.Э. Баумана (национальный исследовательский университет), Москва, Россия; Институт машиноведения им. А.А. Благонравова Российской академии наук, Москва, Россия).

Scopus AuthorID: [6507067486](#)

ResearcherID: [AAT-8610-2020](#)

ORCID: <https://orcid.org/0000-0002-6547-1351>

Герштейн Григорий, доктор технических наук, заведующий лабораторией (Ганноверский университет имени Готфрида Вильгельма Лейбница, Ганновер, Германия).

Scopus AuthorID: [55001912200](#)

Гречников Федор Васильевич, академик РАН, доктор технических наук, профессор, заведующий кафедрой обработки металлов давлением (Самарский национальный исследовательский университет имени академика С.П. Королева, Самара, Россия).

Scopus AuthorID: [6506174877](#)

ResearcherID: [P-2319-2016](#)

ORCID: <https://orcid.org/0000-0002-3767-4004>

Денисенко Александр Федорович, доктор технических наук, профессор, профессор кафедры «Технология машиностроения, станки и инструменты» (Самарский государственный технический университет, Самара, Россия).

Scopus AuthorID: [36131150100](#)

Казаков Александр Анатольевич, доктор технических наук, профессор, профессор кафедры «Металлургические и литейные технологии», руководитель научно-испытательной лаборатории «Металлургическая экспертиза» (Санкт-Петербургский политехнический университет Петра Великого, Санкт-Петербург, Россия).

Scopus AuthorID: [56037035400](#)

ResearcherID: [E-6090-2014](#)

ORCID: <https://orcid.org/0000-0001-6511-1228>

Карнов Михаил Иванович, член-корреспондент РАН, доктор технических наук, профессор, заведующий лабораторией материаловедения (Институт физики твердого тела Российской академии наук, Черноголовка, Россия).

Scopus AuthorID: [7004130343](#)

ResearcherID: [Q-9288-2016](#)

Кацман Александр Владимирович, кандидат физико-математических наук, PhD, старший научный сотрудник (Технион – Израильский технологический институт, Хайфа, Израиль).

Scopus AuthorID: [7004225554](#)

Кудря Александр Викторович, доктор технических наук, профессор, заместитель заведующего кафедрой металловедения и физики прочности (Национальный исследовательский технологический университет «МИСиС», Москва, Россия).

Scopus AuthorID: [6603628218](#)

Кузьмин Сергей Викторович, член-корреспондент РАН, доктор технических наук, профессор, первый проректор, профессор кафедры «Оборудование и технология сварочного производства» (Волгоградский государственный технический университет, Волгоград, Россия).

Scopus AuthorID: [57217278342](#)

ResearcherID: [I-7424-2012](#)

ORCID: <https://orcid.org/0000-0003-2802-8497>

Макаров Алексей Викторович, член-корреспондент РАН, доктор технических наук, главный научный сотрудник, заведующий отделом материаловедения и лабораторией механических свойств (Институт физики металлов имени М.Н. Михеева Уральского отделения Российской академии наук, Екатеринбург, Россия).

Scopus AuthorID: [57195590138](#)

ResearcherID: [D-5663-2016](#)

ORCID: <https://orcid.org/0000-0002-2228-0643>

Мулюков Радик Рафикович, член-корреспондент РАН, доктор физико-математических наук, профессор, директор (Институт проблем сверхпластичности металлов Российской академии наук, Уфа, Россия).

Scopus AuthorID: [7003520439](#)

ResearcherID: [B-3800-2016](#)

ORCID: <https://orcid.org/0000-0002-0452-3816>

Наймарк Олег Борисович, доктор физико-математических наук, профессор, заведующий лабораторией «Физические основы прочности» (Институт механики сплошных сред Уральского отделения Российской академии наук, Пермь, Россия).

Scopus AuthorID: [6701720806](#)

Носов Николай Васильевич, доктор технических наук, профессор, профессор кафедры «Технология машиностроения, станки и инструменты» (Самарский государственный технический университет, Самара, Россия).

Scopus AuthorID: [6602506825](#)

Пилинский Александр Вениаминович, кандидат технических наук, доцент, MSME (Master of Science in Mechanical Engineering), Лос-Анджелес, США.

ORCID: <https://orcid.org/0009-0009-8933-195X>

Романов Алексей Евгеньевич, доктор физико-математических наук, профессор Института перспективных систем передачи данных, руководитель научно-исследовательского центра перспективных функциональных материалов и лазерных коммуникационных систем (Национальный исследовательский университет ИТМО, Санкт-Петербург, Россия).

Scopus AuthorID: [7202768874](#)

Рубаник Василий Васильевич, член-корреспондент Национальной академии наук Беларуси, доктор технических наук, заведующий лабораторией физики металлов (Институт технической акустики Национальной академии наук Беларуси, Витебск, Республика Беларусь).

Scopus AuthorID: [57215218253](#)

Сонар Тушар Мадхукар, кандидат технических наук, старший научный сотрудник кафедры «Оборудование и технология сварочного производства» (Южно-Уральский государственный университет, Челябинск, Россия).

Scopus AuthorID: [57200800257](#)

ResearcherID: [AAS-6037-2021](#)

ORCID: <https://orcid.org/0000-0002-3997-5337>

Сундер Рамасуббу, член Индийской академии наук, кандидат технических наук, директор (“BISS (P) Ltd”, Бангалор, Индия).

Scopus AuthorID: [7003530245](#)

ResearcherID: [H-6740-2016](#)

ORCID: <https://orcid.org/0000-0001-6143-0723>

Табакон Владимир Петрович, доктор технических наук, профессор, заведующий кафедрой «Инновационные технологии в машиностроении» (Ульяновский государственный технический университет, Ульяновск, Россия).

Scopus AuthorID: [6701501345](#)

ResearcherID: [E-1832-2017](#)

ORCID: <https://orcid.org/0000-0002-2568-9401>

Шишков Владимир Александрович, доктор технических наук, начальник технического отдела (ООО «Палладио», Тольятти, Россия).

AuthorID РИНЦ: [596086](#)

SPIN-код: [9504-4454](#)

Эстрин Юрий Захарович, доктор физико-математических наук, профессор, профессор кафедры инженерных материалов (Университет им. Монаша, Мельбурн, Австралия).

Scopus AuthorID: [7005031984](#)

CONTENT

Influence of roller characteristics on powder layer applying in additive technologies Bogdanov V.M.	9
Computer prediction of fracture of magnesium alloy cylindrical billet during equal channel angular pressing Volkova E.P., Khudododova G.D., Botkin A.V., Valiev R.Z.	19
Phase composition, structure and microhardness of the VT23 titanium alloy after deformation in a Bridgman chamber Gladkovsky S.V., Pilyugin V.P., Veselova V.E., Patselov A.M.	29
Study of centrifugal atomisation mechanisms based on a simulated experiment Zhukov E.Yu., Naurzalinov A.S., Pashkov I.N.	39
On the formation of thermal barrier coatings by magnetron sputtering Kachalin G.V., Medvedev K.S., Mednikov A.F., Zilova O.S., Tkhabisimov A.B., Ilyukhin D.I., Kasyanenko V.A.	51
Electrochemical interaction between biodegradable ZX10 and WZ31 magnesium alloys and medical Ti6Al4V titanium alloy Myagkikh P.N., Merson E.D., Poluyanov V.A., Merson D.L., Begun M.E.	63
Intensification of the process of equal channel angular pressing using ultrasonic vibrations Rubanik V.V., Lomach M.S., Rubanik V.V. Jr., Lutsko V.F., Gusakova S.V.	73
Universal model for predicting the phase composition of multicomponent brasses based on chemical analysis data Svyatkin A.V., Kostin G.V.	87
Effect of alloy composition on machining parameters and surface quality through comprehensive analysis Shailesh Rao A., Rao S.	97
Predictive fatigue life modelling for aluminum alloys winder high temperature and shot peening interact Alwin A.H., Ksibi H.	111
OUR AUTHORS	123

СОДЕРЖАНИЕ

Влияние характеристик ролика на нанесение порошкового слоя в аддитивных технологиях Богданов В.М.	9
Компьютерное прогнозирование разрушения цилиндрической заготовки из магниевого сплава в процессе равноканального углового прессования Волкова Е.П., Худододова Г.Д., Боткин А.В., Валиев Р.З.	19
Фазовый состав, структура и микротвердость титанового сплава VT23 после деформации в камере Бриджмена Гладковский С.В., Пилюгин В.П., Веселова В.Е., Пацелов А.М.	29
Исследование механизмов центробежного распыления на основе модельного эксперимента Жуков Е.Ю., Наурзалинов А.С., Пашков И.Н.	39
К вопросу о формировании термобарьерных покрытий методом магнетронного распыления Качалин Г.В., Медведев К.С., Медников А.Ф., Зилова О.С., Тхабисимов А.Б., Илюхин Д.И., Касьяненко В.А.	51
Электрохимическое взаимодействие между биорезорбируемыми магниевыми сплавами ZX10 и WZ31 и медицинским титановым сплавом Ti6Al4V Мягих П.Н., Мерсон Е.Д., Полуянов В.А., Мерсон Д.Л., Бегун М.Э.	63
Интенсификация процесса равноканального углового прессования с помощью ультразвуковых колебаний Рубаник В.В., Ломач М.С., Рубаник В.В. мл., Луцко В.Ф., Гусакова С.В.	73
Универсальная модель прогнозирования фазового состава многокомпонентных латуней на основе данных химического анализа Святкин А.В., Костин Г.В.	87
Оценка влияния состава сплава на параметры обработки и качество поверхности посредством комплексного анализа Шайлеш Рао А., Рао Ш.	97
Прогнозное моделирование усталостной долговечности алюминиевых сплавов при повышенных температурах после воздействия дробеструйного упрочнения Элвин А.Х., Ксиби Х.	111
НАШИ АВТОРЫ	123

Influence of roller characteristics on powder layer applying in additive technologies

Valery M. Bogdanov, postgraduate student

Peter the Great St. Petersburg Polytechnic University, St. Petersburg (Russia)

*E-mail: bogdanov.vm@edu.spbstu.ru

ORCID: <https://orcid.org/0009-0006-6865-3579>

Received 08.05.2024

Revised 18.09.2024

Accepted 07.11.2024

Abstract: In the study and analysis of additive technologies, special attention is paid to increasing the productivity and quality of printed products. However, to improve the 3D printing productivity, it is impossible to increase simply the speed of the squeegee without changing its shape or type. In this case, the quality of the powder layer may suffer, which will lead to a deterioration in the qualities of the final part. To study the effect of roller characteristics on the powder layer deposition, a series of computer simulations of simulation models was carried out. The effect of roller characteristics on the powder layer applying, was assessed, for roller diameters of 30, 50, 70, 100, 150, 200, 250, 300 mm. The simulation was carried out with three application methods: by a rotating and non-rotating roller, as well as by a rotating roller with additional powder feed. It was determined that when applying a layer with a rotating roller with additional powder feed, it is possible to achieve constancy of the forces acting on the roller. This can positively affect the homogeneity of the applied layer. The application of a layer by a rotating roller with additional powder feed is most suitable for 3D printers with a large print area. This method allows avoiding the movement of a large mass of powder over the previous layer, which positively influences the quality of the final part. The study revealed the influence of roller characteristics on the deposition of a powder layer. In particular, with an increase in the roller diameter from 30 to 300 mm, the peak force value also increases. With an increase in the roller diameter by 7.9 %, the powder layer density also increases. It was found that the non-rotating roller is affected by the greatest force, and the forces acting on the rotating rollers differ slightly. A rotating roller, without adding powder, creates the densest layer and allows achieving a powder layer compaction of 5.35 %.

Keywords: roller characteristics; powder layer; additive technologies; additive manufacturing; roller diameter; powder layer levelling; powder layer applying; powder layer density; squeegee.

For citation: Bogdanov V.M. Influence of roller characteristics on powder layer applying in additive technologies. *Frontier Materials & Technologies*, 2024, no. 4, pp. 9–18. DOI: 10.18323/2782-4039-2024-4-70-1.

INTRODUCTION

Additive technologies are advanced technologies at the current stage of mechanical engineering development. They allow creating complex products that are impractical or impossible to produce using traditional methods. In the study and analysis of additive technologies, special attention is paid to increasing the productivity and quality of printed products. Increasing requirements for the accuracy of a part leads to an increase in the time for its creation. The time of creating a part, consists of the time of applying the powder layer, and the time of its fusion. Powder deposition is a fundamental aspect of additive manufacturing, and requires great research efforts to improve the reliability and repeatability of the process, and consequently, the quality of printed components.

The main device for applying and levelling the powder layer in additive installations is a squeegee. Currently, two squeegee designs are used, most often as a levelling device: in the form of a plate (blade) and in the form of a rotating roller. Roller application mechanisms are used when applying finely dispersed, or highly cohesive powders, to ensure the desired technological characteristics and/or properties of components. The blade-type squeegee has a simpler design and can be used to apply powders with high flowabi-

lity, that do not require large applied forces to overcome interparticle adhesion.

To increase productivity, it is impossible to increase simply the squeegee speed without changing its shape or type. This may affect the quality of the powder layer, which will lead to a deterioration in the quality of the final part [1]. Therefore, the main trend in the field of powder applying and levelling, is to study possible squeegee designs to find a design with the highest deposition rate without losing the quality of the layer.

Research shows that a high powder layer density is required to produce a high-quality layer, and a metal powder with the smallest average particle size should be used [2]. To improve the powder layer density, the author proposed technologies for powder layer compaction [3; 4], vibration application [5; 6], and repeated passing by rotating rollers [7; 8]. The geometry and speed of the levelling device have the greatest influence on the powder packing density [9; 10]. The following squeegee profiles were considered – a square with a chamfer, a rotating and fixed roller [9], a parallelogram, a triangle and a square [10]. Research shows that by optimising the squeegee geometry, it is possible to achieve higher packing density values, and lower roughness of the applied powder layer [10; 11].

The author considered 48 models with different parameters of the squeegee edge profile [11]. As a result, the optimum values for these parameters were determined. When comparing the optimised profile with the roller, it was noted that the squeegee with the optimised profile created a slightly lower powder layer density (0.4 %) at the lowest speed (0.03 m/s). However, it turned out to be much less sensitive to increasing the squeegee speed, so that when the speed was increased to 0.06 m/s, the powder layer density was 2 % higher for the squeegee with the optimised profile. This is a significant advantage and means that the speed can be increased (which means higher productivity) while maintaining quality. When comparing the roughness of the powder layer surface, it was found that the new squeegee profile is superior to the roller at all tested speeds, and has an average of 15 % lower roughness values [11].

A distinctive feature of the considered studies [3–11] is that the powder layer is applied to a smooth, hard surface. The literature does not consider the case of applying a new layer to the previous powder layer, and no studies have been found on the effect of the rotating roller diameter on the applied layer. The force acting on the roller from the powder side, and the distribution of this force over the surface, as well as the dependence of the compressive force and powder density on the roller diameter and on this application method are of interest.

The purpose of the work is to identify the optimal method for applying a powder layer, by studying the influence of the rotating roller diameter on the quality of the applied layer using simulation modelling.

METHODS

Simulation model creation

The simulation of the process of powder material applying and levelling was carried out using the Altair EDEM

2021 software package. This is software for modelling bulk and granular materials. EDEM software package is based on the discrete element method (DEM) and is applicable to modelling and analysing the behaviour of coal, mined ores, soils, fibres, grains, tablets, powders, etc.

Most additive technologies included in the PBF (Powder Bed Fusion) group have a similar process of powder layer applying. Fig. 1 shows the basic diagram of the process.

The cycle of building each layer begins with raising the feeder platform and lowering the build platform by the layer thickness. Then, the squeegee moves along the platforms, simultaneously applying and levelling the powder material. Since only one powder layer will be applied during the process simulation, a feeding hopper is not required. To simplify the simulation model, the preparation stage is limited to creating the previous powder layer and powder for applying a new layer.

The created simulation model consists of two sections (Fig. 2). The first section is a hard surface simulating a feeder with metal powder, which will need to be applied as a new layer using a squeegee. The second section is a hard surface simulating a build platform lowered to the height of the layer being applied. This section contains an imitation of the finished applied layer.

Metal powder applying to the finished layer imitation is performed in three ways: 1) by a non-rotating roller; 2) by a rotating roller; 3) by a rotating roller with additional powder feed (Fig. 3).

Identification and selection of modelling parameters

First, it is necessary to select the application speed V_{ROL} and the roller rotation speed V_{ROT} . The application speed affects the powder layer roughness [12] (Fig. 4), which is one of the characteristics of the powder layer quality. Based on Fig. 4, we assume that the permissible roughness of the applied layer surface is $\delta=7.5 \mu\text{m}$. To obtain the powder layer surface of the required quality, the roller

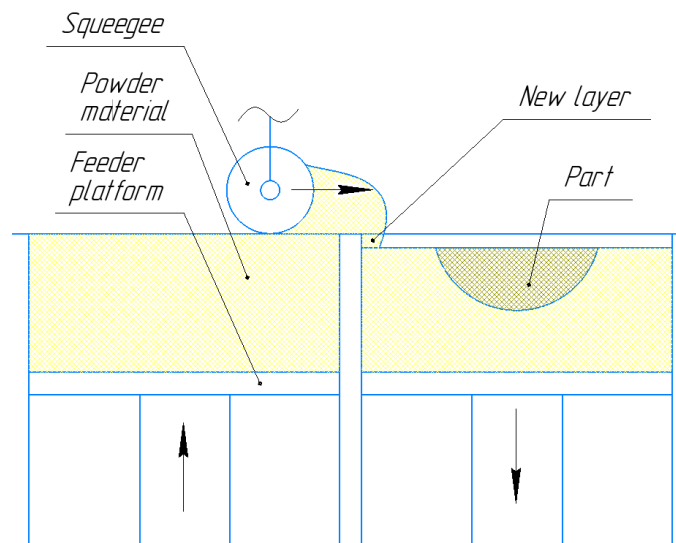


Fig. 1. Basic diagram of the process of applying a powder layer
Рис. 1. Принципиальная схема процесса нанесения порошкового слоя

linear speed V_{ROL} must not exceed 60 mm/s. In studies, the application speed was most often chosen equal to $V_{ROL}=50$ mm/s [10; 13; 14], which meets our requirements. The rotation speed V_{ROT} was chosen equal to 60 rpm assuming that the roller rotation speed has little effect on the powder layer density, however, at high speeds, powder particles begin to be thrown above the surface, which can lead to the previous layer damage [15].

To identify the optimal method for applying a powder layer, studies were conducted on a simulation model with different roller diameters: a non-rotating roller $\varnothing 50$ mm, a rotating roller $\varnothing 30, 50, 70$ mm, a rotating roller with the addition of powder $\varnothing 30, 50, 70, 100, 150, 200, 250, 300$ mm.

The diameter of the powder particles used in 3D printing varies from 20 to 100 μm . However, the available

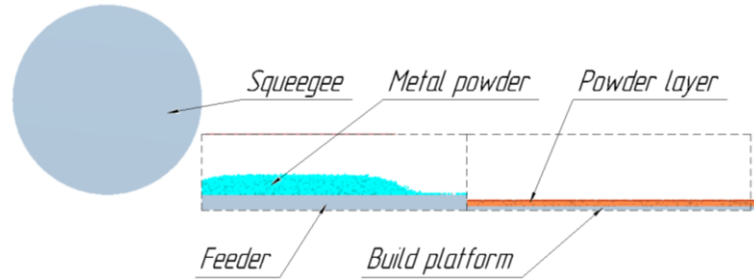


Fig. 2. Simulation model
Рис. 2. Имитационная модель

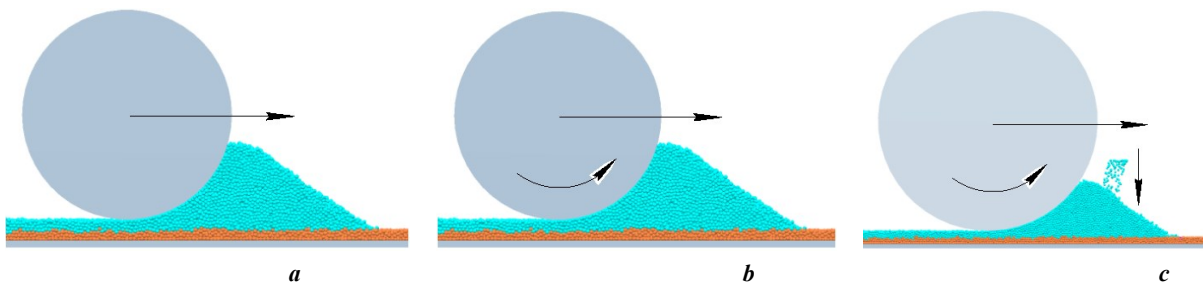


Fig. 3. Ways of applying a powder layer:
a – a non-rotating roller; b – a rotating roller; c – a rotating roller with additional powder feed

Рис. 3. Способы нанесения порошкового слоя:
a – невращающийся ролик; b – вращающийся ролик; c – вращающийся ролик с подачей дополнительного порошка

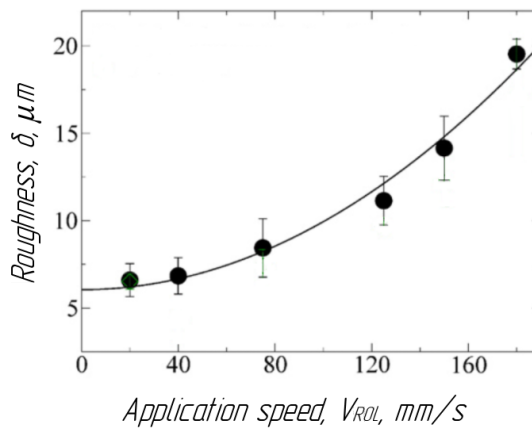


Fig. 4. Dependence of layer roughness on application speed
Рис. 4. Зависимость шероховатости слоя от скорости нанесения

computer processing power will not be enough to simulate particles of such a small size in a short time, because when the particle diameter decreases, it is also necessary to decrease the time step, and therefore, the calculations will be more time-consuming. DSL 05 365 GOST 11964-81 shot was chosen as the powder material.

For the study, the powder granulometric composition having a normal distribution with a mean value of $m=0.5$ mm and a standard deviation of $\sigma=0.05$ was chosen, because wider ranges of particle sizes lead to greater fluctuations in density and surface roughness due to the uneven distribution of particles [16].

The computer for the simulation has an Intel Core i3-6100 3.70 GHz processor, 8 GB of RAM, and an NVIDIA GeForce GTX 1050 Ti video card.

Processing the simulation results

To measure the force acting on the roller, the entire study area was divided into layers. The height of each layer is equal to the diameter of the particles (0.5 mm). Data on the force acting on the roller from the powder along the X and Z axes were obtained from each separately selected area (Fig. 5).

In the analysis, we will assume that the force is applied to the roller at the centre of the selected layer. After calculating the force, it is necessary to plot the force distribution over the roller surface. To do this, we will analytically calculate the dependence of the angle α on the layer height. The calculation scheme is shown in Fig. 6.

Calculation of the dependence of the angle α on the layer height:

$$\cos \alpha = \frac{R-t}{R} \rightarrow \alpha = \arccos \left(1 - \frac{t}{R} \right).$$

Now, we can associate the obtained force values with the angle α , and apply them to the roller. As a result, you will get a graph of the force distribution over the roller.

RESULTS

From the graphs of the total force acting on a non-rotating roller with a diameter of 50 mm, depending on the pressure angle, one can see that the force acting on the roller becomes smaller over time (Fig. 7). This is

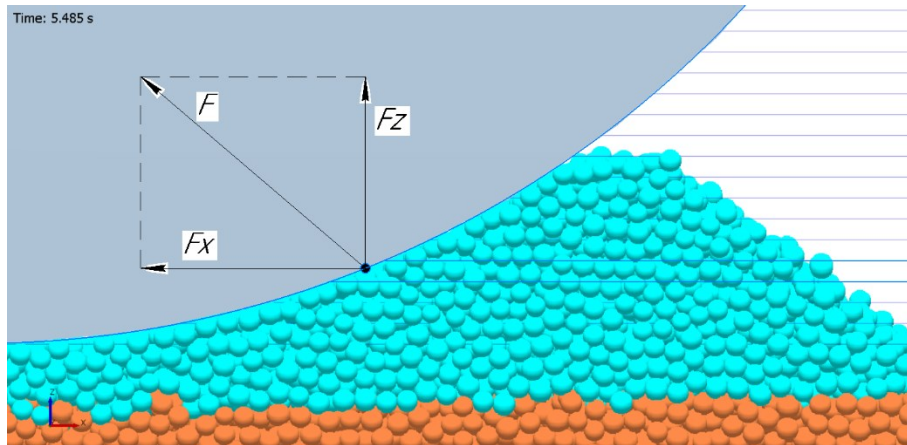


Fig. 5. Calculation of the total force of powder pressure on the roller in each layer
Рис. 5. Расчет общей силы давления порошка на ролик в каждом слое

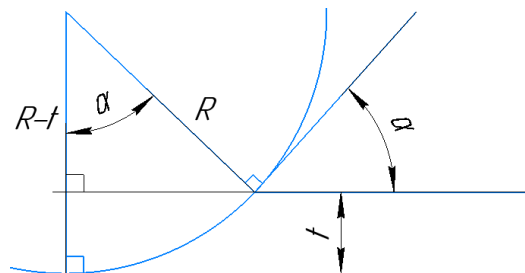


Fig. 6. Scheme for calculating the pressure angle α .
 R – roller radius; t – layer height; α – pressure angle
Рис. 6. Схема для расчета угла давления α .
 R – радиус ролика; t – высота слоя; α – угол давления

explained by the fact that the amount of powder applied by the roller decreases over time.

One of the most important parameters of the powder layer is its density. The maximum value of the powder layer density during application reached 4.573 g/cm^3 , which corresponds to a layer compaction of 1.61%. According to GOST 11964-81, the bulk density of steel powder should be greater than 4.2 g/cm^3 , with a particle diameter of 0.5 mm and a density of the particles themselves of more than 7.2 g/cm^3 . The result obtained satisfies this condition, which indicates the proximity of the characteristics of the simulated and real powders.

From the graphs of the total force acting on a rotating roller with diameters of 30, 50 and 70 mm, depending on the pressure angle, it is evident that with an increase in the roller diameter, the peak force value also increases (Fig. 8). This can increase roller wear and reduce its service life. For a better understanding of the meaning of this graph (Fig. 8), the curves were applied to the roller, which allowed obtaining a visual representation of the force distribution over the roller (Fig. 9). Analysing the maximum density values for the studied roller diameters, one can notice a clear dependence manifested in an increase in density, with an increase in the roller diameter (Table 1).

From the graphs of the total force acting on a rotating roller with additional powder feed, depending on the pressure angle, it is evident that with an increase in the roller diameter from 30 to 300 mm, the peak force value increases, and the pressure angle decreases (Fig. 10). From Table 2 it is evident that as the roller diameter increases, the powder layer density also increases, and after overcoming the roller diameter of $D=200 \text{ mm}$, it reaches a plateau and stops growing significantly.

DISCUSSION

The EDEM software package has proven itself as a promising tool for predicting the behaviour of bulk media [17]. The results of computer modelling using the discrete element method, qualitatively correspond to the data obtained in experiments [18]. Based on this, the obtained modelling results can be considered to correspond to reality.

To identify the best application method, the graphs of the total force acting on a roller with a diameter of $D=50 \text{ mm}$, depending on the pressure angle for each application method were compared (Fig. 11). As a result, it can be concluded that the non-rotating roller is affected by the greatest force, and the forces acting on rotating rollers differ slightly. When comparing the maximum density values for the studied application methods, it can be concluded that a denser powder layer can be achieved when using a rotating roller without adding powder (Table 3).

Based on the analysis of a series of computer simulations of powder layer application, it was found that the total force acting on the rollers, without additional powder supply, becomes smaller over time. This is explained by the fact that the amount of powder applied by the roller decreases over time. This application method is suitable for 3D printers with a small printing zone. As the printing zone increases, the amount of powder that needs to be applied also increases. This poses two problems. First, the powder bed height with a large printing zone may exceed the roller diameter, making it impossible to form a layer. Second, moving a large mass of powder over the previously applied layer may damage it, and adversely affect the quality of the final part.

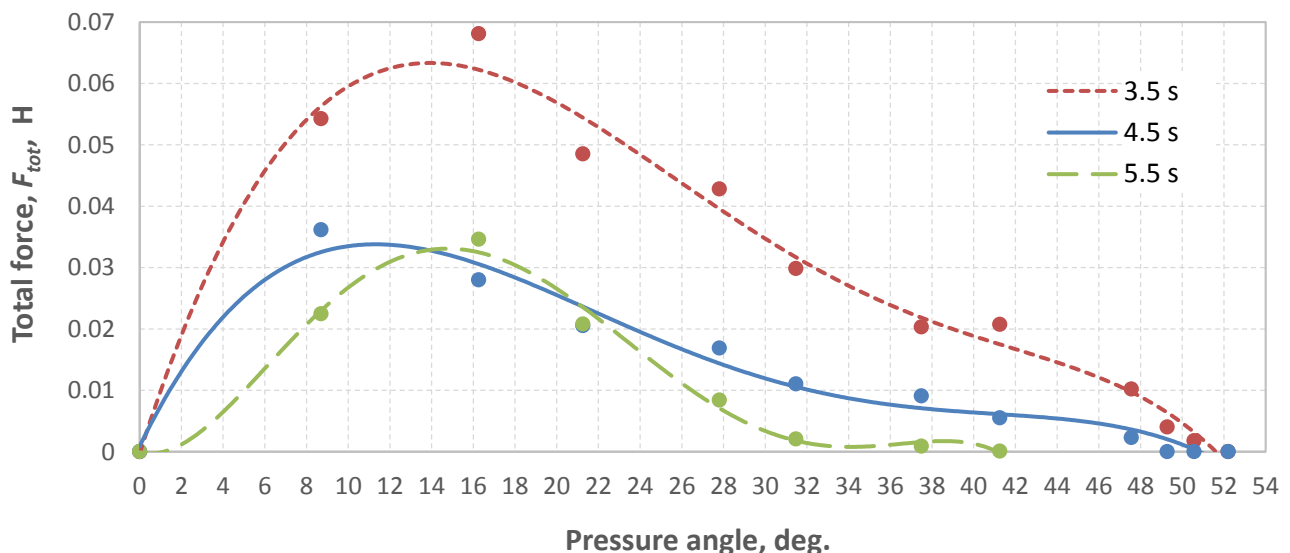


Fig. 7. Dependence of the total force acting on a non-rotating roller with a diameter of 50 mm on the pressure angle.

Three time points of the steady-state application mode are given: start – 3.5 s, centre – 4.5 s, end – 5.5 s

Рис. 7. Зависимость общей силы, действующей на невращающийся ролик диаметром 50 мм, от угла давления. Приведены три временные точки установившегося режима нанесения: начало – 3,5 с, центр – 4,5 с, конец – 5,5 с

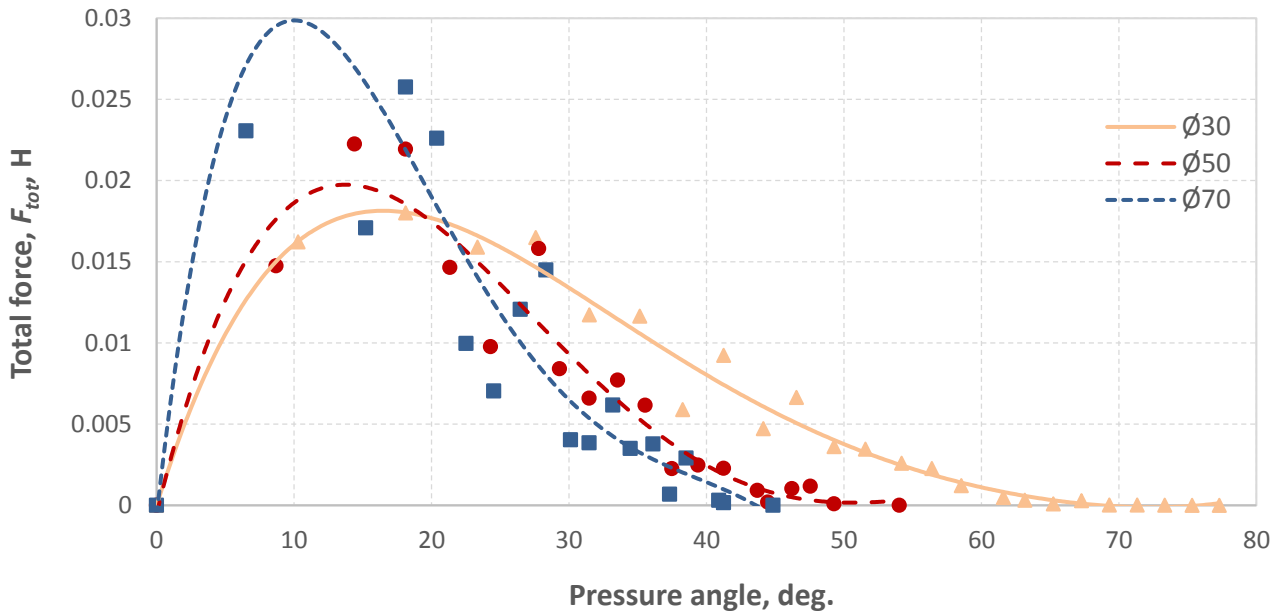


Fig. 8. Dependence of the total force acting on a rotating roller on the pressure angle.

Graphs are given for three roller diameters: 30, 50, 70 mm

Рис. 8. Зависимость общей силы, действующей на вращающийся ролик, от угла давления.

Приведены графики для трех диаметров ролика: 30, 50, 70 мм

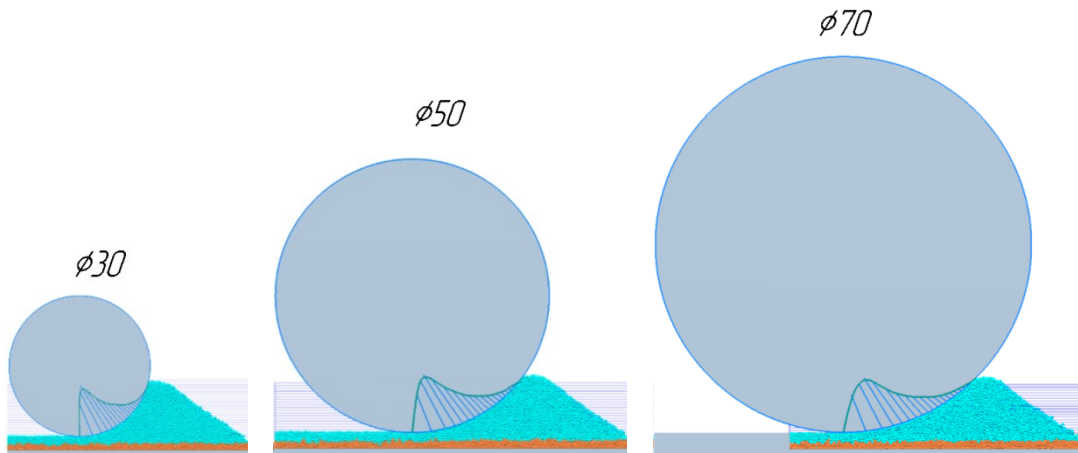


Fig. 9. Force distribution over the rollers with the diameters of 30, 50, 70 mm

Рис. 9. Распределение силы по роликам с диаметрами 30, 50, 70 мм

Table 1. Powder layer density and compaction for rotating rollers

Таблица 1. Плотность и уплотнение порошкового слоя для вращающихся роликов

Roller diameter, mm	Layer density, g/cm ³	Layer compaction, %
Before application	4.500	—
30	4.692	4.26
50	4.740	5.35
70	4.796	6.59

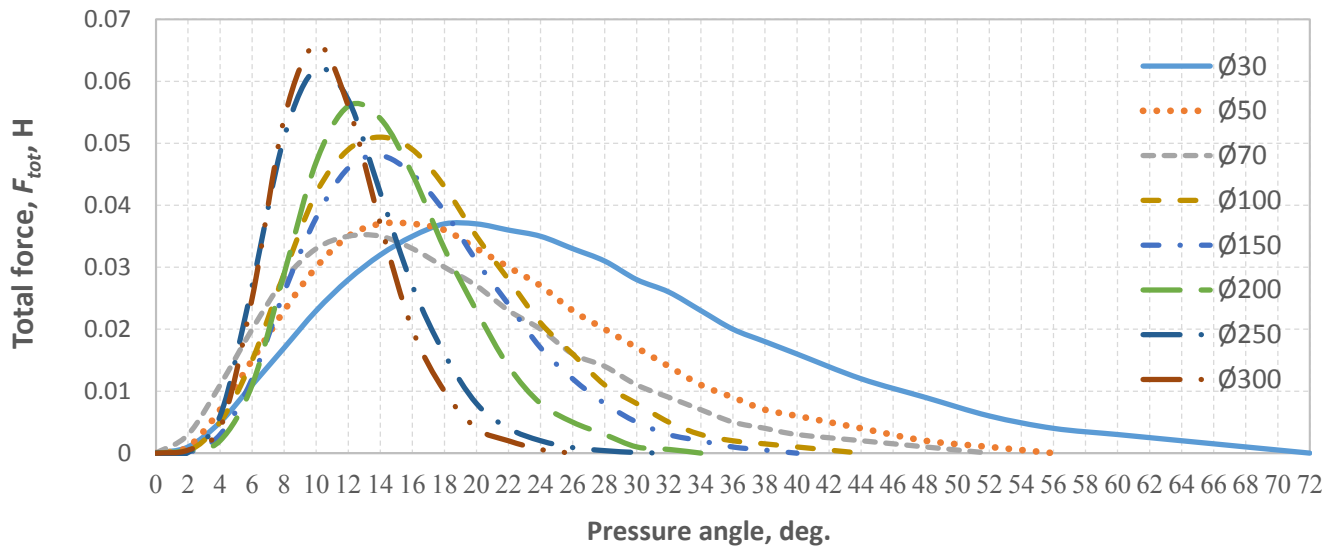


Fig. 10. Dependence of the total force acting on a rotating roller with additional powder feed on the pressure angle.

Graphs are given for eight roller diameters: 30, 50, 70, 100, 150, 200, 250, 300 mm

Рис. 10. Зависимость общей силы, действующей на вращающийся ролик с дополнительной подачей порошка, от угла давления. Приведены графики для восьми диаметров ролика: 30, 50, 70, 100, 150, 200, 250, 300 мм

Table 2. Powder layer density and compaction for rotating rollers with additional powder feed

Таблица 2. Плотность и уплотнение порошкового слоя для вращающихся роликов с дополнительной подачей порошка

Roller diameter, mm	Layer density, g/cm ³	Layer compaction, %
Before application	4.500	–
30	4.675	3.89
50	4.679	3.98
70	4.682	4.04
100	4.800	6.66
150	4.810	6.89
200	4.854	7.87
250	4.849	7.75
300	4.855	7.90

When applying a layer with a rotating roller with an additional powder feed, it is possible to achieve a constant force acting on the roller, since there is the same amount of powder in front of the roller during application. This can have a positive effect on the homogeneity of the applied layer.

It has been found that when the roller diameter increases from 30 to 300 mm, the peak force value also increases. This can increase roller wear and reduce its service life. With an increase in the roller diameter, the powder layer density also increases by 7.9 % and after overcoming

the roller diameter of $D=200$ mm, the powder layer density reaches a plateau and stops growing significantly.

Summarising the data, we can conclude that the non-rotating roller is affected by the greatest force, and the forces acting on the rotating rollers, differ slightly. It was also found that a rotating roller without adding powder, creates the densest layer and allows achieving compaction of the powder layer by 5.35 %. The obtained data contradict the study, which revealed that a non-rotating roller creates a 5 % denser layer than a rotating roller [9]. This discrepancy can be explained by a significant

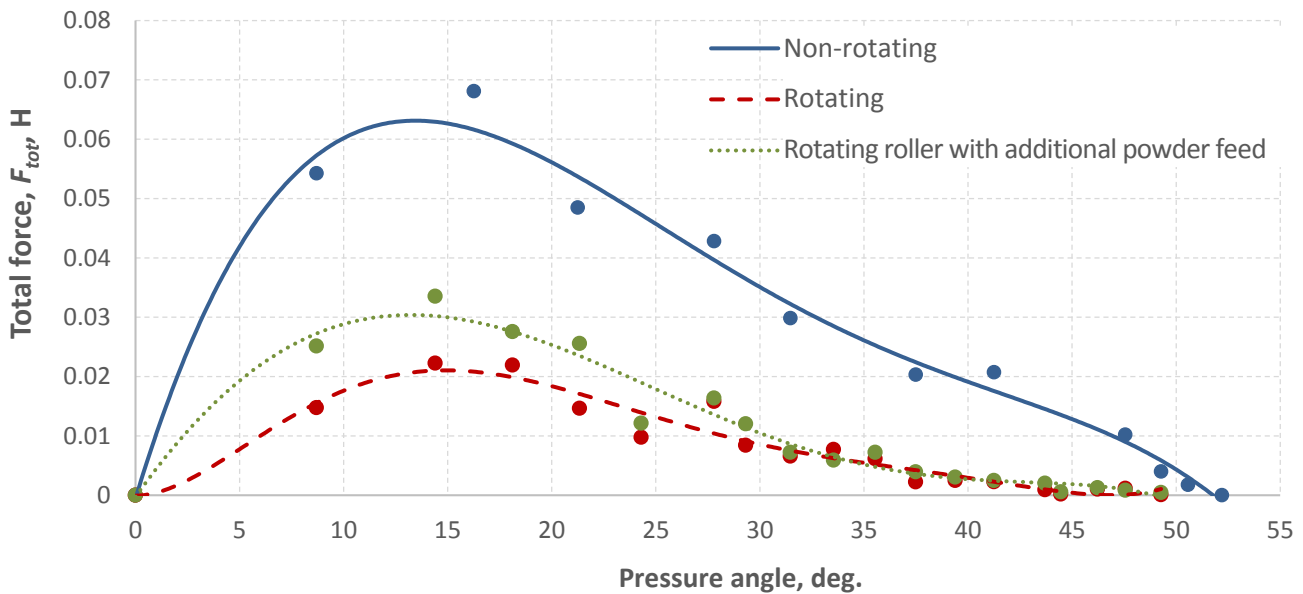


Fig. 11. Dependence of the total force acting on a non-rotating roller and a rotating roller with additional powder feed on the pressure angle. Graphs are given for the roller with a diameter of 50 mm

Рис. 11. Зависимость общей силы, действующей на неврвращающийся ролик, вращающийся ролик и вращающийся ролик с дополнительной подачей порошка, от угла давления. Приведены графики для ролика диаметром 50 мм

Table 3. Powder layer density and compaction for various methods of application
Таблица 3. Плотность и уплотнение порошкового слоя для различных способов нанесения

Method of application	Roller diameter, mm	Layer density, g/cm ³	Layer compaction, %
Before application	–	4.500	–
Non-rotating roller	50	4.573	1.61
Rotating roller		4.740	5.35
Rotating roller with additional powder feed		4.679	3.98

difference in the powder layer application speed (0.5 and 50 mm/s). When analysing the effect of application speed on powder layer density, it was found that with an increase in application speed, the powder layer density tends to decrease linearly [9].

In a study on optimising squeegee geometry, when comparing an optimised profile with a roller, it was noted that the squeegee with an optimised profile created a slightly higher powder bed density (0.7 %) at an application speed of 50 mm/s [11].

The study was the first to examine the influence of roller diameter on powder bed density. The data obtained indicate that the correct choice of application method can significantly affect the quality of printed products.

CONCLUSIONS

1. The dependences of the roller characteristics on powder layer application were revealed. In particular, with an

increase in the roller diameter from 30 to 300 mm, the peak force value also increases. With an increase in the roller diameter by 7.9 %, the powder layer density also increases, and after overcoming the roller diameter of $D=200$ mm, it reaches a plateau and stops growing significantly.

2. When studying the application methods, it was found that the non-rotating roller is affected by the greatest force, and the forces acting on the rotating rollers differ slightly. A rotating roller without adding powder creates the densest layer, and allows achieving compaction of the powder layer by 5.35 %.

3. When optimising powder layer application for 3D printers with a large printing area, it is recommended to select layer application using a roller with additional powder feed, since this helps to avoid moving a large mass of powder over the previously applied layer, which has a positive effect on the quality of the final product. This can also have a positive effect on the homogeneity of the applied layer.

REFERENCES

- Chen Hui, Chen Yuxiang, Liu Ying, Wei Qingsong, Shi Yusheng, Yan Wentao. Packing quality of powder layer during counter-rolling-type powder spreading process in additive manufacturing. *International Journal of Machine Tools and Manufacture*, 2020, vol. 153, article number 103553. DOI: [10.1016/j.ijmactools.2020.103553](https://doi.org/10.1016/j.ijmactools.2020.103553).
- Cao Liu. Numerical simulation of the impact of laying powder on selective laser melting single-pass formation. *International Journal of Heat and Mass Transfer*, 2019, vol. 141, pp. 1036–1048. DOI: [10.1016/j.ijheatmasstransfer.2019.07.053](https://doi.org/10.1016/j.ijheatmasstransfer.2019.07.053).
- Budding A., Vaneker T.H.J. New strategies for powder compaction in powder-based rapid prototyping techniques. *Procedia CIRP*, 2013, vol. 6, pp. 527–532. DOI: [10.1016/j.procir.2013.03.100](https://doi.org/10.1016/j.procir.2013.03.100).
- Li Ming, Wei Xingjian, Pei Zhijian, Ma Chao. Binder jetting additive manufacturing: observations of compaction-induced powder bed surface defects. *Manufacturing Letters*, 2021, vol. 28, pp. 50–53. DOI: [10.1016/j.mfglet.2021.04.003](https://doi.org/10.1016/j.mfglet.2021.04.003).
- Nasato D.S., Briesen H., Pöschel T. Influence of vibrating recoating mechanism for the deposition of powders in additive manufacturing: Discrete element simulations of polyamide 12. *Additive Manufacturing*, 2021, vol. 48-A, article number 102248. DOI: [10.1016/j.addma.2021.102248](https://doi.org/10.1016/j.addma.2021.102248).
- Zhang Jiangtao, Tan Yanqiang, Bao Tao, Xu Yangli, Jiang Shengqiang. Discrete element simulation for effects of roller's vibrations on powder spreading quality. *China Mechanical Engineering*, 2020, vol. 31, pp. 1717–1723. DOI: [10.3969/j.issn.1004-132X.2020.14.011](https://doi.org/10.3969/j.issn.1004-132X.2020.14.011).
- Chen Hui, Cheng Tan, Wei Qingsong, Yan Wentao. Dynamics of short fiber/polymer composite particles in paving process of additive manufacturing. *Additive Manufacturing*, 2021, vol. 47, article number 102246. DOI: [10.1016/j.addma.2021.102246](https://doi.org/10.1016/j.addma.2021.102246).
- Meyer L., Wegner A., Witt G. Influence of the ratio between the translation and contra-rotating coating mechanism on different laser sintering materials and their packing density. *Solid Freeform Fabrication 2017: Proceedings of the 28th Annual International Solid Freeform Fabrication Symposium – An Additive Manufacturing Conference Reviewed Paper*. Texas, University of Texas at Austin Publ., 2017, pp. 1432–1447.
- Cao Liu. Study on the numerical simulation of laying powder for the selective laser melting process. *The International Journal of Advanced Manufacturing Technology*, 2019, vol. 105, pp. 2253–2269. DOI: [10.1007/s00170-019-04440-4](https://doi.org/10.1007/s00170-019-04440-4).
- Wang Lin, Yu Aibing, Li Erlei, Shen Haopeng, Zhou Zongyan. Effects of spreader geometry on powder spreading process in powder bed additive manufacturing. *Powder Technology*, 2021, vol. 384, pp. 211–222. DOI: [10.1016/j.powtec.2021.02.022](https://doi.org/10.1016/j.powtec.2021.02.022).
- Haeri S. Optimization of blade type spreaders for powder bed preparation in Additive Manufacturing using DEM simulations. *Powder Technology*, 2017, vol. 321, pp. 94–104. DOI: [10.1016/j.powtec.2017.08.011](https://doi.org/10.1016/j.powtec.2017.08.011).
- Parteli E.J.R., Poschel Th. Particle-based simulation of powder application in additive manufacturing. *Powder Technology*, 2016, vol. 288, pp. 96–102. DOI: [10.1016/j.powtec.2015.10.035](https://doi.org/10.1016/j.powtec.2015.10.035).
- Wang L., Li E.L., Shen H., Zou R.P., Yu A.B., Zhou Z.Y. Adhesion effects on spreading of metal powders in selective laser melting. *Powder Technology*, 2020, vol. 363, pp. 602–610. DOI: [10.1016/j.powtec.2019.12.048](https://doi.org/10.1016/j.powtec.2019.12.048).
- Yao Dengzhi, An Xizhong, Zhang Haitao, Yang Xiaohong, Zou Qingchuan, Dong Kejun. Dynamic investigation on the powder spreading during selective laser melting additive manufacturing. *Additive Manufacturing*, 2021, vol. 37, pp. 101–113. DOI: [10.1016/j.addma.2020.101707](https://doi.org/10.1016/j.addma.2020.101707).
- Zhang Jiangtao, Tan Yuanqiang, Bao Tao, Xu Yangli, Xiao Xiangwu, Jiang Shengqiang. Discrete element simulation of the effect of roller-spreading parameters on powder-bed density in additive manufacturing. *Materials*, 2020, vol. 13, no. 10, pp. 2285–2300. DOI: [10.3390/ma13102285](https://doi.org/10.3390/ma13102285).
- Ya Zhao, Jia Wei Chew. Effect of lognormal particle size distributions on particle spreading in additive manufacturing. *Advanced Powder Technology*, 2021, vol. 32, no. 4, pp. 1127–1144. DOI: [10.1016/j.apt.2021.02.019](https://doi.org/10.1016/j.apt.2021.02.019).
- Feoktistov A.Yu., Kamenetskiy A.A., Blekhman L.I., Vasilkov V.B., Skryabin I.N., Ivanov K.S. The application of discrete element method to mining and metallurgy process modeling. *Zapiski Gornogo instituta*, 2011, vol. 192, pp. 145–149. EDN: [ROWFBF](https://doi.org/10.1016/j.zgorn.2011.04.003).
- Lee Y., Simunovic S., Gurnon A.K. *Quantification of powder spreading process for metal additive manufacturing: technical report*. Tennessee: OAK Ridge National Laboratory Publ., 2019. 36 p.

СПИСОК ЛИТЕРАТУРЫ

- Chen Hui, Chen Yuxiang, Liu Ying, Wei Qingsong, Shi Yusheng, Yan Wentao. Packing quality of powder layer during counter-rolling-type powder spreading process in additive manufacturing // International Journal of Machine Tools and Manufacture. 2020. Vol. 153. Article number 103553. DOI: [10.1016/j.ijmactools.2020.103553](https://doi.org/10.1016/j.ijmactools.2020.103553).
- Cao Liu. Numerical simulation of the impact of laying powder on selective laser melting single-pass formation // International Journal of Heat and Mass Transfer. 2019. Vol. 141. P. 1036–1048. DOI: [10.1016/j.ijheatmasstransfer.2019.07.053](https://doi.org/10.1016/j.ijheatmasstransfer.2019.07.053).
- Budding A., Vaneker T.H.J. New strategies for powder compaction in powder-based rapid prototyping techniques // Procedia CIRP. 2013. Vol. 6. P. 527–532. DOI: [10.1016/j.procir.2013.03.100](https://doi.org/10.1016/j.procir.2013.03.100).
- Li Ming, Wei Xingjian, Pei Zhijian, Ma Chao. Binder jetting additive manufacturing: observations of compaction-induced powder bed surface defects // Manufacturing Letters. 2021. Vol. 28. P. 50–53. DOI: [10.1016/j.mfglet.2021.04.003](https://doi.org/10.1016/j.mfglet.2021.04.003).
- Nasato D.S., Briesen H., Pöschel T. Influence of vibrating recoating mechanism for the deposition of powders in additive manufacturing: Discrete element simulations of polyamide 12 // Additive Manufacturing. 2021. Vol. 48-A. Article number 102248. DOI: [10.1016/j.addma.2021.102248](https://doi.org/10.1016/j.addma.2021.102248).
- Zhang Jiangtao, Tan Yanqiang, Bao Tao, Xu Yangli, Jiang Shengqiang. Discrete element simulation for effects of roller's vibrations on powder spreading quality // China Mechanical Engineering. 2020. Vol. 31. P. 1717–1723. DOI: [10.3969/j.issn.1004-132X.2020.14.011](https://doi.org/10.3969/j.issn.1004-132X.2020.14.011).
- Chen Hui, Cheng Tan, Wei Qingsong, Yan Wentao. Dynamics of short fiber/polymer composite particles in paving process of additive manufacturing // Additive Manufacturing. 2021. Vol. 47. Article number 102246. DOI: [10.1016/j.addma.2021.102246](https://doi.org/10.1016/j.addma.2021.102246).

8. Meyer L., Wegner A., Witt G. Influence of the ratio between the translation and contra-rotating coating mechanism on different laser sintering materials and their packing density // Solid Freeform Fabrication 2017: Proceedings of the 28th Annual International Solid Freeform Fabrication Symposium – An Additive Manufacturing Conference Reviewed Paper. Texas: University of Texas at Austin, 2017. P. 1432–1447.
9. Cao Liu. Study on the numerical simulation of laying powder for the selective laser melting process // The International Journal of Advanced Manufacturing Technology. 2019. Vol. 105. P. 2253–2269. DOI: [10.1007/s00170-019-04440-4](https://doi.org/10.1007/s00170-019-04440-4).
10. Wang Lin, Yu Aibing, Li Erlei, Shen Haopeng, Zhou Zongyan. Effects of spreader geometry on powder spreading process in powder bed additive manufacturing // Powder Technology. 2021. Vol. 384. P. 211–222. DOI: [10.1016/j.powtec.2021.02.022](https://doi.org/10.1016/j.powtec.2021.02.022).
11. Haeri S. Optimization of blade type spreaders for powder bed preparation in Additive Manufacturing using DEM simulations // Powder Technology. 2017. Vol. 321. P. 94–104. DOI: [10.1016/j.powtec.2017.08.011](https://doi.org/10.1016/j.powtec.2017.08.011).
12. Parteli E.J.R., Poschel Th. Particle-based simulation of powder application in additive manufacturing // Powder Technology. 2016. Vol. 288. P. 96–102. DOI: [10.1016/j.powtec.2015.10.035](https://doi.org/10.1016/j.powtec.2015.10.035).
13. Wang L., Li E.L., Shen H., Zou R.P., Yu A.B., Zhou Z.Y. Adhesion effects on spreading of metal powders in selective laser melting // Powder Technology. 2020. Vol. 363. P. 602–610. DOI: [10.1016/j.powtec.2019.12.048](https://doi.org/10.1016/j.powtec.2019.12.048).
14. Yao Dengzhi, An Xizhong, Zhang Haitao, Yang Xiaohong, Zou Qingchuan, Dong Kejun. Dynamic investigation on the powder spreading during selective laser melting additive manufacturing // Additive Manufacturing. 2021. Vol. 37. P. 101–113. DOI: [10.1016/j.addma.2020.101707](https://doi.org/10.1016/j.addma.2020.101707).
15. Zhang Jiangtao, Tan Yuanqiang, Bao Tao, Xu Yangli, Xiao Xiangwu, Jiang Shengqiang. Discrete element simulation of the effect of roller-spreading parameters on powder-bed density in additive manufacturing // Materials. 2020. Vol. 13. № 10. P. 2285–2300. DOI: [10.3390/ma13102285](https://doi.org/10.3390/ma13102285).
16. Ya Zhao, Jia Wei Chew. Effect of lognormal particle size distributions on particle spreading in additive manufacturing // Advanced Powder Technology. 2021. Vol. 32. № 4. P. 1127–1144. DOI: [10.1016/j.apt.2021.02.019](https://doi.org/10.1016/j.apt.2021.02.019).
17. Феоктистов А.Ю., Каменецкий А.А., Блехман Л.И., Васильков В.Б., Скрыбин И.Н., Иванов К.С. Применение метода дискретных элементов для моделирования процессов в горно-металлургической промышленности // Записки Горного института. 2011. Т. 192. С. 145–149. EDN: [ROWFBF](https://www.edn.ru/rowfbf/).
18. Lee Y., Simunovic S., Gurnon A.K. Quantification of powder spreading process for metal additive manufacturing: technical report. Tennessee: OAK Ridge National Laboratory, 2019. 36 p.

Влияние характеристик ролика на нанесение порошкового слоя в аддитивных технологиях

Богданов Валерий Михайлович, аспирант

Санкт-Петербургский политехнический университет Петра Великого, Санкт-Петербург (Россия)

*E-mail: bogdanov.vm@edu.spbstu.ru

ORCID: <https://orcid.org/0009-0006-6865-3579>

Поступила в редакцию 08.05.2024

Пересмотрена 18.09.2024

Принята к публикации 07.11.2024

Аннотация: При исследовании и анализе аддитивных технологий особое внимание уделяется повышению производительности и качества напечатанных изделий. Однако для повышения производительности 3D-печати нельзя просто увеличить скорость перемещения ракеля без изменения его формы или типа. Из-за этого может страдать качество порошкового слоя, что приведет к ухудшению качества конечной детали. Для исследования влияния характеристик ролика на нанесение порошкового слоя проведена серия компьютерных моделирований имитационных моделей. Оценка влияния характеристик ролика на нанесение порошкового слоя проводилась для диаметров ролика 30, 50, 70, 100, 150, 200, 250, 300 мм. Моделирование проводилось с тремя способами нанесения: вращающимся и невращающимся роликом, а также вращающимся роликом с подачей дополнительного порошка. Определено, что при нанесении слоя вращающимся роликом с дополнительной подачей порошка можно достичь постоянства сил, действующих на ролик. Это может положительно повлиять на однородность наносимого слоя. Нанесение слоя вращающимся роликом с дополнительной подачей порошка наиболее пригодно в 3D-принтерах с большой зоной построения. Данный способ позволяет избежать перемещения большой массы порошка по предыдущему слою, что положительно влияет на качество конечной детали. Выявлено влияние характеристик ролика на нанесение порошкового слоя. В частности, при увеличении диаметра ролика с 30 до 300 мм увеличивается и значение пиковой силы. При увеличении диаметра ролика на 7,9 % увеличивается и плотность порошкового слоя. Выявлено, что на невращающийся ролик действует наибольшая сила, а силы, действующие на вращающиеся ролики, незначительно отличаются. Вращающийся ролик без добавления порошка создает наиболее плотный слой и позволяет добиться уплотнения порошкового слоя на 5,35 %.

Ключевые слова: характеристики ролика; порошковый слой; аддитивные технологии; аддитивное производство; диаметр ролика; разравнивание порошкового слоя; нанесение порошкового слоя; плотность порошкового слоя; ракель.

Для цитирования: Богданов В.М. Влияние характеристик ролика на нанесение порошкового слоя в аддитивных технологиях // Frontier Materials & Technologies. 2024. № 4. С. 9–18. DOI: [10.18323/2782-4039-2024-4-70-1](https://doi.org/10.18323/2782-4039-2024-4-70-1).

Computer prediction of fracture of magnesium alloy cylindrical billet during equal channel angular pressing

*Elena P. Volkova*¹, junior researcher

of the Research Institute of Physics of Advanced Materials

*Gandzhina D. Khudododova*², junior researcher

of the Research Institute of Physics of Advanced Materials

*Aleksandr V. Botkin*³, Doctor of Sciences (Engineering),

professor of Chair of Materials Science and Physics of Metals

Ruslan Z. Valiev^{*4}, Doctor of Sciences (Physics and Mathematics), Professor,

Director of the Research Institute of Physics of Advanced Materials

Ufa University of Science and Technology, Ufa (Russia)

*E-mail: ruslan.valiev@ugatu.su

¹ORCID: <https://orcid.org/0009-0004-7183-4077>

²ORCID: <https://orcid.org/0000-0002-1273-8518>

³ORCID: <https://orcid.org/0000-0001-9522-280X>

⁴ORCID: <https://orcid.org/0000-0003-4340-4067>

Received 03.05.2024

Revised 18.09.2024

Accepted 21.10.2024

Abstract: The main challenge in using magnesium alloys, applied in medicine as biodegradable materials, is their difficult deformability, which in turn leads to frequent failure of samples during severe plastic deformation. This paper shows that the temperature mode of equal channel angular pressing (ECAP) of a Mg–Zn–Ca system magnesium alloy, which ensures deformation of samples without failure, can be determined based on the results of finite-element computer simulation of the stress-strain state of the billet, calculation of alloy damage using the Cockcroft–Latham model, and prediction of the sample failure area. Modelling showed that the surface area of the billet adjacent to the matrix inner corner during ECAP, is the area of possible failure of the magnesium alloy. The value of alloy damage during ECAP in this area at $T=350$ °C is less than 1, which corresponds to non-failure of the metal. To verify the computer simulation results, ECAP physical simulation was performed; billets without signs of failure were produced. A study of the mechanical properties of the Mg–1%Zn–0.06%Ca magnesium alloy was conducted before and after ECAP processing according to the selected mode: the ultimate strength limit increased by 45 %, the hardness increased by 16 %, while the plasticity increased by 5 %.

Keywords: magnesium alloys; stress-strain state; finite-element computer simulation; alloy damage; equal channel angular pressing; microhardness; ultimate strength limit.

Acknowledgments: The work was supported by the Russian Science Foundation, project No. 24-43-20015 (<https://rscf.ru/project/24-43-20015/>). The experimental part was carried out using the equipment of the “Nanotech” Shared Research Facility of Ufa University of Science and Technology.

For citation: Volkova E.P., Khudododova G.D., Botkin A.V., Valiev R.Z. Computer prediction of fracture of magnesium alloy cylindrical billet during equal channel angular pressing. *Frontier Materials & Technologies*, 2024, no. 4, pp. 19–28. DOI: 10.18323/2782-4039-2024-4-70-2.

INTRODUCTION

In the last decade, magnesium alloys have attracted increased attention from researchers studying biomaterials for medical use. These alloys contain chemical elements that interact beneficially with the human body. However, these alloys in the cast state have low strength, and corrosion resistance for their successful application when producing biosoluble implants used in maxillofacial surgery and orthopaedics [1; 2]. In this work, to increase the strength of the Mg–1%Zn–0.06%Ca alloy, one of the effective approaches was used – the formation of an ultrafine-grained structure in them by the severe plastic deformation methods [3–5], namely, processing of billets by equal channel angular pressing (ECAP).

Cast magnesium alloys are difficult-to-form materials, have low plasticity during deformation at room temperature, and are prone to destruction [6–8]. In experimental studies, the temperature of deformation treatment is often determined empirically, which requires considerable time and material resources. The use of models of metal destruction, during pressure treatment, is an alternative to the experimental determination of the temperature regime.

In the mechanics of pressure metal treatment, a quantitative assessment of damage [9] – microscopic discontinuities (submicro- and micropores, microcracks) of the metal is performed using indirect relative indicators. For example, according to the methodology of V.L. Kolmogorov,

A.A. Bogatov¹, the metal damage in the material point of the deformed body, is the ratio of the strain degree accumulated by the material point during the deformation process, to the maximum possible degree of metal strain accumulated by the moment of exhaustion of the ability to deform without fracture, i.e. by the moment of accumulation of the metal maximum damage equal to 1, when macrocracks occur in an avalanche-like manner – this moment is called destruction. If the accumulation of maximum damage equal to 1 occurs at a material point on the surface of a deformed specimen, then the metal fracture at this point on the surface is visually detected by the appearance of a crack. If the accumulation of maximum damage equal to 1 occurs at any material point inside a deformed specimen, then the metal fracture at this point in the form of a pore is detected not visually, but using special equipment, for example, a device using ultrasonic radiation.

In [10], it was shown for the first time that metal damage within the Cockcroft–Latham model can be quantitatively and indirectly calculated, taking into account the changing stress state, as the ratio of the specific work of positive internal forces (principal normal positive stresses), acting on a material point during deformation to the maximum possible specific work of positive internal forces, corresponding to the moment when the metal exhausts its ability to deform without destruction. In [11; 12] it is shown that the normalised Cockcroft–Latham fracture model has a higher accuracy of predicting cracks in various technological processes. This approach was further developed in [13; 14].

As noted in [15], the difficulty of choosing and optimising the ECAP scheme is that the wall flow fields, "overhardening" and hidden damage are difficult to observe and poorly predicted. Therefore, the development of new and verification of existing methods for predicting metal fracture during ECAP, especially when applied to magnesium alloys, is an urgent and important task. A promising solution to this problem is the use of computer simulation to analyse the processes of billet damage during ECAP, which is based on predicting the area of sample fracture [16].

The purpose of this study is to determine, using computer simulation, such a temperature mode of equal channel angular pressing (ECAP) of Mg–Zn–Ca alloy, which ensures deformation of samples without fracture, and the achievement of increased mechanical properties in the alloy.

METHODS

The conducted studies included a physical experiment and finite-element computer simulation of the stress-strain state of the billet in the DEFORM-3D software package, as well as calculation of alloy damage.

The initial cylindrical samples (billets) of Mg–1%Zn–0.06%Ca magnesium alloy with a diameter of 20 mm and a length of 100 mm for physical simulation were made on

a lathe from a round cast produced by gravity casting. The Mg–1%Zn–0.06%Ca alloy was cast at the Solikamsk Experimental Metallurgical Plant (Russia). The chemical composition was determined using a Thermo Fisher Scientific ARL 4460 OES optical emission spectrometer (USA), and is presented in Table 1. In order to equalise the chemical composition throughout the sample volume, and eliminate the effects of dendritic liquation, the cast samples were heat-treated (subjected to homogenization annealing) in a Nabertherm muffle furnace at 450 °C for 24 h with cooling in water [17]. This state of the sample was taken as the initial one.

Physical simulation was performed on an ECAP equipment manufactured with an intersection angle of cylindrical channels of 120°. The tooling was heated to the required temperature using two electric heating elements in the form of clamps installed on the matrix. Before ECAP, the initial billet was heated in a chamber resistance furnace to the required temperature. Each subsequent ECAP pass was performed with a 90° rotation around the longitudinal axis of the billet. ECAP processing was carried out according to the mode described in [18] for the Mg–Zn–Ca system alloy: the first and second passes were performed at 400 °C; the third and fourth – at 350 °C; the fifth and sixth – at 300 °C; the seventh and eighth – at 250 °C.

At the first stage of theoretical research, a thermoplastic problem was solved using the DEFORM-3D software product: the non-uniform stress-strain state in the volume of the billet was determined stepwise. Finite-element computer simulation of the billet stress-strain state during ECAP (Fig. 1) was carried out under the following assumptions (usually used in modelling practice):

- 1) the problem was solved under conditions of a volumetric stress-strain state;
- 2) under non-isothermal conditions, taking into account the thermal effect of plastic deformation at the initial temperature of the billet (20...350) °C;
- 3) the billet material model is a plastic medium, the yield stress dependences on the degree of deformation of the Mg–1%Zn–0.06%Ca alloy, obtained from the results of preliminary mechanical tensile tests in the temperature and strain rate ranges corresponding to those realised during ECAP, were entered in tabular form during the preparation of the database;
- 4) the matrix and punch material for ECAP is a non-deformable rigid medium with a temperature of (20...350) °C.

The punch movement speed was set constant at 0.56 mm/s (equal to the movement speed of the movable crosshead of the hydraulic press during ECAP, with a nominal force of 160 tf). The ψ index of friction (according to Siebel) between the tool and the billet was taken equal to 0.3, and determined based on the results of preliminary virtual and physical modelling of the longitudinal upsetting of samples using graphite-molybdenum lubricant. The simulation was performed using a uniform grid of elements. The minimum size of the finite element (the length of the tetrahedron edge) was 1.2 mm. Verification of the results of computer simulation with the specified assumptions, the number of finite elements and the results of physical modelling of

¹ *Plasticity and destruction / edited by V.L. Kolmogorov. M.: Metallurgy, 1977. 336 p.*

Table 1. Chemical composition of the Mg-1%Zn-0.06%Ca alloy
Таблица 1. Химический состав сплава Mg-1%Zn-0,06%Ca

Element mass content										
Zn	Zr	Al	Fe	Mn	Ni	Cu	Si	Ca	Pb	Sn
0.953	≤0.001	0.011	0.027	0.0026	0.0008	0.0008	0.0025	0.0641	0.018	≤0.001

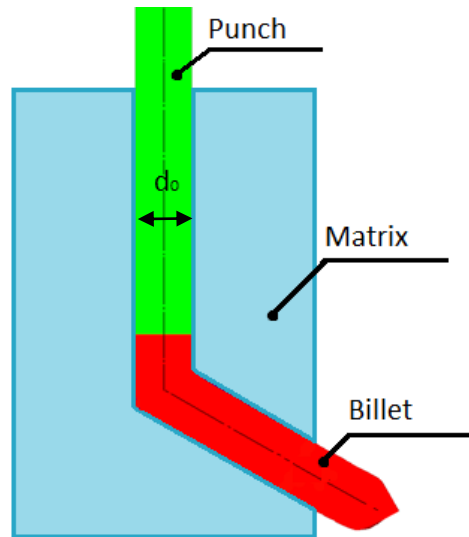


Fig. 1. ECAP equipment diagram
Рис. 1. Схема оснастки для РКУП

ECAP, showed a relative excess of the calculated deformation force over the value experimentally measured at the quasi-stationary stage of ECAP by 5 %.

At the second stage, the alloy damage was calculated using the results of simulating the billet stress-strain state during ECAP, and the well-known Cockcroft–Latham fracture model [19].

In the DEFORM-3D software package for predicting the failure of metals and alloys under large plastic deformation, the Cockcroft–Latham fracture model is traditionally used as the main technique. However, it does not take into account the effect of the metal stress state on the maximum possible value of the specific work of positive internal forces, corresponding to the moment when the metal exhausts its ability to deform without failure.

According to the Cockcroft–Latham fracture model, the condition of nonfailure of a material point is verified by the inequality:

$$c < c_{ult}, \tag{1}$$

where the left-hand side of the inequality $c = \int_0^{\varepsilon_i} \frac{\sigma_1}{\sigma_i} d\varepsilon_i$ is the damage index, the Cockcroft–Latham energy index of the relative specific work of elementary tensile forces,

σ_1 is the principal positive normal stress,

σ_i is the stress intensity,

ε_i is the deformation intensity;

c_{ult} is the ultimate (maximum possible) value of the Cockcroft–Latham index corresponding to the moment of metal fracture.

Metal fracture in accordance with the Cockcroft–Latham fracture model occurs when the condition $c \geq c_{ult}$ is met.

The damage was calculated using the formula obtained in [10] that takes into account the effect of the stress state on the ultimate (maximum possible) value of the Cockcroft–Latham index:

$$\omega = \sum_{k=1}^r \frac{\Delta C_k}{\left(\left(\frac{\sigma_1}{\sigma_i} \right)_{av} \varepsilon_{i,p} \right)_k}, \tag{2}$$

where r is the number of stages of deformation of the material point;

$\Delta C_k = \int_{\varepsilon_{i,k}}^{\varepsilon_{i,k+1}} \frac{\sigma_1}{\sigma_i} d\varepsilon_i$ is the increment of the Cockcroft–Latham index (the increment of the specific work of the positive internal forces acting on the material point at the k -th stage of deformation of the billet material point);

$\varepsilon_{i, k}$ is the degree of deformation accumulated by the material point of the billet by the beginning of the k -th stage of deformation;

$\varepsilon_{i, k+1}$ is the degree of deformation accumulated by the material point of the billet by the end of the k -th stage of deformation;

σ_1 is the principal positive normal stress;

σ_i is the stress intensity;

$(\sigma_1/\sigma_i)_{av}$ is average value of the ratio of the principal normal stress to the stress intensity at the k -th stage of deformation of the material point of the billet;

$\varepsilon_{i,p}$ is degree of deformation accumulated by the material point of the sample by the moment of fracture (quantitative measure of alloy plasticity) at a constant value of the σ_1/σ_i stress state index.

Functions

$$\varepsilon_{i,p} = -0.19 \ln \left(\frac{\sigma_1}{\sigma_i} \right) + 0.16; \tag{3}$$

$$\varepsilon_{i,p} = -0.21 \ln \left(\frac{\sigma_1}{\sigma_i} \right) + 0.18,$$

determining the plasticity of the Mg–1%Zn–0.06%Ca magnesium alloy at temperatures of 20 and 350 °C, depending on the stress state index were found experimentally using the method given in [20].

To take into account the change in the stress state index of the material point, the damage in it was calculated for $r=150$ stages, while the duration of all deformation stages was the same and equal to $t_s=1$ s, satisfying the condition [10]:

$$0.99 \leq \frac{\sum_{k=1}^r \left[\left(\frac{\sigma_1}{\sigma_i} \right)_{av} t_s \right]_k}{S} \leq 1, \tag{4}$$

where S is the area determined using the graph of the stress state index σ_1/σ_i of the material point of the billet, versus the deformation time. The alloy damage during ECAP was calculated for the material point, with the maximum value of the c damage index in the billet area determined, based on the simulation results.

The calculation of the alloy damage using formulas (2), (3), and the results of modelling the stress-strain state of the billet was performed in Excel, since the DEFORM-3D software product developers do not provide the ability for a user to enter any constitutive relations, metal fracture models, etc. into the solver.

Microhardness (HV) was measured using the Vickers method on an Emco-Test Durascan 50 micro-macrohardness tester, with an indenter load of 0.49 N and a holding time of 10 s. Microhardness measurements were performed using disk-shaped specimens with a diameter of 20 mm and a thickness of 1.5 mm, cut in the transverse direction from a deformed billet. For each specimen, 20 measurements were taken. Tensile tests were performed on an Instron 5982 testing machine at room temperature

and a strain rate of 10^{-3} s^{-1} on the specimens with a working part size of $0.6 \times 1 \times 4.5 \text{ mm}^3$. Flat specimens were cut from the disk-shaped samples. At least 5 specimens were tested for each condition.

RESULTS

Results of computer simulation

The distribution of the damage index obtained by computer simulation showed that the surface area of the billet, adjacent to the inner corner of the matrix during ECAP, is the area of possible fracture of the magnesium alloy (Fig. 2). The point from this area indicated in Fig. 2 enters the plastic deformation zone when the matrix outlet channel is completely filled with the alloy, i.e., at the steady-state stage of ECAP.

A significant increase in the c damage index (Fig. 3) at the point of the billet occurs in the time interval of 68–85 s due to the action of the σ_1 positive normal stress (Fig. 4).

The degree of deformation (Fig. 5) at the material point in the time range of 68–85 s, as well as the damage index, increases.

The value of metal damage at $T=20$ °C calculated by formula (2) was obtained equal to $\omega=1.19$. Therefore, the condition $\omega < 1$ is not met, and the billet will fail during ECAP deformation in the first pass in the area of the surface adjacent during ECAP to the inner corner of the matrix. The calculated value of the alloy damage at $T=350$ °C was obtained as $\omega=0.9$, which is less than 1, the nonfailure condition of the metal $\omega < 1$ is met, and the billet will not fail during the first pass of ECAP.

Physical experiment results

Fig. 6 a shows an image of sample 1 deformed in one pass at room temperature – the sample failed into two separate parts. One of the parts shows a macrocrack in the area of the billet adjacent during deformation to the inner corner of the matrix. Fig. 6 b shows an image of sample 2 deformed in one pass at $T=400$ °C – there are no visible signs of failure on the sample. The results of the studies of the mechanical properties of the samples are shown in Fig. 7 and listed in Table 2.

Fig. 7 a shows the stress-strain diagram of the studied alloy before and after ECAP. The Mg–1%Zn–0.06%Ca alloy in the homogenised state has a strength of 144 MPa. In the deformed state, its strength increased with an increase in the strain degree using the ECAP method. Thus, after 8 ECAP passes, the strength increased to 210 MPa, which is 45 % higher compared to the alloy in the homogenised state (Fig. 7 a, Table 2). The yield strength increased significantly – from 42 MPa in the homogenised state to 68 MPa after ECAP deformation. This result indicates the importance of ECAP for increasing the strength properties of this alloy. The microhardness of the homogenised state of the Mg–1%Zn–0.06%Ca alloy was 44 ± 2.8 HV. The microhardness value increased from 44 ± 2.8 to 51.2 ± 3.4 HV as a result of plastic deformation by the ECAP method, with a strain degree of $\varepsilon=5.04$, accumulated over 8 passes (Fig. 7 b, Table 2).

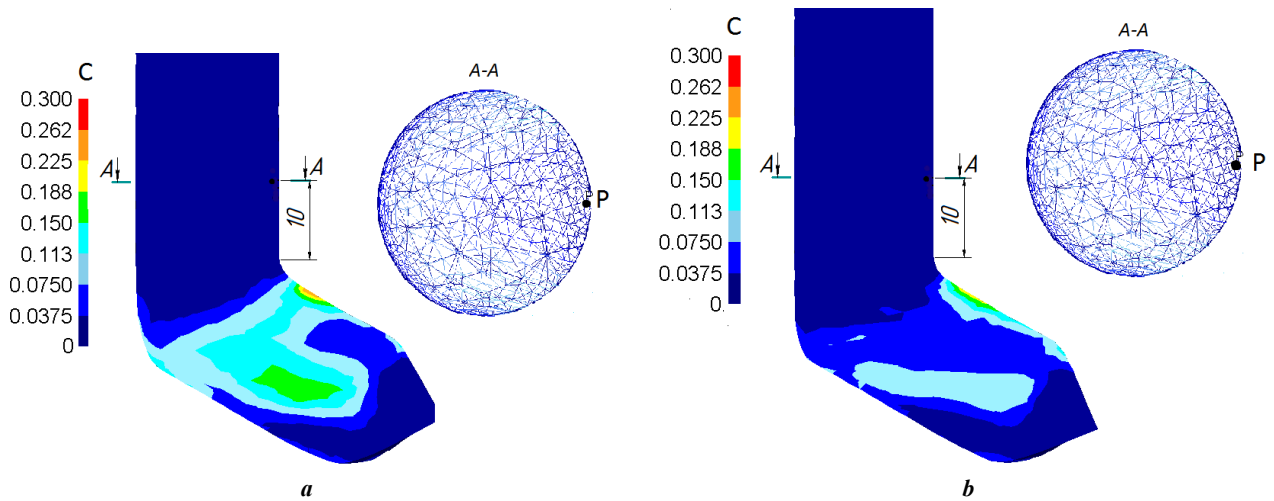


Fig. 2. Scheme of the position of the material point selected for damage calculation and the distribution of the c index in the longitudinal section of the virtually deformed billet at the initial temperature:

$a - T=20\text{ }^{\circ}\text{C}$; $b - T=350\text{ }^{\circ}\text{C}$

Рис. 2. Схема положения материальной точки, выбранной для расчета поврежденности, и распределение показателя c в продольном сечении виртуально деформированной заготовки при начальной температуре:

$a - T=20\text{ }^{\circ}\text{C}$; $b - T=350\text{ }^{\circ}\text{C}$

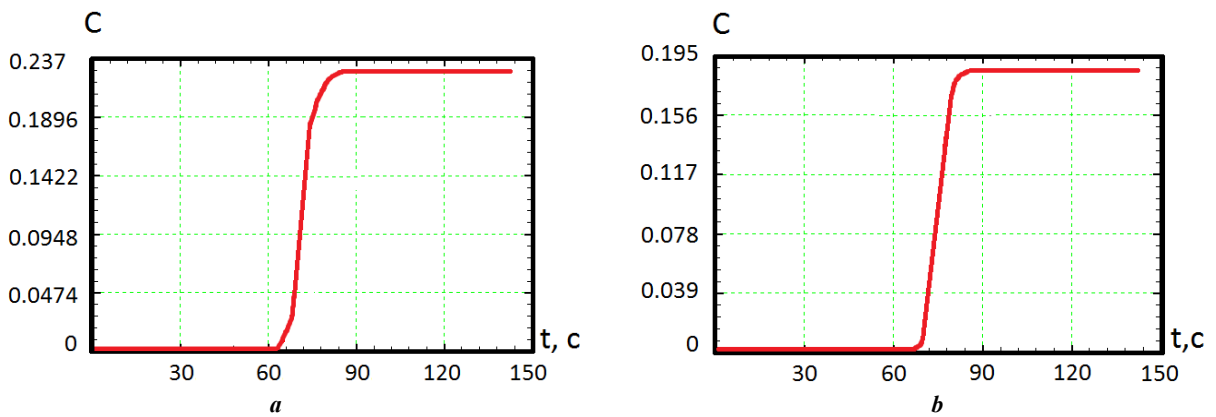


Fig. 3. Change in damage index over time at a point: $a - T=20\text{ }^{\circ}\text{C}$; $b - T=350\text{ }^{\circ}\text{C}$

Рис. 3. Изменение во времени показателя поврежденности в точке: $a - T=20\text{ }^{\circ}\text{C}$; $b - T=350\text{ }^{\circ}\text{C}$

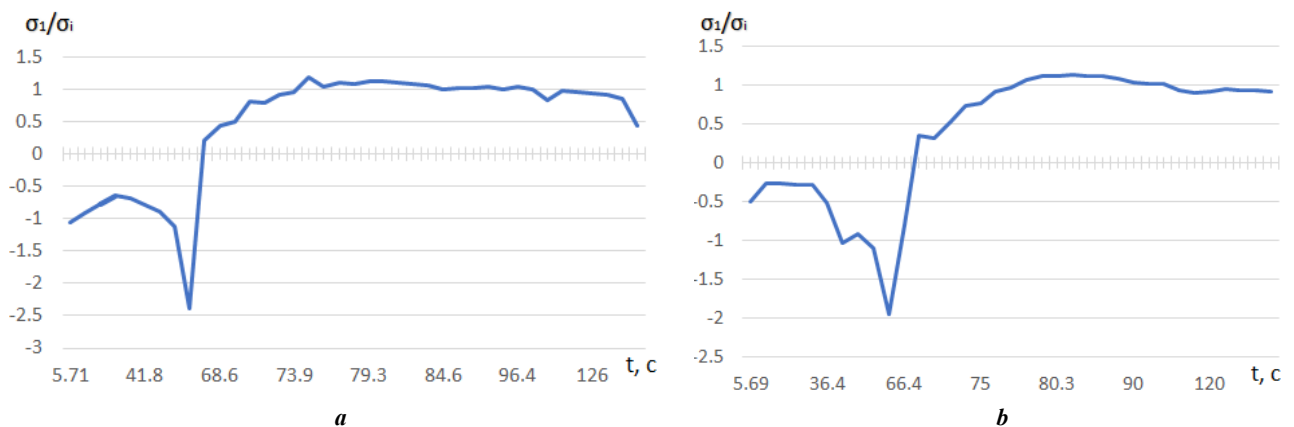


Fig. 4. Change of the σ_1/σ_i index of the stress state at a material point of the billet over time:

$a - T=20\text{ }^{\circ}\text{C}$; $b - T=350\text{ }^{\circ}\text{C}$

Рис. 4. Изменение во времени показателя σ_1/σ_i напряженного состояния в материальной точке заготовки:

$a - T=20\text{ }^{\circ}\text{C}$; $b - T=350\text{ }^{\circ}\text{C}$

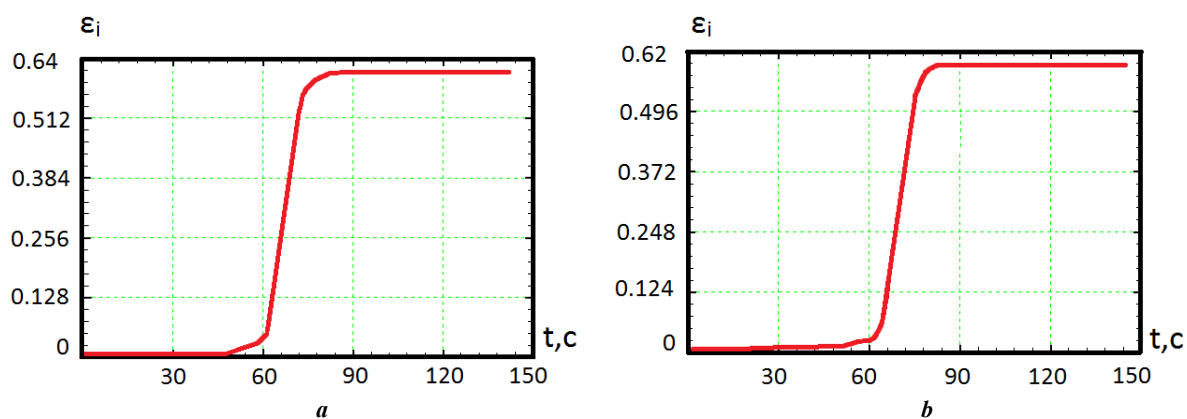


Fig. 5. Change in the degree of deformation in a material point of the billet over time: **a** – $T=20\text{ }^{\circ}\text{C}$; **b** – $T=350\text{ }^{\circ}\text{C}$
Рис. 5. Изменение во времени степени деформации в материальной точке заготовки: **a** – $T=20\text{ }^{\circ}\text{C}$; **b** – $T=350\text{ }^{\circ}\text{C}$

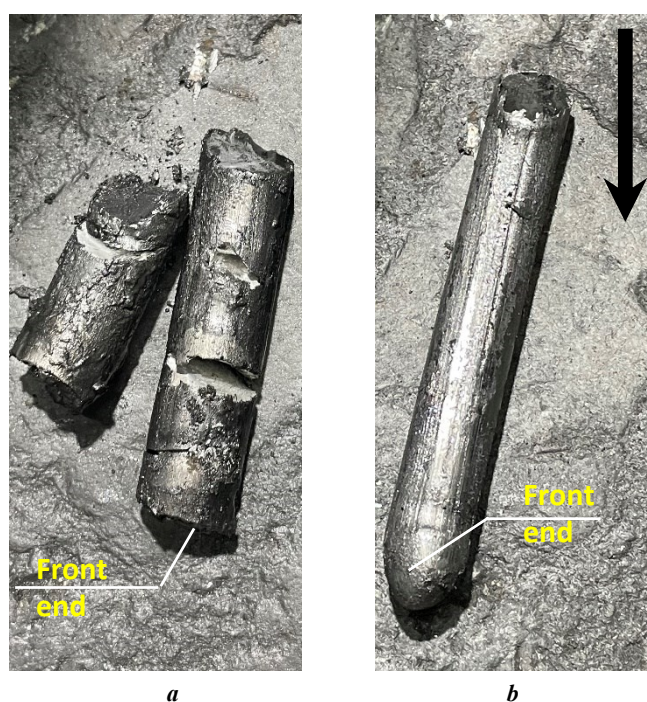


Fig. 6. Samples after one equal channel angular pressing (ECAP) pass:
a – $T=20\text{ }^{\circ}\text{C}$; **b** – $T=400\text{ }^{\circ}\text{C}$ (arrow indicates the ECAP pass direction)
Рис. 6. Образцы после одного прохода равноканального углового прессования (РКУП):
a – $T=20\text{ }^{\circ}\text{C}$; **b** – $T=400\text{ }^{\circ}\text{C}$ (стрелкой указано направление прохода при РКУП)

DISCUSSION

Functions (3) defining the plasticity of Mg–1%Zn–0.06%Ca magnesium alloy at temperatures of 20 and 350 °C, depending on the stress state index, established experimentally within the conducted studies correspond to the known pattern – the plasticity of magnesium alloys increases significantly with increasing temperature. The conducted studies have shown for the first time the possibility of successful application of the Cockcroft–Latham fracture model, taking into account the varying stress state [10], to the Mg–1%Zn–0.06%Ca alloy to determine the processing temperature. Until recently, this model was successfully applied to steels [14] and titanium

alloys [21]. Based on the results of computer simulation of the stress-strain state of the billet, and calculation of metal damage in the area with the most unfavorable stress state ($\sigma_1 > 0$), it was decided to perform physical simulation of ECAP for the first pass at an initial temperature of the billet and tooling equal to 400 °C. This temperature was chosen with a conservative value, to ensure guaranteed nonfailure of the billet in the physical experiment. It was shown theoretically and experimentally that at the initial sample temperature of less than 250 °C, cracking occurs precisely in the area of the billet, where the c damage index has a maximum value according to the results of computer simulation. Earlier in the work [22],

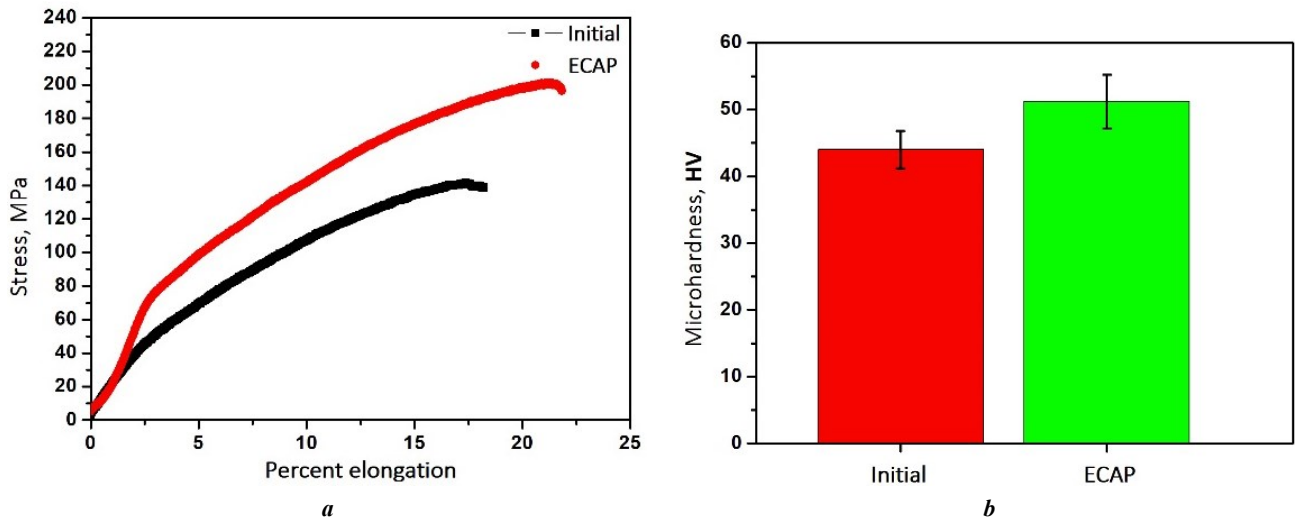


Fig. 7. Results of mechanical tests:
a – stress-strain curve of the Mg–1%Zn–0.06%Ca alloy before and after ECAP;
b – comparison of the initial microhardness and microhardness obtained after ECAP

Рис. 7. Результаты механических испытаний:
a – диаграмма растяжения сплава Mg–1%Zn–0,06%Ca до и после РКУП;
b – сравнение исходной и полученной после РКУП микротвердости

Table 2. Results of tensile tests of samples and microhardness measurements
Таблица 2. Результаты испытаний на растяжение образцов и измерения микротвердости

State	T, °C	HV (average value)	σ_{UTS} , MPa	$\sigma_{0.2}$, MPa	δ , %
Initial state	20	44.0±2.8	144	42	18
After ECAP	20	51.2±3.4	210	68	23

similar behaviour of an alloy with a similar composition was noted for the specified processing temperature range.

Physical simulation of billets in 8 passes showed the successful use of a well-known approach, ECAP with a gradual decrease in the processing temperature [18], as applied to the Mg–1%Zn–0.06%Ca alloy. Samples that were not destroyed in the first pass at $T=400$ °C were subjected to subsequent successful ECAP deformation in 7 more passes with a decrease in temperature from 400 to 250 °C.

The results of modelling the distribution of strain degree in the billet are in good agreement with the analytical estimate of the strain degree for 8 passes $\epsilon=5.04$ performed using the well-known formula [23]:

$$\epsilon_i = \frac{N}{\sqrt{3}} \left[2 \operatorname{ctg} \left(\frac{\Phi}{2} + \frac{\Psi}{2} \right) + \Psi \cos \epsilon c \left(\frac{\Phi}{2} + \frac{\Psi}{2} \right) \right], \quad (5)$$

where N is the number of passes;
 Ψ is the external angle;
 Φ is the internal angle.

During the calculation, the external angle was taken to be 20°; the internal angle (the angle of intersection of

the channels corresponding to the equipment in Fig. 1) was 120°. The value of deformation of 0.63 for one ECAP pass calculated using formula (5) is in good agreement with the value obtained by modelling (Fig. 5).

As in [18], an increase in the mechanical properties of the magnesium alloy was found, but not as significant, which is due to the lower content of calcium in the composition: the tensile strength increased by 45 %, the hardness – by 16 % compared to the homogenised state. This is probably caused by the formation of a structure with a finer average grain size due to the increase in the strain degree to 5.

CONCLUSIONS

1. The use of complex modelling of the process of severe plastic deformation of magnesium alloys, including computer and physical simulation on an experimental equipment, allows developing modes of billet deformation due to the alloy damage calculation using the Cockcroft–Latham model. Physical simulation of sample deformation confirmed the possibility of determining the thermomechanical mode of ECAP of a magnesium alloy of the Mg–Zn–Ca system, which ensures

deformation of samples without destruction, by computer simulation. The results of physical modelling are in good agreement with the values of damage calculated during computer simulation: room temperature $\omega=1.19$ ($\omega \geq 1$, failure condition) corresponded to sample failure during severe plastic deformation; $T=350$ °C and $\omega=0.9$ ($\omega < 1$, nonfailure condition) corresponded to nonfailure of the sample. This demonstrates the reliability of the processing mode obtained by complex modelling and the validity of its application to bulk billets.

2. Severe plastic deformation is an effective method for improving mechanical properties: after 8 ECAP passes, the alloy strength values increased from 144 to 210 MPa, which is 45 % higher compared to the homogenised state of the untreated sample, the microhardness value increased as well from 44 ± 2.8 to 51.2 ± 3.4 HV.

REFERENCES

- Sun Yu, Zhang Baoping, Wang Yin, Geng Lin, Jiao Xiaohu. Preparation and characterization of a new biomedical Mg-Zn-Ca alloy. *Materials and Design*, 2012, vol. 34, pp 58–64. DOI: [10.1016/j.matdes.2011.07.058](https://doi.org/10.1016/j.matdes.2011.07.058).
- Vinogradov A., Merson E., Myagkikh P., Linderov M., Brilevsky A., Merson D. Attaining High Functional Performance in Biodegradable Mg-Alloys: An Overview of Challenges and Prospects for the Mg-Zn-Ca System. *Materials*, 2023, vol. 16, no. 3, article number 1324. DOI: [10.3390/ma16031324](https://doi.org/10.3390/ma16031324).
- Valiev R.Z., Zhilyaev A.P., Lengdon T.Dzh. *Obemnye nanostrukturnye materialy: fundamentalnye osnovy i primeneniya* [Bulk nanostructural materials: fundamental principle and application]. Sankt Petersburg, Eko-Vektor Publ., 2017. 479 p.
- Martynenko N.S., Anisimova N.Y., Rybalchenko O.V. et al. Rationale for Processing of a Mg-Zn-Ca Alloy by Equal-Channel Angular Pressing for Use in Biodegradable Implants for Osteoreconstruction. *Crystals*, 2021, vol. 11, article number 1381. DOI: [10.3390/cryst11111381](https://doi.org/10.3390/cryst11111381).
- Medeiros M.P., Lopes D.R., Kawasaki M., Langdon T.G., Figueiredo R.B. An Overview on the Effect of Severe Plastic Deformation on the Performance of Magnesium for Biomedical Applications. *Materials*, 2023, vol. 16, no. 6, article number 2401. DOI: [10.3390/ma16062401](https://doi.org/10.3390/ma16062401).
- Rezaei-Baravati A., Kasiri-Asgarani M., Bakhsheshi-Rad H.R., Omidi M., Karamian E. Microstructure, Biodegradation, and Mechanical Properties of Biodegradable Mg-Based Alloy Containing Calcium for Biomedical Applications. *Physical Mesomechanics*, 2023, vol. 26, no. 2, pp. 176–195. DOI: [10.1134/S1029959923020078](https://doi.org/10.1134/S1029959923020078).
- Alper Incesu, Ali Gungor. Mechanical properties and biodegradability of Mg-Zn-Ca alloys: homogenization heat treatment and hot rolling. *Journal of materials science. Materials in medicine*, 2020, vol. 31, no. 12, article number 123. DOI: [10.1007/s10856-020-06468-5](https://doi.org/10.1007/s10856-020-06468-5).
- Roche V., Koga G.Y., Matias T.B., Kiminami C.S., Bolfarini C., Botta W.J., Nogueira R.P., Jorge Junior A.M. Degradation of Biodegradable Implants: The Influence of Microstructure and Composition of Mg-Zn-Ca Alloys. *Journal of Alloys and Compounds*, 2019, vol. 774, pp. 168–181. DOI: [10.1016/j.jallcom.2018.09.346](https://doi.org/10.1016/j.jallcom.2018.09.346).
- Kolmogorov V.L. Numerical simulation of large plastic deformations and failure of metals. *Kuznechno-shtampovochnoe proizvodstvo*, 2003, no. 2, pp. 4–16.
- Botkin A.V., Valiev R.Z., Stepin P.S., Baymukhamev A.Kh. Estimation of metal damage during cold plastic deformation using the Cockcroft–Latham failure model. *Deformatsiya i razrushenie materialov*, 2011, no. 7, pp. 17–22. EDN: [NXAHSN](https://www.edn.ru/NXAHSN).
- Kwak Eun Jeong, Bok Cheon Hee, Seo Min Hong, Kim Taek-Soo, Kim Hyoung Seop. Processing and mechanical properties of fine-grained magnesium by equal channel angular pressing. *Materials Transactions*, 2008, vol. 49, no. 5, pp. 1006–1010. DOI: [10.2320/matertrans.MC200725](https://doi.org/10.2320/matertrans.MC200725).
- Christiansen P., Nielsen C.V., Martins P.A.F., Bay N. Predicting the onset of cracks in bulk metal forming by ductile damage criteria. *Procedia Engineering*, 2017, vol. 207, pp. 2048–2053. DOI: [10.1016/j.proeng.2017.10.1106](https://doi.org/10.1016/j.proeng.2017.10.1106).
- Vlasov A.V. On the application of the Cockcroft–Latham criterion to predict fracture in cold forging. *Izvestiya Tul'skogo gosudarstvennogo universiteta. Tekhnicheskie nauki*, 2017, no. 11-1, pp. 46–58. EDN: [ZVLXNV](https://www.edn.ru/ZVLXNV).
- Matveev M.A. Numerical estimation of the probability of metal failure under hot plastic deformation by means of the Cockcroft – Latham criterion. *Nauchno-tehnicheskie vedomosti SPbPU. Estestvennye i inzhenernye nauki*, 2017, vol. 23, no. 2, pp. 109–126. DOI: [10.18721/JEST.230211](https://doi.org/10.18721/JEST.230211).
- Shtremel M.A. *Razrushenie. Razrushenie materialov* [Destruction. Destruction of materials]. Moscow, MISIS Publ., 2014. Kn. 1, 670 p.
- Chen Xuewen, Yang Zhen, Zhang Bo, Sun Jiawei, Su Zhiyi, Mao Yiran. An Inverse Optimization Method for the Parameter Determination of the High-Temperature Damage Model and High-Temperature Damage Graph of Ti6Al4V Alloy. *Materials*, 2023, vol. 16, article number 4770. DOI: [10.3390/ma16134770](https://doi.org/10.3390/ma16134770).
- Khudododova G.D., Kulyasova O.B., Nafikov R.K., Islamgaliev R.K. The structure and mechanical properties of biomedical magnesium alloy Mg–1%Zn–0.2%Ca. *Frontier Materials & Technologies*, 2022, no. 2, pp. 105–112. DOI: [10.18323/2782-4039-2022-2-105-112](https://doi.org/10.18323/2782-4039-2022-2-105-112).
- Kulyasova O.B., Islamgaliev R.K. The influence of the structural changes in the Mg-1%Zn-0,2%Ca alloy, produced by ECAP on its mechanical properties. *Vestnik Ufimskogo gosudarstvennogo aviatsionnogo tekhnicheskogo universiteta*, 2018, vol. 22, no. 3, pp. 24–29. EDN: [YAAWLZ](https://www.edn.ru/YAAWLZ).
- Cockcroft M.G., Latham D.J. Ductility and Workability of metals. *Journal of the Institute of Metals*, 1968, vol. 96, pp. 33–39.
- Botkin A.V., Valiev R.Z., Kublikova A.A., Dubinina S.V. Determining the shear plasticity of metals on the basis of torsion-tension tests. *Steel in Translation*, 2013, vol. 43, no. 6, pp. 360–364. DOI: [10.3103/S096709121306003X](https://doi.org/10.3103/S096709121306003X).
- Gao Lin, Zhao Jiang, Quan Guo-zheng, Xiong Wei, An Chao. Study on the Evolution of Damage Degradation

- tion at Different Temperatures and Strain Rates for Ti-6Al-4V Alloy // High Temperature Materials and Processes. 2018. Vol. 38. P. 332–341. DOI: [10.1515/htmp-2018-0091](https://doi.org/10.1515/htmp-2018-0091).
22. Козулин А.А., Скрипняк В.А., Красновейкин В.А., Скрипняк В.В., Каравацкий А.К. Исследование физико-механических свойств ультрамелкозернистых магниевых сплавов после интенсивной пластической деформации // Известия высших учебных заведений. Физика. 2014. Т. 57. № 9. С. 98–104. EDN: [SXZFZX](https://www.edn.ru/SXZFZX).
23. Iwahashi Y., Wang J., Horita Z., Nemoto M., Langdon T.G. Principle of equal-channel angular pressing for the processing of ultra-fine-grained materials // Scripta Materialia. 1996. Vol. 35. № 2. P. 143–146. DOI: [10.1016/1359-6462\(96\)00107-8](https://doi.org/10.1016/1359-6462(96)00107-8).

Компьютерное прогнозирование разрушения цилиндрической заготовки из магниевого сплава в процессе равноканального углового прессования

Волкова Елена Павловна¹, младший научный сотрудник

Научно-исследовательского института физики перспективных материалов

Худододова Ганджина Дастамбуевна², младший научный сотрудник

Научно-исследовательского института физики перспективных материалов

Боткин Александр Васильевич³, доктор технических наук,

профессор кафедры материаловедения и физики металлов

Валиев Руслан Зуфарович^{*4}, доктор физико-математических наук, профессор,

директор Научно-исследовательского института физики перспективных материалов

Уфимский университет науки и технологий, Уфа (Россия)

*E-mail: ruslan.valiev@ugatu.su

¹ORCID: <https://orcid.org/0009-0004-7183-4077>

²ORCID: <https://orcid.org/0000-0002-1273-8518>

³ORCID: <https://orcid.org/0000-0001-9522-280X>

⁴ORCID: <https://orcid.org/0000-0003-4340-4067>

Поступила в редакцию 03.05.2024

Пересмотрена 18.09.2024

Принята к публикации 21.10.2024

Аннотация: Основной сложностью в использовании магниевых сплавов, применяемых в медицине в качестве биоразлагаемых материалов, является труднодеформируемость, что, в свою очередь, приводит к частым разрушениям образцов во время интенсивной пластической деформации. В работе показано, что температурный режим равноканального углового прессования (РКУП) магниевого сплава системы Mg–Zn–Ca, обеспечивающий деформирование образцов без разрушения, возможно определять по результатам конечно-элементного компьютерного моделирования напряженно-деформированного состояния заготовки, расчета поврежденности сплава с использованием модели Кокрофта – Лэтэма и прогнозирования области разрушения образца. Моделирование показало, что поверхностная область заготовки, примыкающая при РКУП к внутреннему углу матрицы, является областью возможного разрушения магниевого сплава. Значение поврежденности сплава при РКУП в этой области при $T=350$ °C меньше 1, что соответствует неразрушению металла. Для верификации результатов компьютерного моделирования выполнено физическое моделирование РКУП, получены заготовки без признаков разрушения. Произведено исследование механических свойств магниевого сплава Mg–1%Zn–0,06%Ca до и после обработки РКУП по выбранному режиму: предел прочности повысился на 45 %, твердость увеличилась на 16 %, при этом пластичность повысилась на 5 %.

Ключевые слова: магниевые сплавы; напряженно-деформированное состояние; конечно-элементное компьютерное моделирование; поврежденность сплава; равноканальное угловое прессование; микротвердость; предел прочности.

Благодарности: Работа выполнена при поддержке РФФ, проект № 24-43-20015 (<https://rscf.ru/project/24-43-20015/>). Экспериментальная часть работы выполнена с использованием оборудования ЦКП «Нанотех» ФГБОУ ВО «УУНиТ».

Для цитирования: Волкова Е.П., Худододова Г.Д., Боткин А.В., Валиев Р.З. Компьютерное прогнозирование разрушения цилиндрической заготовки из магниевого сплава в процессе равноканального углового прессования // Frontier Materials & Technologies. 2024. № 4. С. 19–28. DOI: [10.18323/2782-4039-2024-4-70-2](https://doi.org/10.18323/2782-4039-2024-4-70-2).

Phase composition, structure and microhardness of the VT23 titanium alloy after deformation in a Bridgman chamber

Sergey V. Gladkovsky^{1,3}, Doctor of Sciences (Engineering), chief researcher,
Head of the Laboratory of Deformation and Fracture

Vitaly P. Pilyugin^{2,4}, PhD (Physics and Mathematics), leading researcher, Head of the High Pressure Physics Laboratory

Valeria E. Veselova^{*1,5}, PhD (Engineering), researcher at the Laboratory of Deformation and Fracture

Aleksandr M. Patselov^{2,6}, PhD (Physics and Mathematics), senior researcher at the High Pressure Physics Laboratory

¹*Institute of Engineering Science of the Ural Branch of RAS, Yekaterinburg (Russia)*

²*M.N. Mikheev Institute of Metal Physics of the Ural Branch of RAS, Yekaterinburg (Russia)*

*E-mail: veselova@imach.uran.ru

³ORCID: <https://orcid.org/0000-0002-3542-6242>

⁴ORCID: <https://orcid.org/0000-0002-5150-6605>

⁵ORCID: <https://orcid.org/0000-0002-4955-6435>

⁶ORCID: <https://orcid.org/0000-0001-6438-0725>

Received 13.09.2024

Revised 21.10.2024

Accepted 05.11.2024

Abstract: The authors have studied for the first time the phase composition, microhardness and fine structure of the VT23 ($\alpha+\beta$)-titanium alloy, with stable and metastable β -phase, after torsional deformation in a Bridgman chamber under a pressure of 4 GPa at room temperature. It has been found that the alloy microhardness, depending on the true degree of deformation under high hydrostatic pressure, changes along a curve with a maximum. The role of stress-induced $\beta\text{m}\rightarrow\alpha''$ martensitic transformation in the formation of alloy structure, and microhardness under high-pressure torsion was revealed. The highest microhardness of the alloy with stable β -phase was 395 HV 0.05, and with metastable – 470 HV 0.05. At the same time, the maximum microhardness of metastable alloy, compared to stable alloy, was shifted to the region of lower true strain $\epsilon=2.6$. Using X-ray diffraction analysis, and transmission electron microscopy methods, made it possible to trace the evolution of alloy structure under high-pressure deformation consisting in grinding of α -, and α'' -phase plates compared to the quenched state, as well as in the development of deformation $\beta\text{m}\rightarrow\alpha''$, and $\alpha''\rightarrow\beta\text{m}$ martensitic transformations. An increase in the degree of deformation by high-pressure torsion to $\epsilon=7.7\dots7.9$, regardless of the deformation stability of the β -phase, leads to a decrease in the alloy microhardness to a level of 185...205 HV 0.05. This is associated with the development of the dynamic recrystallisation process, and the formation of equiaxed α -phase nanoparticles with a size of 20...50 nm. The differences in the loading-unloading curves revealed by kinetic indentation, corresponded to the nature of the change in the VT23 alloy microhardness, depending on the quenching temperature and the true deformation degree.

Keywords: VT23 titanium alloy; phase composition; Bridgman chamber; high-pressure torsion; true deformation degree; metastable β -phase; martensitic transformations.

Acknowledgments: The work was carried out within the state assignments No. 124020600045-0 to the Institute of Engineering Science, UB RAS and No. 122021000032-5 to the Institute of Metal Physics, UB RAS using the equipment of the Plastometry Collective Centre of the Institute of Engineering Science, UB RAS. The authors express their gratitude to S.N. Sergeev (Institute for Metals Superplasticity Problems of RAS) for assistance in carrying out microstructural analysis using transmission electron microscopy.

For citation: Gladkovsky S.V., Pilyugin V.P., Veselova V.E., Patselov A.M. Phase composition, structure and microhardness of the VT23 titanium alloy after deformation in a Bridgman chamber. *Frontier Materials & Technologies*, 2024, no. 4, pp. 29–38. DOI: 10.18323/2782-4039-2024-4-70-3.

INTRODUCTION

The strength of titanium alloys for structural purposes can be effectively increased by means of thermomechanical treatment, using methods of severe plastic deformation (SPD), or “megaplastic deformation” (MD) [1–3]. The high level of strength properties of these materials while maintaining a sufficient reserve of plasticity and ductility, is determined by the formation of an ultrafine-grained (UFG) or nanocrystalline microstructure, with predominantly high-angle grain boundaries (HAB) under intense deformation [3].

Among the known SPD methods, such as equal channel angular pressing, multi-axial isothermal forging, accumulative pack rolling with layer bonding (Accumulative Roll Bonding – ARB process), allowing increasing significantly the strength properties of metallic materials, due to the formation of UFG, and nanocrystalline structure while maintaining sufficient plasticity [4], the method of torsion (shear) under pressure has become widespread. Such deformation treatment, with the imposition of high hydrostatic pressure, due to the implementation of the “softest” stress-

strain state, allows achieving very high true deformation degrees ($e \approx 8$) without destroying the samples [5; 6]. According to the data of [4], high-pressure torsion at room temperature allows increasing significantly the tensile strength of VT1-00 pure titanium, and Ti-6Al-4V (VT6) alloy to the level of $\sigma_u = 1200$ MPa and $\sigma_u = 1750$ MPa, respectively due to the creation of an UFG and nanocrystalline structure with a grain size of up to 80–100 nm. To achieve the best combination of strength and plastic properties of titanium, and its alloys after SPD torsion under pressure, it is advisable to use additional short-term low-temperature annealing at temperatures of 300–400 °C. In a number of titanium alloys, after high-pressure torsion, as a result of $\beta \rightarrow \omega$ - and partial $\alpha \rightarrow \omega$ -transitions, the formation of an embrittling ω -phase characteristic of high-pressure deformation in an amount from tenths to tens of percent was recorded, and the possibility of developing a reverse $\omega \rightarrow \alpha$ -transformation during SPD was found [7; 8].

In [9], when studying the features of phase and structural transformations in metastable titanium alloys under SPD conditions, it was found that during high-pressure torsion of the metastable Ti-5553 alloy (Ti-5Al-5V-5Mo-3Cr), the grain microstructure refinement to $d < 50$ nm is achieved, due to the crushing of the initial β -grains by plates of the forming stress α'' -martensite. When high (critical) deformation degrees are reached, the β -phase is stabilised, with respect to the formation of deformation martensite and the reverse $\alpha'' \rightarrow \beta$ -martensite transformation develops. The authors of [10] revealed a change in the shape and dispersion of strengthening precipitates, as well as an increase in the microhardness of the aged metastable Ti-15Mo alloy after high-pressure torsion deformation, compared to the undeformed state. Formation of stress-assisted α'' -martensite in titanium alloys with deformation-metastable β -phase, activates the processes of dispersion hardening, and promotes additional strengthening during subsequent annealing (aging) [3].

One should note that a comparative study of the effect of SPD in Bridgman anvils, on the structure and mechanical properties of domestic two-phase titanium alloys in a stable and metastable state has not been previously conducted.

The aim of the work is to study the effect of the accumulated degree of deformation by compression and torsion under pressure on the microhardness, phase composition and fine microstructure of the domestic two-phase VT23 alloy in a stable and metastable state with respect to plastic deformation.

METHODS

The initial material was two-phase VT23 titanium alloy (Ti-5Al-5V-2Mo-Cr) produced by PJSC VSM-PO-AVISMA Corporation (Russia). The chemical composition of the VT23 titanium alloy was determined using a NITON XL2 980 GOLDD X-ray fluorescence spectrometer (Table 1), and complied with OST1 90013-81.

The blanks of VT23 titanium alloy in the as-delivered condition after annealing at 750 °C, were quenched from temperatures of 800 and 860 °C in water, in order to form different β -phase stability, since according to the data [11; 12], after quenching from 800 °C, the β -phase is in a state stable with respect to mechanical loading, and after quenching from 860 °C, it is in a metastable state.

The process of intensive plastic (megaplastic) deformation of monolithic samples of VT23 titanium alloy with a height of 0.5 mm and a diameter of 10 mm, was carried out at room temperature in a Bridgman chamber by compression, under a pressure of 4 GPa followed by torsion. Steel anvils with a contact pad diameter of 10 mm were used in the work. Torsion under a pressure of 4 GPa was carried out with the lower anvil rotating at a speed of $\omega = 0.3$ rpm. The rotation angle φ varied within the range from 0 to 1080° (0...3 revolutions). The true accumulated deformation was estimated using the relationship given in [13]:

$$e = \ln \left(1 + \frac{\varphi^2 r^2}{h_0^2} \right)^{1/2} + \ln \left(\frac{h_0}{h_K} \right),$$

where φ is the rotation angle during torsion;

r is the disk radius;

h_0 is the initial disk thickness;

h_K is the disk thickness after deformation.

Kinetic microindentation was performed on a Fischer-scope HM2000 XYm measuring system (Germany), using a Vickers indenter and WIN-HCU software at a maximum load of 0.005 N. The measurement error did not exceed 2%. The measurements were taken at the middle of the sample radius. X-ray phase analysis of the samples was performed on a DRON-3 diffractometer in Co-K α radiation, in the angle range of 25–105° with a step of 0.05°. Electron microscopic analysis of the microstructure of VT23 titanium alloy was carried out by transmission electron microscopy (TEM) on a JEOL JEM-2100 plus microscope (Japan) at an accelerating voltage of 80 keV. Preparation of thin foils for research included cutting out blanks 300...500 μ m

Table 1. Chemical composition of the VT23 alloy, wt. %
Таблица 1. Химический состав сплава VT23, мас. %

Element	Ti	V	Al	Mo	Cr	Fe	Si	Zr
Content	85.870	4.780	4.855	1.865	1.305	0.800	0.150	0.025

thick, with a thin abrasive disk under water cooling conditions, mechanical processing to a thickness of 100 μm , and subsequent electropolishing in a methyl electrolyte at a temperature no higher than $-50\text{ }^\circ\text{C}$.

RESULTS

The microhardness of the VT23 alloy after quenching from temperatures of 800 and 860 $^\circ\text{C}$ was 132 HV 0.05 and 48 HV 0.05, respectively (Fig. 1). As can be seen from Fig. 1, the microhardness of the VT23 alloy samples, depending on the degree of true plastic deformation e in Bridgman anvils, changes along a curve with a maximum. A significant increase in the alloy microhardness, compared to the initial state, occurs already at the initial stage of deformation at a value of $e=1.5$ under compression, under a pressure of 4 GPa without torsion. In this case, the microhardness of the sample of the alloy with a metastable β -phase, quenched from a temperature of 860 $^\circ\text{C}$, grows more intensively compared to the alloy with a stable β -phase after quenching from 800 $^\circ\text{C}$ and reaches a maximum (470 HV 0.05), at a true deformation of $e=2.6$. The maximum microhardness of the alloy with a stable β -phase (395 HV 0.05) is observed after torsion under pressure upon reaching a higher degree of true deformation $e=5.4$. The microhardness of the alloy, regardless of the quenching temperature, and accordingly, the deformation stability of the β -phase at the maximum degree of true deformation $e=7.7\dots 7.9$, is approximately at the same level – 185...205 HV 0.05.

The loading – unloading curves of the samples of the alloy with a stable and metastable β -phase, in the initial state, have characteristic differences (Fig. 2). At deformation degrees from $e=1.6$ to 4.5...4.7, the loading curve of the alloy with a metastable β -phase, has a smoother increase in stress with deformation, which is associated with the martensitic transformation. Further, with an increase in the degree of true deformation from $e=5.2\dots 5.4$ to 7.7...7.9, the difference in the position of the curves gradually decreases, and at a degree of deformation

of 7.7...7.9 they practically coincide, which is associated with the stabilisation of the β -phase.

The quantitative phase composition of the studied samples is given in Table 2. X-ray phase analysis showed that after deformation the alloy has a three-phase ($\alpha+\beta+\alpha''$) state (α -phase with a hcp lattice, β -phase with a bcc lattice and α'' -phase with orthorhombic lattice), and the ω -phase, the formation of which is possible at pressures above 2 GPa, was not recorded in the diffraction patterns in the angle range of 20...105 $^\circ$ (Fig. 3). As can be seen from Fig. 3, the lines of the α -phase (100), (110), (112) broaden as the deformation degree increases, and their intensity decreases, which indicates the refinement of α -crystallites, and the presence of internal microstresses as a result of plastic deformation. A redistribution of the integral intensities between the X-ray peaks of the α/α'' - and β -phase is also observed, which indicates both the texture formation, and the phase transformation of the metastable phase $\beta\text{m}\rightarrow\alpha''$.

The study of the fine microstructure of the alloy, quenched from 800 $^\circ\text{C}$ by the TEM method (Fig. 4), revealed the presence of α -plates with a thickness of 150...250 nm located in the β -matrix, corresponding to the crystallographic relationship $[110]\beta \parallel [001]\alpha$. Reflections from the α'' -phase formed in the β -matrix during quenching were also revealed in the microdiffraction patterns of the quenched samples. Thin and distinct inter-phase boundaries indicate a high degree of coherence of these phases. After quenching from a temperature of 860 $^\circ\text{C}$, a complex tweed contrast was found when studying the β -matrix (Fig. 4 b), which indicates a reduced stability of the β -phase with respect to martensitic transformations caused by stress.

TEM study of the microstructure of the VT23 alloy, quenched from 800 $^\circ\text{C}$ after SPD with a degree of $e=1.6$, showed the presence of fragments of the initial α -phase plates of varying thickness from 50 to 250 nm with β -phase interlayers (Fig. 5 a). The plates have an irregular shape,

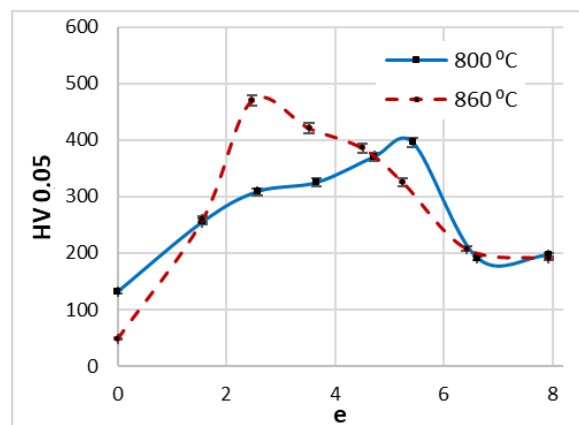


Fig. 1. Effect of true deformation degree e during torsion under pressure on the VT23 alloy microhardness

Рис. 1. Влияние истинной степени деформации e в процессе кручения под давлением на микротвердость сплава VT23

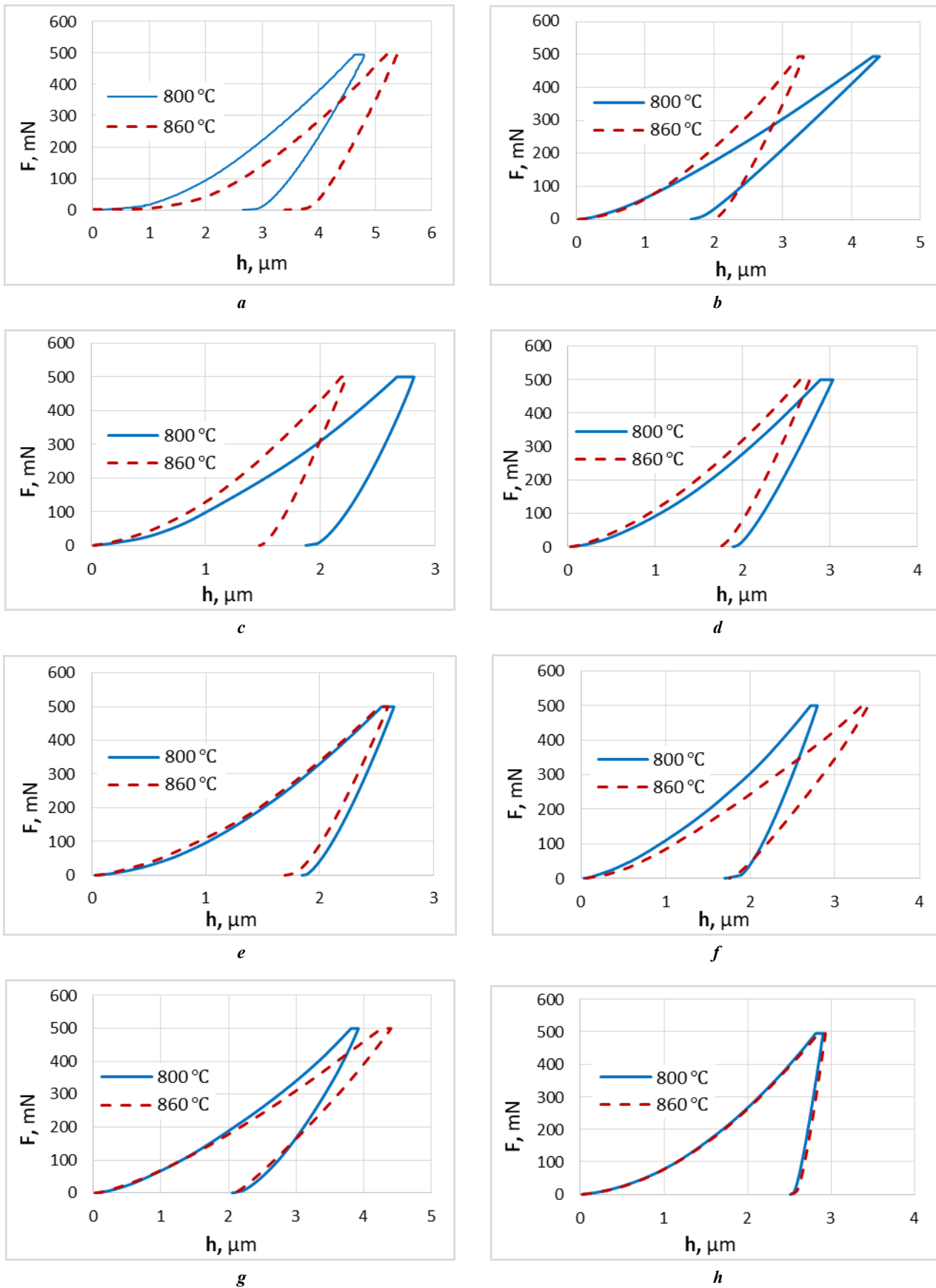


Fig. 2. Loading – unloading curves of VT23 alloy samples after various degrees of deformation under pressure: **a** – without deformation; **b** – $e=1,6$; **c** – $e=2,5...2,6$; **d** – $e=3,5...3,7$; **e** – $e=4,5...4,7$; **f** – $e=5,2...5,4$; **g** – $e=6,4...6,6$; **h** – $e=7,7...7,9$
Рис. 2. Кривые нагружения – разгружения образцов сплава VT23 при различных степенях деформации под давлением: **a** – без деформации; **b** – $e=1,6$; **c** – $e=2,5...2,6$; **d** – $e=3,5...3,7$; **e** – $e=4,5...4,7$; **f** – $e=5,2...5,4$; **g** – $e=6,4...6,6$; **h** – $e=7,7...7,9$

Table 2. Phase composition of the VT23 titanium alloy [11]
Таблица 2. Фазовый состав титанового сплава VT23 [11]

Heat treatment conditions	α , %	β/β_m , %	α'' , %
Quenching at 800 °C	32	50	18
Quenching at 860 °C	7	8	85

strongly distorted areas and a high density of the dislocation structure. This indicates their deformation origin, resulting from deformation fragmentation of structural elements. In the sample quenched from a temperature of 860 °C with a metastable β -phase, the processes of deformation by compression under pressure, with a degree of $\epsilon=1.6$ are characterised mainly by phase transformations, caused by deformation of the metastable phase $\beta_m \rightarrow \alpha''$ (Fig. 5 b). The TEM structure is represented by fragments of plates of the initial α -phase with a thickness of 50...250 nm, as well as by more dispersed particles of α'' -martensite (stress) (Fig. 5 b).

In the electron diffraction patterns of the samples, deformed with a degree of $\epsilon=7.7...7.9$, a significant number of reflections located along the circumference are observed (Fig. 6, 7), which indicates the presence of multiple crystalline orientations associated with grain refinement. The presence of an insignificant amount (up to 5 %) of the high-pressure ω -phase, which was not detected by the X-ray phase analysis method, was recorded. A TEM study of the microstructure of the alloy quenched from 800 °C after deformation, with a degree of $\epsilon=7.7$, revealed the presence of equiaxed grains with a weak dislocation contrast, with a diameter of 20...30 nm and smaller grains up to 20 nm of irregular shape, with a characteristic banded contrast (Fig. 6). In the TEM images of the alloy quenched from 860 °C, larger homogeneous particles, and particles with a banded contrast with a size of 30...50 nm were recorded (Fig. 7).

DISCUSSION

The difference in the nature of the curves of microhardness change, depending on the degree of deformation of the samples after quenching, from temperatures of 800 and 860 °C (Fig. 1 a), can be explained by their phase composition (Table 2). Thus, the smoother nature of the growth of microhardness of the sample quenched from 800 °C is associated with a gradual increase in the density of dislocations in the alloy crystalline structure, the refinement of the α -phase plates and athermal α'' -martensite. In accordance with the Hall–Petch dependence, smaller grains contribute to an increase in microhardness [14]. An increase in the amount of athermal α'' -martensite, which has a more dispersed microstructure compared to the initial α -phase [11], in the sample quenched from a temperature of 860 °C, contributes to a more active growth of microhardness, since the large surface area of the martensite plates compared to large α -phase plates, allows them to interact with a large number of dislocations, creating obstacles to their movement, and increasing the strengthening effect [15]. More-

over, the β -phase in the alloy quenched from a temperature of 860 °C, which is in a metastable state, with respect to mechanical loading [12], undergoes a martensitic transformation $\beta \rightarrow \alpha''$ during torsional deformation with the formation of stress-induced martensite, which increases the alloy microhardness. It should also be noted that the crystalline structure of athermal martensite, as well as stress-induced martensite, is strongly distorted compared to the initial α - and β -phases, which leads to a high dislocation density and internal stresses (Fig. 4).

The softening of the alloys in a stable and metastable state after quenching from 800 and 860 °C is associated with the process of low-temperature dynamic recrystallisation occurring at high degrees of plastic deformation, described in [2]. The Vickers microhardness decreases due to a decrease in the dislocation density, and the formation of equiaxed grains.

The sharp difference in the loading-unloading curves of the initial samples (Fig. 2 a) can be explained by the presence of a metastable β_m -phase. Metastable phases can have a high resistance to initial deformation, which leads to a longer loading curve before the onset of significant plastic flow [16] (Fig. 2 a). The coincidence of the loading-unloading curves at a deformation degree of 7.7...7.9, indicates that the processes of decomposition of metastable phases and dynamic recrystallisation were fully realised (Fig. 2 h).

Analysis of TEM images at deformation degrees of 7.7...7.9 (Fig. 6, 7) showed that the formation of equiaxed grains without deformation contrast, is associated with low-temperature dynamic recrystallisation of the α phase, described in [2; 17]: the formation of high-angle boundaries during deformation, leads to the appearance of new grains by the continuous recrystallisation mechanism, i. e. due to the increase in the misorientation of sub-boundaries. Particles with banded contrast, according to [5], are deformation fragments, formed during the subsequent deformation of recrystallised grains. The larger size of recrystallised grains in the alloy quenched from 860 °C is associated with the fact that the processes of low-temperature dynamic recrystallisation of the alloy in the deformation-metastable state, occurred more completely during torsional deformation under pressure.

Therefore, based on the conducted study, the authors revealed the extreme nature of the change in the VT23 alloy microhardness, with an increase in the true degree of torsional deformation under pressure associated with the gradual development of the processes of the structure dispersion, and subsequent dynamic recrystallisation, as well as differences in the level of microhardness maximum, and the corresponding degrees of deformation for the alloy with a stable and deformation-metastable β -phase.

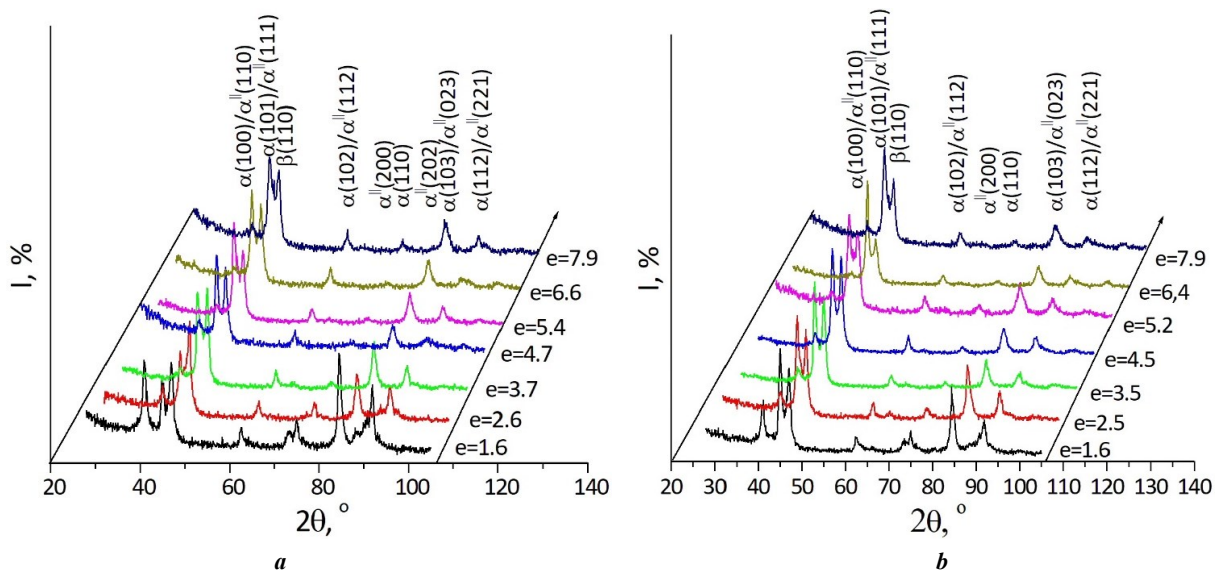


Fig. 3. Diffraction patterns of VT23 alloy samples:
a – after quenching from 800 °C and torsional deformation under pressure;
b – after quenching from 860 °C and torsional deformation under pressure
Рис. 3. Дифрактограммы образцов сплава VT23:
a – после закалки от 800 °C и деформации кручением под давлением;
b – после закалки от 860 °C и деформации кручением под давлением

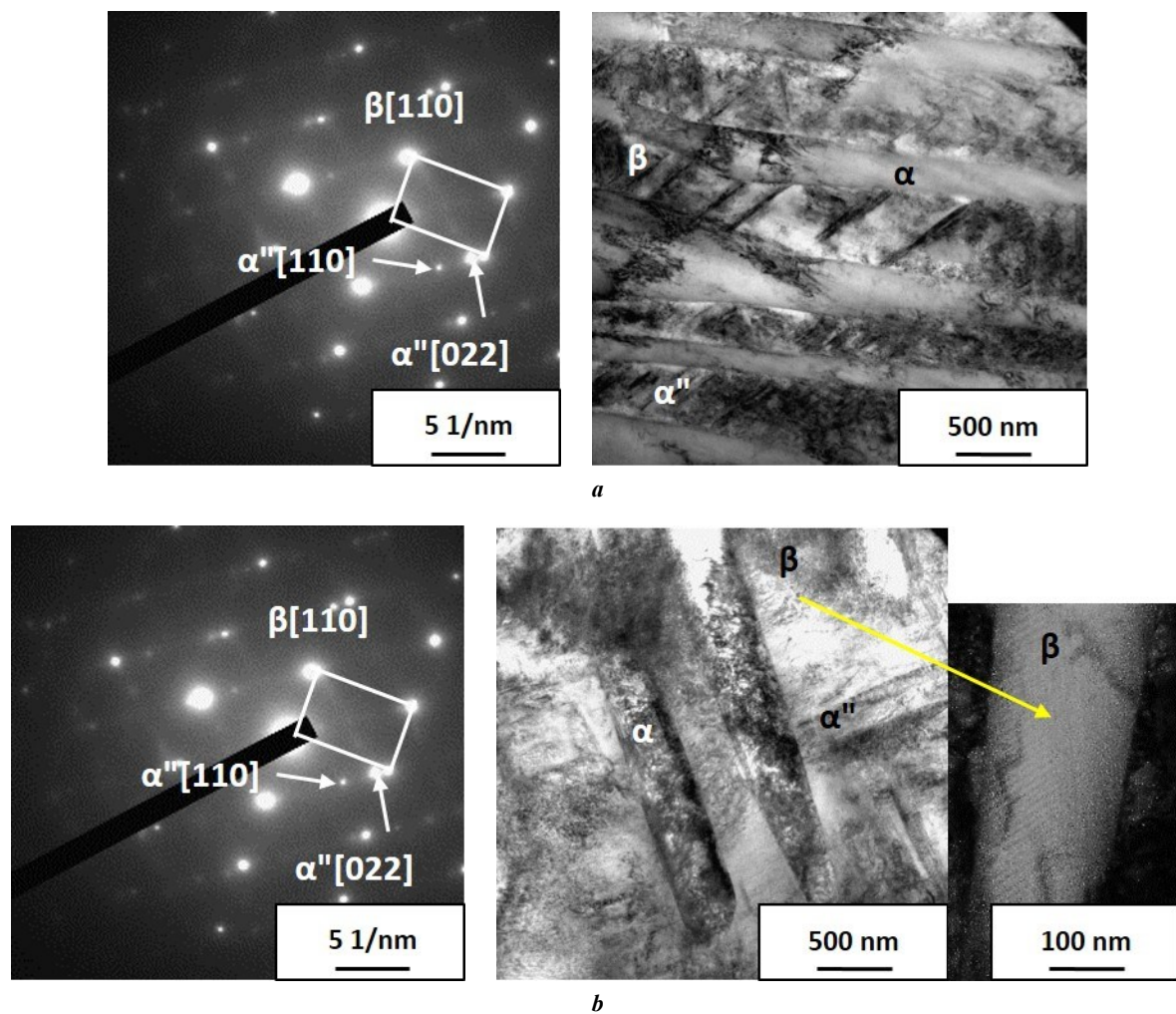


Fig. 4. TEM image of the microstructure of VT23 alloy after quenching: **a** – from 800 °C; **b** – from 860 °C
Рис. 4. ПЭМ-изображения микроструктуры сплава VT23 после закалки: **a** – от 800 °C; **b** – от 860 °C

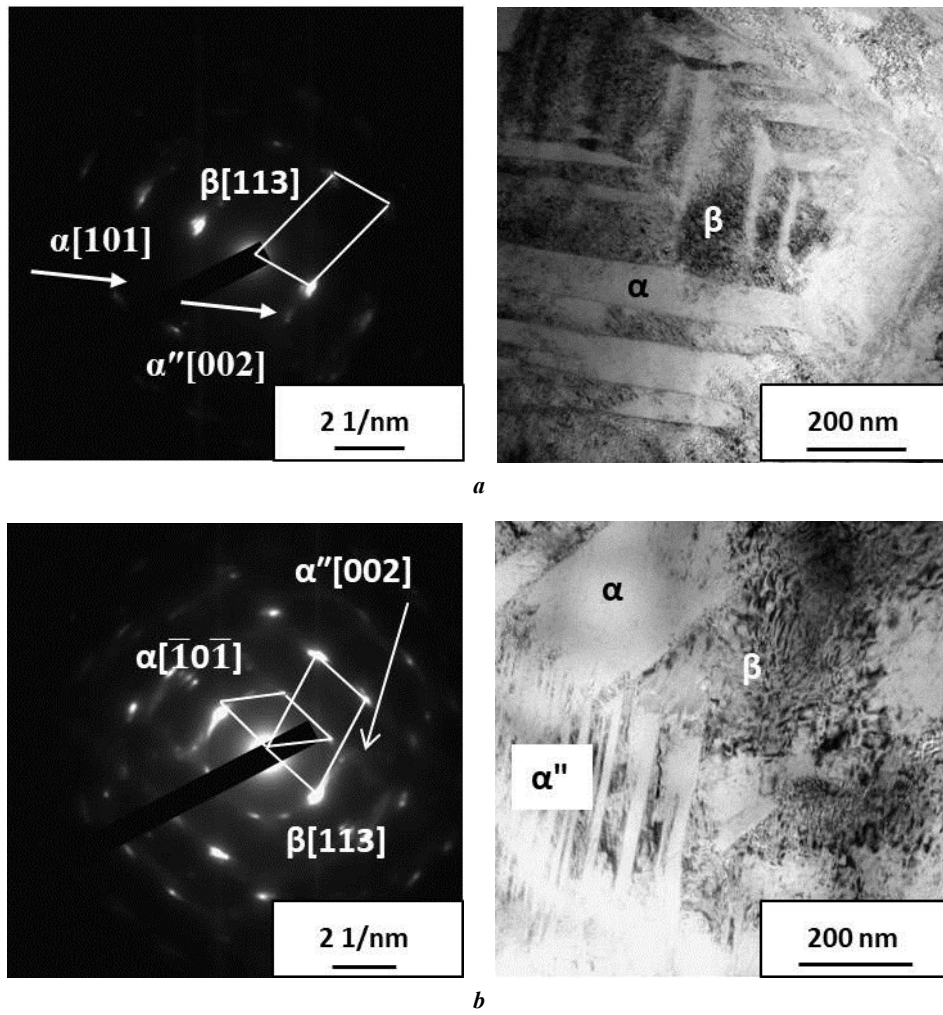


Fig. 5. TEM images of VT23 titanium alloy:
a – after quenching from 800 °C and SPD, $e=1.6$; *b* – after quenching from 860 °C and SPD, $e=1.6$
Рис. 5. ПЭМ-изображения титанового сплава VT23:
a – после закалки от 800 °C и ИПД, $e=1,6$; *b* – после закалки от 860 °C и ИПД, $e=1,6$

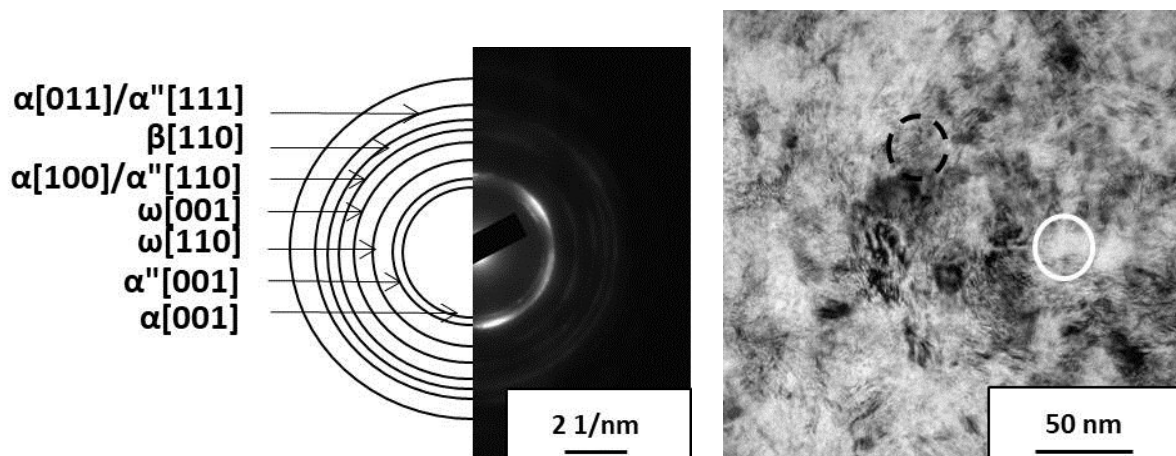


Fig. 6. TEM images of VT23 titanium alloy after quenching from 800 °C and torsion under pressure, $e=7.7$.
 The solid line highlights α -phase equiaxed particles with weak dislocation contrast,
 and the dotted line highlights those with banded contrast
Рис. 6. ПЭМ-изображения титанового сплава VT23 после закалки от 800 °C и кручения под давлением, $e=7,7$.
 Сплошной линией выделены равноосные частицы α -фазы со слабым дислокационным контрастом,
 пунктирной – с полосчатым контрастом

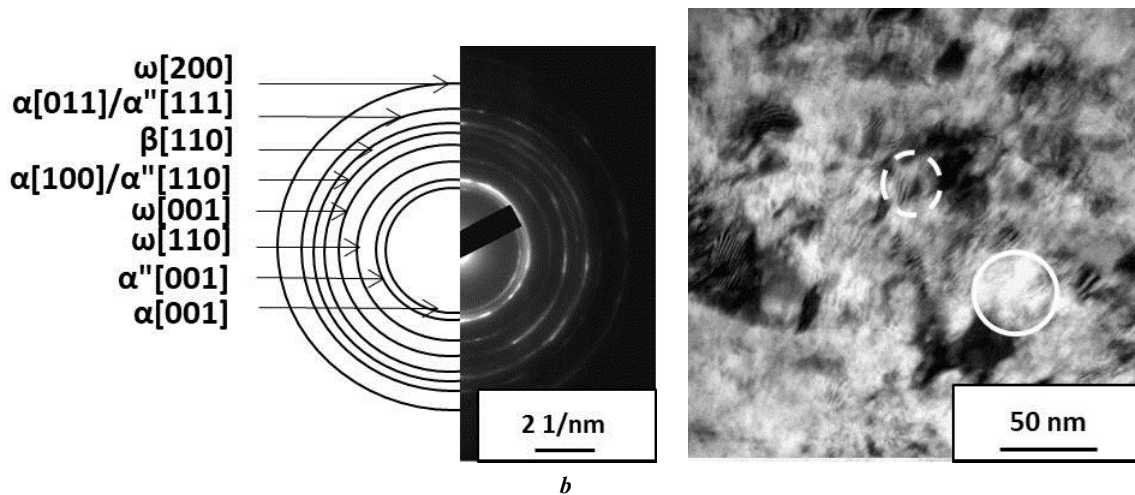


Fig. 7. TEM images of VT23 titanium alloy after quenching from 860 °C and torsion under pressure, $e=7.9$.
The solid line highlights α -phase equiaxed particles with weak dislocation contrast,
and the dotted line highlights those with banded contrast

Рис. 7. ПЭМ-изображения титанового сплава VT23 после закалки от 860 °C и кручения под давлением, $e=7,9$.
Сплошной линией выделены равноосные частицы α -фазы со слабым дислокационным контрастом,
пунктирной – с полосчатым контрастом

CONCLUSIONS

A nonlinear dependence of the alloy microhardness on the degree of true high-pressure torsional deformation was found. The maximum level of microhardness of samples quenched from temperatures of 800 and 860 °C was 395 HV 0.05 and 470 HV 0.05 at a deformation of 5.3 and 2.6, respectively. The increase in the microhardness of the sample quenched from 800 °C is associated with an increase in the dislocation density in the initial α - and β -phases, and refinement of the structural components. The greatest increase in the microhardness of the sample quenched from a temperature of 860 °C is associated with the intense strengthening of athermal α' -martensite and the phase transformation of metastable phases according to the schemes $\beta_m \rightarrow \alpha'$ and $\alpha'' \rightarrow \beta_m$. The subsequent softening of the alloy in the deformation range of $e > 5.4$ for the sample quenched from 800 °C, and $e > 2.6$ for the sample after quenching from 860 °C, estimated by the decrease in microhardness, occurs as a result of low-temperature dynamic recrystallisation of the α -phase. At the maximum value of the true deformation degree $e=7.7...7.9$, regardless of the quenching temperature, the alloy microhardness differed insignificantly, and corresponded to the level of 185...205 HV 0.05.

Using X-ray phase analysis, it was shown that during deformation in a Bridgman chamber, the alloy retains a three-phase ($\alpha+\beta+\alpha''$) composition, at the degree of deformation from $e=1.6$ and more, there is a refinement of α - and α'' -plates, as well as a phase transformation – the β_m -phase decomposition during quenching from 860 °C according to the scheme $\beta_m \rightarrow \alpha''$.

At the deformation degree of $e=1.6$, a fragmentation of the α and α'' plates occurs, as well as an increase in dislocation contrast. In a sample with a metastable β_m -phase (quenching from 860 °C), it decomposes with the formation of dispersed needles of α'' -stress martensite. An increase in the deformation degree to $e=7.7...7.9$ leads to the formation of equiaxed α -particles with a size of 20...30 nm (quenching from 800 °C), and 30...50 nm (quenching from 860 °C)

due to the processes of low-temperature dynamic recrystallisation and deformation fragments with a banded contrast.

REFERENCES

1. Semenova I.P., Raab G.I., Valiev R.Z. Nanostructured titanium alloys: new developments and application prospects. *Nanotechnologies in Russia*, 2014, vol. 9, no. 5, pp. 311–324. DOI: [10.1134/S199507801403015X](https://doi.org/10.1134/S199507801403015X).
2. Glezer A.M., Metlov L.S. Physics of megaplastic (severe) deformation in solids. *Physics of the Solid State*, 2010, vol. 52, no. 6, pp. 1162–1169. DOI: [10.1134/S1063783410060089](https://doi.org/10.1134/S1063783410060089).
3. Sergueeva A.V., Stolyarov V.V., Valiev R.Z., Mukherjee A.K. Enhanced superplasticity in a Ti6Al4V alloy processed by severe plastic deformation. *Scripta Materialia*, 2000, vol. 43, no. 9, pp. 819–824. DOI: [10.1016/S1359-6462\(00\)00496-6](https://doi.org/10.1016/S1359-6462(00)00496-6).
4. Valiev R.Z., Aleksandrov I.V. *Obemnye nanostrukturnye metallicheskie materialy: poluchenie, struktura i svoystva* [Bulk nanostructured metallic materials: preparation, structure and properties]. Moscow, Akademiya Publ., 2007. 398 p.
5. Shurygina N.A., Cheretaeva A.O., Glezer A.M., Medvedeva A.D., D'yakonov D.L., Sundeev R.V., Tomchuk A.A. Effect of Microalloying Elements on the Physicochemical Properties of Commercial-Purity Titanium Subjected to Severe Plastic Deformation. *Russian Metallurgy (Metally)*, 2021, vol. 2021, no. 4, pp. 410–417. DOI: [10.1134/S0036029521040303](https://doi.org/10.1134/S0036029521040303).
6. Zhilyaev A.P., Langdon T.G. Using high-pressure torsion for metal processing: fundamentals and applications. *Progress in Materials Science*, 2008, vol. 53, no. 6, pp. 893–979. DOI: [10.1016/j.pmatsci.2008.03.002](https://doi.org/10.1016/j.pmatsci.2008.03.002).
7. Zel'dovich V.I., Frolova N.Yu., Patselov A.M., Gundyrev V.M., Kheifets A.E., Pilyugin V.P. The ω -phase formation in titanium upon deformation under pressure. *Physics of Metals and Metallography*, 2010, vol. 109, no. 1, pp. 30–38. DOI: [10.1134/S0031918X10010059](https://doi.org/10.1134/S0031918X10010059).

8. Korneva A., Straumal B., Kilmametov A., Gondek Ł., Wierzbicka-Miernika A., Lityńska-Dobrzyńska L., Ciosg G., Chulista R., Zięba P. Thermal stability and microhardness of metastable ω -phase in the Ti-3.3 at.% Co alloy subjected to high pressure torsion. *Journal of Alloys and Compounds*, 2020, vol. 834, no. 5, article number 155132. DOI: [10.1016/j.jallcom.2020.155132](https://doi.org/10.1016/j.jallcom.2020.155132).
9. Zafari A., Wei X.S., Xu W., Xia K. Formation of nanocrystalline β structure in metastable beta Ti alloy during high pressure torsion: The role played by stress induced martensitic transformation. *Acta Materialia*, 2015, vol. 97, pp. 146–155. DOI: [10.1016/j.actamat.2015.06.042](https://doi.org/10.1016/j.actamat.2015.06.042).
10. Bartha K., Stráský J., Veverková A. et al. Effect of the High-Pressure Torsion (HPT) and Subsequent Isothermal Annealing on the Phase Transformation in Biomedical Ti15Mo Alloy. *Metals*, 2019, vol. 9, no. 11, article number 1194. DOI: [10.3390/met9111194](https://doi.org/10.3390/met9111194).
11. Gladkovsky S.V., Veselova V.E., Sergeev S.N., Patselov A.M. Influence of Heat Treatment on Microstructure and Mechanical Characteristics of the Titanium Alloy Ti–5Al–5V–2Mo–Cr with Metastable β -Phase. *Transactions of the Indian Institute of Metals*, 2023, vol. 76, pp. 2091–2097. DOI: [10.1007/s12666-023-02908-2](https://doi.org/10.1007/s12666-023-02908-2).
12. Veselova V.E., Gladkovskiy S.V., Kovalev N.I. Influence of heat treatment modes on the microstructure and mechanical properties of the metastable titanium alloy VT23. *Vestnik Permskogo natsionalnogo issledovatel'skogo politekhnicheskogo universiteta. Mashinostroenie, materialovedenie*, 2021, vol. 23, no. 4, pp. 31–39. EDN: [ZNGDLZ](https://www.edn.ru/ZNGDLZ).
13. Egorova L.Yu., Khlebnikova Yu.V., Pilyugin V.P., Chernyshev E.G. Initial Stages in the Evolution of the Structure of a Zirconium Pseudo-Single Crystal During Shear Deformation under Pressure. *Diagnostics, Resource and Mechanics of materials and structures*, 2017, no. 5, pp. 70–79. DOI: [10.17804/2410-9908.2017.5.070-079](https://doi.org/10.17804/2410-9908.2017.5.070-079).
14. Guan Bo, Xin Yunchang, Huang Xiaoxu, Liu Chenglu, Wu Peidong, Liu Qing. The mechanism for an orientation dependence of grain boundary strengthening in pure titanium. *International Journal of Plasticity*, 2022, vol. 153, article number 103276. DOI: [10.1016/j.ijplas.2022.103276](https://doi.org/10.1016/j.ijplas.2022.103276).
15. Kostryzhev A. Strengthening Mechanisms in Metallic Materials. *Metals*, 2021, vol. 11, no. 7, article number 1134. DOI: [10.3390/met11071134](https://doi.org/10.3390/met11071134).
16. Lyasotskaya V.S., Knyazeva S.I. Metastable phases in titanium alloys and conditions of their formation. *Metal Science and Heat Treatment*, 2008, vol. 50, no. 7-8, pp. 373–377. DOI: [10.1007/s11041-008-9064-x](https://doi.org/10.1007/s11041-008-9064-x).
17. Blinova E.N., Libman M.A., Glezer A.M., Isaenkova M.G., Tomchuk A.A., Komlev A.S., Krymskaya O.A., Filippova V.P., Shurygina N.A. Phase transformations in a metastable Fe–18Cr–10Ni alloy during megaplastic deformation. *Russian Metallurgy (Metally)*, 2022, vol. 2022, no. 10, pp. 1174–1180. DOI: [10.1134/s0036029522100032](https://doi.org/10.1134/s0036029522100032).
2. Глезер А.М., Метлов Л.С. Физика мегапластической (интенсивной) деформации твердых тел // Физика твердого тела. 2010. Т. 52. № 6. С. 1090–1097. EDN: [RCRYIV](https://www.edn.ru/RCRYIV).
3. Sergueeva A.V., Stolyarov V.V., Valiev R.Z., Mukherjee A.K. Enhanced superplasticity in a Ti6Al4V alloy processed by severe plastic deformation // *Scripta Materialia*. 2000. Vol. 43. № 9. P. 819–824. DOI: [10.1016/S1359-6462\(00\)00496-6](https://doi.org/10.1016/S1359-6462(00)00496-6).
4. Валиев Р.З., Александров И.В. Объемные наноструктурные металлические материалы: получение, структура и свойства. М.: Академкнига, 2007. 398 с.
5. Shurygina N.A., Cheretaeva A.O., Glezer A.M., Medvedeva A.D., D'yakonov D.L., Sundeev R.V., Tomchuk A.A. Effect of Microalloying Elements on the Physicochemical Properties of Commercial-Purity Titanium Subjected to Severe Plastic Deformation // *Russian Metallurgy (Metally)*. 2021. Vol. 2021. № 4. P. 410–417. DOI: [10.1134/S0036029521040303](https://doi.org/10.1134/S0036029521040303).
6. Zhilyaev A.P., Langdon T.G. Using high-pressure torsion for metal processing: fundamentals and applications // *Progress in Materials Science*. 2008. Vol. 53. № 6. P. 893–979. DOI: [10.1016/j.pmatsci.2008.03.002](https://doi.org/10.1016/j.pmatsci.2008.03.002).
7. Зельдович В.И., Фролова Н.Ю., Пацелов А.М., Гундырев В.М., Хейфец А.Э., Пилиugin В.П. Образование омега-фазы в титане при деформации под давлением // Физика металлов и металловедение. 2010. Т. 109. № 1. С. 33–42. EDN: [KZLPSE](https://www.edn.ru/KZLPSE).
8. Korneva A., Straumal B., Kilmametov A., Gondek Ł., Wierzbicka-Miernika A., Lityńska-Dobrzyńska L., Ciosg G., Chulista R., Zięba P. Thermal stability and microhardness of metastable ω -phase in the Ti-3.3 at.% Co alloy subjected to high pressure torsion // *Journal of Alloys and Compounds*. 2020. Vol. 834. № 5. Article number 155132. DOI: [10.1016/j.jallcom.2020.155132](https://doi.org/10.1016/j.jallcom.2020.155132).
9. Zafari A., Wei X.S., Xu W., Xia K. Formation of nanocrystalline β structure in metastable beta Ti alloy during high pressure torsion: The role played by stress induced martensitic transformation // *Acta Materialia*. 2015. Vol. 97. P. 146–155. DOI: [10.1016/j.actamat.2015.06.042](https://doi.org/10.1016/j.actamat.2015.06.042).
10. Bartha K., Stráský J., Veverková A. et al. Effect of the High-Pressure Torsion (HPT) and Subsequent Isothermal Annealing on the Phase Transformation in Biomedical Ti15Mo Alloy // *Metals*. 2019. Vol. 9. № 11. Article number 1194. DOI: [10.3390/met9111194](https://doi.org/10.3390/met9111194).
11. Gladkovsky S.V., Veselova V.E., Sergeev S.N., Patselov A.M. Influence of Heat Treatment on Microstructure and Mechanical Characteristics of the Titanium Alloy Ti–5Al–5V–2Mo–Cr with Metastable β -Phase // *Transactions of the Indian Institute of Metals*. 2023. Vol. 76. P. 2091–2097. DOI: [10.1007/s12666-023-02908-2](https://doi.org/10.1007/s12666-023-02908-2).
12. Веселова В.Е., Гладковский С.В., Ковалев Н.И. Влияние режимов термической обработки на структуру и механические свойства метастабильного титанового сплава VT23 // Вестник Пермского национального исследовательского политехнического университета. Машиностроение, материалovedenie. 2021. Т. 23. № 4. С. 31–39. EDN: [ZNGDLZ](https://www.edn.ru/ZNGDLZ).
13. Egorova L.Yu., Khlebnikova Yu.V., Pilyugin V.P., Chernyshev E.G. Initial Stages in the Evolution of the Structure of a Zirconium Pseudo-Single Crystal During Shear Deformation under Pressure // *Diagnostics*.

СПИСОК ЛИТЕРАТУРЫ

1. Семенова И.П., Рааб Г.И., Валиев Р.З. Наноструктурные титановые сплавы: новые разработки и перспективы применения // Российские нанотехнологии. 2014. Т. 9. № 5-6. С. 84–95. EDN: [SMKYOB](https://www.edn.ru/SMKYOB).

- tics, Resource and Mechanics of materials and structures. 2017. № 5. P. 70–79. DOI: [10.17804/2410-9908.2017.5.070-079](https://doi.org/10.17804/2410-9908.2017.5.070-079).
14. Guan Bo, Xin Yunchang, Huang Xiaoxu, Liu Chenglu, Wu Peidong, Liu Qing. The mechanism for an orientation dependence of grain boundary strengthening in pure titanium // International Journal of Plasticity. 2022. Vol. 153. Article number 103276. DOI: [10.1016/j.ijplas.2022.103276](https://doi.org/10.1016/j.ijplas.2022.103276).
15. Kostyryzhev A. Strengthening Mechanisms in Metallic Materials // Metals. 2021. Vol. 11. № 7. Article number 1134. DOI: [10.3390/met11071134](https://doi.org/10.3390/met11071134).
16. Лясоцкая В.С., Князева С.И. Метастабильные фазы в титановых сплавах и условия их образования // Металловедение и термическая обработка металлов. 2008. № 8. С. 15–19. EDN: [KVXLNV](https://www.edn.ru/kvxlrv/).
17. Блинова Е.Н., Либман М.А., Глезер А.М., Исаенкова М.Г., Томчук А.А., Комлев А.С., Крымская О.А., Филиппова В.П., Шурыгина Н.А. Особенности фазовых превращений в метастабильном сплаве Fe-18Cr-10Ni при мегапластической деформации // Деформация и разрушение материалов. 2022. № 4. С. 19–26. EDN: [BIYLUD](https://www.edn.ru/byylud/).

Фазовый состав, структура и микротвердость титанового сплава VT23 после деформации в камере Бриджмена

Гладковский Сергей Викторович^{1,3}, доктор технических наук, главный научный сотрудник, заведующий лабораторией деформирования и разрушения
Пилугин Виталий Прокофьевич^{2,4}, кандидат физико-математических наук, ведущий научный сотрудник, заведующий лабораторией физики высоких давлений
Веселова Валерия Евгеньевна^{*1,5}, кандидат технических наук, научный сотрудник лаборатории деформирования и разрушения
Пацелов Александр Михайлович^{2,6}, кандидат физико-математических наук, старший научный сотрудник лаборатории физики высоких давлений

¹Институт машиноведения имени Э.С. Горкунова Уральского отделения РАН, Екатеринбург (Россия)

²Институт физики металлов имени М.Н. Михеева Уральского отделения РАН, Екатеринбург (Россия)

*E-mail: veselova@imach.uran.ru

³ORCID: <https://orcid.org/0000-0002-3542-6242>

⁴ORCID: <https://orcid.org/0000-0002-5150-6605>

⁵ORCID: <https://orcid.org/0000-0002-4955-6435>

⁶ORCID: <https://orcid.org/0000-0001-6438-0725>

Поступила в редакцию 13.09.2024

Пересмотрена 21.10.2024

Принята к публикации 05.11.2024

Аннотация: Впервые изучены фазовый состав, микротвердость и тонкая структура (α + β)-титанового сплава VT23 со стабильной и метастабильной β -фазой после деформации в камере Бриджмена кручением под давлением 4 ГПа при комнатной температуре. Установлено, что микротвердость сплава в зависимости от истинной степени деформации в условиях высокого гидростатического давления меняется по кривой с максимумом. Выявлена роль инициированного напряжением $\beta_m \rightarrow \alpha''$ мартенситного превращения в формировании структуры и микротвердости сплава при кручении под давлением. Наибольшая микротвердость сплава со стабильной β -фазой составила 395 HV 0,05, а с метастабильной – 470 HV 0,05. При этом максимум микротвердости метастабильного сплава по сравнению со стабильным был смещен в область меньшей истинной деформации $e=2,6$. Использование методов рентгенофазового анализа и просвечивающей электронной микроскопии позволило проследить эволюцию структуры сплава при деформации под давлением, заключающуюся в измельчении по сравнению с закаленным состоянием пластин α - и α'' -фаз, а также в развитии деформационных $\beta_m \rightarrow \alpha''$ и $\alpha'' \rightarrow \beta_m$ мартенситных превращений. Увеличение степени деформации кручением под давлением до $e=7,7...7,9$ независимо от деформационной стабильности β -фазы приводит к снижению микротвердости сплава до уровня 185...205 HV 0,05, что связано с развитием процесса динамической рекристаллизации и формированием равноосных наночастиц α -фазы размером 20...50 нм. Выявленные при кинетическом индентировании различия в кривых нагружения – разгрузки соответствовали характеру изменения микротвердости сплава VT23 в зависимости от температуры закалки и степени истинной деформации.

Ключевые слова: титановый сплав VT23; фазовый состав; камера Бриджмена; кручение под давлением; истинная степень деформации; метастабильная β -фаза; мартенситные превращения.

Благодарности: Работа выполнена в рамках госзадания ИМАШ УрО РАН № 124020600045-0 и ИФМ УрО РАН № 122021000032-5 с использованием оборудования ЦКП «Пластометрия» ИМАШ УрО РАН. Авторы выражают благодарность С.Н. Сергееву (ИПСМ РАН) за помощь в проведении структурного анализа методом просвечивающей электронной микроскопии.

Для цитирования: Гладковский С.В., Пилугин В.П., Веселова В.Е., Пацелов А.М. Фазовый состав, структура и микротвердость титанового сплава VT23 после деформации в камере Бриджмена // Frontier Materials & Technologies. 2024. № 4. С. 29–38. DOI: [10.18323/2782-4039-2024-4-70-3](https://doi.org/10.18323/2782-4039-2024-4-70-3).

Study of centrifugal atomisation mechanisms based on a simulated experiment

*Evgeny Yu. Zhukov**, engineer

of Chair “Technologies and Systems for Automated Design of Metallurgical Processes” (1101)

Alibek S. Naurzalinov, technician

of Chair “Technologies and Systems for Automated Design of Metallurgical Processes” (1101)

*Igor N. Pashkov*¹, Doctor of Sciences (Engineering),

professor of Chair “Technologies and Systems for Automated Design of Metallurgical Processes” (1101)

Moscow Aviation Institute (National Research University), Moscow (Russia)

*E-mail: ZhukovEY@mai.ru,
jezzacome@gmail.com

¹ORCID: <https://orcid.org/0000-0003-2511-2845>

Received 15.02.2024

Revised 16.04.2024

Accepted 28.10.2024

Abstract: The process of melt dispersion on a rotating bowl is a common method for producing metal powders. It is difficult to study the dispersion process on real melts, including by visualisation methods. Therefore, it is proposed to study the influence of such factors as the jet fall height, liquid flow rate, surface wetting, and the presence of a bowl wall on the process of obtaining small droplets using a model liquid without crystallisation, recording the process by high-speed shooting. The purpose of this work is to determine the most favourable dispersion conditions, when all the supplied liquid turns into droplets without the formation of large droplets, additional jets leading to secondary spraying. A glycerol solution in water with a viscosity equal to the viscosity of tin melt was chosen as a model liquid. The dispersion process was shot on a high-speed camera with a shooting frequency of 1,200 frames per second. It was found that when increasing the melt flow, a change in the spray mode is observed. With an increase in pressure, the flow and kinetic interaction of the jet with the surface of the bowl, increase, and consequently, the excess liquid, which is sprayed prematurely, increases. At any flow of the supplied liquid, if the liquid does not get to the centre, secondary spraying occurs due to the destruction of the film, on the hydraulic jump, because of the uneven radial velocity at the peak of the jump. When the feed height changes from 100 to 150 mm, secondary spraying in the form of droplets is observed at the hydraulic jump area. The number of spirals and secondary spraying affect the increase in the size of the particle fraction. In the range of the jet fall height from 50 to 100 mm, an optimal process is observed, in which it is possible to obtain the smallest fraction. In the experiment, a tendency to improve the spraying process when increasing the bowl surface finish was observed. Due to the walls of the bowl, the path of the liquid before it leaves the bowl increases, drops flying above the surface of the bowl are destroyed into a film, therefore, the dispersion process improves.

Keywords: centrifugal melt atomisation; melt dispersion on a rotating bowl; liquid flow; metal powder; hydrodynamic conditions; high-speed shooting.

For citation: Zhukov E.Yu., Naurzalinov A.S., Pashkov I.N. Study of centrifugal atomisation mechanisms based on a simulated experiment. *Frontier Materials & Technologies*, 2024, no. 4, pp. 39–49. DOI: 10.18323/2782-4039-2024-4-70-4.

INTRODUCTION

Centrifugal melt atomisation (CMA) is one of the common methods for producing metal powders by dispersing the melt. Compared to spraying the melt with gas or water, CMA has a narrower range of particle sizes, which gives great advantages to this method in terms of yield. The essence of the method is to destroy the melt under the action of centrifugal forces on a rotating bowl. In this case, the melt can be supplied to the bowl in the form of a jet, films, and drops [1]. In any case, a liquid film is formed on the surface of the bowl, which turns into drops on the edge of the rotating bowl. The CMA method is limited to producing materials with a low melting point. This is mainly associated with the necessity to ensure that the melt wets the surface of the bowl, and makes it resistant to the effects of

the melt. For high-temperature alloys, centrifugal atomisation of a rotating rod is usually used.

The process of obtaining metal particles of a given size is affected by the hydrodynamic conditions of the liquid dispersion process, and the thermal conditions associated with cooling and solidification of the melt. To obtain a given powder particle size, it is necessary first to ensure the supply of a liquid jet to the bowl, its distribution over the surface and dispersion into particles of a certain size. Simultaneous solution of the problems of studying hydrodynamic and thermal processes is cumbersome and difficult, so it makes sense to study them separately.

Analysis of literary sources on CMA shows that the main attention is paid to the problems of the influence of the liquid flow nature, the disk design and the spraying

parameters on the fractional composition of the resulting powder. It is noted that the rotation speed of the bowl mainly determines the size of the resulting powder. To obtain highly dispersed powders, it is necessary to select an electric motor with a rotation frequency of 10,000 rpm [2; 3].

One of the most important parameters during spraying is achieving a certain liquid flow [4; 5]. During centrifugal atomisation, molten metal wets the disk and flows to the disk periphery, where it forms a liquid torus. The instability caused by the disk rotation creates small bundles at the disk edges, which are then thrown off the disk in the form of droplets. At high liquid feed rates, bundles may not form, and the film disintegration mode will occur [6–8]. At low liquid feed rates, droplets can form directly at or in front of the disk edge due to incomplete wetting of the disk [9–11]. In [12], the atomisation process is described when the flow changes from 3 to 10 kg/h; as the flow increases, three mechanisms of liquid atomisation at the bowl edge are observed: droplets, streamlets, and film.

At high rotation speeds, the so-called hydraulic jump often occurs on the bowl [13–15]. A hydraulic jump is an annular jump in the flow, which manifests itself in a sharp increase in the melt thickness, and accordingly, a decrease in the radial velocity, as well as in the separation of liquid particles before reaching the edge of the bowl [13–15].

In [16; 17], it is shown that there is a certain optimal distance from the liquid source to the bowl, at which the powder of the smallest fraction is obtained. If this distance is deviated, the powder size increases, or the range of the fractional composition of the particles expands.

Many sources note that it is necessary to ensure good wettability of the bowl surface with the metal melt [18; 19]. To achieve this, it is even proposed to use a bowl with a coating, the composition of which is similar to the composition of the sprayed material. In this case, good wetting was achieved [19]. For maximum wetting of the bowl surface with the melt during spraying, the bowl can be pre-tinned with the sprayed material. The bowl surface finish affects the adhesion of the melt. A tendency to improve the spraying process when increasing the bowl surface finish is observed. In real processes of metal dispersion on a rough surface, as shown in [20], metal sticks to the bowl surface and solidifies in the form of a torus. On the treated surface, the liquid film will be distributed over the bowl more evenly.

The work [21] describes the effect of bowl slope angle on the size of the resulting particles. The higher this angle, the finer the powders that can be obtained. The finest powder was obtained at an angle of 60–70°. There are no experimental data on the angle of the bowl inclination of 90° [21]. The work [10] shows a decrease in the powder fraction with a bowl with sloped wall. Due to the walls, the path of the liquid before it exits the bowl increases, and as a result, the film decreases closer to the bowl edge.

Therefore, the existing experimental data or calculation models consider the influence of various factors of the dispersion process only on the size of the resulting product, the conditions for maintaining the stability of

the process itself are not taken into account. The important role of hydrodynamic processes is noted, but there are no descriptions of the behaviour of a liquid jet when it hits a rotating bowl, turning it into a film with subsequent destruction into drops. The phenomenon of secondary dispersion of large drops and liquid fragments, which have a different speed compared to the film on the bowl, is not considered as well. Therefore, it is of interest to visualise the dispersion process of a model liquid, without taking into account the solidification processes using high-speed shooting.

The purpose of this work is to determine the most favourable dispersion conditions, when all the supplied liquid turns into drops without the formation of large drops and additional jets leading to secondary spraying.

METHODS

The experiments on dispersion on a rotating bowl were carried out with a model liquid. A glycerol solution in water in a ratio of 60/40 was chosen as a model liquid, the viscosity of which corresponded to the molten tin viscosity. The experiment did not take into account supercooling and solidification of melts in real processes. Only the hydrodynamics of the liquid behaviour was studied. The entire process proceeded in air.

To carry out the experiment, a special facility was created consisting of a high-speed rotation drive, a bowl, and a liquid feed device. The rotation drive was rigidly fixed to a massive body. The spraying bowl had a diameter of 36 mm. Liquid was fed to the surface of the bowl through a 50 ml syringe. The liquid feed rate was changed using the pressure in the syringe, equal to 1, 2 and 4 atm, and the needle diameter of 0.8 and 1.5 mm. The diagram of the facility is shown in Fig. 1.

The rotation speed of the bowl was chosen constant, equal to 10,000 rpm. The height of the liquid feed varied from 20 to 150 mm. The bowl slope angle was 0° and 90°.

The experiments were carried out under conditions of complete wetting of the bowl surface with liquid. To obtain a non-wetting mode, synthetic rubber was applied to the spraying bowl.

The experiment considered three types of bowls: smooth (the working surface of the bowl was polished with abrasive paper with a grain size of 800), rough (achieved using paper with a grain size of 40), and without processing (there are traces of a cutter).

The shooting was carried out using a high-speed Casio EX-F1 camera at a shooting frequency of 1,200 frames per second. The formation of a thick film on the surface of the bowl, secondary formation of jets and premature atomisation of liquid were considered to be incorrect centrifugal atomisation conditions.

To determine the values of the hydraulic jump radius R_c and the height of the liquid film H , the following equations were used [9]:

$$R_c = 0.55 \left(\frac{\rho Q^2}{\mu \omega} \right)^{\frac{1}{4}},$$

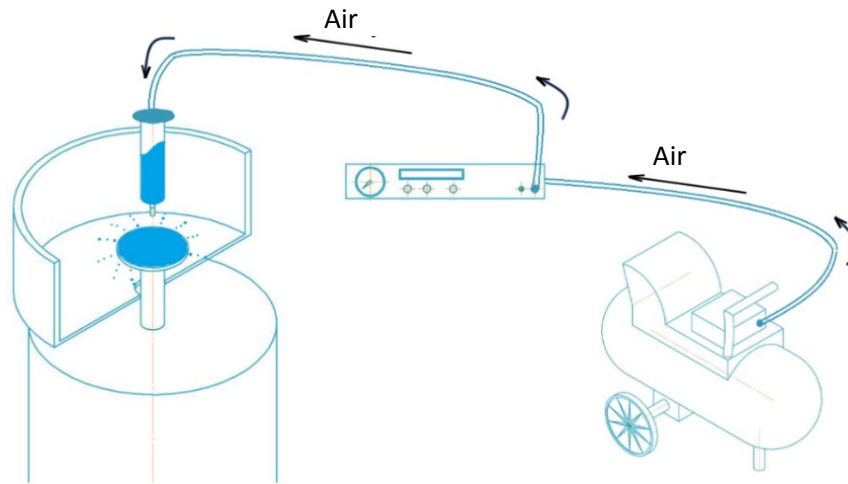


Fig. 1. Diagram of the centrifugal atomization process
Рис. 1. Схема процесса центробежного распыления

where ρ is the density of the liquid, kg/m^3 ;
 Q is the volumetric flow rate, m^3/s ;
 μ is the dynamic viscosity, $\text{Pa}\cdot\text{s}$;
 ω is the rotation speed of the bowl, rad/s ;

$$H = \left[\frac{3 \mu Q}{2 \pi \rho \omega^2 r^2 \cos \alpha} \right]^{\frac{1}{3}},$$

where r is the radius of the bowl, m ;
 α is the angle of inclination of the bowl.

RESULTS

Liquid behaviour at the moment of contact with a rotating disk

When liquid is in contact with a rotating bowl, a disk volume of liquid is formed around the jet, which then stretches to the periphery. When the jet hits the centre of the rotating bowl, a quiet stretching of the film to the pe-

riphery and spraying at the bowl edge is observed. When the jet deviates from the bowl centre, large fragments appear that elastically bounce off the surface forming large drops. Premature spraying of the liquid occurs.

Increasing the distance to the bowl leads to a violation of the continuity of the jet, its disintegration into parts, and an increase in the probability of deviation from the centre, as a result – the appearance of premature spraying at the moment of contact with the bowl surface (Fig. 2).

When changing the surface roughness, we can observe that the higher the purity of the bowl surface, the more evenly the liquid is distributed over the bowl surface (Fig. 3).

Liquid behaviour on the bowl surface during the steady-state rotation process

Changing the liquid flow. Calculation of liquid flows for different needle diameters and pressures, as well as by draulic jump radii and film thicknesses, showed that with an increase in melt flow from 3.96 to 42.35 kg/h , the hydraulic jump radius increases approximately 3 times –



Fig. 2. Changing the height of liquid feed from the bowl at a flow rate of 6.69 kg/h and smooth bowl processing:
a – 20 mm; **b** – 50 mm; **c** – 150 mm
Рис. 2. Изменение высоты подачи жидкости от чаши при потоке 6,69 кг/ч и гладкой обработке чаши:
a – 20 мм; **b** – 50 мм; **c** – 150 мм

from 1.83 mm to 6 mm. At the same time, the liquid film height, according to calculations, increases only 2 times – from 0.34 to 0.62 mm (Table 1).

With a constant supply of liquid to the bowl with a needle diameter of 0.8 mm (Fig. 4), and a pressure of up to 2 atm., the formation of spirals on the surface was observed. Spraying occurred along the trajectory of these spirals. There was a shortage of liquid flow for its distribution over the entire bowl surface. When the pressure exceeds 2 atm., due to an increase in the jet velocity, secondary spraying in the form of directed streams occurs to the bowl edge.

With a needle diameter of 1.5 mm (Fig. 5) and a pressure of up to 2 atm., an almost smooth film surface is observed on the bowl with small spirals, and spraying is carried out along the entire periphery of the bowl, and along the spirals. The film thickness on the surface is greater than with a needle diameter of 0.8 mm. With an increase in pressure of more than 2 atm., there are no spirals on the surface, and the spraying itself is carried out only through the bowl edge. Thus, with an insufficient liquid flow, spiral flows are

formed, which are sprayed on the bowl edge or up to it. With a sufficient flow, a continuous film of liquid is observed, which is completely sprayed on the bowl edge. An increase in the flow leads to an increase in the film thickness, and therefore, the particle size.

Changing the liquid feed height. If we change the height of the liquid feed to the bowl at a low flow rate of 6.69 kg/h, it is clear that the smaller the distance to the bowl, the more uniform the layer is formed on it, however, spirals are observed that converge at a distance of up to 50 mm (Fig. 6). Along the trajectory of these spiral formations, spraying in the form of streams can be observed at the bowl edge. It is assumed that the main spraying in this case will occur through these streams. At a jet feed height of 100 to 150 mm, double spraying was observed (Fig. 6).

Influence of wetting of the bowl surface. Almost complete non-wetting of the surface was achieved (Fig. 7). During the experiment, various options for treating the bowl surface were tested: applying oil, wax



Fig. 3. Changing the surface roughness at a flow rate of 6.69 kg/h and a distance to the bowl of 50 mm:
a – a smooth bowl; b – a bowl without treatment

Рис. 3. Изменение шероховатости поверхности при потоке 6,69 кг/ч и расстоянии до чаши 50 мм:
a – гладкая чаша; b – чаша без обработки

Table 1. Calculation of liquid parameters during centrifugal atomization
Таблица 1. Расчет параметров жидкости при центробежном распылении

Needle diameter, mm	Pressure, atm.	Flow rate, kg/h	Hydraulic jump radius, mm	Film height, mm
0.8	1	3.96	1.83	0.34
	2	6.69	2.38	0.39
	4	9.25	2.80	0.42
1.5	1	21.18	4.24	0.52
	2	34.45	5.40	0.59
	4	42.35	6.00	0.62

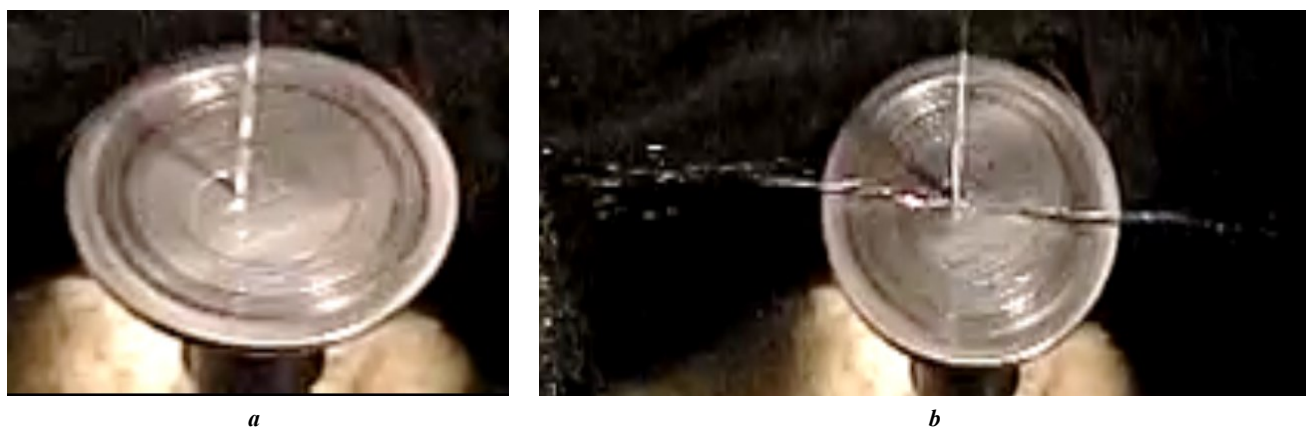


Fig. 4. Changing pressure when liquid is supplied to the surface of the bowl without treatment, needle diameter is 0.8 mm:
a – 1 atm.; *b* – 2 atm.

Рис. 4. Изменение давления при подаче жидкости на поверхность чаши без обработки, диаметр иглы 0,8 мм:
a – 1 атм.; *b* – 2 атм.



Fig. 5. Changing pressure when liquid is supplied to the surface of the bowl without treatment, needle diameter is 1.5 mm:
a – 1 atm.; *b* – 2 atm.

Рис. 5. Изменение давления при подаче жидкости на поверхность чаши без обработки, диаметр иглы 1,5 мм:
a – 1 атм.; *b* – 2 атм.



Fig. 6. Changing the distance from the needle to the smooth surface of the bowl:
a – 50 mm; *b* – 100 mm; *c* – 150 mm

Рис. 6. Изменение расстояния от иглы до гладкой поверхности чаши:
a – 50 мм; *b* – 100 мм; *c* – 150 мм

and other materials, that were not wetted by the experimental solution. However, at bowl rotation speeds of 10,000 rpm, the model liquid washed away the applied layers. In our case, with a constant supply of liquid through a 0.8 mm diameter needle, a decrease in the number and size of spirals is observed on the non-wetted surface. Only after 4 atm., premature spraying of liquid through streams occurs at the moment of liquid entry, and these streams are not formed immediately after the start of liquid supply to the bowl (Fig. 8).

Changing the bowl geometry. Experiments were carried out with a 0.8 mm diameter needle. On the smooth surface of the bowl, the liquid is distributed more evenly, and the film becomes thinner, unlike the bowl without treatment. The nature of the spirals and streams remain unchanged when the pressure changes for these types of bowls (Fig. 9). If the surface roughness is increased by coarse abrasive treatment, then the spraying process deteriorates, both at the initial moment of contact of the liquid with the bowl and during the steady-state process (Fig. 10). It is obvious that the rough surface of the bowl introduces strong disturbances into the liquid flow, leading to its destruction in the form of streams and drops of different sizes.

In the absence of sloped wall, secondary spraying is observed in the form of drops that fly at an angle to the surface of the bowl. The bowl slope angle of 90° ensures the distribution of large streams and drops of liquid that fall as a result of secondary spraying over its surface, and their spraying on the edge of the bowl. Thus, the proportion of secondary spraying decreases in the presence of sloped wall, and the process becomes more stable.

With a needle diameter of 1.5 mm, the size of the film sprayed from a bowl with sloped wall decreases, in contrast to a bowl without sloped wall. On the surface of the bowl, a liquid film is formed similarly to a bowl without sloped wall (Fig. 11).

DISCUSSION

Liquid behaviour at the moment of contact with a rotating disk

When a jet hits the centre of a rotating bowl, the liquid enters a region with zero radial velocity. It spreads over the bowl surface with a constant increase in velocity as it moves away from the centre. When the jet hits at some distance from the centre, part of the liquid spreads over



Fig. 7. A drop of water on a non-wetted surface
Рис. 7. Капля воды на несмачиваемой поверхности



Fig. 8. Changing pressure when supplying to a non-wetted surface of a bowl:
a – 1 atm.; b – 4 atm.
Рис. 8. Изменение давления при подаче на несмачиваемую поверхность чаши:
a – 1 атм.; b – 4 атм.

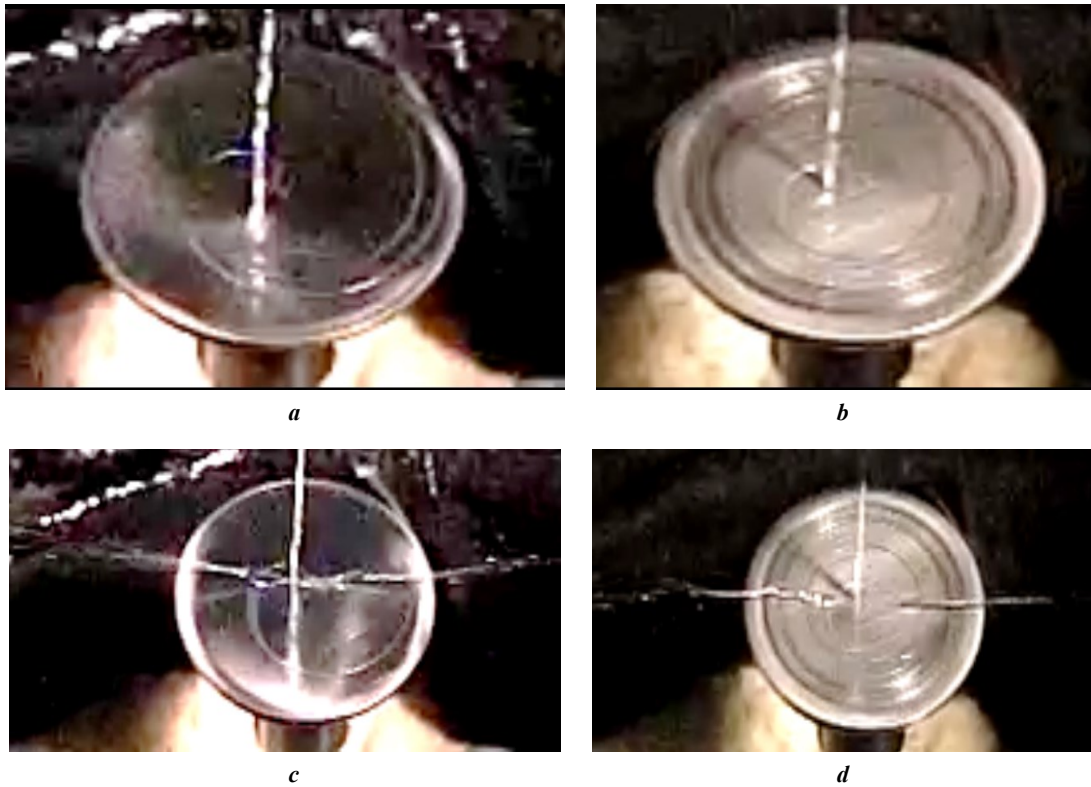


Fig. 9. Changing the pressure of the liquid supplied to the bowl:
a – 1 atm., smooth bowl surface; *b* – 1 atm., untreated bowl surface;
c – 2 atm., smooth bowl surface; *d* – 2 atm., untreated bowl surface

Рис. 9. Изменение давления подаваемой жидкости на чашу:
a – 1 атм., гладкая поверхность чаши; *b* – 1 атм., поверхность чаши без обработки;
c – 2 атм., гладкая поверхность чаши; *d* – 2 атм., поверхности чаши без обработки



Fig. 10. Changing the pressure of the liquid supplied to the rough bowl surface: *a* – 1 atm.; *b* – 2 atm.

Рис. 10. Изменение давления подаваемой жидкости на шероховатую поверхность чаши: *a* – 1 атм.; *b* – 2 атм.

the bowl surface, and part elastically bounces off in the form of large fragments that have a lower speed than the particles from the edge of the bowl have. This part of the liquid does not disperse into small droplets due to a lack of energy. It can be assumed that such premature spraying can lead to the appearance of large powder particles during melt spraying.

Literary sources do not provide a division of the process into the initial (the moment the jet touches the bowl) and steady-state. This is mainly related to the fact that the fractional composition of the resulting powder is usually used to evaluate the spraying process. In general, at the initial stage, all factors that play a decisive role in

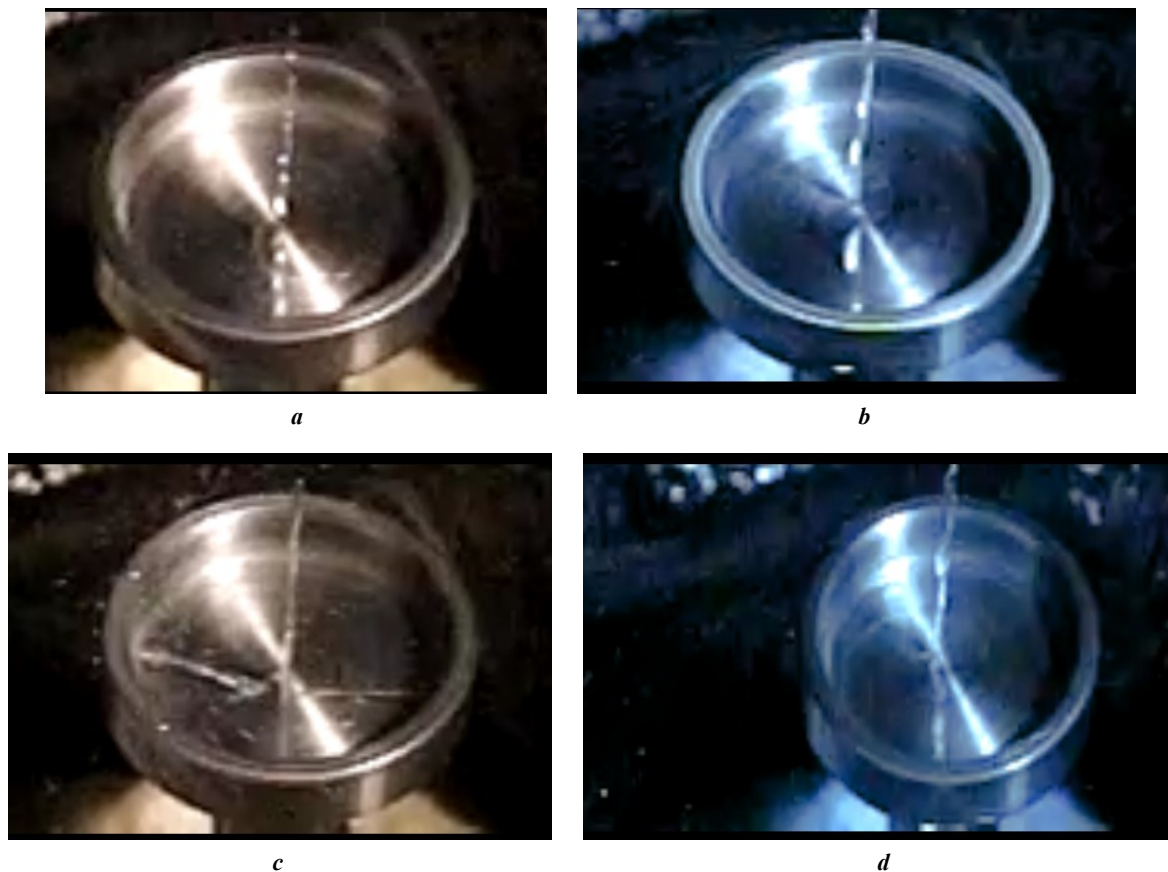


Fig. 11. Changing the pressure and needle diameter when spraying liquid on a bowl with sloped wall:
a – diameter is 0.8 mm, pressure is 1 atm.; *b* – diameter is 1.5 mm, pressure is 1 atm.;
c – diameter is 0.8 mm, pressure is 2 atm.; *d* – diameter is 1.5 mm, pressure is 2 atm.

Рис. 11. Изменение давления и диаметр иглы при распылении жидкости на чаше с бортами:
a – диаметр 0,8 мм, давление 1 атм.; *b* – диаметр 1,5 мм, давление 1 атм.;
c – диаметр 0,8 мм, давление 2 атм.; *d* – диаметр 1,5 мм, давление 2 атм.

the steady-state process are important: the distance of the jet feed [16; 17], the flow rate, wetting of the bowl surface [19]. Increasing the height of the jet fall leads to its partial destruction, and the possibility of elastic reflection of part of the liquid. The appearance of large drops when liquid hits a rough surface is associated with strong disturbance, that occurs when the liquid flow hits the rough surface. Reducing the roughness promotes the formation of a stable film on the bowl surface.

Liquid behaviour on the bowl surface during the steady-state rotation process

Changing the liquid flow. One of the important conditions for liquid dispersion from the bowl edges is the correspondence of its flow to the conditions for the formation of a continuous layer on the bowl surface. Otherwise, sources of secondary spraying appear. Depending on the flow, and the distance to the bowl, a hydraulic jump in the form of a ring of liquid is formed. At the hydraulic jump, the film ruptures due to excess liquid and then develops into jets, which corresponds to the data of work [10]. At any liquid flow, if it does not enter the centre, secondary spraying occurs caused by the film destruction at the hydraulic jump, due to the uneven radial velocity at the peak of the jump.

In the literature, there are no descriptions of the formation of spiral flows on the bowl surface. Their formation is obviously associated with a lack of liquid to fill the entire surface of the bowl. In this case, the liquid should have spread into a very thin layer, so the surface tension led to the formation of spiral flows. In this case, spraying was always observed at the exit of the spirals to the edge of the bowl. It was mostly in the form of droplet spraying. As the flow increases, the liquid is “stretched” over the surface of the bowl with spraying along its entire perimeter. As the flow increases and a continuous layer of liquid forms on the surface of the bowl, the spraying shifts towards jet and film spraying. This is in good agreement with the literature [12].

Influence of wetting of the bowl surface. Despite the indication in [18; 19] of the need to wet the bowl surface with the melt, the model experiment failed to reveal any specific patterns in the behaviour of the liquid on the bowls under conditions of complete wetting and non-wetting. The experiment on the coated bowl showed contradictory data that require additional research. This may have resulted from the destruction and detachment of the applied barrier layer.

Changing the bowl geometry. As the results of process visualisation showed, the presence of sloped wall on

the edge of the bowl is necessary to achieve a stable spraying process. This is in good agreement with the results of [10; 21]. Although the sources describe experiments on bowl slope angle of 60–70°, the use of bowl slope angle of 90° also proved to be effective. The experiment confirmed that the presence of sloped wall increases the distance that the liquid travels before spraying [10], but this, in our opinion, is not the main advantage of having sloped wall on the bowl. The main advantage is that the liquid droplets flying at an angle to the bowl surface as a result of premature spraying can be distributed along the sloped wall, and then sprayed in the form of small droplets through its edge. This can be of particular importance when the bowl surface is poorly wetted by the liquid.

Changing the liquid feed height. Changing the jet fall height within 20–150 mm has a significant effect on the occurrence of secondary spraying. There is an optimal height of liquid jet feed, which is in good agreement with the literature data [11]. In our experiment, the optimal range for stable spraying of the model liquid was 50–100 mm. A too high jet fall height leads to its premature destruction into smaller jets and droplets, which, if they do not hit the exact centre of the bowl, elastically bounce off causing secondary spraying of large particles. When the jet feed point approaches the bowl, it is more likely to hit its centre, which leads to stability of the spraying process. A too close location complicates the technological feasibility of implementing the liquid feed.

CONCLUSIONS

1. In general, the results obtained by the model liquid dispersion correlate with the literature data on the process, and allow evaluating the behaviour of the liquid on the bowl surface in terms of the formation of a uniform dispersion front without secondary spraying.

2. The start of the dispersion process at the moment of contact of the liquid jet should ensure that the jet accurately hits the centre of the rotating bowl; the liquid should be supplied from a height in the range of 50–100 mm. Otherwise, secondary spraying sources appear.

3. The main important parameter of the dispersion process is the creation of a liquid flow, that ensures uniform coating of the bowl surface with a liquid film and spraying from the entire periphery of the bowl. If the flow is insufficient, liquid ruptures and the formation of spirals and jets occur, which are dispersed on the bowl periphery.

4. On a smooth bowl, in contrast to a bowl without treatment, wettability is better and the film that forms on the surface is thinner. A rough bowl is the worst suited for spraying.

5. On a bowl with sloped wall, a decrease in the film thickness at the bowl edge is observed, spraying is more uniform. The sloped wall also break up the jets and drops of liquid into a film, which is then dispersed from the edges.

6. According to the literature, wetting should promote the movement of liquid within the boundary layer to the bowl periphery. On a model liquid under conditions of limited wetting, opposite results were obtained, which requires additional research.

REFERENCES

1. Trufanov D.A., Kotov S.A., Shalashov E.V., Chasov V.V. Receiving metallic powders by centrifugal atomization using a rotating cup. *Metalloobrabotka*, 2016, no. 4, pp. 57–62. EDN: [XBJSYJ](#).
2. Ahmed M., Youssef M.S. Characteristics of mean droplet size produced by spinning disk atomizers. *Journal of Fluids Engineering*, 2012, vol. 134, no. 7, article number 071103. DOI: [10.1115/1.4006819](#).
3. Ahmed M., Youssef M.S. Influence of spinning cup and disk atomizer configurations on droplet size and velocity characteristics. *Chemical Engineering Science*, 2014, vol. 107, pp. 149–157. DOI: [10.1016/j.ces.2013.12.004](#).
4. Ahmed M., Amighi A., Ashgriz N., Tran H.N. Characteristics of liquid sheets formed by splash plate nozzles. *Experiments in Fluids*, 2008, vol. 44, no. 1, pp. 125–136. DOI: [10.1007/s00348-007-0381-4](#).
5. Bao Qieng, Yang Yiru, Wen Xiaochun, Guo Lei, Guo Zhancheng. The preparation of spherical metal powders using the high-temperature remelting spheroidization technology. *Materials & Design*, 2021, vol. 199, article number 109382. DOI: [10.1016/j.matdes.2020.109382](#).
6. Moghimian P., Poirie T., Habibnejad-Korayem M., Zavala J.A., Kroeger J., Marion F., Larouche F. Metal powders in additive manufacturing: A review on reusability and recyclability of common titanium, nickel and aluminum alloys. *Additive Manufacturing*, 2021, vol. 43, article number 102017. DOI: [10.1016/j.addma.2021.102017](#).
7. Runwal J., Ambekar R., Dhokey N.B. A novel process for spheroidization of irregular shaped metallic powders. *Powder Metallurgy*, 2021, vol. 64, no. 1, pp. 1–7. DOI: [10.1080/00325899.2020.1848974](#).
8. Wang Hao, Cui Yujie, Yang Jianwen, Chiba Yumi, Fujieda Masa, Yamanaka Kenta, Chiba Jinghiko. Investigation of dynamic balance process to obtain fine powder by plasma rotating electrode process (PREP) method. *Japan Society of Powder and Powder Metallurgy*, 2024, article number 24-00035. DOI: [10.2497/jjspm.24-00035](#).
9. Liu Junxiang, Yu Qingbo, Qin Qin. Numerical study on film disintegration by centrifugal atomisation using rotating cup. *Powder Metallurgy*, 2013, vol. 56, no. 4, pp. 288–294. DOI: [10.1179/1743290113Y.0000000053](#).
10. Shanthar R., Chen Kun, Abeykoon C. Powder-based additive manufacturing: A critical review of materials, methods, opportunities, and challenges. *Advanced Engineering Materials*, 2023, vol. 25, no. 19, article number 2300375. DOI: [10.1002/adem.202300375](#).
11. Liu Junxiang, Yu Qingbo, Guo Qiang. Experimental investigation of liquid disintegration by rotary cups. *Chemical Engineering Science*, 2012, vol. 73, pp. 44–50. DOI: [10.1016/j.ces.2012.01.010](#).
12. Li Hui Ping, Tsakiroopoulos P., Johnson T. Centrifugal atomisation of alloys. *Key Engineering Materials*, 2001, vol. 189/191, pp. 245–251. DOI: [10.4028/www.scientific.net/KEM.189-191.245](#).
13. Ahmed M., Abou Al-Sood M.M., Ali A. A one-dimensional model of viscous liquid jets breakup. *Journal of Fluids Engineering*, 2011, vol. 133, no. 11, article number 114501. DOI: [10.1115/1.4004909](#).

14. Peng Lei, Li Long, Zhao Wei. Numerical study of inlet eccentricity on liquid film spreading and splitting in centrifugal granulation assisted thermal energy recovery. *Powder Technology*, 2023, vol. 414, article number 118079. DOI: [10.1016/j.powtec.2022.118079](https://doi.org/10.1016/j.powtec.2022.118079).
15. Tan Yu, Ding Bin, Shi Jun, Yan Hui, Wu Yingchun, Wu Junjun. Modelling the film fragmentation of industrial-scale centrifugal granulation of high-temperature molten slag. *Powder Technology*, 2023, vol. 426, article number 118654. DOI: [10.1016/j.powtec.2023.118654](https://doi.org/10.1016/j.powtec.2023.118654).
16. Deng Huaxia, Ouyang Huajiang. Vibration of spinning discs and powder formation in centrifugal atomization. *Proceedings of the Royal Society A. Mathematical, physical and engineering sciences*, 2010, vol. 467, no. 2119, pp. 361–380. DOI: [10.1098/rspa.2010.0099](https://doi.org/10.1098/rspa.2010.0099).
17. Zhao Yuyuan. Analysis of flow development in centrifugal atomization: Part I. Film thickness of a fully spreading melt. *Modelling and Simulation in Materials Science and Engineering*, 2004, vol. 12, no. 5, pp. 959–971. DOI: [10.1088/0965-0393/12/5/013](https://doi.org/10.1088/0965-0393/12/5/013).
18. Zhao Yuyuan. Analysis of flow development in centrifugal atomization: Part II. Disintegration of a non-fully spreading melt. *Modelling and Simulation in Materials Science and Engineering*, 2004, vol. 12, no. 5, pp. 973–983. DOI: [10.1088/0965-0393/12/5/014](https://doi.org/10.1088/0965-0393/12/5/014).
19. Shemyakina O.A., Sheikhalieva Z.I., Sheikhaliev S.M. Obtaining solder powders by centrifugal atomization of melt. *Russian Journal of Non-Ferrous Metals*, 2010, vol. 51, no. 3, pp. 250–254. DOI: [10.3103/S1067821210030107](https://doi.org/10.3103/S1067821210030107).
20. Sungkhaphaitoon P., Likhidkan W., Kitjaidiaw S., Wisutmethangoon S., Plookphol T. Effect of atomizer disc geometry on zinc metal powder production by centrifugal atomization. *Applied Mechanics and Materials*, 2012, vol. 271–272, pp. 232–236. DOI: [10.4028/www.scientific.net/AMM.271-272.232](https://doi.org/10.4028/www.scientific.net/AMM.271-272.232).
21. Peng Hao, Wang Na, Wang Dongxiang, Ling Xiang. Experimental Study on Critical Characteristics of Liquid Atomization by Spinning Disk. *Industrial & Engineering Chemistry Research*, 2016, vol. 55, no. 21, pp. 6175–6185. DOI: [10.1021/acs.iecr.6b00401](https://doi.org/10.1021/acs.iecr.6b00401).
5. Bao Qieng, Yang Yiru, Wen Xiaochun, Guo Lei, Guo Zhancheng. The preparation of spherical metal powders using the high-temperature remelting spheroidization technology // *Materials & Design*. 2021. Vol. 199. Article number 109382. DOI: [10.1016/j.matdes.2020.109382](https://doi.org/10.1016/j.matdes.2020.109382).
6. Moghimian P., Poirie T., Habibnejad-Korayem M., Zavala J.A., Kroeger J., Marion F., Larouche F. Metal powders in additive manufacturing: A review on reusability and recyclability of common titanium, nickel and aluminum alloys // *Additive Manufacturing*. 2021. Vol. 43. Article number 102017. DOI: [10.1016/j.addma.2021.102017](https://doi.org/10.1016/j.addma.2021.102017).
7. Runwal J., Ambekar R., Dhokey N.B. A novel process for spheroidization of irregular shaped metallic powders // *Powder Metallurgy*. 2021. Vol. 64. № 1. P. 1–7. DOI: [10.1080/00325899.2020.1848974](https://doi.org/10.1080/00325899.2020.1848974).
8. Wang Hao, Cui Yujie, Yang Jianwen, Chiba Yumi, Fujieda Masa, Yamanaka Kenta, Chiba Jinghiko. Investigation of dynamic balance process to obtain fine powder by plasma rotating electrode process (PREP) method // *Japan Society of Powder and Powder Metallurgy*. 2024. Article number 24-00035. DOI: [10.2497/jjspm.24-00035](https://doi.org/10.2497/jjspm.24-00035).
9. Liu Junxiang, Yu Qingbo, Qin Qin. Numerical study on film disintegration by centrifugal atomisation using rotating cup // *Powder Metallurgy*. 2013. Vol. 56. № 4. P. 288–294. DOI: [10.1179/1743290113Y.0000000053](https://doi.org/10.1179/1743290113Y.0000000053).
10. Shanthar R., Chen Kun, Abeykoon C. Powder-based additive manufacturing: A critical review of materials, methods, opportunities, and challenges // *Advanced Engineering Materials*. 2023. Vol. 25. № 19. Article number 2300375. DOI: [10.1002/adem.202300375](https://doi.org/10.1002/adem.202300375).
11. Liu Junxiang, Yu Qingbo, Guo Qiang. Experimental investigation of liquid disintegration by rotary cups // *Chemical Engineering Science*. 2012. Vol. 73. P. 44–50. DOI: [10.1016/j.ces.2012.01.010](https://doi.org/10.1016/j.ces.2012.01.010).
12. Li Hui Ping, Tsakiroopoulos P., Johnson T. Centrifugal atomisation of alloys // *Key Engineering Materials*. 2001. Vol. 189/191. P. 245–251. DOI: [10.4028/www.scientific.net/KEM.189-191.245](https://doi.org/10.4028/www.scientific.net/KEM.189-191.245).
13. Ahmed M., Abou Al-Sood M.M., Ali A. A one-dimensional model of viscous liquid jets breakup // *Journal of Fluids Engineering*. 2011. Vol. 133. № 11. Article number 114501. DOI: [10.1115/1.4004909](https://doi.org/10.1115/1.4004909).
14. Peng Lei, Li Long, Zhao Wei. Numerical study of inlet eccentricity on liquid film spreading and splitting in centrifugal granulation assisted thermal energy recovery // *Powder Technology*. 2023. Vol. 414. Article number 118079. DOI: [10.1016/j.powtec.2022.118079](https://doi.org/10.1016/j.powtec.2022.118079).
15. Tan Yu, Ding Bin, Shi Jun, Yan Hui, Wu Yingchun, Wu Junjun. Modelling the film fragmentation of industrial-scale centrifugal granulation of high-temperature molten slag // *Powder Technology*. 2023. Vol. 426. Article number 118654. DOI: [10.1016/j.powtec.2023.118654](https://doi.org/10.1016/j.powtec.2023.118654).
16. Deng Huaxia, Ouyang Huajiang. Vibration of spinning discs and powder formation in centrifugal atomization // *Proceedings of the Royal Society A. Mathematical, physical and engineering sciences*. 2010. Vol. 467. № 2119. P. 361–380. DOI: [10.1098/rspa.2010.0099](https://doi.org/10.1098/rspa.2010.0099).
17. Zhao Yuyuan. Analysis of flow development in centrifugal atomization: Part I. Film thickness of a fully

СПИСОК ЛИТЕРАТУРЫ

1. Труфанов Д.А., Котов С.А., Шалашов Е.В., Часов В.В. Получение металлических порошков методом центробежного распыления с использованием вращающегося стакана // *Металлообработка*. 2016. № 4. С. 57–62. EDN: [XBJSYJ](https://doi.org/10.1016/j.powtec.2022.118079).
2. Ahmed M., Youssef M.S. Characteristics of mean droplet size produced by spinning disk atomizers // *Journal of Fluids Engineering*. 2012. Vol. 134. № 7. Article number 071103. DOI: [10.1115/1.4006819](https://doi.org/10.1115/1.4006819).
3. Ahmed M., Youssef M.S. Influence of spinning cup and disk atomizer configurations on droplet size and velocity characteristics // *Chemical Engineering Science*. 2014. Vol. 107. P. 149–157. DOI: [10.1016/j.ces.2013.12.004](https://doi.org/10.1016/j.ces.2013.12.004).
4. Ahmed M., Amighi A., Ashgriz N., Tran H.N. Characteristics of liquid sheets formed by splash plate nozzles // *Experiments in Fluids*. 2008. Vol. 44. № 1. P. 125–136. DOI: [10.1007/s00348-007-0381-4](https://doi.org/10.1007/s00348-007-0381-4).

- spreading melt // Modelling and Simulation in Materials Science and Engineering. 2004. Vol. 12. № 5. P. 959–971. DOI: [10.1088/0965-0393/12/5/013](https://doi.org/10.1088/0965-0393/12/5/013).
18. Zhao Yuyuan. Analysis of flow development in centrifugal atomization: Part II. Disintegration of a non-fully spreading melt // Modelling and Simulation in Materials Science and Engineering. 2004. Vol. 12. № 5. P. 973–983. DOI: [10.1088/0965-0393/12/5/014](https://doi.org/10.1088/0965-0393/12/5/014).
19. Шемякина О.А., Шейхалиева З.И., Шейхалиев Ш.М. Получение порошков припоев центробежным распылением расплава // Известия вузов. Цветная металлургия. 2010. № 3. С. 52–57. EDN: [MULYST](https://doi.org/10.1088/0965-0393/12/5/014).
20. Sungkhaphaitoon P., Likhidkan W., Kitjaidiaw S., Wisutmethangoon S., Plookphol T. Effect of atomizer disc geometry on zinc metal powder production by centrifugal atomization // Applied Mechanics and Materials. 2012. Vol. 271-272. P. 232–236. DOI: [10.4028/www.scientific.net/AMM.271-272.232](https://doi.org/10.4028/www.scientific.net/AMM.271-272.232).
21. Peng Hao, Wang Na, Wang Dongxiang, Ling Xiang. Experimental Study on Critical Characteristics of Liquid Atomization by Spinning Disk // Industrial & Engineering Chemistry Research. 2016. Vol. 55. № 21. P. 6175–6185. DOI: [10.1021/acs.iecr.6b00401](https://doi.org/10.1021/acs.iecr.6b00401).

Исследование механизмов центробежного распыления на основе модельного эксперимента

Жуков Евгений Юрьевич*, инженер кафедры 1101

«Технологии и системы автоматизированного проектирования металлургических процессов»

Наурзалинов Алибек Серпаевич, техник кафедры 1101

«Технологии и системы автоматизированного проектирования металлургических процессов»

Пашков Игорь Николаевич¹, доктор технических наук, профессор кафедры 1101

«Технологии и системы автоматизированного проектирования металлургических процессов»

Московский авиационный институт (национальный исследовательский университет), Москва (Россия)

*E-mail: ZhukovEY@mai.ru,
jezzacome@gmail.com

¹ORCID: <https://orcid.org/0000-0003-2511-2845>

Поступила в редакцию 15.02.2024

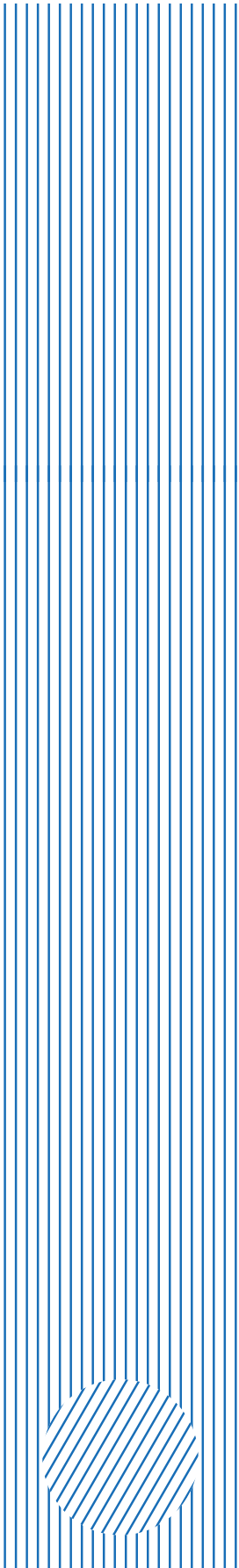
Пересмотрена 16.04.2024

Принята к публикации 28.10.2024

Аннотация: Процесс диспергирования расплава на вращающейся чаше является распространенным методом получения металлических порошков. Изучение процесса диспергирования на реальных расплавах, в том числе методами визуализации, затруднено. Поэтому влияние таких факторов, как высота падения струи, величина потока жидкости, смачивание поверхности, наличие стенки у чаши, на процесс получения мелких капель предложено изучить с помощью модельной жидкости без кристаллизации, фиксируя процесс путем высокоскоростной съемки. Цель работы – определение наиболее благоприятных условий диспергирования, когда вся подаваемая жидкость превращается в капли без образования крупных капель, дополнительных струй, приводящих к вторичному распылению. В качестве модельной жидкости выбран раствор глицерина в воде с вязкостью, равной вязкости расплава олова. Процесс диспергирования снимался на высокоскоростную камеру с частотой съемки 1200 кадров/с. Установлено, что при увеличении потока расплава наблюдается изменение режима распыления. При росте давления увеличивается поток и кинетическое взаимодействие струи с поверхностью чаши, а следовательно, избыток жидкости, который распыляется преждевременно. При любом потоке подаваемой жидкости, если жидкость не попадает в центр, происходит вторичное распыление за счет разрушения пленки на гидравлическом скачке из-за неравномерной радиальной скорости на пике скачка. При изменении высоты подачи от 100 до 150 мм наблюдается вторичное распыление в виде капель в месте гидравлического скачка. Количество спиралей и вторичное распыление влияют на увеличение размера фракции частиц. В диапазоне высоты падения струи от 50 до 100 мм отмечается оптимальный процесс, при котором можно получить наименьшую фракцию. В эксперименте наблюдалась тенденция к улучшению процесса распыления при повышении чистоты обработки поверхности чаши. За счет стенок чаши увеличивается путь жидкости до выхода ее с чаши, разрушаются в пленку капли, летящие над поверхностью чаши, вследствие чего улучшается процесс диспергирования.

Ключевые слова: центробежное распыление расплава; диспергирование расплава на вращающейся чаше; поток жидкости; металлический порошок; гидродинамические условия; высокоскоростная съемка.

Для цитирования: Жуков Е.Ю., Наурзалинов А.С., Пашков И.Н. Исследование механизмов центробежного распыления на основе модельного эксперимента // Frontier Materials & Technologies. 2024. № 4. С. 39–49. DOI: 10.18323/2782-4039-2024-4-70-4.



Togliatti State University is a participant in the Priority-2030 program of strategic academic leadership, a flagship university in the Samara region, a center for innovative and technological development of the region.

Togliatti State University was created in 2001 by merging Togliatti Polytechnic Institute (founded in 1951 as a branch of Kuibyshev Industrial Institute) and Togliatti branch of Samara State Pedagogical University (founded in 1987).

Togliatti State University today

- More than 22,000 students of all modes of study.
- Ten institutes implementing more than 170 higher education programs for 25 integrated groups of training areas, advanced technologies research institute, Zhiguli Valley Institute of Additional Education, military training center.
- 38 resource centers with up-to-date facilities and equipment created since 2011.
- Accreditation in eight systems for standard testing, research, and engineering.
- Main areas: advanced digital, intelligent manufacturing technologies, robotic systems, advanced materials and design methods, environmentally friendly and resource-saving energy engineering, personalized medicine, countering industrial threats.

University main achievements

- Ongoing project and professional practical activity was introduced for 100 % of full-time undergraduate/specialist students.
- Four mega-grants were implemented according to the Resolutions of the Government of the Russian Federation dated April 9, 2010 No. 219 and No. 220 – three laboratories in the field of physical materials science and nanotechnology (with the invitation of leading scientists), as well as an innovation technology center were created. The latter was transformed into a university innovation technopark.
- A member of the extraterritorial scientific and educational center “Engineering of the Future”.
- An initiator of the formation of eight consortiums, which brought together 69 organizations, including 36 universities, six scientific partners, among which there are three organizations of the Russian Academy of Sciences.
- A twice winner of the RF Government award in the field of quality (2009, 2019).
- An Online Higher Education System promoted under the Rosdistant brand was created. The project is the winner of the Project Olympus competition of the Analytical Center under the Government of the Russian Federation in the Project Management in the System of Higher Education and Science nomination (2019).

On the formation of thermal barrier coatings by magnetron sputtering

*Gennady V. Kachalin*¹, PhD (Engineering), leading researcher

*Konstantin S. Medvedev*², leading engineer

*Aleksey F. Mednikov*³, PhD (Engineering), leading researcher

*Olga S. Zilova*⁴, PhD (Engineering), leading researcher

Aleksandr B. Tkhabisimov^{*5}, PhD (Engineering), senior researcher

*Dmitriy I. Ilyukhin*⁶, engineer of the 1st category

*Vladislav A. Kasyanenko*⁷, engineer of the 1st category

National Research University “Moscow Power Engineering Institute”, Moscow (Russia)

*E-mail: TkhabisimovAB@mpei.ru,
abt-bkt@mail.ru

¹ORCID: <https://orcid.org/0000-0001-9506-862X>

²ORCID: <https://orcid.org/0000-0003-1667-458X>

³ORCID: <https://orcid.org/0000-0003-4883-7873>

⁴ORCID: <https://orcid.org/0000-0002-0410-8188>

⁵ORCID: <https://orcid.org/0000-0001-9544-9086>

⁶ORCID: <https://orcid.org/0009-0009-6385-0284>

⁷ORCID: <https://orcid.org/0009-0000-7510-2106>

Received 18.10.2024

Revised 26.11.2024

Accepted 03.12.2024

Abstract: The use of magnetron sputtering systems with extended uncooled targets will allow developing industrial import-substituting technologies for the formation of thermal barrier coatings, based on zirconium oxide doped with rare earth metal oxides to solve urgent problems of gas turbine construction. This paper presents the results of comparing the technology for producing thermal barrier coatings by magnetron sputtering, with two types of extended targets made of Zr–8%Y alloy – a widely used cooled target and an uncooled extended target, of a magnetron sputtering system developed by the authors. This paper gives a comparison of the results of mass-spectrometric studies of the hysteresis of the oxygen partial pressure inherent in the technology for producing oxide films; the influence of the target type on the coating growth rate; studies of the structure of thermal barrier coatings using the scanning electron microscopy method; and the elemental composition of coatings based on zirconium dioxide partially stabilised with yttrium oxide – YSZ. It has been experimentally found that increasing the temperature of the magnetron sputtering system target, allows decreasing the loop width of the characteristic hysteresis of the oxygen partial pressure dependence on its flow rate by 2 times. The obtained dependencies allowed determining the range of oxygen flow rates at various magnetron discharge powers, at which the work can be performed with stable and sustainable process control, without the risk of falling into hysteresis. The conducted metallographic studies showed a characteristic developed porous dendritic structure of the ceramic layer, which is necessary to reduce the thermal conductivity coefficient of the thermal barrier coating. It has been revealed that the use of an uncooled target allows increasing the deposition rate of the thermal barrier coating by more than 10 times compared to the deposition rate for a cooled target. The obtained results demonstrate the possibility of using the magnetron sputtering technology of an extended uncooled target to form a ceramic layer of thermal barrier coatings.

Keywords: magnetron sputtering; uncooled target; thermal barrier coatings; hysteresis phenomena; coating deposition rate.

Acknowledgements: State assignment No. FSWF-2023-0016 (Agreement No. 075-03-2023-383 dated January 18, 2023) in the field of scientific activity for 2023–2025.

For citation: Kachalin G.V., Medvedev K.S., Mednikov A.F., Zilova O.S., Tkhabisimov A.B., Ilyukhin D.I., Kasyanenko V.A. On the formation of thermal barrier coatings by magnetron sputtering. *Frontier Materials & Technologies*, 2024, no. 4, pp. 51–61. DOI: 10.18323/2782-4039-2024-4-70-5.

INTRODUCTION

The problems of ensuring the reliability of aircraft gas turbine engines (GTE) and power gas turbine plants (GTP) are the most complex among the numerous problems arising in the development of modern gas turbines. The most important element of a gas turbine is the rotor

blades, the material and design of which largely determine the service life and permissible temperature of the gas in front of the turbine.

The temperatures of combustion products in gas turbines reach 1700 °C, therefore, thermal barrier coatings (TBC) are used to protect the rotor blades from high-temperature exposure.

Modern thermal barrier coatings are heat-resistant composite coatings with a thickness of 100–400 μm consisting of two layers. The first (lower) layer is a metal heat-resistant binder, usually of the $MeCrAlY$ type, where Me is the γNi or Co matrix, which protects the substrate material from oxidation and creates an adhesive pair with the second (upper) layer, – a ceramic heat-insulating coating consisting of rare earth metal oxides and having low thermal conductivity [1; 2]. The first TBC layer protects the substrate material from oxidation (the coefficient of heat expansion of the layer can reach $16.8 \cdot 10^{-6} \text{K}^{-1}$ from room temperature to 1000 $^{\circ}\text{C}$) [3; 4]. The second layer is a heat-insulating layer with low thermal conductivity (about $0.8 \div 1.2 \text{W}/(\text{m}\cdot\text{K})$) and high resistance to thermal cycling [5].

Among the wide range of ceramic materials, the most interesting one as the upper ceramic coating layer is zirconium dioxide with additives of rare earth metal oxides, in particular stabilised with yttrium oxide – 8% Y_2O_3 (yttria-stabilised zirconia, YSZ). This ceramic composition has low thermal conductivity, high strength, fracture toughness, wear resistance and heat expansion coefficient comparable with the metal first layer of TBC [6]. The use of YSZ is necessary to stabilise pure ZrO_2 , since its monoclinic structure transforms into tetragonal and cubic phases, when exposed to high temperature leading to the development of stresses [7; 8]. It is noted that the monoclinic-tetragonal transition in ZrO_2 occurs with a destructive change in volume, which hinders the manufacture and use of products made of pure oxide [9].

The most widely used methods for forming TBCs are electron beam evaporation and plasma deposition in air and vacuum. Formation of coatings in vacuum allows depositing films with high adhesion to the substrate, but requires a large consumption of target material with a low utilisation factor (0.15–0.25) [8]. In turn, the application of electron beam evaporation and plasma deposition in air allows forming coatings with a high deposition rate and high resistance to thermal cycling, but it is often difficult due to the limited availability of materials, and the impossibility of coating parts with complex shapes [10; 11].

At the same time, one can argue that, due to the development of magnetron sputtering technologies, this method can become an alternative to existing ones. This is caused by the fact that when temperatures rise above 1300 $^{\circ}\text{C}$, the standard YSZ material approaches certain limitations due to sintering, and phase transformations at elevated temperatures. YSZ formed during electron beam evaporation and plasma deposition in air consists of a metastable t' -phase. When exposed to elevated temperatures for a long time, it decomposes into phases with high and low yttrium content. The latter, upon cooling, transforms into a monoclinic phase with a corresponding significant increase in volume, which ultimately leads to the destruction of the coating [12–14].

The main difficulty in implementing standard magnetron sputtering, with a cooled target to obtain TBCs, is the formation of a thin non-conducting film of an oxide compound on its surface during the occurrence of reactive processes in the presence of oxygen. Such oxide films have

high electrical resistance, which prevents the flow of sputtering ion currents [15].

The work [16] presents the results of the study of the temperature dependence of the specific resistance of ZrO_2 -based ceramics, which showed that in the temperature range from 500 to 1000 K, the specific resistance decreases, and the conductivity of the thin oxide film at a temperature above 1000 K is sufficient for stable combustion of the magnetron discharge. Under the influence of heating from ion bombardment, the specific resistance of the YSZ oxide formed on the surface of the uncooled target decreases, and it can be sputtered.

Fig. 1 shows the dependence of the growth rate of the ZrYO coating obtained by sputtering a zirconium target on the oxygen consumption. At an oxygen consumption of more than 3.0 units, the growth rate of the coating drops sharply due to the target surface oxidation. In the oxygen consumption range of 0–3.0 units, a “metallic mode” is realised, in which the deposition rate is about 4 $\mu\text{m}/\text{h}$, and opaque metallic-colored coatings conducting electric current are formed. Such coatings cannot be used as TBC, since when heated in an air environment they burn and peel off.

At oxygen consumption of more than 4.0 units, the “oxidised mode” is realised and transparent and non-conductive coatings are formed, which can be used as TBC, however, the deposition rate of such coatings decreases sharply and is about 0.3 $\mu\text{m}/\text{h}$ (Fig. 1). To apply a ceramic TBC layer 50 μm thick under the conditions of the experiments, it would take more than 160 h, which is ineffective for industrial application of ceramic TBC layers, using magnetron sputtering systems with a cooled target.

The solution to the problem of TBC formation by magnetron sputtering can be the use of uncooled targets, heated to a temperature of more than 1000 $^{\circ}\text{C}$. At these temperatures, oxide films formed on the surface of an uncooled target have electrical conductivity, and do not hinder the magnetron discharge combustion. Due to the high temperature, it is possible as well to evaporate the uncooled target material, which creates an additional flow of atoms from the surface, and allows increasing the deposition rate of the coating [17–19].

The main functional property of the thermal barrier coating is the thermal conductivity coefficient; for YSZ coatings, it is the lowest among oxide systems. A further decrease in the thermal conductivity coefficient is achieved by growth methods – conditions are created for the growth of a porous structure in the form of feathers (dendrites) [20].

The presented analysis showed that a logical stage in the development of the magnetron sputtering technology, with a cooled target for producing TBC with a minimum thermal conductivity coefficient, is the transition to the use of a magnetron sputtering system with an uncooled target. This causes the necessity of comparing two types of targets, based on the results of experimental studies of the hysteresis of the oxygen partial pressure, inherent in the technology of producing oxide films; the effect of the target type on the growth rate of the coating; determination of the structure, and elemental composition of YSZ thermal barrier coatings obtained using an uncooled target.

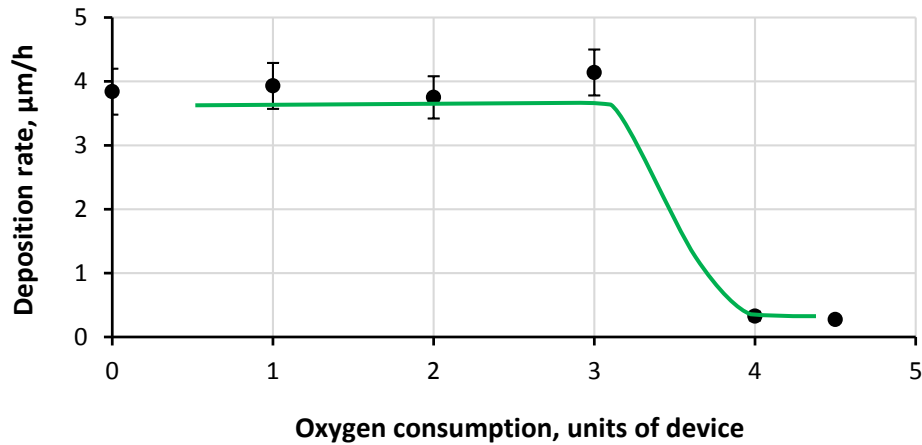


Fig. 1. Dependence of the deposition rate of the ZrYO-based coating on oxygen consumption at a magnetron discharge power of 5 kW (cooled target).

Source: Kachalin G.V., Mednikov A.F., Medvedev K.S., Bychkov A.I., Zilova O.S. Study of the influence of oxygen consumption on the deposition rate of Zr–Y-based coatings at magnetron sputtering with a cooled target. *Vakuumnaya tekhnika i tekhnologii – 2023: sbornik trudov 30-y Vserossiyskoy nauchno-tekhnicheskoy konferentsii s mezhdunarodnym uchastiem. Sankt-Petersburg, Sankt-Peterburgskiy gosudarstvennyy elektrotekhnicheskii universitet "LETI" im. V.I. Ulyanova (Lenina) Publ., 2023, pp. 108–113. EDN: [GTVAVJ](#)*

Рис. 1. Зависимость скорости осаждения покрытия на основе ZrYO от расхода кислорода при мощности магнетронного разряда 5 кВт (охлаждаемая мишень).

Источник: Качалин Г.В., Медников А.Ф., Медведев К.С., Бычков А.И., Зилова О.С. Изучение влияния расхода кислорода на скорость осаждения покрытия на основе Zr–Y при магнетронном распылении с охлаждаемой мишенью // *Вакуумная техника и технологии – 2023: сборник трудов 30-й Всероссийской научно-технической конференции с международным участием. СПб.: Санкт-Петербургский государственный электротехнический университет «ЛЭТИ» им. В.И. Ульянова (Ленина), 2023. С. 108–113. EDN: [GTVAVJ](#)*

The aim of this study is to develop a technology for the formation of thermal barrier coatings, based on zirconium dioxide partially stabilised with yttrium oxide, using magnetron sputtering of an extended uncooled target.

METHODS

The coatings were formed using a vacuum unit developed at the National Research University "Moscow Power Engineering Institute". Fig. 2 shows the schematic diagram of the process unit working volume.

A special feature of the unit is the presence of a rotation system that provides the possibility of both planetary rotation of the processed products and samples and rotation of all or separately selected items of the planetary mechanism in a given position, in particular, directly in front of the magnetron sputter target.

The coatings were formed using a planar magnetron (developed by the National Research University "Moscow Power Engineering Institute", Russia) with an extended target measuring 710×80×8 mm, made of 92%Zr–8%Y alloy. During the process, stainless steel samples were fixed on equipment that rotated directly in front of the magnetron. The distance from the target to the rotation axis was 150 mm. Argon and oxygen of special purity supplied to the vacuum chamber using RRG-10 gas flow regulators were used as the process gases.

The technological process of coating formation, including pumping out the vacuum chamber to a pressure of $5 \cdot 10^{-3}$ Pa combined with heating the chamber and equipment, and supplying plasma-forming argon gas to perform

ion cleaning of samples in a glow discharge in the area of magnetrons with cooled targets. Then the samples were moved to a preheated uncooled target (Fig. 3), and the coating was formed with continuous rotation of the samples in front of the target.

The magnetron discharge power varied in the range from 2.2 to 9 kW. For experiments with a cooled target, coatings were formed immediately after the ion cleaning stage.

The uncooled target temperature was measured by a chromel-alumel thermocouple placed in a channel, drilled in the side end of the target so that the thermocouple junction was located near the magnetron discharge track.

Studies of the surface microstructure and morphology, thickness and composition of the resulting coatings, elemental analysis were carried out using the control and measuring equipment, included in the experimental complex of the Unique Scientific Facilities (USF) "Erosion-M Hydraulic Impact Test Facility" of the National Research University "Moscow Power Engineering Institute".

The microstructure and morphology of the coating surface were studied using a TESCAN MIRA 3 LMU high-resolution scanning electron microscope (Tescan, Czech Republic) with a Schottky-electron emitter. Elemental analysis of the coatings was performed by energy-dispersive X-ray spectrometry, using an Oxford X Max 50 EDS spectrometer (Oxford Instruments, UK), mounted on a TESCAN MIRA 3 LMU microscope. The microstructure and composition of the coatings by depth were studied on transverse metallographic sections made using a Buehler GmbH sample preparation complex (Buehler, USA).

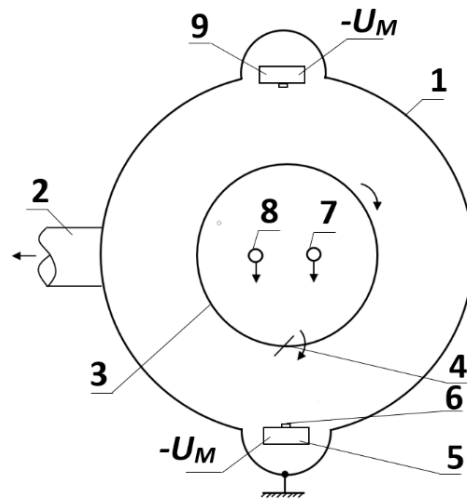


Fig. 2. Scheme of the technological installation for applying thermal barrier coating with a magnetron with an extended uncooled target:

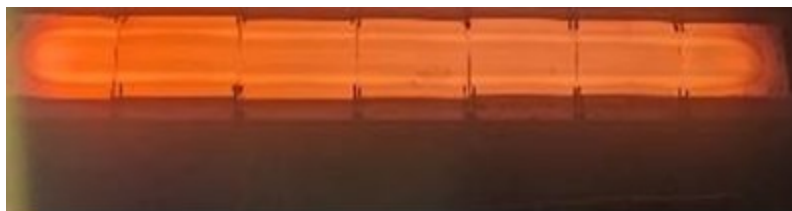
- 1 – vacuum chamber; 2 – high vacuum pumping pipe; 3 – planetary carousel;
- 4 – sample; 5 – magnetron source; 6 – uncooled target;
- 7 – argon supply; 8 – oxygen supply;
- 9 – magnetron for ion purification of samples

Рис. 2. Схема технологической установки нанесения термобарьерного покрытия магнетроном с протяженной неохлаждаемой мишенью:

- 1 – вакуумная камера; 2 – патрубок высоковакуумной откачки;
- 3 – планетарная карусель; 4 – образцы; 5 – магнетронный источник;
- 6 – неохлаждаемая мишень; 7 – подача аргона; 8 – подача кислорода;
- 9 – магнетрон ионной очистки образцов



a



b

Fig. 3. The appearance of the uncooled Zr–Y target:

- a** – before the discharge is turned off; **b** – after the discharge is turned off

Рис. 3. Внешний вид неохлаждаемой мишени Zr–Y:

- a** – до выключения разряда; **b** – после выключения разряда

The coating thickness was determined both on transverse sections during surface microstructure examination on a TESCAN MIRA 3 LMU microscope, and by ball grinding using a Calotest Compact device (Anton Paar, Austria). The deposition rate was calculated based on

the results of determining the thickness and time of coating formation.

The composition of the atmosphere in the vacuum chamber was studied using a Pfeiffer Vacuum Prisma-Plus quadrupole mass spectrometer (Pfeiffer Vacuum,

Germany), equipped with differential pumping. The influence of the oxygen flow rate and magnetron discharge power on the partial pressure of argon and oxygen was studied, using the mass-spectrometric method of analysing the composition of the gas atmosphere in the vacuum chamber cap.

RESULTS

Fig. 4 shows a typical dependence of the partial pressure of oxygen on its flow rate for the formation of an YSZ coating by magnetron sputtering with cooled and uncooled targets.

It is evident that the dependences of the partial pressure of oxygen in the chamber on its flow rate are nonlinear with a pronounced hysteresis. At the same oxygen consumption, two values of partial pressure are observed depending on the direction of change in the oxygen consumption, and for a cooled target, the change in the partial pressure of oxygen is greater than for an uncooled target.

In the case of a cooled target, with an oxygen consumption above 2.5 units, a sharp increase in the partial pressure of oxygen was observed, which tended to saturate at a flow rate of more than 4.5 units (Fig. 4). This indicates a corresponding sharp decrease in the sputtering rate of the cooled target, due to the formation of an oxide film and a decrease in the number of sputtered zirconium and yttrium atoms that bind oxygen. With decreasing oxygen consumption, its partial pressure decreases, and with an oxygen consumption of 0.5 units, the target is completely cleared of the formed oxide film.

The derivatives of the direct and inverse dependencies of the partial pressure of oxygen on its consumption differ several times. Their type depends on the holding time at

each value of oxygen consumption, as well as the stage of formation or etching of the oxide film on the target surface. It is noted that the controllability of the formation process on the inverse dependence is much more stable. The partial pressure of oxygen increases from 0 to 32 %, with an increase in oxygen consumption from 2.0 to 4.5 units, but decreases to 0 % with a decrease in oxygen consumption from 4.5 to 0.5 units.

In turn, for an uncooled target, the obtained dependencies are shifted to the region of higher oxygen consumption values (Fig. 4). The partial pressure begins to increase at an oxygen consumption of 3.5 units, which indicates a significantly higher sputtering rate of the uncooled target. Thus, at an oxygen consumption of 4.0 units on a cooled target, the partial pressure of oxygen in the chamber was 30 %, while on an uncooled target its value is close to zero, i.e. all the incoming oxygen is absorbed by the growing YSZ layer. The obtained dependencies for an uncooled target change monotonically, and the revealed maximum value of the partial pressure of oxygen is 1.5 times less than for a cooled target.

A feature of the reverse branch of the dependence for an uncooled target is the presence of a section with an oxygen consumption of 4.5–5.5 units, with an almost unchanged partial pressure and a derivative value close to zero (Fig. 4). From the point of view of the TBC formation technology, the presence of such a section indicates that work in this area can be performed with stable process control, without the risk of falling into hysteresis. Achieving process stability is possible with a smooth increase in oxygen consumption values from 0.0 to more than 7.0 units and a subsequent decrease to 4.5–5.5 units.

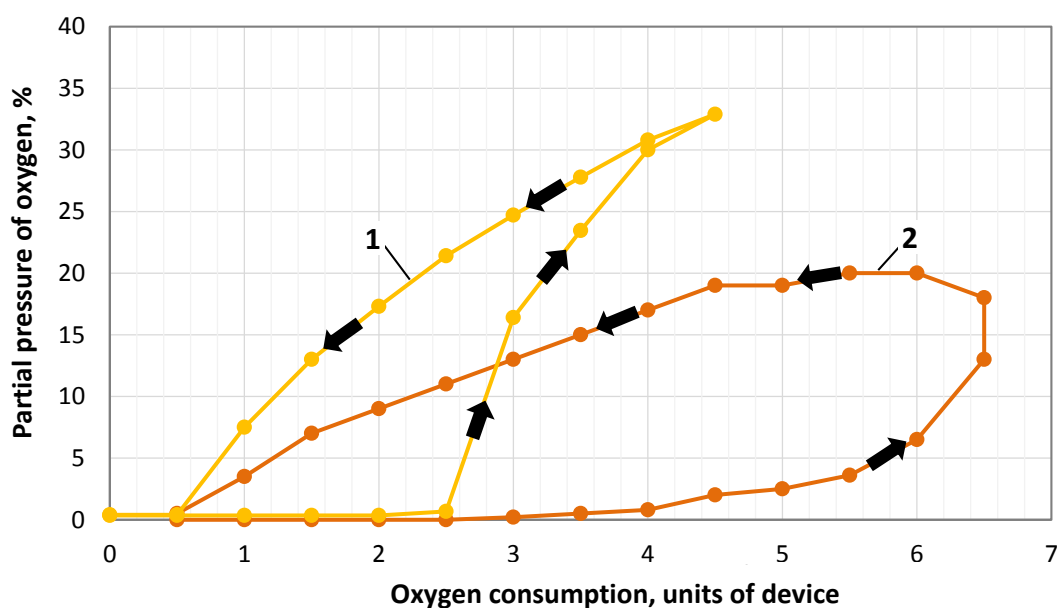


Fig. 4. Dependence of the partial pressure of oxygen for cooled (1) and uncooled (2) targets on the oxygen consumption at a magnetron discharge power of 3 kW (the arrows show the direction of change in oxygen consumption)

Рис. 4. Зависимость парциального давления кислорода для охлаждаемой (1) и неохлаждаемой (2) мишеней от расхода кислорода при мощности магнетронного разряда 3 кВт (стрелками показано направление изменения расхода кислорода)

Fig. 5 shows the measured dependence of the temperature of the uncooled and cooled targets on the magnetron discharge power. The cooled target temperature is determined by the thermal conductivity of the structure of target attachment to the magnetron magnetic system, so a linear dependence of the target temperature on the magnetron discharge power is obtained. The uncooled target temperature is determined by radiation from its surface, so a power dependence with a tendency to saturation is obtained.

From the comparison of the dependences of the partial pressure of argon and oxygen on the oxygen consumption for magnetron discharge powers of 3, 6 and 9 kW on an uncooled target, it is evident that an increase in the discharge power to 9 kW leads to a qualitative change in the type of hysteresis – the curve width decreases by more than 2 times (Fig. 6).

It was revealed that at a magnetron discharge power of more than 6 kW (the uncooled target temperature is more

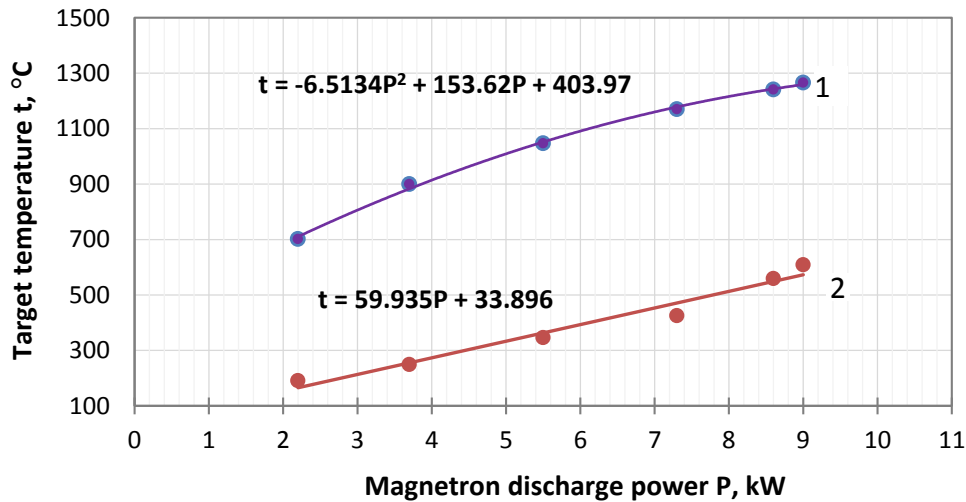


Fig. 5. Dependence of temperatures of uncooled (1) and cooled (2) zirconium targets on the magnetron discharge power

Рис. 5. Зависимость температур неохлаждаемой (1) и охлаждаемой (2) циркониевых мишеней от мощности магнетронного разряда

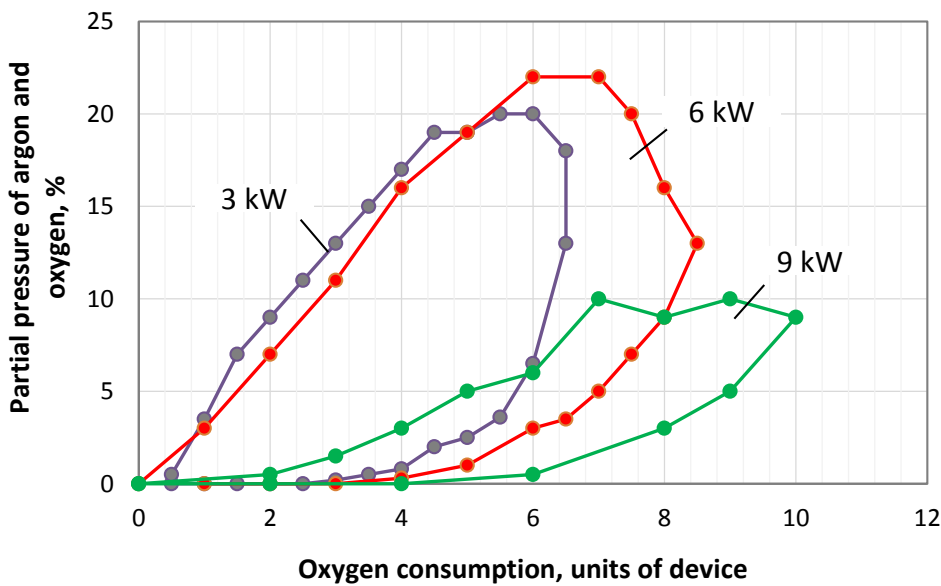


Fig. 6. Dependence of the partial pressure of oxygen on oxygen consumption for various magnetron discharge capacities

Рис. 6. Зависимость парциального давления кислорода от расхода кислорода для различных мощностей магнетронного разряда на неохлаждаемой мишени

than 1100 °C, Fig. 5), the type of the hysteresis curve (Fig. 6) changes qualitatively, and at a power of 9 kW, a significant narrowing of the hysteresis curve occurs. On the reverse branch of the obtained dependence for a power of 9 kW (Fig. 6), an extended range of values from 7.0 to 9.0 units of oxygen consumption is observed, at which the partial pressure of oxygen is stable.

The maximum value of the partial pressure of oxygen on the straight branches of the obtained hysteresis curves, allows judging the intensity of the process of oxygen absorption by the growing oxide film. Thus, an increase in power from 3 to 6 kW increased the maximum value of the partial pressure of oxygen, despite the fact that at a power of 6 kW the sputtering rate is at least 2 times greater than at 3 kW. An increase in power to 9 kW decreased the partial pressure of oxygen more than 2 times, which indicates a significant increase in the flow of sputtered atoms binding oxygen. This is also evidenced by the obtained data on measuring the deposition rate of the YSZ coating (Table 1).

Comparing the rates of deposition using cooled and uncooled targets (Table 1), showed that sputtering from an uncooled target allows increasing the deposition rate by more than 10 times, which is in qualitative agreement with the results of the study of the oxygen partial pressure (Fig. 4).

Fig. 7 shows the initial growth of a similar structure. The initial growth of the YSZ TBC feather structure obtained at a power of 8.7–8.8 kW is characterised by the growth of separately standing feathers with a dendritic structure having a width of 1 to 6 µm with gaps between them of 0.1–0.5 µm.

A study of the microstructure of the YSZ coating formed using an uncooled target at a power of 9 kW with a longer formation time compared to the coating shown in Fig. 7, showed a combination of nanolayer (with layer thicknesses from 60 to 140 nm) and columnar structures (Fig. 8).

When depositing on a polished surface (with R_a equal to 0.04–0.06 µm) (Fig. 8 a), the width of the columns in the lower part of the coating is 0.2–0.4 µm, in the upper part it varies from 0.4 to 2 µm (on average 0.9 µm), in the central layer of the coating, the columnar structure has a clearly visible dendritic structure. When forming a coating on a rougher surface (with R_a over 0.8 µm) (Fig. 8 b), a greater number of cracks and pores are observed, the width of the columns in the upper part of the coating increases reaching 2–7 µm, the dendritic structure acquires a more pronounced feathery structure.

The study of the surface morphology by scanning electron microscopy showed that the surface of the YSZ coating with the corresponding microstructure shown in Fig. 8 b formed using an uncooled target has a hierarchical structure of the cauliflower type (Fig. 8 c). This structure at the nano-level consists of grains with a diameter of 60–90 nm, which are combined into blocks of 400–600 nm, forming globules of 2–4 µm at the microlevel, which, in turn, are combined into conglomerates up to 15 µm in size. The revealed structure of the formed coating of the cauliflower type at the micro level has porosity, which reduces the thermal conductivity coefficient.

Elemental EDS analysis of thermal barrier YSZ coatings formed using an uncooled target, showed the presence of 62–67 wt. % of Zr, 8–11 wt. % of Y, and 22–30 wt. % of O.

Table 1. Deposition rate of thermal barrier YSZ-coatings produced using cooled and uncooled targets
Таблица 1. Скорость осаждения термобарьерных YSZ-покрытий, полученных с использованием охлаждаемой и неохлаждаемой мишеней

Magnetron type, power of 9 kW	Deposition rate, µm/h
With cooled target	0.7±0.2
With uncooled target	7.9±0.4

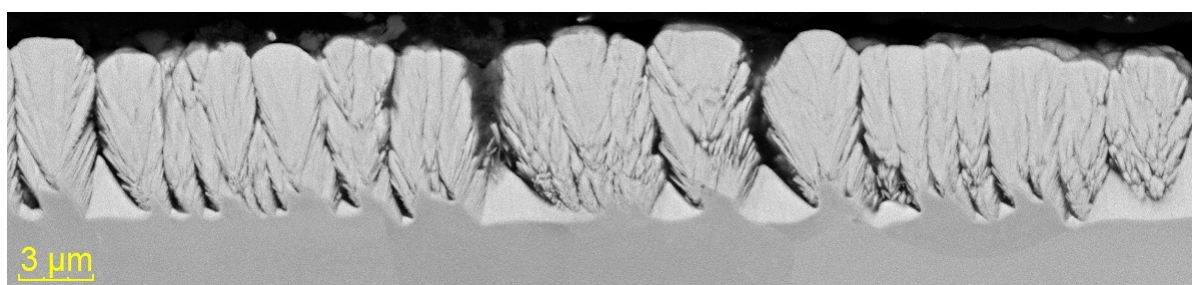


Fig. 7. The structure of the thermal barrier YSZ-coating produced at a power of 8.7 kW
Рис. 7. Структура термобарьерного YSZ-покрытия, полученная при мощности 8,7 кВт

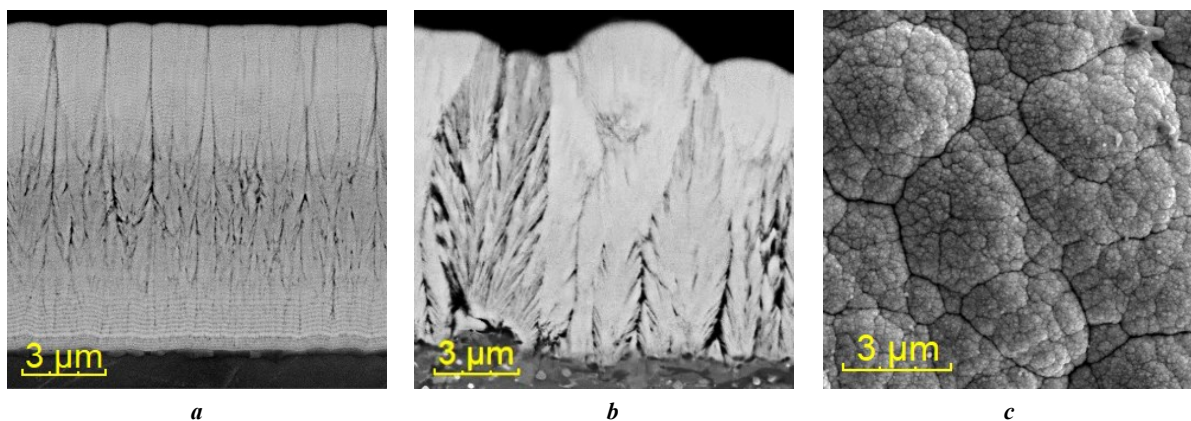


Fig. 8. Transverse section (a, b) and surface morphology (c) of the thermal barrier YSZ-coating formed using an uncooled target at a power of 9 kW

Рис. 8. Поперечный шлиф (a, b) и морфология поверхности (c) термобарьерного YSZ-покрытия, сформированного с использованием неохлаждаемой мишени при мощности 9 кВт

DISCUSSION

The known dependences of the partial pressure of oxygen on its consumption in the form of hysteresis loops, characteristic of the processes of formation of oxide films [15; 16], are also observed during their formation using an uncooled target. In this work, ranges of oxygen consumption values at various magnetron discharge powers are obtained, at which the work can be carried out with steady and stable process control. It was experimentally found that an increase in the temperature of the magnetron sputtering system target allows reducing the width of the hysteresis loop by 2 times.

Comparison of the deposition rates of the ZrYO-based coating on the oxygen consumption obtained for a cooled target (Fig. 1), and the deposition rates of the same coating obtained by the authors for an uncooled target, allows stating the fact of overcoming the occurrence of an oxide film and achieving a multiple increase in coating growth.

The data obtained in [16] that atoms are added to the main flow of sputtered atoms of the target material due to the sublimation process explain the observed fact of an increase in the oxide coating growth rate. One can assume with a high degree of probability that the sublimation process occurs from the entire heated surface of the target. However, at the same time, it should be expected that due to sublimation, the mechanical properties of the coating would change due to the difference in the energies of the sputtered and sublimated atoms, as was demonstrated in [17–19].

Thermal electron emission can occur from the heated surface of the oxide, which will increase the magnetron discharge current, and due to the heating of the uncooled target, oxide evaporation can occur in addition to sputtering. Consequently, on the uncooled target surface, an unambiguous relationship will be observed between three parameters determined by the target surface temperature: the growth rate of the oxide, the rate of its sputtering, and its conductivity.

Compared with the results for a cooled target shown in [8], the formation of coatings using an uncooled target also allows depositing films with high adhesion to the substrate,

but requires a lower consumption of target material with a high coefficient of its use. In turn, a high adhesion value will limit the processes of destruction of coatings from [12; 14] at temperatures above 1300 °C.

The use of an uncooled target expands the possibilities of using target materials, and applying coatings to parts of complex shape, compared with the methods of electron beam evaporation, and plasma deposition in air [10; 11].

The YSZ coating formed using an uncooled target showed a combination of a nanolayer and columnar structure inherent in the structure of the thermal barrier coating produced in [20].

The obtained results open up new possibilities for the development of the technology for magnetron sputtering of an extended uncooled target for producing TBCs based on zirconium dioxide, partially stabilised by yttrium oxide, with a thickness of more than 50 μm and the study of their thermal and mechanical properties.

CONCLUSIONS

The results of the conducted studies of the technology of formation of thermal barrier coatings, show the possibility of using magnetron systems of sputtering of an extended uncooled target for the formation of a ceramic layer of TBC, with a developed porous structure.

It has been experimentally found that an increase in the magnetron target temperature, allows reducing the effect of hysteresis (the hysteresis loop width decreases by 2 times), and increasing the TBC deposition rate by more than 10 times compared to a cooled target.

REFERENCES

1. Banerjee P., Roy A., Sen S., Ghosh A., Saha G., Seikh A.H., Alnaser I.A. Ghosh M. Service life assessment of yttria stabilized zirconia (YSZ) based thermal barrier coating through wear behavior. *Heliyon*, 2023, vol. 9, no. 5, article number e16107. DOI: [10.1016/j.heliyon.2023.e16107](https://doi.org/10.1016/j.heliyon.2023.e16107).
2. Singh M., Sahu P.K., Sampath S., Jonnalagadda K.N. Fracture toughness of freestanding plasma sprayed

- yttria stabilized zirconia coatings via in situ tensile experiments. *Journal of the European Ceramic Society*, 2024, vol. 44, no. 4, pp. 2499–2511. DOI: [10.1016/j.jeurceramsoc.2023.10.074](https://doi.org/10.1016/j.jeurceramsoc.2023.10.074).
3. Liu Qiaomu, Huang Shunzhou, He Aijie. Composite ceramics thermal barrier coatings of yttria stabilized zirconia for aero-engines. *Journal of Materials Science & Technology*, 2019, vol. 35, no. 12, pp. 2814–2823. DOI: [10.1016/j.jmst.2019.08.003](https://doi.org/10.1016/j.jmst.2019.08.003).
 4. Raza M., Boulet P., Pierson J.-F., Snyders R., Konstantinidis S. Thermal stability of oxygen vacancy stabilized zirconia (OVSZ) thin films. *Surface and Coatings Technology*, 2021, vol. 409, article number 126880. DOI: [10.1016/j.surfcoat.2021.126880](https://doi.org/10.1016/j.surfcoat.2021.126880).
 5. De Goes W.U., Markocsan N., Gupta M., Vaßen R., Matsushita T., Illkova K. Thermal barrier coatings with novel architectures for diesel engine applications. *Surface and Coatings Technology*, 2020, vol. 396, article number 125950. DOI: [10.1016/j.surfcoat.2020.125950](https://doi.org/10.1016/j.surfcoat.2020.125950).
 6. Yetim A.F., Tekdir H., Turalioglu K., Taftali M., Yetim T. Tribological behavior of plasma-sprayed Yttria-stabilized zirconia thermal barrier coatings on 316L stainless steel under high-temperature conditions. *Materials Letters*, 2023, vol. 336, article number 133873. DOI: [10.1016/j.matlet.2023.133873](https://doi.org/10.1016/j.matlet.2023.133873).
 7. Karaoglan A.C., Ozgurluk Y., Gulec A., Ozkan D., Binal G. Effect of coating degradation on the hot corrosion behavior of yttria-stabilized zirconia (YSZ) and blast furnace slag (BFS) coatings. *Surface and Coatings Technology*, 2023, vol. 473, article number 130000. DOI: [10.1016/j.surfcoat.2023.130000](https://doi.org/10.1016/j.surfcoat.2023.130000).
 8. Chen Can, Song Xuemei, Li Wei, Zheng Wei, Ji Heng, Zeng Yi, Shi Ying. Relationship between microstructure and bonding strength of yttria-stabilized zirconia thermal barrier coatings. *Ceramics International*, 2022, vol. 48, no. 4, pp. 5626–5635. DOI: [10.1016/j.ceramint.2021.11.107](https://doi.org/10.1016/j.ceramint.2021.11.107).
 9. Sanjai S.G., Srideep S., Krishna B.A., Sumanth M.S., Ramaswamy P. Synthesis of Yttria-Stabilized Zirconia Nano Powders for Plasma Sprayed Nano Coatings. *Materials Today: Proceedings*, 2020, vol. 22, part 4, pp. 1253–1263. DOI: [10.1016/j.matpr.2020.01.418](https://doi.org/10.1016/j.matpr.2020.01.418).
 10. Wang Xin, Zhen Zhen, Huang Guanghong, Mu Rende, He Limin, Xu Zhenhua. Thermal cycling of EB-PVD TBCs based on YSZ ceramic coat and diffusion aluminide bond coat. *Journal of Alloys and Compounds*, 2021, vol. 873, article number 159720. DOI: [10.1016/j.jallcom.2021.159720](https://doi.org/10.1016/j.jallcom.2021.159720).
 11. Mulone A., Mahade S., Björklund S., Lundström D., Kjellman B., Joshi S., Klement U. Development of yttria-stabilized zirconia and graphene coatings obtained by suspension plasma spraying: Thermal stability and influence on mechanical properties. *Ceramics International*, 2023, vol. 49, no. 6, pp. 9000–9009. DOI: [10.1016/j.ceramint.2022.11.055](https://doi.org/10.1016/j.ceramint.2022.11.055).
 12. Berlin E.V., Seydman L.A. *Poluchenie tonkikh plenok reaktivnym magnetronnym raspyleniem* [Production of thin films by reactive magnetron sputtering]. 2nd ed., ispr. i dop. Moscow, URSS Publ., 2022. 316 p.
 13. Tkhabisimov A.B., Mednikov A.F., Dasaev M.R., Kachalin G.V., Zilova O.S. Solid particle erosion resistance of protective ion-plasma coating formed on full-scale objects based on modern additive technologies. *International Journal of Innovative Technology and Exploring Engineering*, 2019, vol. 8, no. 7, pp. 2295–2302. EDN: [YNNMPC](https://doi.org/10.1016/j.jeurceramsoc.2023.10.074).
 14. Dukhopelnikov D.V., Bulychev V.S., Vorobev E.V. Magnetron discharge with liquid-phase cathode. *Herald of the Bauman Moscow State Technical University, Series Natural Sciences*, 2018, no. 1, pp. 95–103. DOI: [10.18698/1812-3368-2018-1-95-103](https://doi.org/10.18698/1812-3368-2018-1-95-103).
 15. Kuritsyna I.E., Bredikhin S.I., Agarkov D.A., Borik M.A., Kulebyakin A.V., Milovich F.O., Lomonova E.E., Myzina V.A., Tabachkova N.Yu. Electrotransport characteristics of ceramic and single crystal materials with the $(ZrO_2)_{0.89}(Sc_2O_3)_{0.10}(Y_2O_3)_{0.01}$ composition. *Russian Journal of Electrochemistry*, 2018, vol. 54, pp. 481–485. DOI: [10.1134/S1023193518060125](https://doi.org/10.1134/S1023193518060125).
 16. Zhang Wanying, Shi Fengyue, Wang Jianwen, Yang Yang, Zhao Guangdong, Zhao Dongyu. Preparation and properties of a porous $ZrO_2/SiZrBOC$ ceramic matrix composite with high temperature resistance and low thermal conductivity. *Journal of the European Ceramic Society*, 2024, vol. 44, no. 4, pp. 2329–2337. DOI: [10.1016/j.jeurceramsoc.2023.11.007](https://doi.org/10.1016/j.jeurceramsoc.2023.11.007).
 17. Lin Jianliang, Stinnett T.C. Development of thermal barrier coatings using reactive pulsed dc magnetron sputtering for thermal protection of titanium alloys. *Surface & Coatings Technology*, 2020, vol. 403, article number 126377. DOI: [10.1016/j.surfcoat.2020.126377](https://doi.org/10.1016/j.surfcoat.2020.126377).
 18. Reddy G.V., Rasu N.G., Kumar M.M., Prasad J., Hari T. Review on Advanced Alternative Thermal Barrier Coatings (TBC's) Materials in Low Heat Rejection Engines. *International Journal of Research in Mechanical Engineering and Technology*, 2016, vol. 6, no. 2, pp. 27–35.
 19. Bleykher G.A., Borduleva A.O., Krivobokov V.P., Sidelev D.V. Evaporation factor in productivity increase of hot target magnetron sputtering systems. *Vacuum*, 2016, vol. 132, pp. 62–69. DOI: [10.1016/j.vacuum.2016.07.030](https://doi.org/10.1016/j.vacuum.2016.07.030).
 20. Chen Dianying, Dambra C., Dorfman M. Process and properties of dense and porous vertically-cracked yttria stabilized zirconia thermal barrier coatings. *Surface and Coatings Technology*, 2020, vol. 404, article number 126467. DOI: [10.1016/j.surfcoat.2020.126467](https://doi.org/10.1016/j.surfcoat.2020.126467).

СПИСОК ЛИТЕРАТУРЫ

1. Banerjee P., Roy A., Sen S., Ghosh A., Saha G., Seikh A.H., Alnaser I.A. Ghosh M. Service life assessment of yttria stabilized zirconia (YSZ) based thermal barrier coating through wear behavior // *Heliyon*. 2023. Vol. 9. № 5. Article number e16107. DOI: [10.1016/j.heliyon.2023.e16107](https://doi.org/10.1016/j.heliyon.2023.e16107).
2. Singh M., Sahu P.K., Sampath S., Jonnalagadda K.N. Fracture toughness of freestanding plasma sprayed yttria stabilized zirconia coatings via in situ tensile experiments // *Journal of the European Ceramic Society*. 2024. Vol. 44. № 4. P. 2499–2511. DOI: [10.1016/j.jeurceramsoc.2023.10.074](https://doi.org/10.1016/j.jeurceramsoc.2023.10.074).
3. Liu Qiaomu, Huang Shunzhou, He Aijie. Composite ceramics thermal barrier coatings of yttria stabilized zirconia for aero-engines // *Journal of Materials Science & Technology*. 2019. Vol. 35. № 12. P. 2814–2823. DOI: [10.1016/j.jmst.2019.08.003](https://doi.org/10.1016/j.jmst.2019.08.003).

4. Raza M., Boulet P., Pierson J.-F., Snyders R., Konstantinidis S. Thermal stability of oxygen vacancy stabilized zirconia (OVSZ) thin films // *Surface and Coatings Technology*. 2021. Vol. 409. Article number 126880. DOI: [10.1016/j.surfcoat.2021.126880](https://doi.org/10.1016/j.surfcoat.2021.126880).
5. De Goes W.U., Markocsan N., Gupta M., Vaßen R., Matsushita T., Illkova K. Thermal barrier coatings with novel architectures for diesel engine applications // *Surface and Coatings Technology*. 2020. Vol. 396. Article number 125950. DOI: [10.1016/j.surfcoat.2020.125950](https://doi.org/10.1016/j.surfcoat.2020.125950).
6. Yetim A.F., Tekdir H., Turalioglu K., Taftali M., Yetim T. Tribological behavior of plasma-sprayed Yttria-stabilized zirconia thermal barrier coatings on 316L stainless steel under high-temperature conditions // *Materials Letters*. 2023. Vol. 336. Article number 133873. DOI: [10.1016/j.matlet.2023.133873](https://doi.org/10.1016/j.matlet.2023.133873).
7. Karaoglan A.C., Ozgurluk Y., Gulec A., Ozkan D., Binal G. Effect of coating degradation on the hot corrosion behavior of yttria-stabilized zirconia (YSZ) and blast furnace slag (BFS) coatings // *Surface and Coatings Technology*. 2023. Vol. 473. Article number 130000. DOI: [10.1016/j.surfcoat.2023.130000](https://doi.org/10.1016/j.surfcoat.2023.130000).
8. Chen Can, Song Xuemei, Li Wei, Zheng Wei, Ji Heng, Zeng Yi, Shi Ying. Relationship between microstructure and bonding strength of yttria-stabilized zirconia thermal barrier coatings // *Ceramics International*. 2022. Vol. 48. № 4. P. 5626–5635. DOI: [10.1016/j.ceramint.2021.11.107](https://doi.org/10.1016/j.ceramint.2021.11.107).
9. Sanjai S.G., Srideep S., Krishna B.A., Sumanth M.S., Ramaswamy P. Synthesis of Yttria-Stabilized Zirconia Nano Powders for Plasma Sprayed Nano Coatings // *Materials Today: Proceedings*. 2020. Vol. 22. Part 4. P. 1253–1263. DOI: [10.1016/j.matpr.2020.01.418](https://doi.org/10.1016/j.matpr.2020.01.418).
10. Wang Xin, Zhen Zhen, Huang Guanghong, Mu Rende, He Limin, Xu Zhenhua. Thermal cycling of EB-PVD TBCs based on YSZ ceramic coat and diffusion aluminate bond coat // *Journal of Alloys and Compounds*. 2021. Vol. 873. Article number 159720. DOI: [10.1016/j.jallcom.2021.159720](https://doi.org/10.1016/j.jallcom.2021.159720).
11. Mulone A., Mahade S., Björklund S., Lundström D., Kjellman B., Joshi S., Klement U. Development of yttria-stabilized zirconia and graphene coatings obtained by suspension plasma spraying: Thermal stability and influence on mechanical properties // *Ceramics International*. 2023. Vol. 49. № 6. P. 9000–9009. DOI: [10.1016/j.ceramint.2022.11.055](https://doi.org/10.1016/j.ceramint.2022.11.055).
12. Берлин Е.В., Сейдман Л.А. Получение тонких пленок реактивным магнетронным распылением. 2-е изд., испр. и доп. М.: URSS, 2022. 316 с.
13. Tkhabisimov A.B., Mednikov A.F., Dasaev M.R., Kachalin G.V., Zilova O.S. Solid particle erosion resistance of protective ion-plasma coating formed on full-scale objects based on modern additive technologies // *International Journal of Innovative Technology and Exploring Engineering*. 2019. Vol. 8. № 7. P. 2295–2302. EDN: [YNNMPC](https://doi.org/10.1016/j.ijite.2019.07.001).
14. Духопельников Д.В., Булычёв В.С., Воробьев Е.В. Магнетронный разряд с жидкофазным катодом // *Вестник Московского государственного технического университета им. Н.Э. Баумана. Серия Естественные науки*. 2018. № 1. С. 95–103. DOI: [10.18698/1812-3368-2018-1-95-103](https://doi.org/10.18698/1812-3368-2018-1-95-103).
15. Kuritsyna I.E., Bredikhin S.I., Agarkov D.A., Borik M.A., Kulebyakin A.V., Milovich F.O., Lomonova E.E., Myzina V.A., Tabachkova N.Yu. Electrotransport characteristics of ceramic and single crystal materials with the $(\text{ZrO}_2)_{0.89}(\text{Sc}_2\text{O}_3)_{0.10}(\text{Y}_2\text{O}_3)_{0.01}$ composition // *Russian Journal of Electrochemistry*. 2018. Vol. 54. P. 481–485. DOI: [10.1134/S1023193518060125](https://doi.org/10.1134/S1023193518060125).
16. Zhang Wanying, Shi Fengyue, Wang Jianwen, Yang Yang, Zhao Guangdong, Zhao Dongyu. Preparation and properties of a porous $\text{ZrO}_2/\text{SiZrBOC}$ ceramic matrix composite with high temperature resistance and low thermal conductivity // *Journal of the European Ceramic Society*. 2024. Vol. 44. № 4. P. 2329–2337. DOI: [10.1016/j.jeurceramsoc.2023.11.007](https://doi.org/10.1016/j.jeurceramsoc.2023.11.007).
17. Lin Jianliang, Stinnett T.C. Development of thermal barrier coatings using reactive pulsed dc magnetron sputtering for thermal protection of titanium alloys // *Surface & Coatings Technology*. 2020. Vol. 403. Article number 126377. DOI: [10.1016/j.surfcoat.2020.126377](https://doi.org/10.1016/j.surfcoat.2020.126377).
18. Reddy G.V., Rasu N.G., Kumar M.M., Prasad J., Hari T. Review on Advanced Alternative Thermal Barrier Coatings (TBC's) Materials in Low Heat Rejection Engines // *International Journal of Research in Mechanical Engineering and Technology*. 2016. Vol. 6. № 2. P. 27–35.
19. Bleykher G.A., Borduleva A.O., Krivobokov V.P., Sidelev D.V. Evaporation factor in productivity increase of hot target magnetron sputtering systems // *Vacuum*. 2016. Vol. 132. P. 62–69. DOI: [10.1016/j.vacuum.2016.07.030](https://doi.org/10.1016/j.vacuum.2016.07.030).
20. Chen Dianying, Dambra C., Dorfman M. Process and properties of dense and porous vertically-cracked yttria stabilized zirconia thermal barrier coatings // *Surface and Coatings Technology*. 2020. Vol. 404. Article number 126467. DOI: [10.1016/j.surfcoat.2020.126467](https://doi.org/10.1016/j.surfcoat.2020.126467).

К вопросу о формировании термобарьерных покрытий методом магнетронного распыления

*Качалин Геннадий Викторович*¹, кандидат технических наук, ведущий научный сотрудник

*Медведев Константин Сергеевич*², ведущий инженер

*Медников Алексей Феликсович*³, кандидат технических наук, ведущий научный сотрудник

*Зилова Ольга Сергеевна*⁴, кандидат технических наук, ведущий научный сотрудник

Тхабисимов Александр Борисович^{*5}, кандидат технических наук, старший научный сотрудник

*Илюхин Дмитрий Игоревич*⁶, инженер 1 категории

*Касьяненко Владислав Александрович*⁷, инженер 1 категории

Национальный исследовательский университет «МЭИ», Москва (Россия)

*E-mail: TkhabisimovAB@mpei.ru,
abt-bkt@mail.ru

¹ORCID: <https://orcid.org/0000-0001-9506-862X>

²ORCID: <https://orcid.org/0000-0003-1667-458X>

³ORCID: <https://orcid.org/0000-0003-4883-7873>

⁴ORCID: <https://orcid.org/0000-0002-0410-8188>

⁵ORCID: <https://orcid.org/0000-0001-9544-9086>

⁶ORCID: <https://orcid.org/0009-0009-6385-0284>

⁷ORCID: <https://orcid.org/0009-0000-7510-2106>

Received 18.10.2024

Revised 26.11.2024

Accepted 03.12.2024

Аннотация: Применение магнетронных распылительных систем с протяженными неохлаждаемыми мишенями позволит разработать промышленные импортозамещающие технологии формирования термобарьерных покрытий на основе оксида циркония, легированного оксидами редкоземельных металлов, для решения актуальных задач газового турбостроения. В работе приведены результаты сравнения технологии получения термобарьерных покрытий методом магнетронного распыления с двумя типами протяженных мишеней из сплава Zr-8%Y – широко распространенной и применяемой охлаждаемой мишенью и разрабатываемой авторами неохлаждаемой протяженной мишенью магнетронной распылительной системы. Приведено сравнение результатов масс-спектрометрических исследований гистерезиса парциального давления кислорода, свойственного технологии получения оксидных пленок; влияния типа мишени на скорость роста покрытия; исследований методом растровой электронной микроскопии структуры термобарьерных покрытий; элементного состава покрытий на основе диоксида циркония, частично стабилизированного оксидом иттрия – YSZ. Экспериментально установлено, что повышение температуры мишени магнетронной распылительной системы позволяет в 2 раза уменьшить ширину петли характерного гистерезиса зависимости парциального давления кислорода от его расхода. Полученные зависимости позволили определить диапазон значений расхода кислорода при различных мощностях магнетронного разряда, при которых работа может производиться с устойчивым и стабильным управлением процесса, без опасности попадания в гистерезис. Проведенные металлографические исследования показали характерную развитую пористую дендритную структуру керамического слоя, необходимую для снижения коэффициента теплопроводности термобарьерного покрытия. Выявлено, что применение неохлаждаемой мишени позволяет повысить скорость осаждения термобарьерного покрытия более чем в 10 раз по сравнению со скоростью осаждения для охлаждаемой мишени. Полученные результаты демонстрируют возможность применения технологии магнетронного распыления протяженной неохлаждаемой мишени для формирования керамического слоя термобарьерных покрытий.

Ключевые слова: магнетронное распыление; неохлаждаемая мишень; термобарьерные покрытия; гистерезисные явления; скорость осаждения покрытия.

Благодарности: Государственное задание № FSWF-2023-0016 (соглашение № 075-03-2023-383 от 18 января 2023 г.) в сфере научной деятельности на 2023–2025 гг.

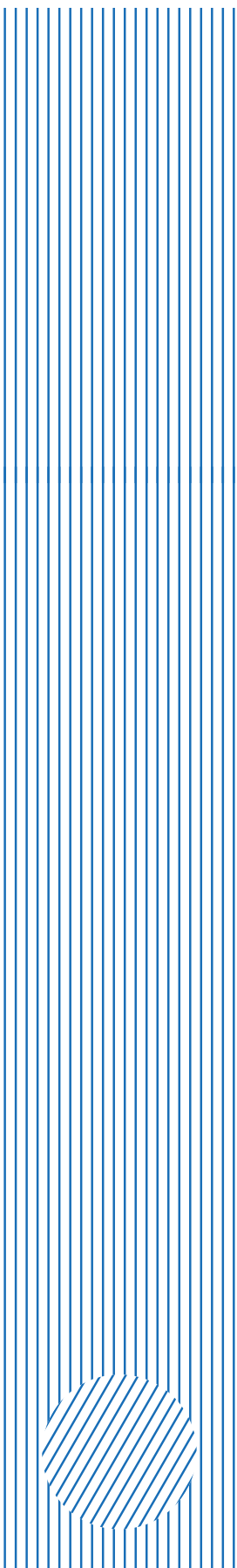
Для цитирования: Качалин Г.В., Медведев К.С., Медников А.Ф., Зилова О.С., Тхабисимов А.Б., Илюхин Д.И., Касьяненко В.А. К вопросу о формировании термобарьерных покрытий методом магнетронного распыления // Frontier Materials & Technologies. 2024. № 4. С. 51–61. DOI: 10.18323/2782-4039-2024-4-70-5.

The Research and Development Institute of Advanced Technologies is a structural division of Togliatti State University.

The Research and Development Institute of Advanced Technologies today

- More than 60 employees, including seven Doctors of Sciences and fourteen PhDs.
- Three centers, four departments, nineteen laboratories equipped with the up-to-date testing and research facilities for amount over 500 million roubles.
- Accreditation in three systems for testing and research, including in the ILAC international system (laboratory accreditation authority – Association of Analytical Centers “Analitika”, a full member and participant of the ILAC and APLAC mutual recognition agreements).
- Basic areas: fundamental research in the field of physical materials science (the development of the promising materials design, the issues of strength, plasticity, corrosion resistance, fatigue strength, stress corrosion cracking, improving the surface functional properties) and chemistry (methods for synthesis of molecules with the properties of selective fluorescent probes); applied research and inventions in the field of non-destructive control, micro-arc oxidation, manufacturing of cast products, etc.; services for testing and research of various materials, metallographic evaluations, environmental analyses, chemical monitoring of the environment.

Main achievements of the Research and Development Institute of Advanced Technologies

- Three mega-grants were implemented according to the Resolution of the Government of the Russian Federation dated April 9, 2010 No. 220; five projects within the Federal Targeted Programme for Research and Development in Priority Areas of Development of the Russian Scientific and Technological Complex for 2014–2020, including three international ones; in 2023, nine projects of the Russian Science Foundation and two state assignments are being implemented; under the auspices of the extraterritorial scientific and educational center “Engineering of the Future”, a youth Laboratory for the design of magnesium alloys was created.
 - Annually:
 - the number of papers is more than 35, half of them are in specialized journals of the Q1 and Q2 levels;
 - more than 1,500 test reports and conclusions at the request of enterprises, arbitration courts, and the prosecutor’s office
 - An initiator and organizer of 11 Physical Materials Science international schools with the participation of leading scientists-material engineers and metal physicists, the lectures of which became the basis for publishing nine volumes of the Advanced Materials textbook
 - International cooperation with the universities of Kumamoto (Japan), Seoul (South Korea), Prague (Czech Republic), and Freiberg (Germany), academic cooperation with IMP UB RAS (Yekaterinburg), IMSP RAS (Ufa), ISPMS SB RAS (Tomsk) and others; technical cooperation with more than 150 organizations in the real sector of the economy.
- 

Electrochemical interaction between biodegradable ZX10 and WZ31 magnesium alloys and medical Ti6Al4V titanium alloy

Pavel N. Myagkikh^{*1}, PhD (Engineering),

junior researcher of the Research Institute of Advanced Technologies

*Evgeny D. Merson*², PhD (Physics and Mathematics),

senior researcher of the Research Institute of Advanced Technologies

*Vitaly A. Poluyanov*³, PhD (Engineering),

junior researcher of the Research Institute of Advanced Technologies

*Dmitry L. Merson*⁴, Doctor of Sciences (Physics and Mathematics),

Professor, Director of the Research Institute of Advanced Technologies

Marina E. Begun, student,

technician of the Research Institute of Advanced Technologies

Togliatti State University, Togliatti (Russia)

*E-mail: p.myagkikh@tltsu.ru

¹ORCID: <https://orcid.org/0000-0002-7530-9518>

²ORCID: <https://orcid.org/0000-0002-7063-088X>

³ORCID: <https://orcid.org/0000-0002-0570-2584>

⁴ORCID: <https://orcid.org/0000-0001-5006-4115>

Received 08.05.2024

Revised 09.10.2024

Accepted 07.11.2024

Abstract: Magnesium-based alloys are a modern material for the production of biodegradable (self-dissolving) surgical implants. Magnesium is a metal with the most negative electrode potential of all structural materials: -2.37 V. This means that close arrangement of implants made of magnesium, and for example, titanium alloys will lead to the occurrence of a galvanic effect, and accelerated electrochemical corrosion of magnesium. However, it is unknown how the ratio of the areas of titanium and magnesium products affects the magnitude of this effect. This work covers this issue. In the presented study, cylindrical samples of biodegradable ZX10 and WZ31 magnesium alloys were placed in physiological Ringer's solution at a distance of 3 cm, from a sample of medical Ti6Al4V alloy of the same shape and size. During the test, the temperature of the corrosive environment was maintained at 37 °C. The series of experiments included corrosion tests lasting three days with the participation of one, two or four magnesium samples, thus the area ratios between the titanium and magnesium alloy were 1:1, 1:2 and 1:4. It was found that for both magnesium alloys, with an increase in the area ratio, the effect of electrochemical action decreases significantly, which is expressed in a decrease in the corrosion rate. At the same time, for the WZ31 alloy, the effect of the presence of Ti6Al4V on the corrosion rate is significantly weaker than for ZX10, which is explained by the presence of the LPSO phase in the alloy, as well as a more alloyed matrix and, accordingly, having a more positive electrode potential.

Keywords: surgical implants; electrochemical corrosion; biodegradable materials; magnesium alloys; ZX10; WZ31; titanium alloys; Ti6Al4V; medical materials; corrosion rate; electrode potential.

Acknowledgments: The research was financially supported by the Russian Science Foundation, project No. 23-23-10041 (<https://rscf.ru/project/23-23-10041/>), project No. 23-19-00636 (<https://rscf.ru/project/23-19-00636/>).

For citation: Myagkikh P.N., Merson E.D., Poluyanov V.A., Merson D.L., Begun M.E. Electrochemical interaction between biodegradable ZX10 and WZ31 magnesium alloys and medical Ti6Al4V titanium alloy. *Frontier Materials & Technologies*, 2024, no. 4, pp. 63–71. DOI: 10.18323/2782-4039-2024-4-70-6.

INTRODUCTION

The idea of a self-dissolving surgical implant for osseointegration has long been under close attention of scientists and medical companies. Such implants do not require an operation to remove them, which is a serious stress for the patient's body. One of the simplest solutions is the use of bioresorbable polymers such as polylactide, polydopamine, polycaprolactone, etc. Indeed, these materials are quite cheap and easy to process. At the same time, the strength properties of poly-

mers cannot be compared with metals. Attempts to solve the problem, for example, by creating a polymer-metal composite [1], continue, but significant progress has not yet been achieved. Similar problems are observed for bioresorbable ceramics, which are also much more fragile. Among the metallic materials, iron, zinc and magnesium are considered as a basis for bioresorbable alloys [2], some researchers consider tungsten [3; 4], and metallic glasses based on calcium, zinc and strontium [5] as a bioresorbable material. Magnesium alloys

are already used for the commercial manufacturing of medical self-dissolving products; moreover, the Young's modulus of magnesium of the presented elements is the closest to that of bone, which is also an important factor, since an implant made of such a material is capable of elastic deformation, in concert with the bone.

The operating conditions of a magnesium alloy implant can directly affect its characteristics, such as the corrosion rate. For example, a titanium implant may already be installed in the immediate proximity to the installation site of a magnesium alloy medical device. It is known that due to the lowest electrode potential among all structural materials, magnesium is prone to electrochemical corrosion in the presence of other metals [6; 7], because of the formation of a galvanic couple between the more negative magnesium, and the more positive metal. In [8], using Kelvin probe atomic force microscopy, evidence was obtained that in some cases, even the corrosion products appearing on the surface of a magnesium alloy, can have a more positive potential and are capable of forming a galvanic couple with the magnesium matrix. In [9], where magnesium alloys doped with silver were studied, it was demonstrated that with the addition of silver, the corrosion properties first improve, and then the corrosion resistance drops sharply. The authors attribute this to the difference in electrode potential between the matrix, and the intermetallic particles released upon reaching the solubility limit of the ligature. However, except for the electrode potential, there are a number of other factors affecting electrochemical corrosion. The most important of these is the distance at which the galvanic effect between magnesium and another metal will have a significant effect on the corrosion rate.

In [10], a magnesium screw was installed directly into a titanium plate (i.e., had direct contact with it) secured, in addition to it, by titanium screws. Based on the results of experiments, including *in vivo* tests on rabbits, the authors note that the magnesium screw contributed to the formation of enlarged callus, and accelerated its mineralization compared to the control group, where only titanium screws were used to attach the titanium plate. At the same time, in the X-ray images presented in this work, the magnesium screw is almost invisible already three weeks after the operation. This indicates that in just 21 days it almost completely dissolved under the influence of the aggressive environment of a living organism and electrochemical interaction with the titanium plate and screws. Obviously, the intensive dissolution of the screw accelerated the formation of bone callus, due to the enrichment of tissues with magnesium. However, at the same time, one should note that the screw itself dissolved too quickly. In the scheme proposed by the authors, where several titanium screws bear the main load, such a dissolution rate is acceptable. However, if we talk about pure magnesium implants that perform their functions independently, based on this work, we can conclude that direct contact with titanium products in the human body threatens the failure of the implant, before the completion of the fusion process. In one of our previous works, it was found that when a titanium implant is located 3 cm from a sample made of ZX10 alloy, the corrosion rate increases by 1.5 times, but at a distance of 6 cm this effect completely disappears [11]. This shows that the electro-

chemical interaction between magnesium and titanium, can manifest itself both in direct contact of metals and at some distance, and that the influence of this effect on the corrosion rate is significant.

Another important parameter is the ratio of the areas of magnesium and titanium alloy products. The main hypothesis is that, an increase in the area of a magnesium product relative to a titanium one, can reduce to some extent the influence of the electrochemical effect on the corrosion rate. Confirmation of this hypothesis will allow the installation of a large magnesium implant, such as an osteosynthesis plate, near a small titanium implant, such as a screw. Finally, it is important to understand whether the galvanic effect is equally strong for different magnesium alloys. Considering that it is caused by the difference in electrode potentials, it can be assumed that for alloys with a large number of secondary phase particles whose potential is more positive than that of magnesium, or a matrix whose electrode potential has been increased by dissolving alloying elements in it, the influence of electrochemical interaction with the titanium alloy will be significantly weaker. In this regard, this study was conducted for two different magnesium alloys.

The aim of the work is to determine the influence of the ratio of the areas of samples of ZX10 and WZ31 magnesium alloys, and a sample of Ti6Al4V titanium alloy on the corrosion rate.

METHODS

Bioresorbable ZX10 and WZ31 alloys were selected for the study. Multi-axial isothermal forging was selected as the thermomechanical treatment, which was carried out in the temperature range of 400–300 °C, and included 5 passes. This treatment mode ensures a uniform fine-grained structure [12]. The chemical composition of magnesium alloys was determined using a Thermo Fisher Scientific ARL 4460 OES optical emission spectrometer (USA). The chemical composition of the titanium alloy was determined on a Bruker Q4 Tasman optical emission spectrometer (Germany). Both spectrometers were calibrated using standard samples.

The samples (including those made of titanium alloy) were cylinders with a diameter of 5 mm and a height of 30 mm prepared by turning. The titanium Ti6Al4V alloy used in the study complied with GOST R ISO 5832-3-2020. Separately, flat samples were made to study the microstructure of the ZX10 and WZ31 alloys, which were successively polished on anhydrous diamond suspensions with an abrasive size of 3, 1 and 0.25 μm, followed by ion polishing in an argon ion stream on a Hitachi IM4000 Plus installation (Japan) at an accelerating voltage of 4.5 kV for 45 min.

The microstructure study was carried out in a Carl Zeiss SIGMA scanning electron microscope (SEM) column (Germany), using EDAX modules (USA), for electron backscatter diffraction (EBSD) and energy-dispersive spectrometry (EDS) analysis. The WZ31 alloy had a large number of secondary phase particles, whose electrode potential was additionally studied using the Kelvin probe method using an NT-MDT Solver NEXT atomic force microscope (Russia).

The corrosion tests included keeping the sample for 72 h in a Ringer solution of 8.36 g of NaCl, 0.3 g of KCl, and 0.15 g of CaCl_2 per 1000 ml of water. The volume of the corrosion cell was 5 l. A Mettler Toledo Delta 320 pH-meter (USA) was used to record the maximum pH level. Tests of the control group (in the absence of titanium alloy) were performed on samples of both alloys. The initial corrosion rate was determined for one and for four samples simultaneously participating in the experiment, since the number of samples in the cell could affect the corrosion rate. During the main series of experiments, the titanium rod was fixed in a groove in the middle of a fluoroplastic washer with a diameter of 7 cm. Grooves for installing magnesium alloy samples were located in a circle at a radius of 3 cm from it. Fig. 1 shows the setup diagram. One, two and four magnesium alloy samples were used in the experiment at a time, so the ratio of the areas of the titanium and magnesium alloys was 1:1, 1:2 and 1:4.

After the tests were completed, the samples were removed, and the corrosion products were removed by immersion for 1 min in an aqueous solution of 20 % CrO_3 + 1 % AgNO_3 . The corrosion rate was determined gravimetrically by the difference in masses.

RESULTS

Table 1 shows the chemical composition of magnesium alloys. Table 2 shows the chemical composition of a titanium alloy.

Fig. 2 shows that the ZX10 alloy has an average grain size of about 5 μm , while the WZ31 alloy has an average grain size of about 1 μm . Both alloys have a disordered structure and no crystallographic texture, which is typical of alloys after multi-axial isothermal forging. This allows avoiding the anisotropy of corrosion properties, caused by crystallographic orientation, which is observed in highly textured materials. Dark areas corresponding to non-indexed regions are visible in Fig. 2 b.

Secondary phase particles in the ZX10 alloy are few in number, and contain zinc and calcium (Fig. 3). Based on the elemental composition, the phase with spongy morphology in the ZX10 alloy (point 1 in Fig. 3) is most likely calcium, and magnesium oxide particles. Particles at points 2 and 3 are most likely intermetallics formed by the matrix metal and alloying elements.

In contrast, the WZ31 alloy is saturated with particles mostly having a morphology characteristic of the LPSO phase (Fig. 4). In addition to large (up to 15 μm) LPSO phase particles, there are small particles 0.2–2 μm in size. Most likely, the small particles were obtained by mechanical crushing of large ones during thermomechanical treatment. The elemental composition of the LPSO phase is shown in Table 3.

The results of the Kelvin probe study of the WZ31 alloy presented in Fig. 5 show both large and small particles, positively charged relative to the matrix, presumably representing the LPSO phase.

Fig. 6 demonstrates that for both magnesium alloys the corrosion rate in the presence of titanium alloy is higher than during the tests of the control group. However, it should be noted that the difference depends significantly on both the chemical composition of the material and the number of anodes (magnesium samples), and accordingly, on

the ratio of the areas of magnesium and titanium alloys: with an increase in the number of magnesium alloys, their corrosion rate decreases.

Table 4 shows the maximum pH level found for each group of samples during the experiments. One should note that in all cases, regardless of the presence of titanium alloy and the number of anodes, the pH level reaches its maximum values in the first day, and then remains virtually unchanged.

DISCUSSION

The presence of the LPSO phase is indirectly confirmed by the results of EBSD analysis: according to the literature, the dark non-indexed areas in Fig. 2 b correspond to the LPSO phase [13; 14].

Based on the elemental composition, the phase with a spongy morphology in the ZX10 alloy (point 1 in Fig. 3) is most likely particles of calcium and magnesium oxides, while the rounded particles (points 2 and 3 in Fig. 3) have a ratio of zinc atoms to calcium atoms of ~2.2. Due to this, they most likely belong to the $\text{Ca}_2\text{Mg}_5\text{Zn}_5$ [15] and $\text{Mg}_6\text{Zn}_3\text{Ca}_2$ [16] phases.

The chemical composition of the LPSO phase in the studied WZ31 alloy is very close to that presented in the literature [17]. It is known that the LPSO phase is more positively charged than the matrix. A study using Kelvin probe atomic force microscopy (Fig. 4), allowed determining that the electrode potential of the LPSO phase (light areas in Fig. 4) in the WZ31 alloy is really 0.3–0.4 V more positive than the matrix, which is fully consistent with the results of [18; 19].

Based on the results of the experiments, several important facts can be noted. Firstly, regardless of the material and number of magnesium samples, the corrosion rate in the presence of the titanium alloy is always higher than without it, i.e. in all cases a galvanic effect occurred between the titanium and magnesium alloys.

The second important result is that the dependence of the corrosion rate on the ratio of the areas of the titanium and magnesium alloys differs significantly for the ZX10 and WZ31 alloys. If for the ZX10 alloy an increase in the area ratio from 1:1 to 1:2 provokes a sharp decrease in the corrosion rate, which gives the curve the appearance of a hyperbola, then for the WZ31 alloy the curve has rather the appearance of a straight line along its entire length (Fig. 6). Moreover, the difference between the corrosion rate of the samples in the presence of the titanium alloy and the samples of the control group is smaller for this alloy. From this, we can conclude that the WZ31 alloy is less sensitive to the galvanic effect caused by the presence of the titanium alloy. This is well explained by the fact that the WZ31 matrix contains zinc and yttrium dissolved in it, due to which its electrode potential is increased, as well as by the presence in the alloy of a large number of LPSO phase particles, which are more positively charged than magnesium. Thus, the difference in electrode potentials between WZ31 and Ti6Al4V is smaller than between Ti6Al4V and ZX10.

An interesting result is the decrease in the corrosion rate of the control samples with an increase in the number of anodes observed for both alloys. This effect can be

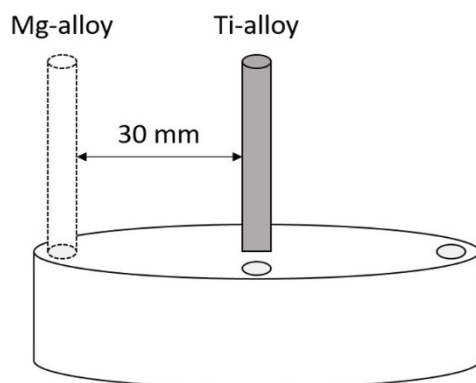


Fig. 1. Schematic diagram of the arrangement of samples during the corrosion tests
Рис. 1. Схема расположения образцов во время коррозионных испытаний

Table 1. Chemical composition of the WZ31 and ZX10 magnesium alloys, % wt.
Таблица 1. Химический состав магниевых сплавов WZ31 и ZX10, вес. %

Alloy	Mg	Zn	Zr	Ca	Fe	Mn	Si	Al	Cu	Y
WZ31	Base	0.69	0.13	<0.001	0.004	0.002	0.002	0.008	<0.001	2.790
ZX10		1.48	<0.01	0.098	0.004	0.003	0.002	0.010	<0.001	<0.001

Table 2. Chemical composition of the Ti6Al4V alloy, % wt.
Таблица 2. Химический состав сплава Ti6Al4V, вес. %

Ti	Si	Mn	Cr	Ni	Mo	Al	Fe	V	C	Cu
Base	0.016	0.002	0.021	0.011	0.011	5.618	0.102	3.950	<0.002	0.006

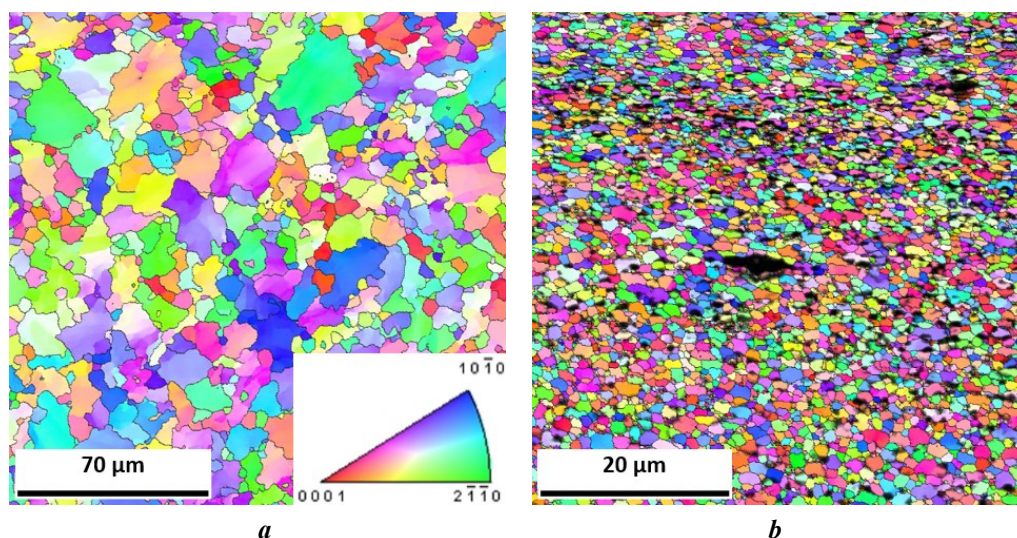


Fig. 2. Maps of crystallographic orientations of grains of the ZX10 (a) and WZ31 (b) alloys
Рис. 2. Карта кристаллографических ориентаций зерен сплавов ZX10 (a) и WZ31 (b)

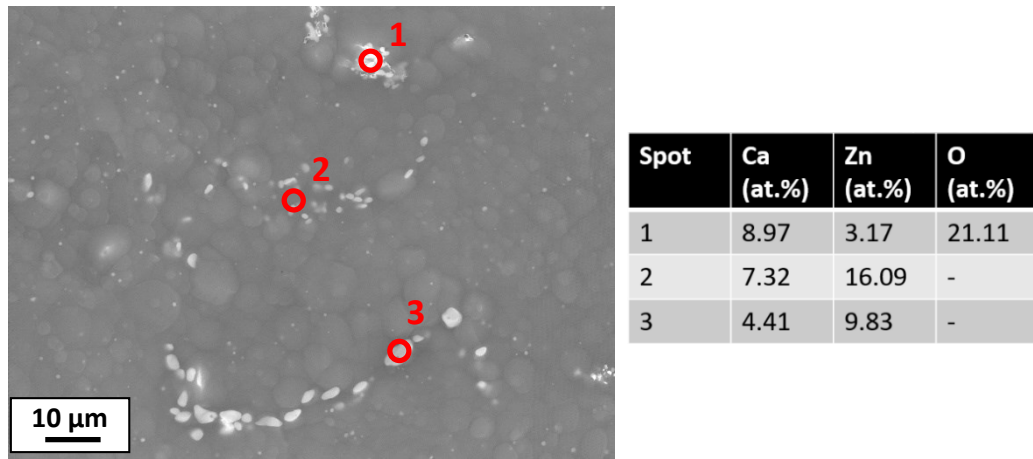


Fig. 3. SEM image and chemical composition of secondary phase particles in the ZX10 alloy
Рис. 3. СЭМ-снимок и химический состав частиц вторичных фаз в сплаве ZX10

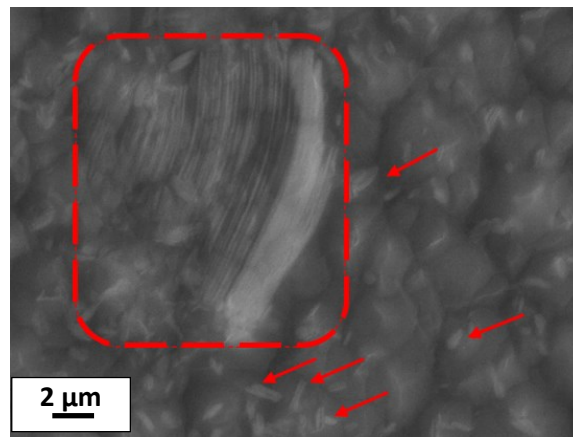


Fig. 4. LPSO phase particles (marked by red arrows and frame) in the WZ31 alloy
Рис. 4. Частицы LPSO-фазы (помечены красными стрелками и рамкой) в сплаве WZ31

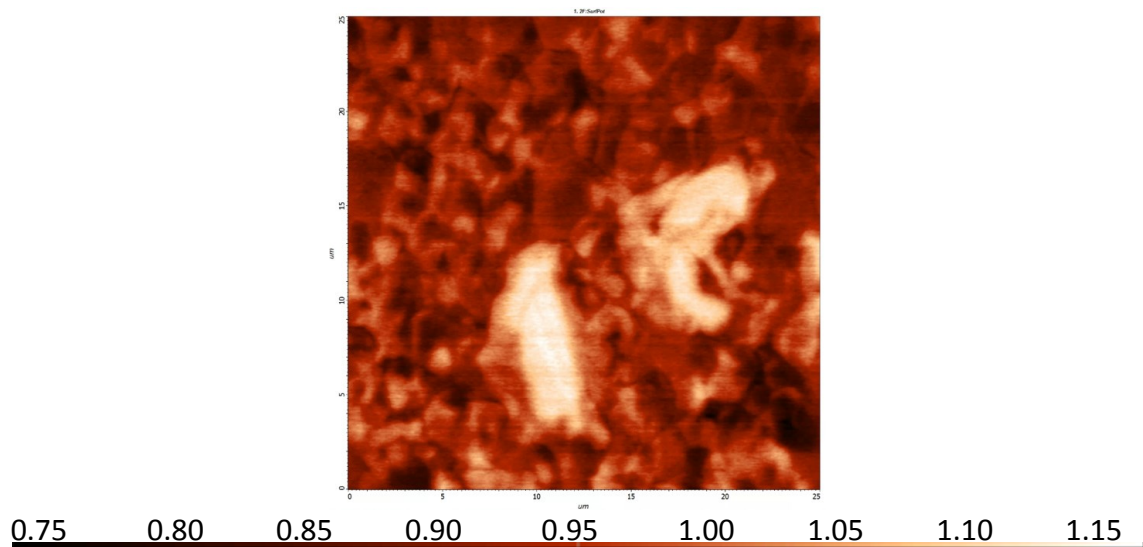


Fig. 5. Electrode potential distribution on the WZ31 alloy surface. Light areas are the LPSO phase
Рис. 5. Распределение электроодного потенциала на поверхности сплава WZ31. Светлые участки – LPSO-фаза

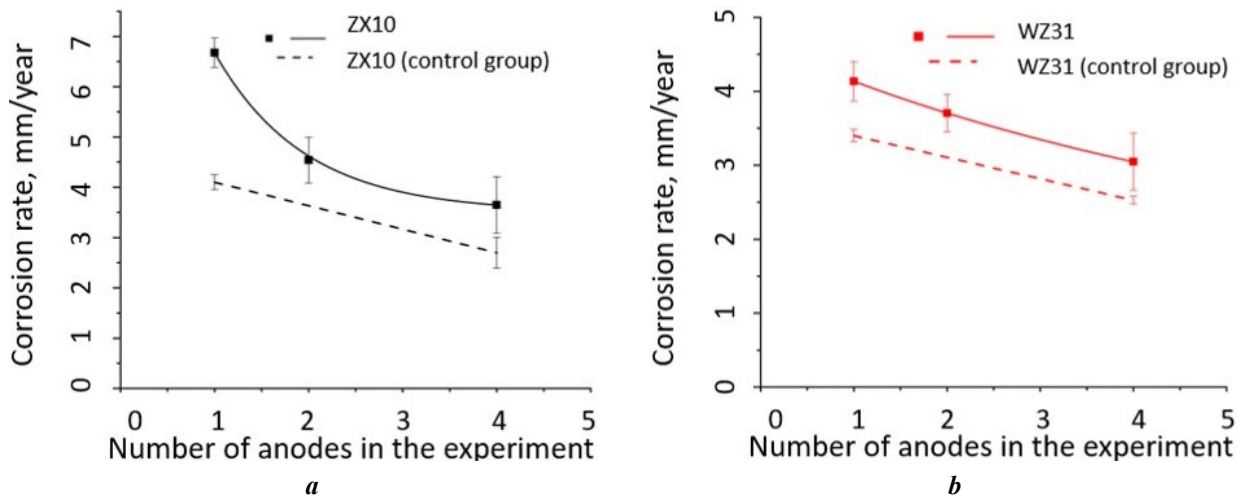


Fig. 6. Dependence of the corrosion rate of the ZX10 (a) and WZ31 (b) alloys on the number of magnesium alloy samples (anodes)
Рис. 6. Зависимость скорости коррозии сплавов ZX10 (a) и WZ31 (b) от числа образцов магниевого сплава (анодов)

Table 3. Chemical composition of the WZ31 alloy matrix and LPSO phase
Таблица 3. Химический состав матрицы сплава WZ31 и его LPSO-фазы

Area	Mg (wt. %)	Y (wt. %)	Zn (wt. %)	Mg (at. %)	Y (at. %)	Zn (at. %)
Matrix	96.65	2.43	0.92	98.97	0.68	0.35
LPSO phase	74.5	17.33	8.17	90.55	5.76	3.69

Table 4. Maximum pH level of the solution achieved during corrosion tests
Таблица 4. Максимальный уровень pH раствора, достигнутый в ходе коррозионных испытаний

Group of samples	Maximum pH level
ZX10 control group, 1 anode	8.52
ZX10 control group, 4 anodes	9.44
ZX10, 1 anode	8.52
ZX10, 2 anodes	8.68
ZX10, 4 anodes	9.39
WZ31 control group, 1 anode	8.32
WZ31 control group, 4 anodes	9.21
WZ31, 1 anode	8.23
WZ31, 2 anodes	8.46
WZ31, 4 anodes	9.24

explained by a significantly higher maximum pH level of the solution in the experiments involving four anodes, which is consistent with the results of [20], where it was shown that at a high pH level, the corrosion of the magnesium AZ31 alloy slows down. In all such cases, the pH le-

vel during the first day took a value of about 9.2–9.4, after which its growth stopped. It was previously demonstrated that a high pH level could contribute to better passivation of the surface of the ZX10 alloy [21]. Apparently, a similar feature is characteristic of WZ31.

CONCLUSIONS

1. Increasing the area ratio of the ZX10 and Ti6Al4V alloy samples from 1:1 to 1:2 leads to a sharp drop in the corrosion rate. Increasing the area ratio from 1:2 to 1:4 also contributes to a decrease in the corrosion rate, but not as significantly.

2. The corrosion rate of the WZ31 alloy decreases almost linearly, with an increase in the area ratio of the ZX10 and Ti6Al4V alloy samples.

3. The WZ31 alloy is less sensitive to the galvanic effect introduced by the presence of a titanium alloy at a distance of 3 cm. This is explained by an increase in the electrode potential of the matrix, due to the dissolution of alloying elements in it and the presence of a large amount of the LPSO phase.

4. Increasing the number of magnesium samples in the control group from 1 to 4 also leads to a decrease in the corrosion rate of both alloys under study. The most likely cause of this phenomenon is a significantly higher maximum pH level of the solution, which can contribute to better passivation of the material.

REFERENCES

- Antoniac I., Popescu D., Zapciu A., Antoniac A., Miculescu F., Moldovan H. Magnesium filled polylactic acid (PLA) material for filament based 3D printing. *Materials (Basel)*, 2019, vol. 12, no. 5, pp. 1–13. DOI: [10.3390/ma12050719](https://doi.org/10.3390/ma12050719).
- Yang Youwen, He Chongxian, E Dianyuan, Yang Wenjing, Qi Fangwei, Xie Deqiao, Shen Lida, Peng Shuping, Shuai Cijun. Mg bone implant: Features, developments and perspectives. *Materials and Design*, 2020, vol. 185, article number 108259. DOI: [10.1016/j.matdes.2019.108259](https://doi.org/10.1016/j.matdes.2019.108259).
- Butler T.J., Jackson R.W., Robson J.Y., Owen R.J.T., Delves H.T., Sieniawska C.E., Rose J.D.G. In vivo degradation of tungsten embolisation coils. *British Journal of Radiology*, 2000, vol. 73, no. 870, pp. 601–603. DOI: [10.1259/bjr.73.870.10911782](https://doi.org/10.1259/bjr.73.870.10911782).
- Peuster M., Fink C., Wohlsein P., Bruegmann M., Günther A., Kaese V., Niemeyer M., Haferkamp H., Schnakenburg C.V. Degradation of tungsten coils implanted into the subclavian artery of New Zealand white rabbits is not associated with local or systemic toxicity. *Biomaterials*, 2003, vol. 24, no. 3, pp. 393–399. DOI: [10.1016/S0142-9612\(02\)00352-6](https://doi.org/10.1016/S0142-9612(02)00352-6).
- Zheng Y.F., Gu X.N., Witte F. Biodegradable metals. *Materials Science and Engineering: R: Reports*, 2014, vol. 77, pp. 1–34. DOI: [10.1016/j.mser.2014.01.001](https://doi.org/10.1016/j.mser.2014.01.001).
- Song G.-L. Corrosion electrochemistry of magnesium (Mg) and its alloys. *Corrosion of Magnesium Alloys*. Sawston, Woodhead Publ., 2011, pp. 3–65. DOI: [10.1533/9780857091413.1.3](https://doi.org/10.1533/9780857091413.1.3).
- Esmaily M., Svensson J.E., Fajardo S., Birbilis N., Frankel G.S., Virtanen S., Arrabal R., Thomas S., Johansson L.G. Fundamentals and advances in magnesium alloy corrosion. *Progress in Materials Science*, 2017, vol. 89, pp. 92–193. DOI: [10.1016/j.pmatsci.2017.04.011](https://doi.org/10.1016/j.pmatsci.2017.04.011).
- Parfenov E.V., Kulyasova O.B., Mukaeva V.R., Mingo B., Farrakhov R.G., Cherneikina Y.V., Yerokhin A., Zheng Y.F., Valiev R.Z. Influence of ultra-fine grain structure on corrosion behaviour of biodegradable Mg-1Ca alloy. *Corrosion Science*, 2020, vol. 163, article number 108303. DOI: [10.1016/j.corsci.2019.108303](https://doi.org/10.1016/j.corsci.2019.108303).
- Ma Yingzhong, Wang Dexin, Li Hongxiang, Yuan Fulong, Yang Changlin, Zhang Jishan. Microstructure, mechanical and corrosion properties of novel quaternary biodegradable extruded Mg-1Zn-0.2Ca-xAg alloys. *Materials Research Express*, 2020, vol. 7, no. 1, article number 015414. DOI: [10.1088/2053-1591/ab6a52](https://doi.org/10.1088/2053-1591/ab6a52).
- Tian Li, Sheng Yifeng, Huang Le et al. An innovative Mg/Ti hybrid fixation system developed for fracture fixation and healing enhancement at load-bearing skeletal site. *Biomaterials*, 2018, vol. 180, pp. 173–183. DOI: [10.1016/j.biomaterials.2018.07.018](https://doi.org/10.1016/j.biomaterials.2018.07.018).
- Myagkikh P.N., Merson E.D., Poluyanov V.A., Merson D.L., Begun M.E. On the compatibility of surgical implants of bioresorbable magnesium alloys with medical devices of titanium alloys. *Frontier Materials & Technologies*, 2022, no. 3-1, pp. 106–114. DOI: [10.18323/2782-4039-2022-3-1-106-114](https://doi.org/10.18323/2782-4039-2022-3-1-106-114).
- Merson D.L., Brilevsky A.I., Myagkikh P.N., Markushev M.V., Vinogradov A. Effect of deformation processing of the dilute Mg-1Zn-0.2Ca alloy on the mechanical properties and corrosion rate in a simulated body fluid. *Letters on Materials*, 2020, vol. 10, no. 2, pp. 217–222. DOI: [10.22226/2410-3535-2020-2-217-222](https://doi.org/10.22226/2410-3535-2020-2-217-222).
- Myagkikh P.N., Merson E.D., Poluyanov V.A., Merson D.L. Structure effect on the kinetics and staging of the corrosion process of biodegradable ZX10 and WZ31 magnesium alloys. *Frontier Materials & Technologies*, 2022, no. 2, pp. 63–73. DOI: [10.18323/2782-4039-2022-2-63-73](https://doi.org/10.18323/2782-4039-2022-2-63-73).
- Zheng Jie, Chen Zhe, Yan Zhaoming, Zhang Zhimin, Wang Qiang, Xue Yong. Preparation of ultra-high strength Mg-Gd-Y-Zn-Zr alloy by pre-ageing treatment prior to extrusion. *Journal of Alloys and Compounds*, 2022, vol. 894, article number 162490. DOI: [10.1016/j.jallcom.2021.162490](https://doi.org/10.1016/j.jallcom.2021.162490).
- Schäublin R.E., Becker M., Cihova M., Gerstl S.S.A., Deiana D., Hébert C., Pogatscher S., Uggowitz P.J., Löffler J.F. Precipitation in lean Mg-Zn-Ca alloys. *Acta Materialia*, 2022, vol. 239, article number 118223. DOI: [10.1016/j.actamat.2022.118223](https://doi.org/10.1016/j.actamat.2022.118223).
- Martynenko N., Anisimova N., Kiselevskiy M. et al. Structure, mechanical characteristics, biodegradation, and in vitro cytotoxicity of magnesium alloy ZX11 processed by rotary swaging. *Journal of Magnesium and Alloys*, 2020, vol. 8, no. 4, pp. 1038–1046. DOI: [10.1016/j.jma.2020.08.008](https://doi.org/10.1016/j.jma.2020.08.008).
- Liu Shimeng, Wei Ziqi, Liu Zheng, Mao Pingli, Wang Feng, Wang Zhi, Zhou Le, Yin Xiunan. Effect of Zn content on hot tearing susceptibility of LPSO enhanced Mg-Zn_x-Y₂-Zr_{0.06} alloys with different initial mold temperatures. *Journal of Alloys and Compounds*, 2022, vol. 904, article number 163963. DOI: [10.1016/j.jallcom.2022.163963](https://doi.org/10.1016/j.jallcom.2022.163963).
- Li C.Q., Xu D.K., Zeng Z.R., Wang B.J., Sheng L.Y., Chen X.B., Han E.H. Effect of volume fraction of LPSO phases on corrosion and mechanical properties of Mg-Zn-Y alloys. *Materials and Design*, 2017, vol. 121, pp. 430–441. DOI: [10.1016/j.matdes.2017.02.078](https://doi.org/10.1016/j.matdes.2017.02.078).

19. Zong Ximei, Zhang Jinshan, Liu Wei, Zhang Yatong, You Zhiyong, Xu Chunxiang. Corrosion Behaviors of Long-Period Stacking Ordered Structure in Mg Alloys Used in Biomaterials: A Review. *Advanced Engineering Materials*, 2018, vol. 20, no. 7, pp. 1–26. DOI: [10.1002/adem.201800017](https://doi.org/10.1002/adem.201800017).
20. Azzeddine H., Hanna A., Dakhouche A. Exploring the Corrosion Performance of AZ31 Magnesium Alloy under Acidic and Alkaline Conditions. *Physics of Metals and Metallography*, 2024, pp. 1–8. DOI: [10.1134/S0031918X24600258](https://doi.org/10.1134/S0031918X24600258).
21. Myagkikh P.N., Merson E.D., Poluyanov V.A., Merson D.L. The dependence of the biodegradable ZX10 alloy corrosion process on the structural factors and local pH level. *Frontier Materials & Technologies*, 2023, no. 2, pp. 59–76. DOI: [10.18323/2782-4039-2023-2-64-3](https://doi.org/10.18323/2782-4039-2023-2-64-3).
- mechanical and corrosion properties of novel quaternary biodegradable extruded Mg-1Zn-0.2Ca-xAg alloys // *Materials Research Express*. 2020. Vol. 7. № 1. Article number 015414. DOI: [10.1088/2053-1591/ab6a52](https://doi.org/10.1088/2053-1591/ab6a52).
10. Tian Li, Sheng Yifeng, Huang Le et al. An innovative Mg/Ti hybrid fixation system developed for fracture fixation and healing enhancement at load-bearing skeletal site // *Biomaterials*. 2018. Vol. 180. P. 173–183. DOI: [10.1016/j.biomaterials.2018.07.018](https://doi.org/10.1016/j.biomaterials.2018.07.018).
11. Мягких П.Н., Мерсон Е.Д., Полуянов В.А., Мерсон Д.Л., Бегун М.Э. О совместимости хирургических имплантатов из биорезорбируемых магниевых сплавов с медицинскими изделиями из титановых сплавов // *Frontier Materials & Technologies*. 2022. № 3-1. С. 106–114. DOI: [10.18323/2782-4039-2022-3-1-106-114](https://doi.org/10.18323/2782-4039-2022-3-1-106-114).
12. Merson D.L., Brilevsky A.I., Myagkikh P.N., Markushev M.V., Vinogradov A. Effect of deformation processing of the dilute Mg-1Zn-0.2Ca alloy on the mechanical properties and corrosion rate in a simulated body fluid // *Letters on Materials*. 2020. Vol. 10. № 2. P. 217–222. DOI: [10.22226/2410-3535-2020-2-217-222](https://doi.org/10.22226/2410-3535-2020-2-217-222).
13. Мягких П.Н., Мерсон Е.Д., Полуянов В.А., Мерсон Д.Л. Влияние структуры на кинетику и стабильность процесса коррозии биорезорбируемых магниевых сплавов ZX10 и WZ31 // *Frontier Materials & Technologies*. 2022. № 2. С. 63–73. DOI: [10.18323/2782-4039-2022-2-63-73](https://doi.org/10.18323/2782-4039-2022-2-63-73).
14. Zheng Jie, Chen Zhe, Yan Zhaoming, Zhang Zhimin, Wang Qiang, Xue Yong. Preparation of ultra-high strength Mg-Gd-Y-Zn-Zr alloy by pre-ageing treatment prior to extrusion // *Journal of Alloys and Compounds*. 2022. Vol. 894. Article number 162490. DOI: [10.1016/j.jallcom.2021.162490](https://doi.org/10.1016/j.jallcom.2021.162490).
15. Schäublin R.E., Becker M., Cihova M., Gerstl S.S.A., Deiana D., Hébert C., Pogatscher S., Uggowitzer P.J., Löffler J.F. Precipitation in lean Mg-Zn-Ca alloys // *Acta Materialia*. 2022. Vol. 239. Article number 118223. DOI: [10.1016/j.actamat.2022.118223](https://doi.org/10.1016/j.actamat.2022.118223).
16. Martynenko N., Anisimova N., Kiselevskiy M. et al. Structure, mechanical characteristics, biodegradation, and in vitro cytotoxicity of magnesium alloy ZX11 processed by rotary swaging // *Journal of Magnesium and Alloys*. 2020. Vol. 8. № 4. P. 1038–1046. DOI: [10.1016/j.jma.2020.08.008](https://doi.org/10.1016/j.jma.2020.08.008).
17. Liu Shimeng, Wei Ziqi, Liu Zheng, Mao Pingli, Wang Feng, Wang Zhi, Zhou Le, Yin Xiunan. Effect of Zn content on hot tearing susceptibility of LPSO enhanced Mg-Zn_x-Y₂-Zr_{0.06} alloys with different initial mold temperatures // *Journal of Alloys and Compounds*. 2022. Vol. 904. Article number 163963. DOI: [10.1016/j.jallcom.2022.163963](https://doi.org/10.1016/j.jallcom.2022.163963).
18. Li C.Q., Xu D.K., Zeng Z.R., Wang B.J., Sheng L.Y., Chen X.B., Han E.H. Effect of volume fraction of LPSO phases on corrosion and mechanical properties of Mg-Zn-Y alloys // *Materials and Design*. 2017. Vol. 121. P. 430–441. DOI: [10.1016/j.matdes.2017.02.078](https://doi.org/10.1016/j.matdes.2017.02.078).
19. Zong Ximei, Zhang Jinshan, Liu Wei, Zhang Yatong, You Zhiyong, Xu Chunxiang. Corrosion Behaviors of Long-Period Stacking Ordered Structure in Mg Alloys Used in Biomaterials: A Review // *Advanced Engineering Materials*. 2018. Vol. 20. № 7. P. 1–26. DOI: [10.1002/adem.201800017](https://doi.org/10.1002/adem.201800017).

СПИСОК ЛИТЕРАТУРЫ

1. Antoniac I., Popescu D., Zapciu A., Antoniac A., Miculescu F., Moldovan H. Magnesium filled polylactic acid (PLA) material for filament based 3D printing // *Materials (Basel)*. 2019. Vol. 12. № 5. P. 1–13. DOI: [10.3390/ma12050719](https://doi.org/10.3390/ma12050719).
2. Yang Youwen, He Chongxian, E Dianyu, Yang Wenjing, Qi Fangwei, Xie Deqiao, Shen Lida, Peng Shuping, Shuai Cijun. Mg bone implant: Features, developments and perspectives // *Materials and Design*. 2020. Vol. 185. Article number 108259. DOI: [10.1016/j.matdes.2019.108259](https://doi.org/10.1016/j.matdes.2019.108259).
3. Butler T.J., Jackson R.W., Robson J.Y., Owen R.J.T., Delves H.T., Sieniawska C.E., Rose J.D.G. In vivo degradation of tungsten embolisation coils // *British Journal of Radiology*. 2000. Vol. 73. № 870. P. 601–603. DOI: [10.1259/bjr.73.870.10911782](https://doi.org/10.1259/bjr.73.870.10911782).
4. Peuster M., Fink C., Wohlsein P., Bruegmann M., Günther A., Kaese V., Niemeyer M., Haferkamp H., Schnakenburg C.V. Degradation of tungsten coils implanted into the subclavian artery of New Zealand white rabbits is not associated with local or systemic toxicity // *Biomaterials*. 2003. Vol. 24. № 3. P. 393–399. DOI: [10.1016/S0142-9612\(02\)00352-6](https://doi.org/10.1016/S0142-9612(02)00352-6).
5. Zheng Y.F., Gu X.N., Witte F. Biodegradable metals // *Materials Science and Engineering: R: Reports*. 2014. Vol. 77. P. 1–34. DOI: [10.1016/j.mser.2014.01.001](https://doi.org/10.1016/j.mser.2014.01.001).
6. Song G.-L. Corrosion electrochemistry of magnesium (Mg) and its alloys // *Corrosion of Magnesium Alloys*. Sawston: Woodhead Publishing, 2011. P. 3–65. DOI: [10.1533/9780857091413.1.3](https://doi.org/10.1533/9780857091413.1.3).
7. Esmaily M., Svensson J.E., Fajardo S., Birbilis N., Frankel G.S., Virtanen S., Arrabal R., Thomas S., Johansson L.G. Fundamentals and advances in magnesium alloy corrosion // *Progress in Materials Science*. 2017. Vol. 89. P. 92–193. DOI: [10.1016/j.pmatsci.2017.04.011](https://doi.org/10.1016/j.pmatsci.2017.04.011).
8. Parfenov E.V., Kulyasova O.B., Mukaeva V.R., Mingo B., Farrakhov R.G., Cherneikina Y.V., Yerokhin A., Zheng Y.F., Valiev R.Z. Influence of ultra-fine grain structure on corrosion behaviour of biodegradable Mg-1Ca alloy // *Corrosion Science*. 2020. Vol. 163. Article number 108303. DOI: [10.1016/j.corsci.2019.108303](https://doi.org/10.1016/j.corsci.2019.108303).
9. Ma Yingzhong, Wang Dexin, Li Hongxiang, Yuan Fulong, Yang Changlin, Zhang Jishan. Microstructure,

20. Azzeddine H., Hanna A., Dakhouche A. Exploring the Corrosion Performance of AZ31 Magnesium Alloy under Acidic and Alkaline Conditions // *Physics of Metals and Metallography*. 2024. P. 1–8. DOI: [10.1134/S0031918X24600258](https://doi.org/10.1134/S0031918X24600258).
21. Мягких П.Н., Мерсон Е.Д., Полуянов В.А., Мерсон Д.Л. Зависимость процесса коррозии биорезорбируемого сплава ZX10 от структурных факторов и локального уровня pH // *Frontier Materials & Technologies*. 2023. № 2. С. 59–76. DOI: [10.18323/2782-4039-2023-2-64-3](https://doi.org/10.18323/2782-4039-2023-2-64-3).

Электрохимическое взаимодействие между биорезорбируемыми магниевыми сплавами ZX10 и WZ31 и медицинским титановым сплавом Ti6Al4V

Мягких Павел Николаевич^{*1}, кандидат технических наук, младший научный сотрудник НИИ прогрессивных технологий
*Мерсон Евгений Дмитриевич*², кандидат физико-математических наук, старший научный сотрудник НИИ прогрессивных технологий
*Полуянов Виталий Александрович*³, кандидат технических наук, младший научный сотрудник НИИ прогрессивных технологий
*Мерсон Дмитрий Львович*⁴, доктор физико-математических наук, профессор, директор НИИ прогрессивных технологий
Бегун Марина Эдуардовна, студент, техник НИИ прогрессивных технологий

Тольяттинский государственный университет, Тольятти (Россия)

*E-mail: p.myagkikh@tltsu.ru

¹ORCID: <https://orcid.org/0000-0002-7530-9518>

²ORCID: <https://orcid.org/0000-0002-7063-088X>

³ORCID: <https://orcid.org/0000-0002-0570-2584>

⁴ORCID: <https://orcid.org/0000-0001-5006-4115>

Поступила в редакцию 08.05.2024

Пересмотрена 09.10.2024

Принята к публикации 07.11.2024

Аннотация: Сплавы на основе магния являются современным материалом для изготовления биорезорбируемых (саморастворяющихся) хирургических имплантатов. Магний – металл с наиболее отрицательным из всех конструкционных материалов электродным потенциалом $-2,37$ В. Это означает, что близкое расположение имплантатов из магниевых и, например, титановых сплавов будет приводить к возникновению гальванического эффекта и ускоренной электрохимической коррозии магния. Однако неизвестно, как влияет соотношение площадей изделий из титана и магния на проявление этого эффекта. Данная работа посвящена этому вопросу. В приведенном исследовании цилиндрические образцы биорезорбируемых магниевых сплавов ZX10 и WZ31 располагались в физиологическом растворе Рингера на расстоянии 3 см от образца из сплава медицинского назначения Ti6Al4V такой же формы и размера. Во время испытания поддерживалась температура коррозионной среды 37 °С. Серия экспериментов включала в себя коррозионные испытания длительностью трое суток с участием одного, двух или четырех магниевых образцов, таким образом, соотношение площадей титанового и магниевых сплавов составляло 1:1, 1:2 и 1:4. Выявлено, что для обоих магниевых сплавов при увеличении соотношения площадей эффект от электрохимического воздействия значительно снижается, что выражено в уменьшении скорости коррозии. В то же время влияние присутствия Ti6Al4V на скорость коррозии для сплава WZ31 существенно слабее, чем для ZX10, что объясняется наличием в сплаве LPSO-фазы, а также более легированной и, соответственно, имеющей более положительный электродный потенциал матрицей.

Ключевые слова: хирургические имплантаты; электрохимическая коррозия; биорезорбируемые материалы; магниевые сплавы; ZX10; WZ31; титановые сплавы; Ti6Al4V; медицинские материалы; скорость коррозии; электродный потенциал.

Благодарности: Исследование выполнено при финансовой поддержке Российского научного фонда, проект № 23-23-10041 (<https://rscf.ru/project/23-23-10041/>), проект № 23-19-00636 (<https://rscf.ru/project/23-19-00636/>).

Для цитирования: Мягких П.Н., Мерсон Е.Д., Полуянов В.А., Мерсон Д.Л., Бегун М.Э. Электрохимическое взаимодействие между биорезорбируемыми магниевыми сплавами ZX10 и WZ31 и медицинским титановым сплавом Ti6Al4V // *Frontier Materials & Technologies*. 2024. № 4. С. 63–71. DOI: 10.18323/2782-4039-2024-4-70-6.

In 2003, at the initiative of D. Merson and A. Vikarchuk and upon the recommendation of the Interstate Coordination Council for Physics of Strength and Plasticity, it was decided, every two years starting from 2004, to hold the “Physical Materials Science” International School (hereinafter – SPhM) hosted by Togliatti State University (TSU) in order to solve the issues of training and rejuvenation of personnel.

The need for the SPhM was justified by the fact that “at present, there is no scientific event where young scientists, employees of factory laboratories, postgraduate students, university professors, and other relevant skill profile employees could attend a course of lectures on the hottest issues of physical materials science and receive a competent advice of leading metal physicists”.

Over the past 20 years, eleven SPhMs have taken place. During this time, dozens of prominent scientists from Russia (E. Kozlov, Yu. Golovin, A. Glezer, V. Betekhtin, R. Andrievsky), Ukraine (Yu. Milman, V. Gavrilyuk, D. Orlov), as well as V. Rubanik (Belarus), A. Vinogradov (Japan), Yu. Estrin (Australia), A. Weidner (Germany) and many others participated in it as visiting lecturers. The audience was more than one thousand specialists, among which at least 50 % are young researchers.

A distinctive feature of the SPhM is that following the results of each of them, based on the lecture materials, a new volume of the “Advanced Materials” educational guidance is published under the general editorship of D. Merson. Consequently, by the beginning of the 11th SPhM in September, 2023, the 10th volume was published, where A. Romanov, A. Kazakov, A. Makarov, M. Vyboyshchik, A. Kudrya, and other well-known scientists are the authors of the chapters.

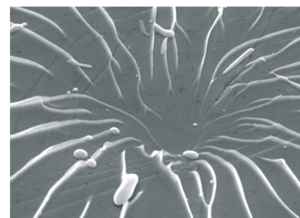
Another feature of the SPhM is the competition of works by young scientists, the winners of which (about 40 people) are granted relief both from the registration fee and from the residence fee. Moreover, each time the employees of the Research Institute of Advanced Technologies of TSU organize master classes for the SPhM participants, demonstrating the possibilities of the unique application of research equipment to solve materials science problems.

The SPhM is also famous for its remarkable performances, which are organized by efforts of its participants, who are talented in all respects.

There is no doubt that the 11th SPhM, as ever, has been held at the highest level and that it will be remembered by its participants for a long time.

Министерство образования Российской Федерации
Научный Совет РАН по физике конденсированных сред
Межгосударственный координационный совет
по физике прочности и пластичности материалов
Тольяттинский государственный университет

I Международная школа
«Физическое
материаловедение»



22–26 ноября 2004 года
Тольятти, Россия

First information message

Intensification of the process of equal channel angular pressing using ultrasonic vibrations

Vasily V. Rubanik^{1,3}, Doctor of Sciences (Engineering), Professor,

Head of the Laboratory of Physics of Metals, Corresponding Member of the National Academy of Sciences of Belarus

Marina S. Lomach^{*1,4}, junior researcher

Vasily V. Rubanik Jr.^{1,5}, Doctor of Sciences (Engineering), Professor, Director

Valery F. Lutsko¹, senior researcher

Sofya V. Gusakova², PhD (Physics and Mathematics),

leading engineer of radiation and vacuum equipment in the Scientific Research Service Sector

¹*Institute of Technical Acoustics of the National Academy of Sciences of Belarus, Vitebsk (Republic of Belarus)*

²*Belarusian State University, Minsk (Republic of Belarus)*

*E-mail: ita@vitebsk.by

³ORCID: <https://orcid.org/0000-0002-0350-1180>

⁴ORCID: <https://orcid.org/0009-0005-9930-1798>

⁵ORCID: <https://orcid.org/0000-0002-9268-0167>

Received 30.06.2023

Revised 09.10.2024

Accepted 28.10.2024

Abstract: The work presents a new method of equal channel angular pressing (ECAP) using powerful ultrasonic vibrations (UV). The authors have developed an original device of ultrasonic ECAP, in which the waveguide with the matrix are made as a single unit, and the waveguide fastening elements are located in the nodal plane of mechanical displacements of the standing wave, the excitation of which occurs directly in the matrix and the blank during pressing. For the first time, it has been proposed to transmit ultrasonic vibrations to the zone of intersection of the matrix channels through which the blank moves, not through the punch, but by exciting vibrations in the matrix itself, i. e. the matrix is simultaneously a waveguide for longitudinal ultrasonic vibrations. This allowed increasing repeatedly the efficiency of ultrasonic action by reducing the friction forces between the surface of the blank and the surface of the matrix channels, as well as by reducing the deformation forces in the zone of intersection of the matrix channels, where a simple shift of the deformed metal occurs. As a result, in comparison with the known methods of ultrasonic ECAP, when the reduction in pressing force is less than 15 %, the excitation of ultrasonic vibrations directly in the waveguide – matrix allowed reducing the pressing force by 1.5–4 times. At the same time, the structure of the pressed materials also changes significantly: the grain size and their crystallographic orientations decrease, the microhardness increases. Changes in the phase composition for all samples produced by ECAP with ultrasonic vibrations, and by conventional technology are not observed.

Keywords: equal channel angular pressing; ECAP; ultrasonic vibrations; UV; bulk nanostructuring; severe plastic deformation; SPD; waveguide; matrix; deformation forces; grain structure; zinc; aluminium.

Acknowledgments: The work was supported by the Belorussian Republican Foundation for Fundamental Research (Project No. T22KITG-011).

The paper was written on the reports of the participants of the XI International School of Physical Materials Science (SPM-2023), Togliatti, September 11–15, 2023.

For citation: Rubanik V.V., Lomach M.S., Rubanik V.V. Jr., Lutsko V.F., Gusakova S.V. Intensification of the process of equal channel angular pressing using ultrasonic vibrations. *Frontier Materials & Technologies*, 2024, no. 4, pp. 73–85. DOI: 10.18323/2782-4039-2024-4-70-7.

INTRODUCTION

The production of bulk nanostructured metallic materials is a relevant and hot topic of modern materials science. Such metals and alloys are attractive for innovative applications, as they have unique properties. At the same time, the structural features of such materials (the proportion of low- and high-angle boundaries, grain size, etc.) are determined by the methods of their production. The two most widely used and studied methods of severe plastic deformation (SPD) are equal channel angular pressing (ECAP), and high-pressure torsion.

ECAP, as a method of severe plastic deformation (SPD) of metallic materials, using which it became possible to produce blanks with a fine-grained structure due to bulk nanostructuring, was proposed by V.M. Segal and coworkers in the 70s of the XX century [1]. Since the early 90s, it has been used for SPD to produce submicron and nanosized metallic structures [2]. Such structures have significantly better mechanical properties optimally combining strength and ductility. In particular, the method is used to obtain submicron crystalline structures of metals such as Pd, Fe, Ni, Co, alloys based on Al, Mg, Ti, Zn, etc.

The SPD method using ECAP involves forcing samples through intersecting at a certain angle channels of a constant cross section matrix. As a result, the samples are subjected to shear deformation in the intersection zone of the channels, which leads to a change in their structure and physical and mechanical properties¹ [3]. Thus, when carrying out the ECAP process, it is possible to accumulate an arbitrarily large shear deformation without changing the dimensions of the blank. In the process of passing through the channels, the total shear characteristics in the metal sample can be changed, due to its rotation between individual passes, i. e., structure formation during deformation directly depends on the ECAP route [4]. By repeated passes of the blank through intersecting channels, it is possible to achieve accumulation of the desired deformation degree, and as a result, the necessary structural changes. In this case, the geometric shape of the sample, with the exception of the areas near its ends, does not change. The ultrafine-grained (UFG) structure of samples with predominantly high-angle grain boundary misorientations obtained by the ECAP method, depends on many parameters: the number of passes, the route, the deformation temperature, the angle of channel intersection, the rounded radius at the intersection of the channels, the speed of the sample passage, the sample material, the type of lubricant [2; 5].

One of the ways to reduce the deformation forces during pressure metal treatment (PMT), is the use of ultrasonic vibrations (UV), for which various devices and schemes for supplying UV to the deformation zone are developed [6; 7]. In this case, the ultrasonic effect during the PMT process leads to a change in the structure, and physical and mechanical properties of materials. Depending on the frequency, UV amplitude, and the locality of the effect, it is possible to achieve both metal strengthening and its softening, plasticisation [6].

Pressure metal treatment with the UV imposition began to be widely used after the discovery of the acousto-plastic effect [8]. The effect consisted in a sharp decrease in the stress of plastic flow of the metal under ultrasonic action. The degree of reduction depends on many factors, primarily on the power of ultrasonic action and the technological parameters of metal forming processes. In particular, the vibrational speed of the ultrasonic tool should be much higher than the deformation rate of the metal [6; 7]. From this point of view, ECAP is an ideal process for intensification using UV, since the pressing speeds are low (except for explosive ECAP), and the friction forces are high, i. e. UV, by reducing friction forces, should affect both the force conditions of the ECAP process, and the properties of the resulting blanks [6; 7]. However, despite the obvious effectiveness of ultrasonic action on ECAP, ultrasonic vibrations have not been used in this process until recently, due to the complexity of introducing them into the deformation

zone. The authors of studied the reduction in the sliding friction force of metals using longitudinal or transverse UV² [9]. The results of their study show that vibrations in the longitudinal or transverse direction can be used to reduce significantly the sliding friction forces between the interacting surfaces. In the works [10; 11] the effect of applying ultrasonic vibrations to a punch, during the ECAP process, was numerically investigated. Calculations showed that a reduction in the deformation force should occur, which depends on the amplitude of vibrations and the speed of movement of the punch.

In fact, the results of experimental studies of ECAP of aluminium alloys with ultrasonic action on the deformed metal through a punch confirmed that the use of ultrasonic vibrations reduces the pressing force by 10 % [11]. At the same time, the amplitude and frequency of ultrasonic vibrations have a significant impact on reducing the pressing force [11–13]. The use of USV in ECAP leads to an increase in the yield strength, tensile strength and hardness of metallic materials [12; 14]. The disadvantage of the proposed method of ultrasonic action on ECAP is its low efficiency [10; 12; 15]. This is associated with the impossibility of introducing significant ultrasonic energy into the deformation zone through the punch, which is an element of the acoustic system – a waveguide for longitudinal ultrasonic vibrations.

The Institute of Technical Acoustics of the National Academy of Sciences of Belarus has developed an original device for ultrasonic ECAP, in which the waveguide with the matrix are made as a single unit with a total length equal to

$$l = n \frac{\lambda}{2},$$

where λ is the length of the longitudinal ultrasonic wave in the matrix-waveguide material;

n is an integer.

The waveguide fastening elements are located in the nodal plane of mechanical displacements of the standing wave, the excitation of which occurs directly in the matrix and the blank during pressing [16].

The purpose of the work is to intensify the equal channel angular pressing process using ultrasonic vibrations, as well as to study their effect on the force characteristics of ECAP of metal materials, and the properties of the produced samples when ultrasonic vibrations are excited in the matrix, i. e. directly in the deformation zone.

METHODS

Zinc with a purity of 99.9 wt. % and A7 aluminium alloy of standard chemical composition (Table 1) were selected as the material.

The initial samples of zinc and A7 aluminium alloy had a length of 20 mm and a diameter of 5 mm. The source of

¹ Shivashankara B.S., Gopi K.R., Pradeep S., Raghavendra Rao R. Investigation of mechanical properties of ECAP processed AL7068 aluminium alloy. *IOP Conference Series: Materials Science and Engineering*, 2021, vol. 1189, article number 012027. DOI: [10.1088/1757-899X/1189/1/012027](https://doi.org/10.1088/1757-899X/1189/1/012027).

² Gudimetla K., Kumar S.R., Ravisankar B., Prathipati R.P., Kumaran S. Consolidation of commercial pure aluminium particles by hot ECAP. *IOP Conference Series: Materials Science and Engineering*, 2018, vol. 330, article number 012031. DOI: [10.1088/1757-899X/330/1/012031](https://doi.org/10.1088/1757-899X/330/1/012031).

Table 1. Chemical composition of the A7 material (GOST 11069-2001), %
Таблица 1. Химический состав материала А7 (ГОСТ 11069-2001), %

Fe	Si	Mn	Ti	Al	Cu	Mg	Zn	Ga	Impurities
≤0.16	≤0.15	≤0.03	≤0.01	min 99.7	≤0.01	≤0.02	≤0.04	≤0.03	Others, 0.02 each

ultrasonic vibrations was an ultrasonic generator with a power of 4.0 kW with a PMS-15A-18 magnetostrictive transducer (Russia). The amplitude of vibrations at the end of the waveguide-matrix was up to 30 μm, the vibration frequency was ~18 kHz. The ECAP process was carried out at a temperature of 20–22 °C using a PGPR hydraulic hand press with a punch travel speed of 4–10 mm/s.

The structure of the samples was examined using a MICRO-200 optical microscope (Republic of Belarus), as well as a LEO1455VP scanning electron microscope (SEM) (Germany). The obtained raster electron microscopic images were adapted to the NEXSYS ImageExpert Pro 3 software environment. The grain structure was studied by the electron backscattered diffraction (EBSD) method, implemented using the HKL EBSD Premium System Channel 5 (UK) phase analysis diffraction attachment to the SEM. To determine the orientation of the grain structure, longitudinal (in the direction of deformation) sections of samples were prepared both in zinc and in the aluminium alloy.

Using a PMT-3M microhardness tester (Russia), the microhardness of zinc and aluminium alloy samples was determined after conventional ECAP and ECAP with ultrasonic vibrations. The microhardness value was determined using the Vickers method by measuring the lengths of

the indentation diagonals, taking into account the load value of 0.196 N. To calculate the microhardness value, the average value of four measurements in each area under consideration was taken.

Graphite lubricant was used when pressing the samples. Zinc and A7 aluminium alloy blanks were forced through a matrix with two channels of equal cross-section with a diameter of 5 mm intersecting at an angle of 90° (Fig. 1).

RESULTS

It was found that the application of ultrasonic vibrations during ECAP of zinc and A7 aluminium alloy leads to a decrease in the pressing force by 1.5 times or more (Fig. 2). Changing the pressing speed within 4–10 mm/s has virtually no effect on the pressing force, and the dynamics of its change is determined by the value of the punch displacement. After one pass of ECAP with the application of USV (Fig. 3 a), the microstructure of zinc differs from the microstructure of zinc obtained with conventional ECAP (Fig. 3 b), and from the microstructure of the initial sample (Fig. 3 c). Grain refinement occurs, and the grains take a more equiaxial shape. The grain refinement process does not depend on changing the pressing speed in the studied speed range.

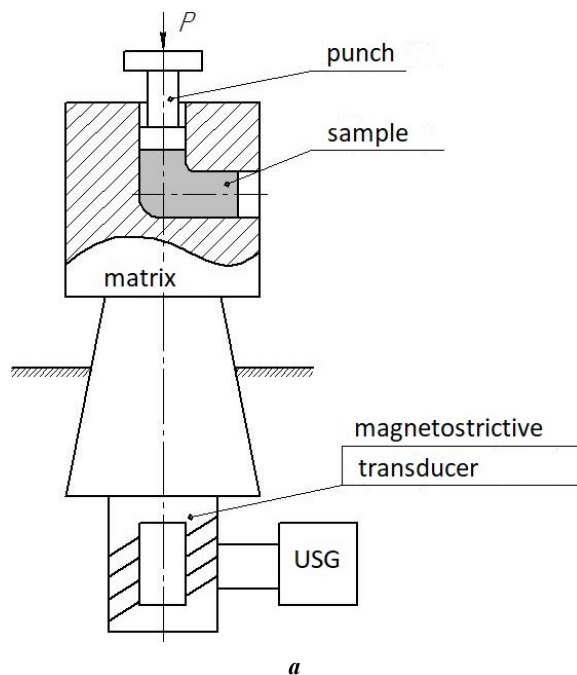


Fig. 1. Schematic (a) and external appearance (b) of the acoustic unit of the ultrasonic assisted ECAP device
Рис. 1. Схема (a) и внешний вид (b) акустического узла устройства ультразвукового РКУП

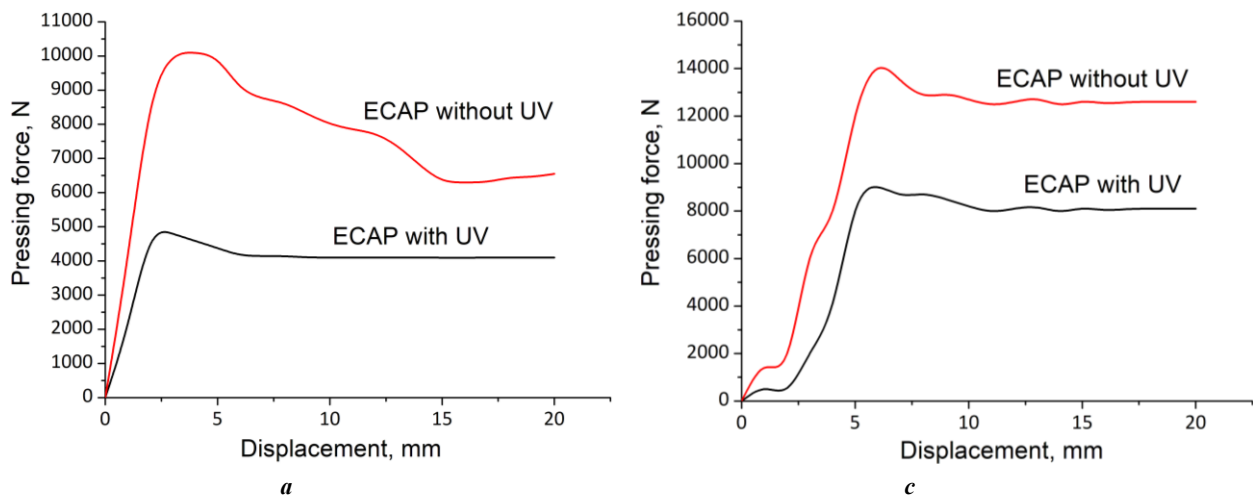


Fig. 2. Dependence of the pressing force of zinc on the displacement of the punch (a) and A7 aluminium alloy (b)
Рис. 2. Зависимость усилия прессования цинка от перемещения пуансона (a) и алюминиевого сплава А7 (b)

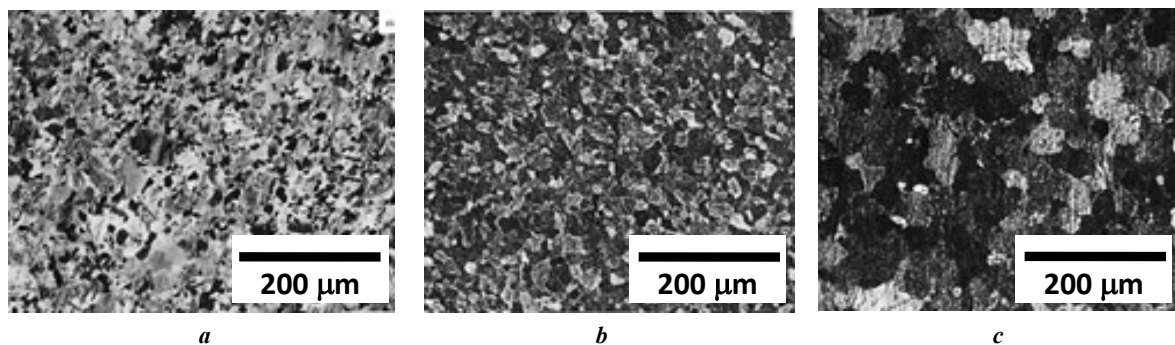


Fig. 3. Microstructure of zinc: a – initial; b – after 1 pass of ECAP without UV; c – after 1 pass of ECAP with UV
Рис. 3. Микроструктура цинка: a – исходного; b – после 1 прохода РКУП без УЗК; c – после 1 прохода РКУП с УЗК

The results of the study of the analysis of the grain structure of zinc are shown in Figs. 4–7. In the initial alloy, the average grain size is 10.6 μm. However, according to the data of the grain size distribution by size groups (Fig. 6 a), there is a large scatter of grain sizes. Comparison of the SEM images of the microstructure and the EBSD results allows stating that the volume fraction of large grains with a size exceeding 20 μm is high. At the same time, a high density of low-angle grain boundaries is observed in large grains, as shown in the grain misorientation histogram (Fig. 5 a).

After deformation during the ECAP process, the average grain size decreases to 3.6 μm (Fig. 6 b). Analysis of the grain structure shows that small grains are formed at the boundaries of large grains (Fig. 4 b). The proportion of low-angle boundaries in the grain decreases by 2 times (Fig. 5 b). This allows assuming that during one ECAP pass, deformation is carried out due to the movement of low-angle boundaries to the grain boundary. Since zinc has a pronounced anisotropy of the crystal lattice and, accordingly, mechanical properties, such a mechanism can occur for grains with a favourable orientation.

In the samples subjected to ECAP with the imposition of ultrasonic vibrations, a decrease in the average grain size

to 2.9 μm was revealed (Fig. 7). At the same time, a narrowing of the grain size distribution by size groups and a low concentration of low-angle grain boundaries are observed, as shown in Fig. 4 c and 5 c, respectively. The obtained result allows asserting that during deformation under the influence of ultrasound, the movement of dislocations is activated both in favourably oriented grains, and in the entire volume of the sample. From the analysis of the grain misorientation histograms, it is evident that in the sample of zinc subjected to one ECAP pass without ultrasonic vibrations, and with ultrasonic vibrations, the share of low-angle boundaries has an advantage (Fig. 5).

The zinc texture was studied by the EBSD method after ECAP without UV (Fig. 8 a) and ECAP with UV (Fig. 8 b). Fig. 8 shows the direct pole figures of the projections of the planes {0001}, {10–1–2}, {10–11} onto the OX-OY plane of the sample. The projection of the normal to the surface is located in the centre of the circle (Fig. 8). The maximum density of projections located near the centre of the circle in both cases falls on the reflection from the plane (0001).

The average microhardness value for zinc samples obtained by ECAP with UV was ~30.6 HV, for samples without UV – ~26.9 HV. At the same time, for all zinc samples,

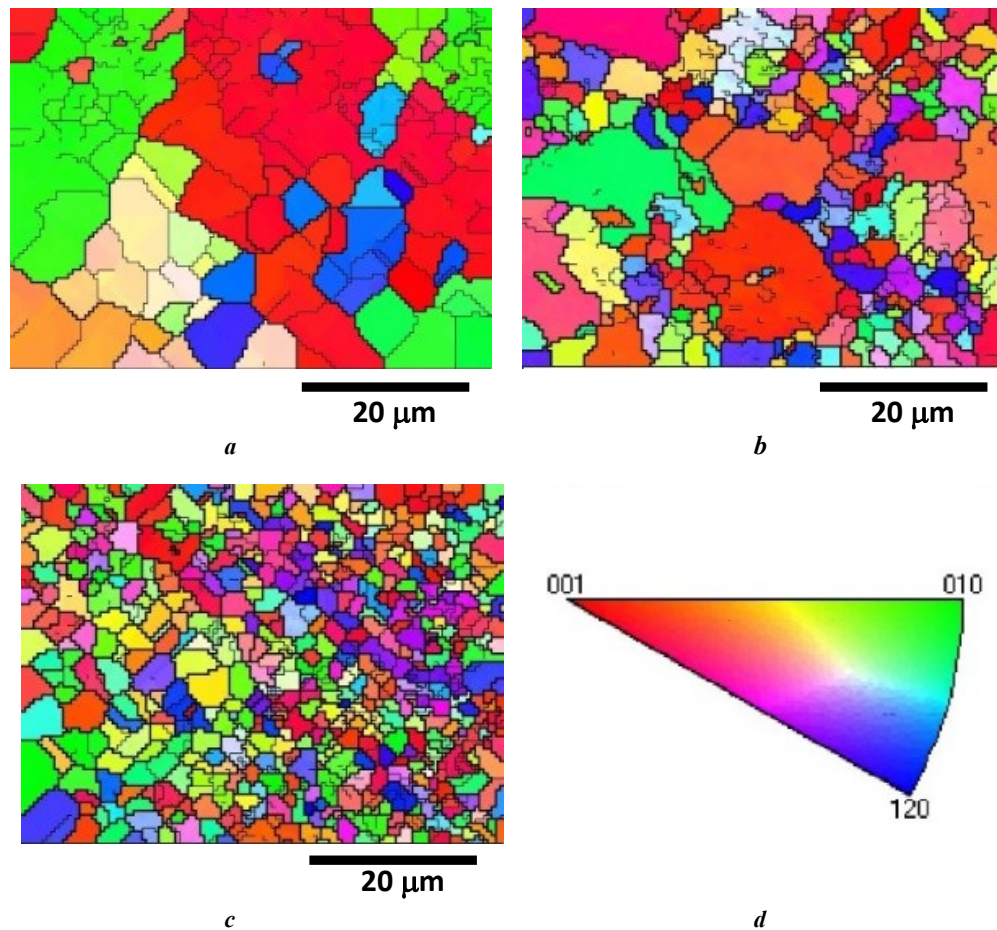


Fig. 4. Grain structure of zinc: **a** – initial; **b** – after 1 pass of ECAP without UV; **c** – after 1 pass of ECAP with UV; **d** – colour code. Bold black lines highlight grain boundaries with a misorientation greater than 10° , thin black lines highlight low-angle boundaries with a misorientation greater than 2° and less than 10°

Рис. 4. Зеренная структура цинка: **a** – исходного; **b** – после 1 прохода РКУП без УЗК; **c** – после 1 прохода РКУП с УЗК; **d** – цветовой код. Жирными черными линиями выделены границы зерен с разориентацией больше 10° , тонкими черными линиями – малозуловые границы с разориентацией больше 2 и меньше 10°

a slight increase in microhardness is observed from the centre to the edges in the cross section.

As for the A7 aluminium alloy, the average grain size in the initial sample was $\sim 16 \mu\text{m}$ (Fig. 9 a, 10 a). The application of ultrasonic vibrations during ECAP changed both the grain size and shape (Fig. 9 b, 9 c). From the analysis of the grain size distribution histograms, it follows that ECAP results in grain fragmentation. The average grain size in the A7 aluminium alloy sample, after one ECAP pass without ultrasonic vibrations was $6.0 \mu\text{m}$ (Fig. 10 b), while with ultrasonic vibrations it was $3.5 \mu\text{m}$ (Fig. 11).

In the A7 aluminium alloy samples subjected to one ECAP pass without ultrasonic vibrations, an increase in the proportion of high-angle boundaries, and a two-fold decrease in the proportion of low-angle boundaries was found. The application of ultrasound resulted in a four-fold decrease in the proportion of low-angle boundaries compared to the initial alloy (Fig. 12).

Fig. 13 shows the results of the study of the texture of the aluminium samples. It was found that the initial sample had a pronounced (101) texture. After one ECAP pass without ultrasound, the proportion of grains oriented by

the (101) plane decreases by 24 times. After exposure to ultrasound, the preferred orientation of the grains disappears.

The average microhardness value for A7 samples obtained by ECAP with ultrasonic vibrations was $\sim 23.4 \text{ HV}$, for samples without ultrasonic vibrations – $\sim 19.1 \text{ HV}$. A slight increase in microhardness from the centre to the edges in the cross section is also observed.

DISCUSSION

The results obtained in this work showed that the use of ultrasonic vibrations in the ECAP process reduces the friction forces between the sample and the matrix, and therefore the pressing force of metal materials, changes the structure and physical and mechanical properties of the deformed metal.

A similar result was previously obtained for AA-1050 industrial aluminium³. However, in the device described

³ Donič T., Martikán M., Hadzima B. New unique ECAP system with ultrasound and backpressure. IOP Conference Series: Materials Science and Engineering, 2014, vol. 63, article number 012047. DOI: [10.1088/1757-899X/63/1/012047](https://doi.org/10.1088/1757-899X/63/1/012047).

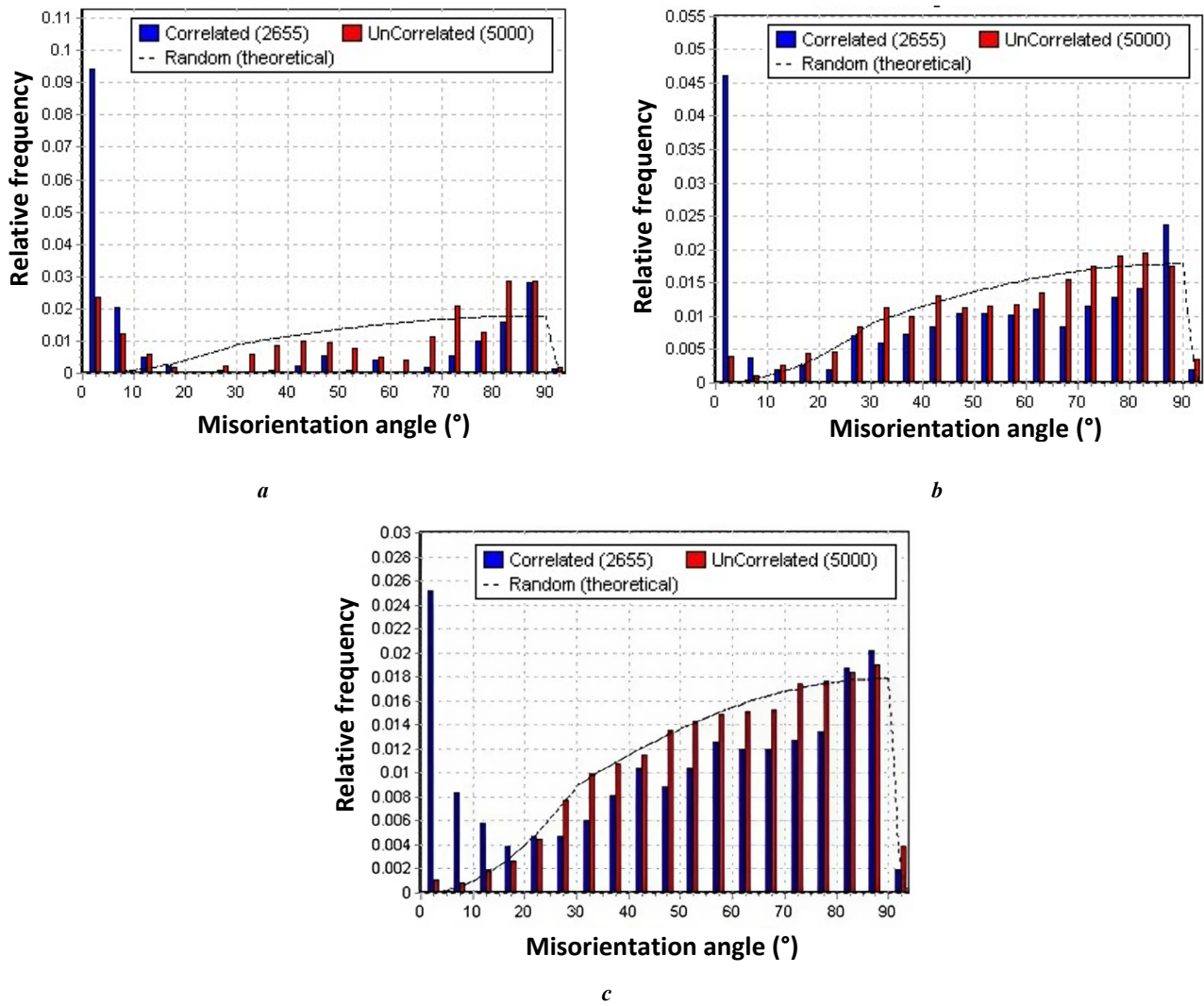


Fig. 5. Histograms of grain misorientation of zinc:
a – initial; *b* – after 1 pass of ECAP without UV; *c* – after 1 pass of ECAP with UV

Рис. 5. Гистограммы разориентации зерен цинка:
a – исходного; *b* – после 1 прохода РКУП без УЗК; *c* – после 1 прохода РКУП с УЗК

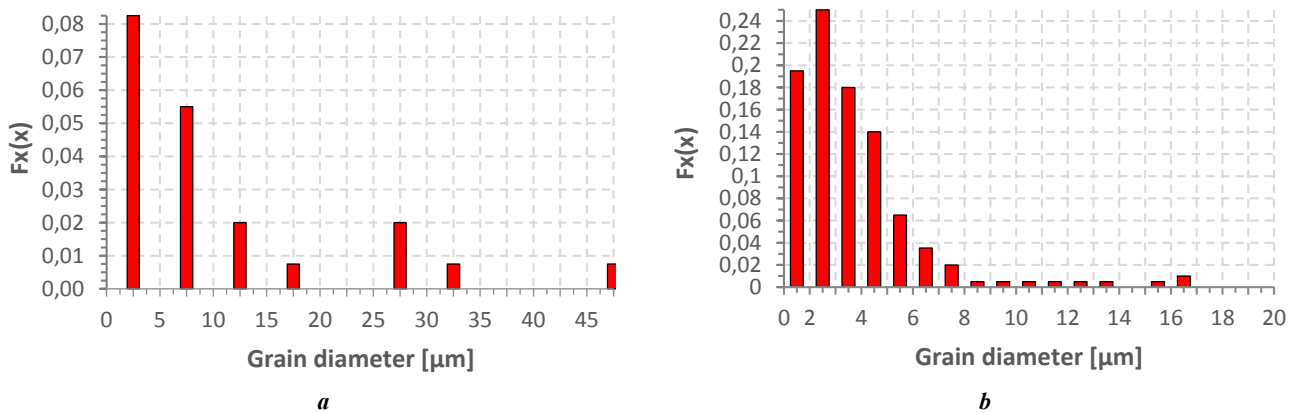


Fig. 6. Histograms of grain sizes of zinc:
a – initial; *b* – after 1 pass of ECAP without UV

Рис. 6. Гистограммы размеров зерен цинка:
a – исходного; *b* – после 1 прохода РКУП без УЗК

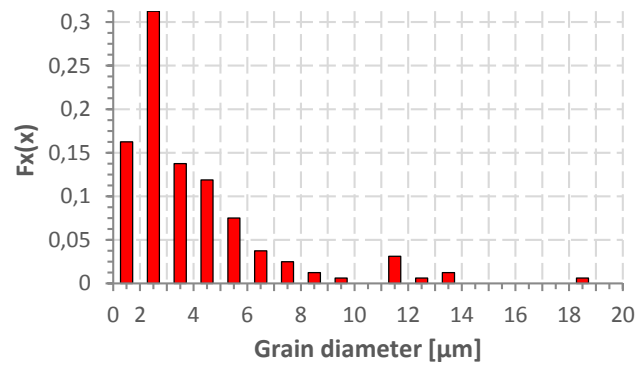


Fig. 7. Histograms of grain sizes of zinc after 1 pass of ECAP with UV
Рис. 7. Гистограммы размеров зерен цинка после 1 прохода РКВИ с УЗК

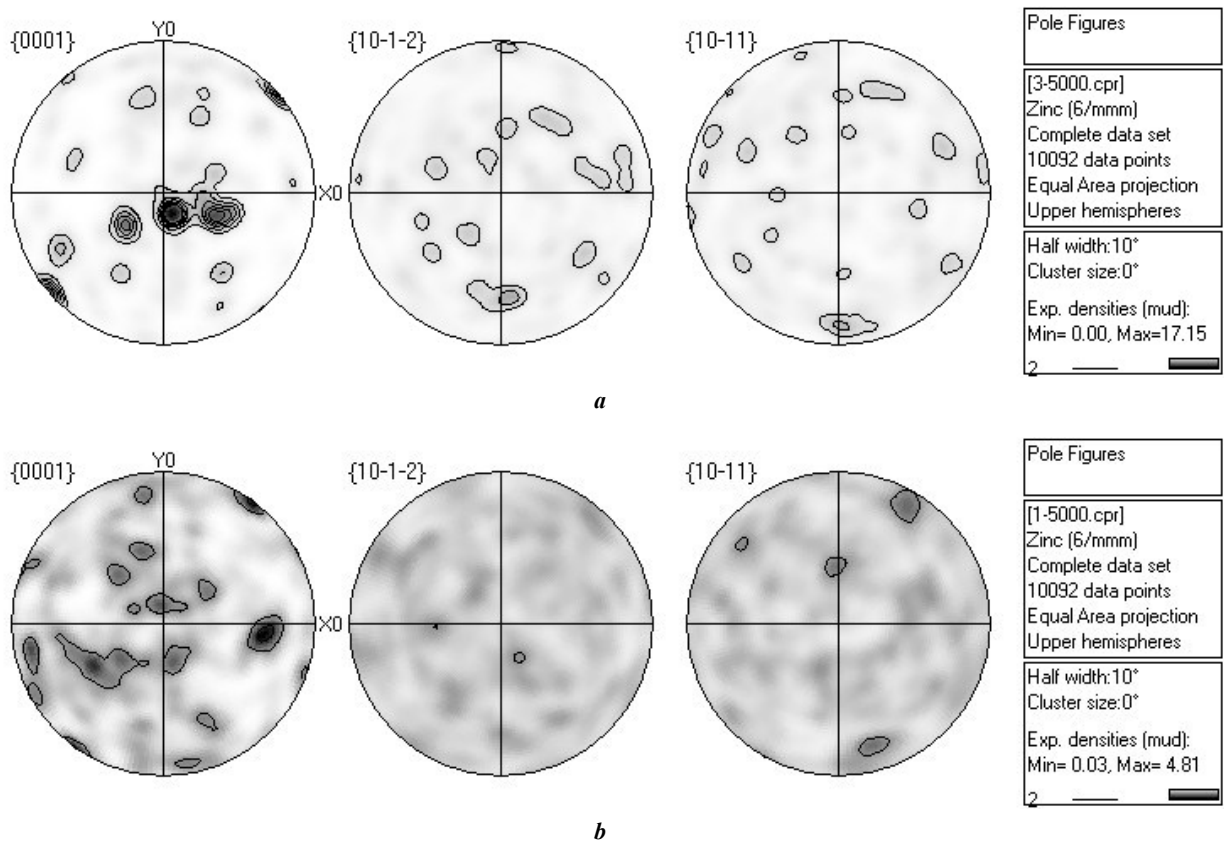


Fig. 8. Direct pole figures of zinc: **a** – after 1 pass of ECAP without UV; **b** – after 1 pass of ECAP with UV

Рис. 8. Прямые полюсные фигуры цинка:
a – после 1 прохода РКВИ без УЗК; **b** – после 1 прохода РКВИ с УЗК

in [12; 14; 17], the UV energy was used inefficiently. When the UV source, which was a magnetostrictive transducer with a vibration amplitude of 12 μm, and a frequency of 20 kHz, makes contact with the moving part of the deformation unit (punch), the mass and geometric size of the vibrating system of the device change. As a result, the vibrating system goes out of resonance, the amplitude of the punch vibrations decreases sharply. As a result, the achieved reduction in the deformation force was less than 15 %.

The results of the studies described in [11] also confirmed that the use of UV reduces the pressing force, but only by 10 %: 162.5 kN and 147.7 kN for conventional ECAP, and ECAP using UV, respectively. The main reason for this decrease is associated with a decrease in the contact friction force between the sample and the matrix.

In our studies, the UV effect on the sample was carried out not through the movable part of the deformation unit (punch), but through the matrix [16], i. e., the excitation of a standing ultrasonic wave occurred directly in the matrix,

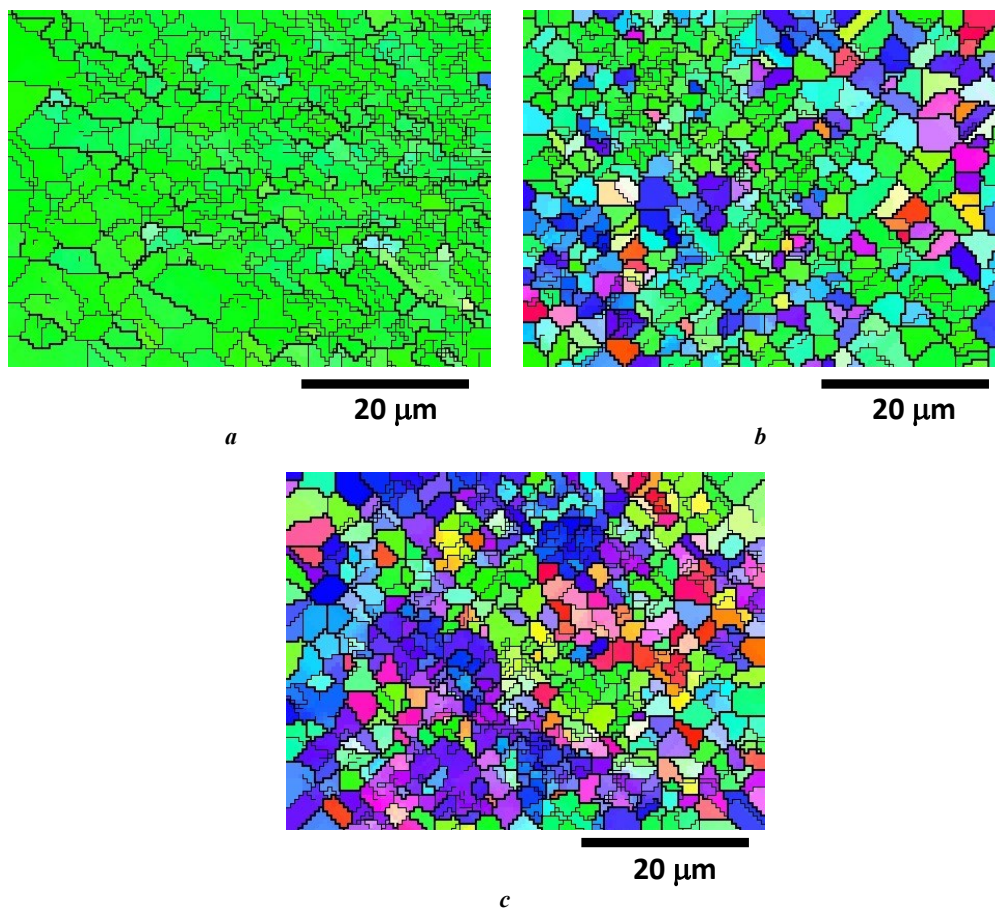


Fig. 9. Grain structure of the A7 aluminium alloy: **a** – initial; **b** – after 1 pass of ECAP without UV; **c** – after 1 pass of ECAP with UV
Рис. 9. Зеренная структура алюминиевого сплава А7: **a** – исходного; **b** – после 1 прохода РКУП без УЗК; **c** – после 1 прохода РКУП с УЗК

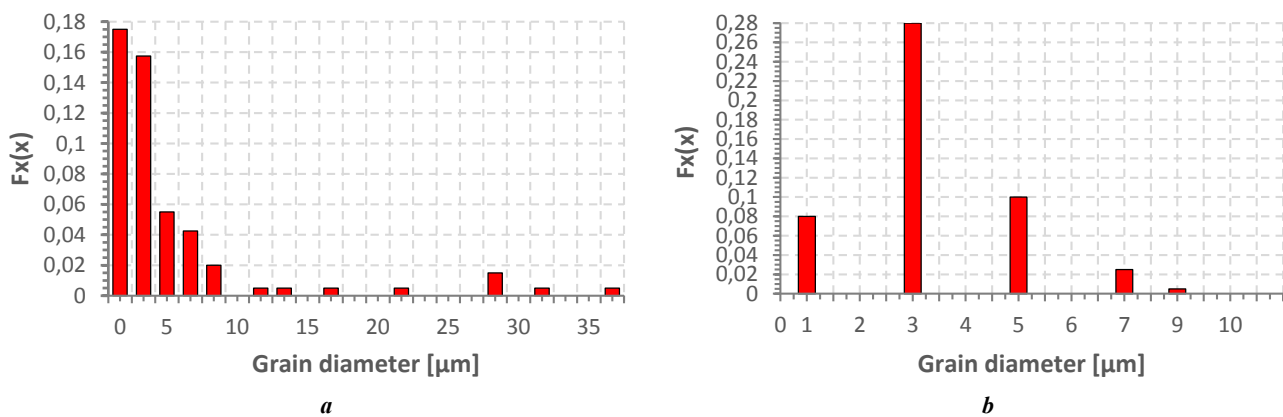


Fig. 10. Histograms of grain sizes of the A7 aluminium alloy: **a** – initial; **b** – after 1 pass of ECAP without UV
Рис. 10. Гистограммы размеров зерен алюминиевого сплава А7: **a** – исходного; **b** – после 1 прохода РКУП без УЗК

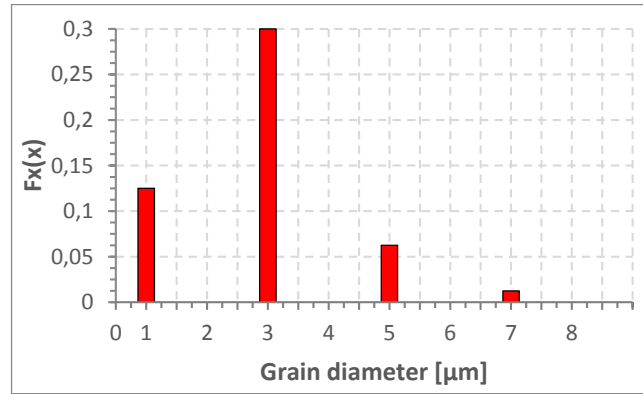


Fig. 11. Histograms of grain sizes of the A7 aluminium alloy after 1 pass of ECAP with UV
Рис. 11. Гистограммы размеров зерен алюминиевого сплава А7 после 1 прохода РКУП с УЗК

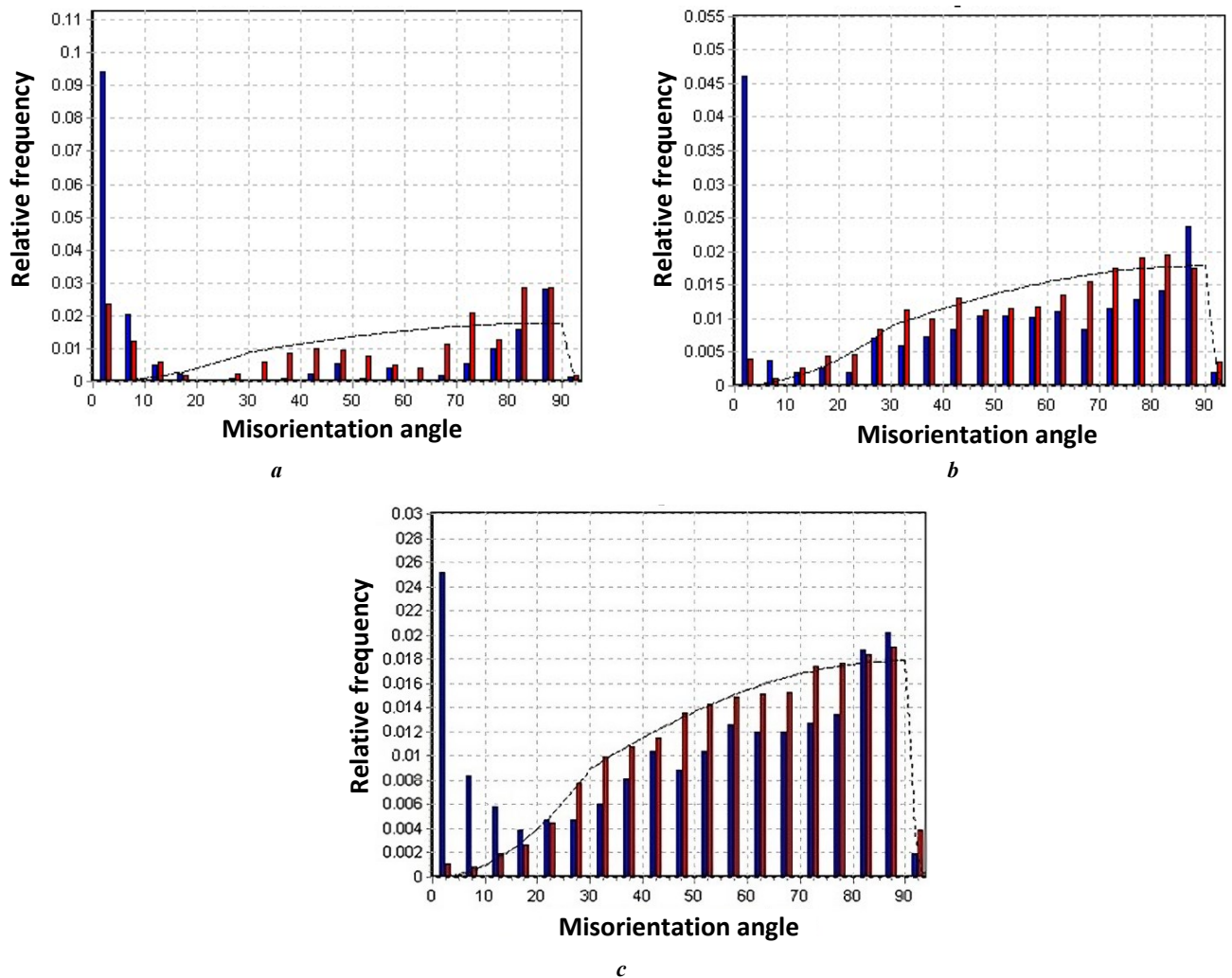


Fig. 12. Histograms of grain misorientation of the A7 aluminium alloy:
a – initial; *b* – after 1 pass of ECAP without UV; *c* – after 1 pass of ECAP with UV
Рис. 12. Гистограммы разориентации зерен алюминиевого сплава А7:
a – исходного; *b* – после 1 прохода РКУП без УЗК; *c* – после 1 прохода РКУП с УЗК

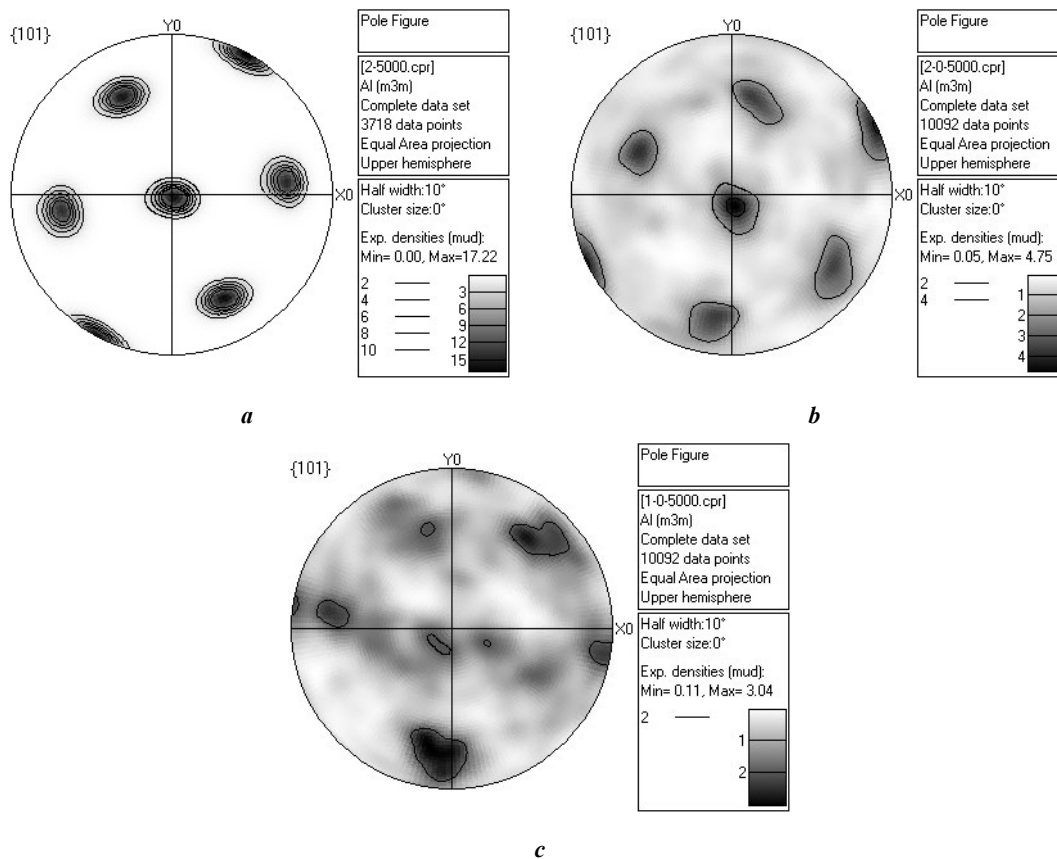


Fig. 13. Direct pole figures of the A7 aluminium alloy: *a* – initial; *b* – after 1 pass of ECAP without UV; *c* – after 1 pass of ECAP with UV
Рис. 13. Прямые полюсные фигуры алюминиевого сплава А7: *a* – исходного; *b* – после 1 прохода РКУП без УЗК; *c* – после 1 прохода РКУП с УЗК

and the blank during ECAP. The use of a waveguide with a matrix made as a single whole (waveguide-matrix) ensured the exclusion of the transition region between them as such. The UV energy is supplied directly to the processing zone without losses at the waveguide-matrix interface. The absence of this boundary also provides a significant increase in the service life of the device as a whole. At the same time, the deformation force is significantly reduced both by reducing the friction forces between the punch surface, and the waveguide-matrix channels, and by reducing the forces of metal deformation shear in the channel intersection zone. The degree of refinement of the blank structure increases, and the sinks of dislocations of the blank are facilitated. As for the grain misorientation of both zinc and A7 aluminium alloy, the proportion of low-angle boundaries has an advantage (Fig. 5 and 12). This is associated with the increase in the deformation degree. It is difficult to achieve a homogeneous equiaxial structure with a high content of high-angle grain boundaries in one ECAP pass, with and without ultrasonic vibrations. In the future, it is necessary to carry out ECAP with a large number of passes both with and without ultrasonic vibrations.

This work aimed at improving the ECAP technology as one of the SPD methods is relevant. The use of ultrasonic vibrations in ECAP fundamentally changes the properties of metals and alloys when forming UFG structures in them,

which will make it possible to implement largely a combination of high strength and ductility. Research into the unusual combination of strength and ductility of nanostructured materials is of great fundamental and practical importance. From a fundamental point of view, these studies are of interest for investigating new deformation mechanisms. From a practical point of view, the creation of nanomaterials with high strength and ductility can sharply increase their fatigue strength, impact toughness, and reduce the brittle-viscous transition temperature, which will increase the service life, and consequently, the scope of application of many promising materials.

CONCLUSIONS

An original ECAP device, where the waveguide with the matrix are made as a single unit, has been developed.

For the first time, the ECAP method has been applied to metal materials such as zinc and A7 aluminium alloy, with longitudinal ultrasonic vibrations applied directly to the deformation zone by exciting them in the matrix-waveguide.

It has been found that the application of ultrasonic vibrations during ECAP of zinc and A7 aluminium alloy, leads to a decrease in the pressing force by 1.5 times or more due to the excitation of vibrations in the matrix itself, which served as a waveguide for longitudinal ultrasonic vibrations.

Changing the pressing speed within 4–10 mm/s has virtually no effect on the pressing force.

The effect of ultrasonic vibrations on the ECAP process is also an effective way to change the structure of metal materials. Thus, after one pass, the microstructure of the material obtained by pressing with the application of ultrasonic vibrations differs significantly from the microstructure of samples obtained without ultrasonic vibrations: a decrease in the grain size, and a change in their crystallographic orientation, an increase in the mechanical properties of the deformed metal, and an increase in microhardness are observed.

Therefore, one can argue that ultrasonic exposure in the ECAP process allows changing significantly the force characteristics of the process, and the properties of metallic materials.

REFERENCES

- Segal V.M., Reznikov V.I., Kopylov V.I. *Protsessy plasticheskogo strukturoobrazovaniya metallov* [Processes of plastic structure formation of metals]. Minsk, Nauka i tekhnika Publ., 1994. 231 p.
- Valiev R.Z., Aleksandrov I.V. *Obemnye nanostrukturnye materialy: poluchenie, struktura i svoystva* [Bulk nanostructured materials: preparation, structure and properties]. Moscow, Akademkniga Publ., 2007. 397 p.
- Khelfa T., Lachhab R., Azzeddine H., Chen Z., Muñoz J.A., Cabrera-Marrero J.M., Brisset F., Helbert A.-L., Baudin T., Khitouni M. Effect of ECAP and subsequent annealing on microstructure, texture, and microhardness of an AA6060 aluminum alloy. *Journal of Materials Engineering and Performance*, 2022, vol. 31, no. 4, pp. 2606–2623. DOI: [10.1007/s11665-021-06404-w](https://doi.org/10.1007/s11665-021-06404-w).
- Puspasari V., Astava I.N.G.P., Kherbairovo S., Maburri E. Mechanical properties and microstructure of Al–Mg (5052) alloy processed by equal-channel angular pressing (ECAP) with variation of ECAP routes and heat treatment. *Izvestiya vysshikh uchebnykh zavedeniy. Chernaya metallurgiya*, 2024, vol. 67, no. 1, pp. 37–46. DOI: [10.17073/0368-0797-2024-1-37-46](https://doi.org/10.17073/0368-0797-2024-1-37-46).
- Agarwal K.M., Tyagi R.K., Choubey V., Saxena K.K. Mechanical behaviour of Aluminium Alloy AA6063 processed through ECAP with optimum die design parameters. *Advances in Materials and Processing Technologies*, 2022, vol. 2, pp. 1901–1915. DOI: [10.1080/2374068X.2021.1878705](https://doi.org/10.1080/2374068X.2021.1878705).
- Severdenko V.P., Klubovich V.V., Stepanenko A.V. *Ul'trazvuk i plastichnost* [Ultrasound and plasticity]. Minsk, Nauka i tekhnika Publ., 1976. 446 p.
- Klubovich V.V., Rubanik V.V., Tsarenko Yu.V. *Ul'trazvuk v tekhnologii proizvodstva kompozitsionnykh kabeley* [Ultrasonic processing of materials]. Minsk, Belaruskaya navuka Publ., 2012. 294 p.
- Langenecker B. Effects of ultrasound on deformation characteristics of metals. *IEEE Transactions on Sonics and Ultrasonics*, 1966, vol. 13, no. 1, pp. 1–8. DOI: [10.1109/T-SU.1966.29367](https://doi.org/10.1109/T-SU.1966.29367).
- Kumar V.C., Hutchings I.M. Reduction of the sliding friction of metals by the application of longitudinal or transverse ultrasonic vibration. *Tribology International*, 2004, vol. 37, no. 10, pp. 833–840. DOI: [10.1016/j.triboint.2004.05.003](https://doi.org/10.1016/j.triboint.2004.05.003).
- Ahmadi F., Farzin M. Finite element analysis of ultrasonic-assisted equal channel angular pressing. *Proceedings of the Institution of Mechanical Engineers, Part C: Journal of Mechanical Engineering Science*, 2013, vol. 16, pp. 249–255. DOI: [10.1177/0954406213514961](https://doi.org/10.1177/0954406213514961).
- Djavanroodi F., Ahmadian H., Naseri R., Koohkan K., Ebrahimi M. Experimental investigation of ultrasonic assisted equal channel angular pressing process. *Archives of Civil and Mechanical Engineering*, 2016, vol. 16, no. 3, pp. 249–255. DOI: [10.1016/j.acme.2015.10.001](https://doi.org/10.1016/j.acme.2015.10.001).
- Shao Guangda, Li Hongwei, Zhan Mei. A review on ultrasonic-assisted forming: mechanism, model, and process. *Chinese Journal of Mechanical Engineering*, 2021, vol. 34, article number 99. DOI: [10.1186/s10033-021-00612-0](https://doi.org/10.1186/s10033-021-00612-0).
- Bagherzadeh S., Abrinia K., Han Qingyou. Analysis of plastic deformation behavior of ultrafine-grained aluminum processed by the newly developed ultrasonic vibration enhanced ECAP: Simulation and experiments. *Journal of Manufacturing Processes*, 2020, vol. 50, pp. 485–497. DOI: [10.1016/j.jmapro.2020.01.010](https://doi.org/10.1016/j.jmapro.2020.01.010).
- Wu Bo, Lu Jianxun, Wu Zhaozhi, Wu Xiaoyu, Lou Yan, Ruan Shuangchen. Mechanical Properties and Microstructure of AZ31 Magnesium Alloy Processed by Intermittent Ultrasonic-Assisted Equal Channel Angular Pressing. *Journal of Materials Engineering and Performance*, 2021, vol. 30, no. 1, pp. 346–356. DOI: [10.1007/s11665-020-05389-2](https://doi.org/10.1007/s11665-020-05389-2).
- Ahmadi F., Farzin M., Meratian M., Loeian S.M., Forouzan M.R. Improvement of ECAP process by imposing ultrasonic vibrations. *International Journal of Advanced Manufacturing Technology*, 2015, vol. 79, pp. 503–512. DOI: [10.1007/s00170-015-6848-1](https://doi.org/10.1007/s00170-015-6848-1).
- Rubanik V.V., Rubanik V.V., Lomach M.S., Lutsko V.F. *Press dlya ravnokanalnogo uglovogo pressovaniya* [Press for equal-channel angular pressing], opisaniye k poleznoy modeli k patentu Respubliki Belarus no. BY 13457, 2024, 6 p.
- Eskandarzade M., Masoumi A., Faraji G. Numerical and analytical investigation of an ultrasonic assisted ECAP process. *Journal of Theoretical and Applied Vibration and Acoustics*, 2016, vol. 2, no. 2, pp. 167–184. DOI: [10.22064/TAVA.2016.22472](https://doi.org/10.22064/TAVA.2016.22472).

СПИСОК ЛИТЕРАТУРЫ

- Сегал В.М., Резников В.И., Копылов В.И. Процессы пластического структурообразования металлов. Минск: Наука и техника, 1994. 231 с.
- Валиев Р.З., Александров И.В. Объемные наноструктурные материалы: получение, структура и свойства. М.: Академкнига, 2007. 397 с.
- Khelfa T., Lachhab R., Azzeddine H., Chen Z., Muñoz J.A., Cabrera-Marrero J.M., Brisset F., Helbert A.-L., Baudin T., Khitouni M. Effect of ECAP and subsequent annealing on microstructure, texture, and microhardness of an AA6060 aluminum alloy // *Journal of Materials Engineering and Performance*. 2022. Vol. 31. № 4. P. 2606–2623. DOI: [10.1007/s11665-021-06404-w](https://doi.org/10.1007/s11665-021-06404-w).

4. Пуспасари В., Астава И.Н.Г.П., Хербирово С., Мабрури Э. Механические свойства и микроструктура сплава Al–Mg (5052), обработанного методом равноканального углового прессования (РКУП) с вариациями методов РКУП и термической обработки // Известия высших учебных заведений. Черная металлургия. 2024. Т. 67. № 1. С. 37–46. DOI: [10.17073/0368-0797-2024-1-37-46](https://doi.org/10.17073/0368-0797-2024-1-37-46).
5. Agarwal K.M., Tyagi R.K., Choubey V., Saxena K.K. Mechanical behaviour of Aluminium Alloy AA6063 processed through ECAP with optimum die design parameters // Advances in Materials and Processing Technologies. 2022. Vol. 2. P. 1901–1915. DOI: [10.1080/2374068X.2021.1878705](https://doi.org/10.1080/2374068X.2021.1878705).
6. Северденко В.П., Клубович В.В., Степаненко А.В. Ультразвук и пластичность. Минск: Наука и техника, 1976. 446 с.
7. Клубович В.В., Рубаник В.В., Царенко Ю.В. Ультразвук в технологии производства композиционных кабелей. Минск: Беларуская навука, 2012. 294 с.
8. Langenecker V. Effects of ultrasound on deformation characteristics of metals // IEEE Transactions on Sonics and Ultrasonics. 1966. Vol. 13. № 1. P. 1–8. DOI: [10.1109/T-SU.1966.29367](https://doi.org/10.1109/T-SU.1966.29367).
9. Kumar V.C., Hutchings I.M. Reduction of the sliding friction of metals by the application of longitudinal or transverse ultrasonic vibration // Tribology International. 2004. Vol. 37. № 10. P. 833–840. DOI: [10.1016/j.triboint.2004.05.003](https://doi.org/10.1016/j.triboint.2004.05.003).
10. Ahmadi F., Farzin M. Finite element analysis of ultrasonic-assisted equal channel angular pressing // Proceedings of the Institution of Mechanical Engineers, Part C: Journal of Mechanical Engineering Science. 2013. Vol. 16. P. 249–255. DOI: [10.1177/0954406213514961](https://doi.org/10.1177/0954406213514961).
11. Djavanroodi F., Ahmadian H., Naseri R., Koohkan K., Ebrahimi M. Experimental investigation of ultrasonic assisted equal channel angular pressing process // Archives of Civil and Mechanical Engineering. 2016. Vol. 16. № 3. P. 249–255. DOI: [10.1016/j.acme.2015.10.001](https://doi.org/10.1016/j.acme.2015.10.001).
12. Shao Guangda, Li Hongwei, Zhan Mei. A review on ultrasonic-assisted forming: mechanism, model, and process // Chinese Journal of Mechanical Engineering. 2021. Vol. 34. Article number 99. DOI: [10.1186/s10033-021-00612-0](https://doi.org/10.1186/s10033-021-00612-0).
13. Bagherzadeh S., Abrinia K., Han Qingyou. Analysis of plastic deformation behavior of ultrafine-grained aluminum processed by the newly developed ultrasonic vibration enhanced ECAP: Simulation and experiments // Journal of Manufacturing Processes. 2020. Vol. 50. P. 485–497. DOI: [10.1016/j.jmapro.2020.01.010](https://doi.org/10.1016/j.jmapro.2020.01.010).
14. Wu Bo, Lu Jianxun, Wu Zhaozhi, Wu Xiaoyu, Lou Yan, Ruan Shuangchen. Mechanical Properties and Microstructure of AZ31 Magnesium Alloy Processed by Intermittent Ultrasonic-Assisted Equal Channel Angular Pressing // Journal of Materials Engineering and Performance. 2021. Vol. 30. № 1. P. 346–356. DOI: [10.1007/s11665-020-05389-2](https://doi.org/10.1007/s11665-020-05389-2).
15. Ahmadi F., Farzin M., Meratian M., Loeian S.M., Forouzan M.R. Improvement of ECAP process by imposing ultrasonic vibrations // International Journal of Advanced Manufacturing Technology. 2015. Vol. 79. P. 503–512. DOI: [10.1007/s00170-015-6848-1](https://doi.org/10.1007/s00170-015-6848-1).
16. Рубаник В.В., Рубаник В.В., Ломач М.С., Луцко В.Ф. Пресс для равноканального углового прессования: описание к полезной модели к патенту Республики Беларусь № BY 13457, 2024. 6 с.
17. Eskandarzade M., Masoumi A., Faraji G. Numerical and analytical investigation of an ultrasonic assisted ECAP process // Journal of Theoretical and Applied Vibration and Acoustics. 2016. Vol. 2. № 2. P. 167–184. DOI: [10.22064/TAVA.2016.22472](https://doi.org/10.22064/TAVA.2016.22472).

Интенсификация процесса равноканального углового прессования с помощью ультразвуковых колебаний

Рубаник Василий Васильевич^{1,3}, доктор технических наук, профессор, заведующий лабораторией физики металлов, член-корреспондент Национальной академии наук Беларуси

Ломач Марина Сергеевна^{*1,4}, младший научный сотрудник

Рубаник Василий Васильевич мл.^{1,5}, доктор технических наук, профессор, директор

*Луцко Валерий Федорович*¹, старший научный сотрудник

*Гусакова Софья Викторовна*², кандидат физико-математических наук,

ведущий инженер радиационной и вакуумной аппаратуры сектора обслуживания научных исследований

¹Институт технической акустики Национальной академии наук Беларуси, Витебск (Республика Беларусь)

²Белорусский государственный университет, Минск (Республика Беларусь)

*E-mail: ita@vitebsk.by

³ORCID: <https://orcid.org/0000-0002-0350-1180>

⁴ORCID: <https://orcid.org/0009-0005-9930-1798>

⁵ORCID: <https://orcid.org/0000-0002-9268-0167>

Поступила в редакцию 30.06.2023

Пересмотрена 09.10.2024

Принята к публикации 28.10.2024

Аннотация: Представлен новый способ равноканального углового прессования (РКУП) с использованием мощных ультразвуковых колебаний (УЗК). Разработано оригинальное устройство ультразвукового РКУП, в котором волновод с матрицей выполнены как единое целое, а элементы крепления волновода расположены в узловой плоскости механических смещений стоячей волны, возбуждение которой происходит непосредственно в матрице

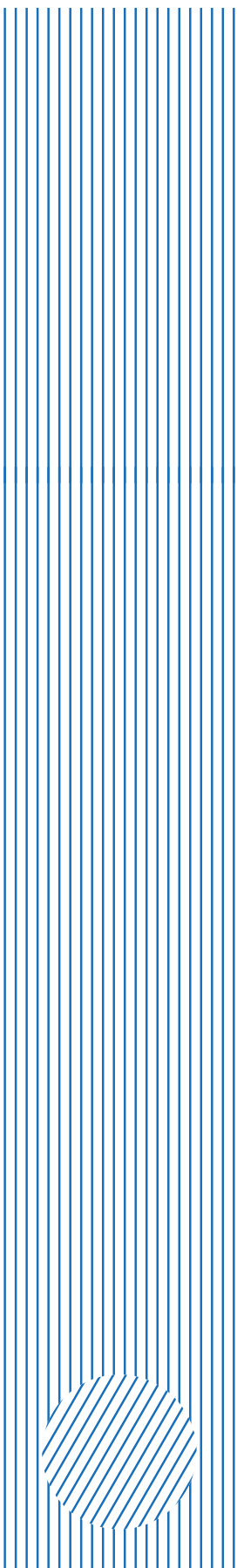
и заготовке в процессе прессования. Впервые предложено передавать УЗК в зону пересечения каналов матрицы, через которые перемещается заготовка, не через пуансон, а посредством возбуждения колебаний в самой матрице, т. е. матрица одновременно является волноводом продольных УЗК. Это позволило многократно повысить эффективность ультразвукового воздействия за счет снижения сил трения между поверхностью заготовки и поверхностью каналов матрицы, а также за счет снижения деформационных усилий в зоне пересечения каналов матрицы, где происходит простой сдвиг деформируемого металла. В результате по сравнению с известными способами ультразвукового РКУП, в которых снижение усилия прессования составляет менее 15 %, возбуждение УЗК непосредственно в волноводе-матрице позволило снизить усилие прессования в 1,5–4 раза. При этом существенно меняется и структура прессуемых материалов: уменьшается размер зерен и их кристаллографические ориентировки, увеличивается микротвердость. Изменения фазового состава для всех образцов, полученных РКУП с УЗК и по обычной технологии, не наблюдается.

Ключевые слова: равноканальное угловое прессование; РКУП; ультразвуковые колебания; УЗК; объемное наноструктурирование; интенсивная пластическая деформация; ИПД; волновод; матрица; деформационные усилия; зеренная структура; цинк; алюминий.

Благодарности: Работа выполнена при поддержке Белорусского республиканского фонда фундаментальных исследований (проект № T22КИТГ-011).

Статья подготовлена по материалам докладов участников XI Международной школы «Физическое материаловедение» (ШФМ-2023), Тольятти, 11–15 сентября 2023 года.

Для цитирования: Рубаник В.В., Ломач М.С., Рубаник В.В. мл., Луцко В.Ф., Гусакова С.В. Интенсификация процесса равноканального углового прессования с помощью ультразвуковых колебаний // *Frontier Materials & Technologies*. 2024. № 4. С. 73–85. DOI: 10.18323/2782-4039-2024-4-70-7.



The Publishing Center (until November 1, 2011 – the Editorial and Publishing Center) is a structural subdivision of Togliatti State University, which takes an important place in providing the educational process with high-quality instructional, educational, methodological, and scientific literature.

TSU Publishing Center today

– Publishing center includes an editorial office and a printing shop. In recent years, the base of computer equipment, printing and post-printing equipment has been almost completely updated.

– It publishes books and electronic textbooks for students, graduate students, lecturers, and specialists in almost all branches of modern scientific knowledge, as well as popular science and reference literature, fiction, books of reports (papers) of conferences. Published literature corresponds to all areas of the educational cycles of the university disciplines.

– A considerable volume of printing job is the prompt execution of promotional and information products.

– The publishing center team is a collaboration of highly skilled professionals with wide work experience and young motivated employees.

– Publishing center employees participate in practical seminars to become acquainted with new opportunities in the field of printing technologies and equipment, as well as with advanced materials for digital printing.

Main areas of activity

– Publication of paper-based educational and scientific literature, production of electronic educational and scientific aids.

– Implementation of editorial and publishing cycle stages: editing, production of original layouts, replication, pre-printing and post-printing treatment.

– Methodological and advisory work with the university departments on the issue of educational and scientific publications.

– Interaction with the Russian Book Chamber on the assignment of ISBNs to publications issued by Togliatti State University.

– Preparation of publications issued by Togliatti State University for state registration and sending of statutory copies.

– Markup of papers published in the TSU journals in the Articulus program to place on the eLibrary platform.

Main achievements

– The results of the work were awarded with diplomas of the winners of the annual interregional and all-Russian University Book competitions.

– Publishing center regularly participates in the academic book exhibition of publishing activities “University – Science – City”.

Universal model for predicting the phase composition of multicomponent brasses based on chemical analysis data

*Aleksey V. Svyatkin**¹, PhD (Engineering),

assistant professor of Chair “Nanotechnology, Materials Science and Mechanics”

Gleb V. Kostin, student of Chair “Nanotechnology, Materials Science and Mechanics”

Togliatti State University, Togliatti (Russia)

*E-mail: astgl@mail.ru

¹ORCID: <https://orcid.org/0000-0002-8121-9084>

Received 04.06.2024

Revised 04.10.2024

Accepted 20.11.2024

Abstract: When developing technical requirements for alloys, it is important to apply an integrated approach. Combining analytical and simulation modelling, it is possible to reduce technological risks at the stage of creating or modifying requirements. The implementation of this approach directly depends on the degree of consideration of all factors included in the models, as well as on their influence on the variability of characteristics. However, known models do not provide satisfactory convergence with real industrial alloys. Using the example of a complex-alloyed CuZn13Mn8Al5Si2Fe1Pb brass, an approach is proposed that allows describing the variability in the structural state of multicomponent brasses. The analysis of statistical data on the chemical composition and microstructure of industrial batches, made it possible to establish that the alloy matrix solution is a ($\alpha+\beta$)-brass, and corresponds to the phase ratio at 700 °C on the polythermal pseudo-binary cross-section of the Cu–Zn–Mn₅Si₃ diagram. The distribution of alloying elements in the main phases was studied using X-ray spectral analysis. The complete binding of iron in silicides and uniform distribution of manganese in the hot-pressed state were confirmed. A calculation of the silicon proportion in the solid solution was proposed. The measured density of the alloy is 7650 kg/m³, while the calculated density of the matrix solution is 8100 kg/m³. Based on the updated parameters of the universal model, the authors used the Monte Carlo method to assess the variability of the microstructure in relation to the requirements for the chemical composition. The instability of technological properties is attributed to significant variability in the ratio of the α - and β -phases. The content of the α -phase in the alloy ranges from 37.5 % to 66.5 %, while the β -phase varies from 17.5 % to 55.2 %. The simulation model developed in this study enables both to analyse the existing alloys and to predict the behaviour of new alloys. This is critically important for optimising technological processes, and improving the operational properties of materials.

Keywords: multicomponent brass; CuZn13Mn8Al5Si2Fe1Pb; stability of technological processes; chemical composition of special brasses; statistical simulation modelling of phase composition; brass microstructure; brass density; zinc equivalent; silicides.

For citation: Svyatkin A.V., Kostin G.V. Universal model for predicting the phase composition of multicomponent brasses based on chemical analysis data. *Frontier Materials & Technologies*, 2024, no. 4, pp. 87–95. DOI: 10.18323/2782-4039-2024-4-70-8.

INTRODUCTION

Modern mass production places strict requirements for the manufacturability of metal products. The development of domestic brands of special multicomponent brasses comparing favourably in manufacturability, and performance characteristics with brands of foreign manufacturers is an urgent task. Increasing the stability of the manufacturability of processes in mass production is considered within the theory of variability [1; 2] and statistical thinking (Six Sigma concept) [3]. Managing the phase composition variability is the main factor determining manufacturability. It is possible to reduce the time for designing requirements for alloys by introducing modern methods of statistical modelling. One of such methods is the Monte Carlo method, based on the reproduction of a large number of executions of a random process, specially created for the conditions of the problem being solved. The random process is

formed in such a way that its probabilistic characteristics are equal to the observed ones, or it would be possible to calculate through them the desired values of the problem under consideration.

The LMtsAZhKS 70-7-5-2-2-1 alloy (European analogues: CuZn13Mn8Al5Si2Fe1Pb – EN, Diel470HT by Diehl) is used in the domestic automotive industry, has high wear resistance, but unstable technological and operational characteristics [4; 5]. Alloying elements such as aluminium, manganese, iron, silicon, on the one hand, contribute to the improvement of mechanical properties [6; 7]. On the other hand, they have conflicting effects on the manufacturability of casting processes and plasticity in hot and cold states, slowing down diffusion processes [8; 9]. Lead, filling the pores, allows increasing machinability by cutting due to the formation of small intermittent chips [10], but also contributes to crack formation during stamping [10];

11]. Therefore, for the engineering of brass multicomponent alloys, it is important to understand how changes in the content of alloying elements will affect the variability of the phase composition.

The works [12; 13] proposed methods for assessing the phase composition of multicomponent brasses, based on the calculation of the zinc equivalent, taking into account the Guillet coefficients proposed more than 100 years ago [14], but still actively used in technical literature. The main provisions of the forecasting methods [12; 13] are the following.

1. The calculation of the zinc equivalent (Zn_e) according to the Cu–Zn diagram is performed using the formula

$$Zn_e = \frac{Zn + \sum K_i \cdot C_i}{Cu + Zn + \sum K_i \cdot C_i}, \quad (1)$$

where Cu, Zn are the actual content of copper and zinc in the alloy, %;

C_i is the content of the i -th element in the alloy, %;

K_i is the corresponding Guillet equivalence coefficient (Table 1).

2. It is taken into account that lead is in a free state, silicon is completely bound in silicides, and manganese and iron are partially bound.

3. The predicted content of silicides is estimated by the formula

$$Me_5Si_3 = (1 + \alpha_{Fe} + \alpha_{Mn} + \alpha_{Ni}) \cdot Si \cdot \frac{\rho_{brass}}{\rho_{Me_5Si_3}}, \quad \% \text{ vol.}, \quad (2)$$

where α_{Fe} , α_{Mn} , α_{Ni} are the coefficients of connectivity for silicon [12; 13];

$\rho_{Me_5Si_3} \approx 6.0 \text{ kg/dm}^3$ is the average density of Fe and Mn silicides.

4. Moreover, it is noted that after pressing, the phase composition corresponding to the Cu–Zn diagram at 500 °C [12] or 400 °C [13] is fixed.

However, the indicated works do not contain information on checking the quality of the models. When testing the methods on industrial batches of CuZn13Mn8Al5Si2Fe1Pb brass, low quality indices of the models were obtained¹. The described approach seems to be justified, but the model does not take into account a number of factors that can introduce significant errors. The brass density corresponds to the reference data for less alloyed brasses. The mechanism of nucleation and growth of silicides during crystallisation is diffusion, therefore, in case of a decrease in the crystallisation rate, the number and size of silicides should increase to the maximum possible value, specified by the chemical composition [15]. With an increase in the crystallisation rate, diffusion does not have time to occur, and part of Si, Mn, Fe remains in the solid solution. The solid solution will

change depending on the interaction of the above elements. Therefore, the volume of silicides in alloys depends on the cooling conditions of the blanks after casting. Considering the variable solubility of silicides in brass in the range of 200...800 °C, the statement about the complete binding of silicon in silicides requires rechecking. At the same time, it is known that iron barely dissolves in brass, forming γ -Fe [16]. To describe the equilibrium state of special brass alloys doped with Mn and Si, it is logical to use the pseudo-binary polythermal cross-section of the Cu–Zn_e–Mn₅Si₃ diagram (Fig. 1). Note that in [17], the calculation of alternative equivalence coefficients is given, based on electron concentrations calculated as the sum of the products of the atomic concentration of each component, and the number of its collective electrons.

The aim of this work is to update the universal forecasting model based on information on the chemical composition of the phases of a multicomponent brass.

METHODS

The objects of the work were industrial batches of CuZn13Mn8Al5Si2Fe1Pb brass tubes in a hot-pressed state (heating temperature is 750 °C).

A batch of samples was formed from 20 real industrial melts of CuZn13Mn8Al5Si2Fe1Pb brass in a hot-pressed state. Technical requirements for the chemical composition are given in Table 2, which shows as well the average values for chemical elements, and the standard deviation for the analysed batch of samples. For each element, the nature of the distribution of the population was assessed. As a rule, the main elements of the alloy from batch to batch have a normal distribution; impurities have a uniform (rectangular) distribution. The hypothesis of the normal distribution was tested using the Pearson criterion.

Further, metallographic analysis was carried out to identify actual structural relationships. The results were compared with the Cu–Zn_e–Mn₅Si₃ phase diagram (Fig. 1). Quantitative metallographic analysis was performed using an Olympus GX51 microscope (Japan), with a SIAMS 800 panoramic microscopy system (Russia). The proportion of silicides ((Fe, Mn)₅Si₃) was determined on unetched sections in longitudinal and cross sections. The amount of α - and β -phases was recorded after etching (FeCl₃ – 5 g; HCl – 30 ml; H₂O – 100 ml).

To refine the chemical composition of the phases, X-ray spectral analysis was performed on an EVO18 Carl Zeiss scanning electron microscope (SEM) (Germany), with EDX from Bruker (Germany). Measurements were carried out after studying the fields at a magnification in the range of $\times 2000$...7000 to exclude the influence of highly dispersed silicides, using the Point Analysis function.

For project activities when developing and adjusting technical requirements, the main indicator in mass production is the statistical convergence of the mathematical expectation and standard deviation of models and direct observations.

The solution density was refined based on the following considerations:

¹ Kostin G.V., Svyatkin A.V. Evaluation of the adequacy of models for predicting the phase composition of silicon-manganese brass. *Fizicheskoe materialovedenie: sbornik materialov XI mezhdunarodnoy shkoly. Togliatti, Togliatti State University Publ., 2023, pp. 163–164. EDN: QNACBO.*

Table 1. Equivalence coefficients of zinc in brasses
Таблица 1. Коэффициенты эквивалентности цинка в латунях

Element	Si	Al	Mn	Fe	Ni	Sn	Pb	Mg
According to Guillet [14]	10.0	5.0	0.5	0.9	-1.3	2.0	1.0	2.0
According to Efremov [17]	6.0	4.0	-0.2	-	-0.6...1.5	1.7	-	1.7

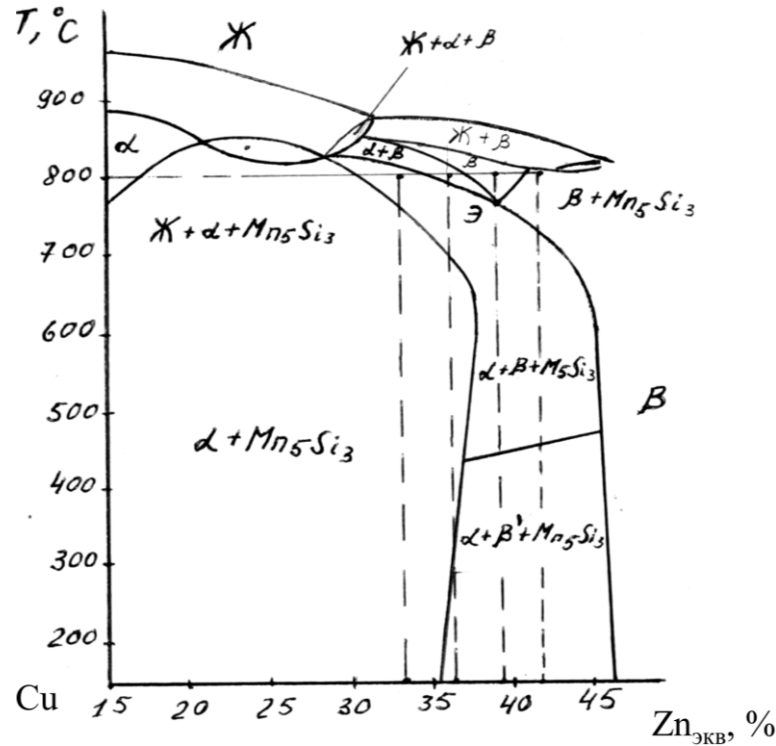


Fig. 1. Pseudo-binary polythermal section of the Cu-Zn-Mn₅Si₃ diagram with a constant content of silicides.

Source: Kotlyarov I.V., Kopyl M.D., Tropotov A.V. Special brass alloys for synchronizer rings: optimization of compositions and technological processes. *Problemy razvitiya avtomobilestroeniya v Rossii: sbornik izbrannykh dokladov II-IV mezhdunarodnykh nauchno-prakticheskikh konferentsiy. Tolyatti, TGU Publ., 1996, pp. 130-134, p. 131.*

Рис. 1. Псевдобинарный политемпературный разрез диаграммы Cu-Zn-Mn₅Si₃, с постоянным содержанием силицидов.

Источник: Котляров И.В., Копыл М.Д., Тропотов А.В. Специальные латунные сплавы для колец синхронизаторов: оптимизация составов и технологических процессов // Проблемы развития автомобилестроения в России: сборник избранных докладов II-IV международных научно-практических конференций. Тольятти: ТГУ, 1996. С. 130-134. С. 131.

$$M = M_{mat} + M_{MeSi}, \quad (3)$$

where M is the sample mass;
 M_{mat} is the mass of the matrix solution;
 M_{MeSi} is the mass of silicides.

Having expanded the formula for finding the sample mass, we obtain

$$\rho \cdot V = \rho_{mat} \cdot V_{mat} + \rho_{MeSi} \cdot V_{MeSi}, \quad (4)$$

where ρ is the sample total density measured according to GOST 20018-74;
 V is the sample volume taken equal to 1;

$$\rho_{MeSi} = 5990 \text{ kg/m}^3;$$

according to the law of stereometric metallography on the correspondence of phase volumes and areas:

$V_{mat} \approx S_{mat}$, $V_{MeSi} \approx S_{MeSi}$ are the volumes occupied by the matrix and silicides, respectively, calculated according to the data of metallographic analysis;

S_{mat} и S_{MeSi} are the ratio of the surface area measured by metallographic analysis of the matrix solid solution and silicides, respectively.

To determine the actual density of brass, samples from 20 batches of the CuZn13Mn8Al5Si2Fe1Pb alloy were measured.

After refining the method of phase composition forecasting, the authors simulated its variability using the Monte

Table 2. Chemical composition of the CuZn13Mn8Al5Si2Fe1Pb alloy components, wt. %
Таблица 2. Химический состав компонентов сплава ЛМцАЖКС, мас. %

Element	Al	Cu	Fe	Mn	Ni	Pb	Si	Sn	Zn	Impurities
Norm	5.0–6.0	69.5–71.5	1.4–2.4	6.5–7.5	≤0.1	0.6–1.2	1.7–2.5	≤0.1	res.	≤0.5
Average	5.35	70.06	1.61	7.10	0.07	0.88	1.87	0.03	12.98	0.13
Standard deviation	0.16	0.41	0.12	0.17	0.02	0.04	0.06	0.02	0.43	0.02
Distribution	+	+	+	+	–	+	+	–	+	–

Note. "+" corresponds to normal distribution, "–" corresponds to rectangular distribution, the α -phase amount is not less than 50 %.
Примечание. «+» соответствует нормальному распределению, «–» – прямоугольному, количество α -фазы не менее 50 %.

Carlo method for 500 iterations. The average value corresponded to the middle of the tolerance field; the standard deviation was calculated using the Six Sigma rule:

$$6\sigma = \frac{UTL - LTL}{6}, \quad (5)$$

where UTL and LTL are the upper and lower tolerance limits.

The element value for each iteration:

$$E_1 = \bar{E} \pm K_e \cdot \sigma, \quad (6)$$

where E is the corresponding element of the chemical composition;

K_e is a random coefficient from 0 to 1 generated for the corresponding distribution.

A set of random numbers was obtained and regression models were built using the Analysis Package of Microsoft Excel.

RESULTS

Table 3 presents the results of the metallographic study of 20 batches of the CuZn13Mn8Al5Si2Fe1Pb alloy as the average and standard deviation. The α - and β' -phases change in a fairly wide range: $\alpha=43.1...63.2\%$,

$\beta'=26.0...53.6\%$. The proportion of silicides $(Fe, Mn)_5Si_3$ in the alloy is stable between batches of the alloy and is $9.2...12.5\%$ with a standard deviation of 0.4 %.

As a result of the density analysis of the sample, it was found that the CuZn13Mn8Al5Si2Fe1Pb alloy has a density of $7650 \pm 20 \text{ kg/m}^3$. Then, from formula (4), it follows that the density of the CuZn13Mn8Al5Si2Fe1Pb brass matrix is $\approx 8100 \text{ kg/m}^3$.

When studying the microstructure, it was found that the CuZn13Mn8Al5Si2Fe1Pb alloy is a 4-component system, and consists mainly of equiaxed grains of the $(\alpha+\beta')$ solid solution, silicides and structurally free lead inclusions. Subsequent examination using an electron microscope confirmed the almost complete absence of signs of eutectoid decomposition. The β' -phase consists of dispersed plates oriented transversely to the pressing direction (Fig. 2). Intermetallides are represented by two main types – large primary $(Fe, Mn)_5Si_3$ silicides, and secondary dispersed rod-shaped Mn_5Si_3 inclusions.

Statistics on the chemical composition of the α - and β' -phases are given in Table 4. The chemical composition of the α - and β' -phases is rather stable from batch to batch. It was found that iron is completely bound in silicides – $(Fe, Mn)_5Si_3$, silicon is unevenly distributed in the solid solution, and is part of the α -phase with a content of $0.14 \pm 0.09\%$ by weight, and of the β' -phase with a content

Table 3. Results of metallographic study of the CuZn13Mn8Al5Si2Fe1Pb alloy microstructure
Таблица 3. Результаты металлографического исследования микроструктуры сплава ЛМцАЖКС

Indicator	α -phase, vol. %	β -phase, vol. %	α/β	$(Fe, Mn)_5Si_3$, vol. %
Average	52.2	36.3	1.5	11.5
Standard deviation	4.8	6.3	0.4	0.9
Minimum	43.1	26.0	0.9	9.2
Maximum	63.2	53.6	2.4	12.5

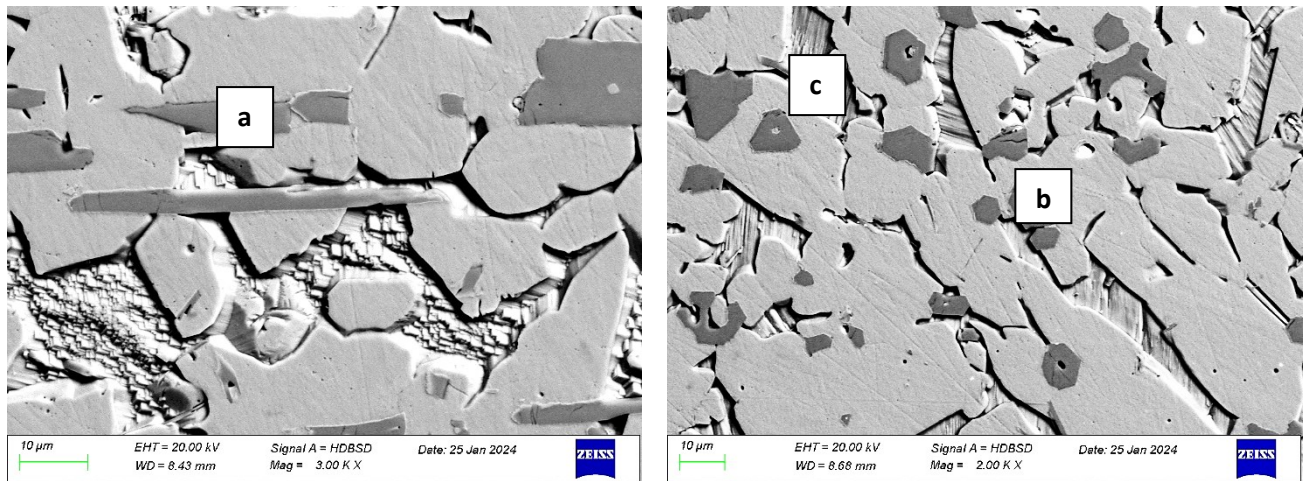


Fig. 2. Microstructure of the CuZn13Mn8Al5Si2Fe1Pb alloy:
a – section in the pressing direction; *b* – radial section; *c* – view of the β -phase plates with the radial section

Рис. 2. Микроструктура сплава ЛМцАЖКс:
a – сечение в направлении прессования; *b* – радиальное сечение; *c* – вид пластин β -фазы с радиальным сечением

Table 4. Statistics of chemical composition of α - and β -phases
Таблица 4. Статистика химического состава α - и β -фаз

Element	α -phase						β -phase					
	Al	Si	Mn	Cu	Fe	Zn	Al	Si	Mn	Cu	Fe	Zn
\bar{X}	4.78	0.14	2.72	78.80	0	13.63	7.72	0.05	2.75	74.83	0	14.69
σ	0.29	0.09	0.12	0.26	0	0.20	0.44	0.06	0.14	0.55	0	0.29

of 0.06 ± 0.05 % by weight. Manganese is uniformly distributed between the α - and β' -phases with a concentration of 2.72...2.75 %. Aluminium is detected in both phases, despite the fact that it belongs to the β -forming elements. In the α -phase, the aluminium concentration is 4.78 ± 0.29 %, in the β' -phase – 7.72 ± 0.44 %.

Linear scanning showed that the manganese concentration peaks are caused only by the transition from the matrix solution to silicides. Manganese is distributed uniformly between the α - and β -phases. The amount of α -phase in the alloy determined by the Six Sigma rule varies from 37.5 to 66.5 %, and the amount of β' -phase varies from 17.5 to 55.2 %.

Based on the results obtained, a different approach was used: the calculation for silicon was performed taking into account the provision that in CuZn13Mn8Al5Si2Fe1Pb brass, silicon forms a stable $(Fe, Mn)_5Si_3$ silicide with iron and manganese, and iron is completely bound in silicides. Since the centre of the intermetallic compound is enriched with iron, and the periphery is enriched with manganese [18], the amount of silicon bound by iron is

$$Si_{Fe} = \frac{3}{5} \cdot \frac{Fe \cdot Ar(Si)}{Ar(Fe)}, \quad (7)$$

where Fe is the concentration of iron in the alloy;

$Ar(Fe)$ is the atomic mass of iron, equal to 55.845 amu;
 $Ar(Si)$ is the atomic mass of silicon, equal to 28.086 amu.

The proportion of silicon bound with manganese:

$$Si_{Mn} = \frac{3}{5} \cdot \frac{Mn \cdot Ar(Si)}{Ar(Mn)}, \quad (8)$$

where Mn is the concentration of manganese in the alloy;
 $Ar(Mn)$ is the atomic mass of manganese, equal to 54.938 amu.

The amount of silicon in the matrix:

$$Si_{mat} = Si - Si_{Fe} - Si_{Mn}. \quad (9)$$

By comparing the result of determining the amount of total silicon in the alloy with the amount of silicon dissolved in the matrix, it was found that it is possible to use the regression equation

$$Si_{mat} = 0.07 \cdot Si + 0.03. \quad (10)$$

By analysing Table 2, and comparing it with the Cu-Zn-((Fe,Mn)₅Si₃) diagram (Fig. 1), the authors found that the obtained results correspond to the phase ratio at a temperature of 700 °C, which is somewhat different from

the works [12; 13]. In this case, the formulas for the prediction methods take the form:

$$\alpha_{press} = \frac{41.6 - Zn_e}{41.6 - 34.4}, \quad (11)$$

$$\alpha_{anneal} = \frac{45.6 - Zn_e}{45.6 - 36.5}. \quad (12)$$

Similarly to [12], we multiply the obtained result by the *K* coefficient, which takes into account the weight fraction of lead and silicides, adjusting the amount of silicon in accordance with calculation (7)–(10):

$$K = \frac{100 - Pb_{(volume)} - (Fe, Mn)_5Si_3_{(volume)}}{100}. \quad (13)$$

The volume fraction of lead and silicides is determined in accordance with the formula [12]:

$$W_{volume} = W_{mas} \cdot \frac{\rho_{brass}}{\rho_c}, \quad (14)$$

where *W_{mas}* is the mass fraction of the corresponding substance; ρ_{brass} and ρ_c are the densities of brass and the corresponding substance.

Next, the *R*² determination coefficient was calculated for the methods [12; 13] and according to formulas (9)–(12), using the Guillet [14] and Efremov [17] coefficients. When calculating according to [14; 17], in all cases we obtain single-phase α -brass. The calculation indicators according to (11)–(14) are given in Table 5.

The calculation of the zinc equivalent, according to Table 4, showed that $Zn_e=33.0\%$ is for the α -phase, $Zn_e=41.8\%$ is for the β -phase, which corresponds to the α -phase at 750 °C and to the β -phase at 700 °C in the diagram (Fig. 1). The result corresponds to the data obtained in the metallographic analysis.

Based on the current requirements (Table 2), the authors determined the minimum and maximum amounts of α - and β -phases in the alloy: α -phase=39...70% ($\alpha \geq 50\%$ in 88% of cases), β -phase=18...50%. In 99% of cases, the α -phase predominates in the microstructure.

DISCUSSION

It is known [18], that the silicides in the alloy are the (Fe, Mn)₅Si₃ compound. However, no signs of the $\beta \rightarrow \alpha + \beta$ eutectoid decomposition identified earlier in [18] were revealed.

The microstructure of the CuZn13Mn8Al5Si2Fe1Pb alloy in the cited work was investigated in the annealed state, which is the reason for the difference in the results. Thus, in the industrially produced CuZn13Mn8Al5Si2Fe1Pb alloy, after pressing, the eutectoid decomposition of the high-temperature β -phase, is almost completely suppressed, and the alloy is in a nonequilibrium state. High variability of the microstructure $\alpha/\beta=0.9...2.4$ is a factor determining the instability of the technological properties.

The alloy microstructure is not optimal in terms of manufacturability, since the main operations of the technological process are associated with hot deformation. In [19], it is shown that the correction of aluminium by 0.4% wt. allows stabilising significantly the process, without qualitatively changing the requirements of the standards. In our case, with an aluminium content of 5.3...6.0%, the α -phase will be 40...65% ($\alpha \geq 50\%$ in 67% of cases), the β' -phase will be 23.5...50%. From the point of view of a qualitative increase in manufacturability, it is advisable, to ensure a ratio of α - and β -phases of 50/50 [17]. This can be achieved by limiting the content of copper to 68.45...70.40%, of aluminium – 5.3...6.0%. Then the amount of α -phase is 28.5...58.3% ($\alpha \geq 50\%$ in 18% of cases), β -phase – 30...61%. It is known that maximum wear resistance is ensured with the amount of β' -phase of 45...50%, α -phase – 30...45% [20; 21]. This ratio corresponds to a content of copper of 68.8...70.7%, of aluminium – 5.5...6.1%. To prevent the formation of silicides of unfavourable form, it is recommended to limit the concentration of silicon in the alloy to no more than 2.2% [18].

Testing the prediction technique demonstrated that the resulting model has a determination coefficient (*R*²) equal to 0.62, which indicates an acceptable quality of the model, in contrast to previously known models [12; 13], which can be explained by changed production conditions of the alloy. The provision on the complete connectivity of silicon, and the use of the coefficients of connectivity of manganese and iron with silicon, in our opinion, is one of the main sources of error in the models [12; 13]. As a result, it was found that the predicted values, according to [12; 13], give significantly overestimated results (by 20...30%) and *R*²<0. Therefore, based on the proposed simulation model, it is possible both to analyse technological risks and to predict the behaviour of new alloys with a corrected or fundamentally new chemical composition. This is critically important for optimising technological processes, and improving the performance properties of materials. It is expected that the results of this study will contribute to the development of technologies for the production and processing of multicomponent brasses, and will increase their competitiveness in the modern market.

Table 5. Calculation model indicators
Таблица 5. Показатели расчетной модели

Average for the sample group, %			Standard deviation, %			Coefficient of determination <i>R</i> ²
α	β	(Fe,Mn) ₅ Si ₃	α	β	(Fe,Mn) ₅ Si ₃	
53.1	35.5	11.5	4.4	4.0	0.4	0.62

CONCLUSIONS

Statistical analysis of industrial batches of CuZn13Mn8Al5Si2Fe1Pb brass showed, that the variability of the alloy microstructure ensuring the stability of technological and operational characteristics, can be described by an analytical and simulation model, based on the Guillet coefficients and the Cu–Zn–((Fe,Mn)₅Si₃) diagram.

The formula for predicting the α -phase of the alloy after pressing was refined. At the same time, it was found that the observed microstructure corresponds to the ratio of the α - and β -phases in the pseudo-binary polythermal section of the Cu–Zn₆–Mn₅Si₃ diagram at 700 °C. For the hot-pressed state, complete binding of Fe in silicides, the presence of residual Si content in the α - and β -phases, and uniform distribution of Mn in the α - and β -phases were found.

To improve manufacturability, it is recommended to change the copper and aluminium content to 68.45...70.40 % and 5.3...6.0 %, respectively. It is assumed that maximum wear resistance is ensured by a copper content of 68.8...70.7 %, aluminium content of 5.5...6.1 %.

The proposed simulation model will reduce the risks of deviations in technological processes, when adjusting the requirements for chemical composition, and developing new brass grades co-doped with aluminium, manganese, iron and silicon.

REFERENCES

- Istomina E.E., Kuranov M.N. Principles of lean production in industrial enterprise management mechanisms. *Kompetentnost*, 2020, no. 6, pp. 38–42. EDN: [IWBBKZ](#).
- Shper V.L., Sheremeteva S.A., Smelov V.Yu., Khunuzidi E.I. Shewhart control charts – A simple but not easy tool for data analysis. *Izvestiya vysshikh uchebnykh zavedeniy. Chernaya metallurgiya*, 2024, vol. 67, no. 1, pp. 121–131. DOI: [10.17073/0368-0797-2024-1-121-131](#).
- Trofimova N.N. Features and prospects of implementation of the integrated Lean Six Sigma methodology at the enterprise. *Vestnik universiteta*, 2021, no. 4, pp. 123–129. DOI: [10.26425/1816-4277-2021-4-123-129](#).
- Ovchinnikov A.S., Loginov Yu.N. Special aspects of pressing pipes from complex alloyed LMtAZhKS brass. *Proizvodstvo prokata*, 2012, no. 4, pp. 38–41. EDN: [PALEBN](#).
- Pugacheva N.B., Ovchinnikov A.S., Lebed A.V. Analysis of defects of industrial brass blanks. *Tsvetnye metally*, 2014, no. 10, pp. 71–77. EDN: [SQVRLB](#).
- Dong Zhuangzhuang, Jie Jinchuan, Dong Bowen, Wang Xianlong, Liu Shichao, Li Tingju. Effect of aluminium addition on microstructure and properties of a novel nickel-silicon-containing brass. *Journal of Materials Research*, 2020, vol. 35, pp. 1598–1611. DOI: [10.1557/jmr.2020.141](#).
- Hendrawan Ch.N., Setyani A., Pertiwi D.R.K., Sofyan B.T. Effect of 9 wt% Mn addition on cold rolling and annealing behaviour of Cu-31Zn alloy. *Materials Today: Proceedings*, 2021, vol. 46, part 9, pp. 3346–3351. DOI: [10.1016/j.matpr.2020.11.476](#).
- Yakovtseva O.A., Mikhaylovskaya A.V., Kotov A.D., Medvedeva S.V., Irzhak A.V. Comparison of contributions of the mechanisms of the superplastic deformation of binary and multicomponent brasses. *Physics of Metals and Metallography*, 2020, vol. 121, no. 6, pp. 582–589. DOI: [10.1134/S0031918X20060186](#).
- Yakovtseva O.A., Kaboyi P.K., Irzhak A.V., Mikhaylovskaya A.V. Influence of minor aluminum addition on the superplastic deformation of a microduplex Cu–Zn alloy. *Physical Mesomechanics*, 2023, vol. 26, no. 5, pp. 533–541. DOI: [10.1134/s1029959923050065](#).
- Stavroulakis P., Toulfatzis A.I., Pantazopoulos G.A., Paipetis A.S. Machinable Leaded and Eco-Friendly Brass Alloys for High Performance Manufacturing Processes. *Metals*, 2022, vol. 12, no. 2, article number 246. DOI: [10.3390/met12020246](#).
- Levin D.O., Sulitsin A.V., Kareva N.T., Galimov D.M. Effects of chemical composition of brass alloy type LS59-1 on the quality of ball valves. *Vestnik Yuzhno-Uralskogo gosudarstvennogo universiteta. Seriya: Metallurgiya*, 2022, vol. 22, no. 4, pp. 38–55. EDN: [IQCHZH](#).
- Kotov D.A., Mysik R.K., Eremin A.A., Volkov M.I., Zhukova L.M. Prediction of phase composition of complex alloyed brasses. *Liteyshchik Rossii*, 2005, no. 9, pp. 17–21.
- Tropotov A.V., Pugacheva N.B., Ryazantsev Yu.V., Zhukova L.M. A study of residual stresses in articles produced from complexly-alloyed brass. *Metal Science and Heat Treatment*, 2006, vol. 48, no. 1-2, pp. 31–35. DOI: [10.1007/s11041-006-0039-5](#).
- Guillet L., Portevin A. *Revue de Metallurgie Memoirs XVII*. Paris, 1920. 561 p.
- Vasilev M.A. *Struktura i dinamika poverkhnosti perekhodnykh metallov* [Structure and Dynamics of the Surface of Transition Metals]. Kiev, Naukova dumka Publ., 1988. 248 p.
- Kamali-Moghaddam S., Häggström L., Ericsson T., Wappling R. Metallurgical behavior of iron in brass studied using Mössbauer spectroscopy. *Hyperfine Interact*, 2006, vol. 168, pp. 995–999. DOI: [10.1007/s10751-006-9386-2](#).
- Efremov B.N. *Latuni. Ot fazovogo stroeniya k strukture i svoystvam* [Brasses. From phase composition to structure and properties]. Moscow, INFRA-M Publ., 2014. 312 p.
- Pugacheva N.B. Structure of commercial $\alpha + \beta$ brasses. *Metal Science and Heat Treatment*, 2007, vol. 49, no. 1-2, pp. 67–74. DOI: [10.1007/s11041-007-0013-x](#).
- Svyatkin A.V., Vyboyschik M.A., Gnusina A.M. Effect of metastable compounds on susceptibility to cracking of multicomponent brasses. *Deformatsiya i razrushenie materialov*, 2024, no. 4, pp. 32–40. EDN: [OGLZJL](#).
- Kurbatkin I.I., Belov N.A., Raykov Yu.N., Rumyantseva O.V., Pokhlebenina L.A., Antipov V.V. Effect of alloying elements and technological factors on phase composition and properties of brass tubes used in the automotive industry. *Tsvetnye metally*, 2001, no. 5, pp. 73–76.
- Kurbatkin I.I., Mochalov S.N., Kotov V.V., Pruzhinin I.F. The influence of chemical elements on the formation of the structure and properties of special brasses during their processing. *Tsvetnye metally*, 2000, no. 2, pp. 85–88.

СПИСОК ЛИТЕРАТУРЫ

- Истомина Е.Е., Куранов М.Н. Механизмы управления промышленным предприятием: принципы бережливого производства // Компетентность. 2020. № 6. С. 38–42. EDN: [IWBBKZ](#).
- Шпер В.Л., Шереметьева С.А., Смелов В.Ю., Хурузиди Е.И. Контрольные карты Шухарта – простой, но не лёгкий для применения инструмент анализа данных // Известия высших учебных заведений. Черная металлургия. 2024. Т. 67. № 1. С. 121–131. DOI: [10.17073/0368-0797-2024-1-121-131](#).
- Трофимова Н.Н. Особенности и перспективы внедрения интегрированной методологии Lean Six Sigma на предприятии // Вестник университета. 2021. № 4. С. 123–129. DOI: [10.26425/1816-4277-2021-4-123-129](#).
- Овчинников А.С., Логинов Ю.Н. Особенности пресования труб из сложнолегированной латуни ЛМцАЖКС // Производство проката. 2012. № 4. С. 38–41. EDN: [PALEBN](#).
- Пугачева Н.Б., Овчинников А.С., Лебедь А.В. Анализ дефектов промышленных заготовок из латуней // Цветные металлы. 2014. № 10. С. 71–77. EDN: [SQVRLB](#).
- Dong Zhuangzhuang, Jie Jinchuan, Dong Bowen, Wang Xianlong, Liu Shichao, Li Tingju. Effect of aluminum addition on microstructure and properties of a novel nickel-silicon-containing brass // Journal of Materials Research. 2020. Vol. 35. P. 1598–1611. DOI: [10.1557/jmr.2020.141](#).
- Hendrawan Ch.N., Setyani A., Pertiwi D.R.K., Sofyan B.T. Effect of 9 wt% Mn addition on cold rolling and annealing behaviour of Cu-31Zn alloy // Materials Today: Proceedings. 2021. Vol. 46. Part 9. P. 3346–3351. DOI: [10.1016/j.matpr.2020.11.476](#).
- Яковцева О.А., Михайловская А.В., Иржак А.В., Котов А.Д., Медведева С.В. Сравнение вкладов действующих механизмов сверхпластической деформации двойной и многокомпонентных латуней // Физика металлов и материаловедение. 2020. Т. 121. № 6. С. 643–650. DOI: [10.31857/S0015323020060182](#).
- Яковцева О.А., Кабойи П.К., Иржак А.В., Михайловская А.В. Влияние малой добавки алюминия на особенности и механизмы сверхпластической деформации сплава Cu-Zn с микродуплексной структурой // Физическая мезомеханика. 2023. Т. 26. № 3. С. 62–71. DOI: [10.55652/1683-805X_2023_26_3_62](#).
- Stavroulakis P., Toulfatzis A.I., Pantazopoulos G.A., Paipetis A.S. Machinable Leaded and Eco-Friendly Brass Alloys for High Performance Manufacturing Processes // Metals. 2022. Vol. 12. № 2. Article number 246. DOI: [10.3390/met12020246](#).
- Левин Д.О., Сулицин А.В., Карева Н.Т., Галимов Д.М. Влияние химического состава латуни типа ЛС59-1 на качество водозапорных изделий // Вестник Южно-Уральского государственного университета. Серия: Металлургия. 2022. Т. 22. № 4. С. 38–55. EDN: [IQCHZH](#).
- Котов Д.А., Мысик Р.К., Еремин А.А., Волков М.И., Жукова Л.М. Прогнозирование фазового состава сложнолегированных латуней // Литейщик России. 2005. № 9. С. 17–21.
- Тропотов А.В., Пугачева Н.Б., Рязанцев Ю.В., Жукова Л.М. Исследование остаточных напряжений в изделиях, изготовленных из сложнолегированных латуней // Металловедение и термическая обработка металлов. 2006. № 1. С. 28–32. EDN: [KTYOWP](#).
- Guillet L., Portevin A. Revue de Metallurgie Memoirs XVII. Paris, 1920. 561 p.
- Васильев М.А. Структура и динамика поверхности переходных металлов. Киев: Наукова думка, 1988. 248 с.
- Kamali-Moghaddam S., Häggström L., Ericsson T., Wappling R. Metallurgical behavior of iron in brass studied using Mössbauer spectroscopy // Hyperfine Interact. 2006. Vol. 168. P. 995–999. DOI: [10.1007/s10751-006-9386-2](#).
- Ефремов Б.Н. Латунь. От фазового строения к структуре и свойствам. М.: ИНФРА-М, 2014. 312 с.
- Пугачева Н. Б. Структура промышленных $\alpha + \beta$ -латуней // Металловедение и термическая обработка металлов. 2007. № 2. С. 23–29. EDN: [KVXIWF](#).
- Святкин А.В., Выбойщик М.А., Гнусина А.М. Влияние метастабильных соединений на склонность к растрескиванию многокомпонентных латуней // Деформация и разрушение материалов. 2024. № 4. С. 32–40. EDN: [OGLZJL](#).
- Курбаткин И.И., Белов Н.А., Райков Ю.Н., Румянцев О.В., Похлебенина Л.А., Антипов В.В. Влияние легирующих элементов и технологических факторов на фазовый состав и свойства латунных труб, применяемых в автомобильной промышленности // Цветные металлы. 2001. № 5. С. 73–76.
- Курбаткин И.И., Мочалов С.Н., Котов В.В., Пружинин И.Ф. Влияние химических элементов на формирование структуры и свойств специальных латуней при их обработке // Цветные металлы. 2000. № 2. С. 85–88.

Универсальная модель прогнозирования фазового состава многокомпонентных латуней на основе данных химического анализа

Святкин Алексей Владимирович*¹, кандидат технических наук, доцент кафедры «Нанотехнологии, материаловедение и механика»

Костин Глеб Вячеславович, студент кафедры «Нанотехнологии, материаловедение и механика»

Тольяттинский государственный университет, Тольятти (Россия)

*E-mail: astgl@mail.ru

¹ORCID: <https://orcid.org/0000-0002-8121-9084>

Поступила в редакцию 04.06.2024

Пересмотрена 04.10.2024

Принята к публикации 20.11.2024

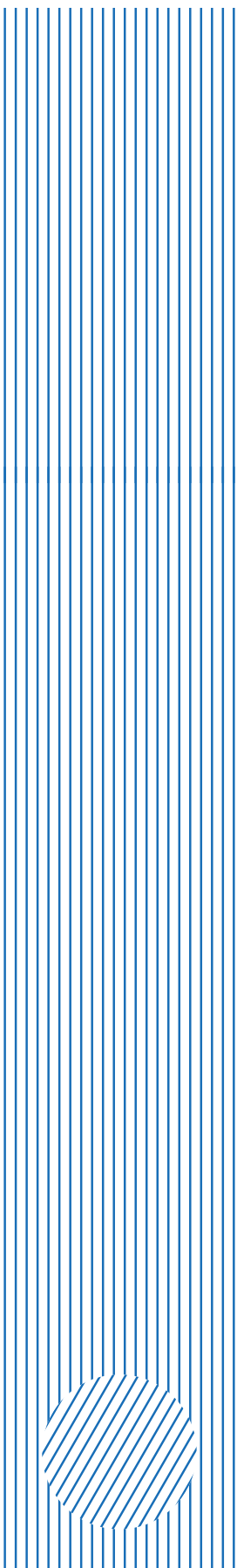
Аннотация: При разработке технических требований к сплавам важно применять комплексный подход. Сочетая аналитическое и имитационное моделирование, можно уменьшить технологические риски на этапе создания или изменения требований. Реализация данного подхода напрямую зависит от степени учета всех факторов, включенных в модели, а также от их влияния на изменчивость характеристик. Однако известные модели не дают удовлетворительной сходимости с реальными промышленными сплавами. На примере сложнолегированной латуни ЛМцАЖКС (CuZn13Mn8Al5Si2Fe1Pb) предложен подход, позволяющий описать изменчивость структурного состояния многокомпонентных латуней. Анализ статистических данных химического состава и микроструктуры промышленных партий позволил установить, что матричный раствор сплава представляет собой ($\alpha+\beta$)-латунь и соответствует соотношению фаз при 700 °С на политермическом псевдобинарном разрезе диаграммы Cu–Zn–Mn₅Si₃. Методами рентгеноспектрального анализа исследовано распределение легирующих элементов в основных фазах. Подтверждена полная связанность железа в силицидах и равномерное распределение марганца в горячепрессованном состоянии. Предложен расчет доли кремния, входящего в твердый раствор. Измеренная плотность сплава составляет 7650 кг/м³, расчетная плотность матричного раствора – 8100 кг/м³. На основании уточненных параметров универсальной модели методом Монте-Карло оценили изменчивость микроструктуры в зависимости от требований к химическому составу. Причиной нестабильности технологических свойств является значительная изменчивость соотношения α - и β -фаз. Содержание α -фазы в сплаве изменяется от 37,5 до 66,5 %, β -фазы – от 17,5 до 55,2 %. Имитационная модель, разработанная в рамках исследования, предоставляет возможность не только анализировать существующие сплавы, но и предсказывать поведение новых сплавов, что является критически важным для оптимизации технологических процессов и улучшения эксплуатационных свойств материалов.

Ключевые слова: многокомпонентная латунь; ЛМцАЖКС 70-7-5-2-2-1; стабильность технологических процессов; химический состав специальных латуней; статистическое имитационное моделирование фазового состава; микроструктура латуней; плотность латуни; цинковый эквивалент; силициды.

Для цитирования: Святкин А.В., Костин Г.В. Универсальная модель прогнозирования фазового состава многокомпонентных латуней на основе данных химического анализа // Frontier Materials & Technologies. 2024. № 4. С. 87–95. DOI: 10.18323/2782-4039-2024-4-70-8.



GENERAL PUBLICATION REQUIREMENTS FOR AUTHORS



The journal publishes two versions of papers: in Russian and in English. The data of manuscript has to be original and never submitted or published before in other journals. All submitted papers are checked in the Anti-Plagiarism system ("Antiplagiat" system).

For publication, authors need to submit an application to the editorial office by sending the materials to the e-mail of the journal vektornaukitgu@yandex.ru or by uploading them to their personal account on the website <https://www.vektornaukitech.ru>.

Required structural elements of the manuscript

- *UDC identifier*;
- *the title* of the scientific manuscript;
- *copyright sign and year*;
- *information about the authors*: surname and initials of the author, academic degree, academic status, occupation; company, city, country; ORCID. The author corresponding to the editorial staff should provide his/her E-mail;
- *abstract* (200–250 words) should contain a brief summary of the paper's concept in order to interest a potential reader;
- *keywords* (the main criterion of choosing keywords is their potential value to summarize the content of the document or to help the readers to find the document);
- *acknowledgements* to individuals, granting organizations;
- *the text of the manuscript* structured in accordance with the rules;
- *references* (at least 20 sources).

Article structure

The structure of the article should conform to the IMRAD (Introduction, Methods, Results, and Discussion) standard, applied by Science World Community:

- INTRODUCTION
- METHODS
- RESULTS
- DISCUSSION
- CONCLUSIONS

Tables and figures formatting

Tables and figures should not fall outside the page layout. The use of landscape pages is not allowed. The titles of the tables and figures captures are required. If the text contains figures, diagrams, and tables from other literary sources, it is necessary to indicate where they were taken from..

Formulas typing

Formulas are edited in Microsoft Equation 3 formula editor. Formulas should not be longer than 80 mm. The size of the formula is 100 %. Converting formulas to figures is not allowed.

References and citations formatting

References are listed in the order of citation in the article. Reference list should not include the sources not cited in the article. In the journal it is not common to cite textbooks and study guides, except the flagship in their respective field, thesis papers and synopsis of a thesis. Not less than a quarter of the sources listed in the reference list should be published in the last 3–5 years. References to print publications only are acceptable (excluding e-journals). References to internet sites are not accepted. Not more than 20 % of the sources can be references on the own author's publications. If a cited source has a DOI, the DOI should be indicated at the end of bibliographic description of this source. All DOIs should be valid links

Effect of alloy composition on machining parameters and surface quality through comprehensive analysis

Shailesh Rao A.*¹, PhD, Professor, Department of Mechanical Engineering
Srilatha Rao², PhD, Professor

Nitte Meenakshi Institute of Technology, Bangalore (India)

*E-mail: shailesh.rao@nmit.ac.in

¹ORCID: <https://orcid.org/0000-0001-6190-9857>

²ORCID: <https://orcid.org/0000-0003-3691-8713>

Received 25.04.2024

Revised 18.06.2024

Accepted 05.11.2024

Abstract: This study examined the influence of alloy composition (mild steel and aluminium) on several machining parameters, such as temperature, cutting force, surface roughness, and chip morphology. Significant variations in these parameters were detected by modifying the alloys while maintaining constant process conditions. In mild steel, rotating speed affected chip morphology, with elevated speeds resulting in continuous chips and reduced rates yielding shorter chips. The augmented rake angle affects the chip properties, resulting in a little decrease in chip length. Moreover, the cutting force influenced the chip length at a designated rotational speed. Conversely, aluminium alloys continuously generated continuous chip fragments irrespective of cutting speed or rake angle. Favourable correlation coefficients are noted among the variables, and a regression model is effectively developed and utilised on the experimental data. The random forest model, indicates that material selection significantly influences temperature, cutting force, surface roughness, and chip morphology during machining. This study offers significant insights into the correlation between tool rake angle and other machining parameters, elucidating the elements that influence surface quality. The results enhance comprehension of machined surface attributes, facilitating the optimisation of machining operations for various materials.

Keywords: turning process; rake angle; chip morphology; predictive modelling.

For citation: Shailesh Rao A., Rao S. Effect of alloy composition on machining parameters and surface quality through comprehensive analysis. *Frontier Materials & Technologies*, 2024, no. 4, pp. 97–110. DOI: 10.18323/2782-4039-2024-4-70-9.

INTRODUCTION

The cylinder components with specified models are made using lathes and/or CNC machines. During the process, the chip detaches from the workpiece because of shear forces applied by a sharp tool. Recent advancements in research activities during the machining process have led to improved output quality. Dogra elucidated the importance of tool geometry in the turning process. The substantial heat generated during chip removal from the workpiece results in tool fatigue and inferior surface finish [1]. The importance of tool geometry throughout the machining process must be accurately articulated. Duc Pham Minh examined the influence of rake angle on material and chip properties. The variation in rake angle with different process conditions resulted in variation in tool wear, surface roughness and distinct chip morphologies [2].

The ductile material produces a continuous chip and offers a longer tool life compared to brittle material, which generates a discontinuous chip and has a shorter tool life [3]. Numerous investigations demonstrated the correlation between a tool's morphology and its durability, as well as its surface irregularities. Tools with a larger radius operating at higher speeds resulted in lower surface roughness compared to those with a smaller radius. Analytical and numerical methods are currently utilised to obtain extensive information on the parameters of the cutting process [4].

Two-dimensional or three-dimensional models are employed in simulation methodologies to illustrate the diverse cutting parameters and materials [5]. Many models rely on a two-dimensional framework, and are not implemented in three dimensions due to heightened computational time and complexity [6].

The proliferation of diverse commercial products has escalated due to the swift technical advancements of the modern environment. Li Bin examined the advancements in theoretical analysis and numerical modelling of tool wear globally [7]. Outeiro conducted numerical modelling and simulation of metal cutting procedures. Numerous numerical methods, including Finite Element method (FEM) and Mesh-free techniques, are being developed to simulate machining operations [8]. The ABAQUS algorithm was employed to model the oblique cutting of nickel-based alloys using coated tools, resulting in a more accurate prediction of cutting forces [9]. The comparison of simulation findings with experimental data revealed that the simulation results aligned with the experimental outcomes. The FEM tool was employed to provide a thorough analysis of the effects of key machining variables on the mechanical properties of mild steel alloys machined using a ceramic tool. The simulation generated a distributed representation of temperature and stress values in the tool tip during the analysis [10]. The simulation or FEM-based approaches

are utilised solely for calculating results; they cannot be compared with other process factors or subjected to comprehensive analysis. Various tools, including MATLAB, ANOVA, and open-source software such as R and Python, are utilised to compare and predict output variables with different predictors. Regression models are employed to ascertain the link between several independent factors, and a dependent variable for future predictions. Numerous numerical algorithms were created from the experimental data collected during the machining process. The selection of suitable predictive models facilitates the determination of optimal cutting parameters and enhances process quality [11; 12]. The researchers have developed predictive models to enhance tool longevity [13], minimise machining duration [14], decrease energy usage [15], and reduce setup time [16], among other factors. These models are crucial for determining optimal cutting parameters and enhancing procedural quality. Li Kuan-Ming and Liang Steven Y. devised a temperature model to forecast tool temperature during oblique rotation, thereby elucidating the stability of the machining process [17]. Ko Jeong Hoon devised a model for attrition rates during the milling process [18]. It is essential to thoroughly investigate the influence of rake angles on different materials to create dependable forecast models. Consequently, further research is necessary to develop predictive models that juxtapose steel with aluminium. The shape of the cutting tool is a critical machining parameter that affects cutting conditions, and consequently, the quality of the completed products¹. A comprehensive understanding of how material properties influence the cutting technique, necessitates a meticulous examination of chip morphology across various materials under defined process parameters.

The primary aim of this study is to analyse machining parameters, including temperature, cutting force, surface roughness, and chip morphology, with the varying alloy compositions.

The objective of the work is to enhance comprehension of the effects of material selection and tool rake angle on surface quality, chip morphology, and other machining results, hence facilitating the optimisation of machining processes for diverse materials. To enhance the outcomes, predictive analysis must be conducted to comprehend surface morphology with varying material compositions.

METHODS

In the present work, the turning process are carried out with aluminium and steel alloys, with varying rake angle as one of the machining parameters. The other possible combination of process parameters, such as cutting velocity, cutting force, surface texture, and temperature are also carried out and quantified. The investigations were conducted utilising a PSG 124 / A 124 heavy-

duty precision lathe machine produced by HMT Machine Tools Ltd. (Hindustan Machine Tools, India). Two specimens, mild steel (EN9) and aluminium (2017-T4), exhibiting comparable mechanical properties as per ASM handbooks, are selected as the workpiece materials. The workpieces measured 24 mm in diameter and 150 mm in length. The specimens were firmly secured in a three-jaw chuck and revolved at cutting speeds of 160 rpm and 360 rpm, maintaining a constant feed rate of 0.12 mm/rev. We employed an Indian-manufactured high-speed steel tool containing 10 % cobalt, featuring a square cross-section of 12.7 mm and a length of 50 mm. We adjusted the tool rake angles (3°, 5°, 8°, and 11°) and taken a depth of cut of 0.5 mm as process parameters. A typical lathe tool dynamometer was affixed to the lathe machine to measure the forces produced during machining. The profile projector was utilised to analyse chip formation and ascertain the length of the chip's serrations from enlarged images. The surface roughness was assessed using an SJ-218 Talysurf (Mitutoyo, Japan) on the machined surface.

With the detailed experiment values, a predictive model is proposed to provide an early assessment of the relationship between variables, focusing on temperature as the output. The R software tool is employed to create a predictive model utilising experimental data. The study was conducted by importing the data into the tool environment. The "read.csv()" function was employed to import the tabular data, with appropriate formatting and variable allocation. The correlation coefficients between the dependent and independent variables are computed first from the available data. Additionally, linear regression and the random forest technique are employed to forecast surface roughness based on provided data.

RESULTS

Chip formation

The chip formation provides insight into the workpiece quality and dictates machining stability. Fig. 1 illustrates the chip pictures on the profile projectors and facilitates the measurement of chip geometry. Initial observations indicate that alterations in the rake angle have affected the chip length. This phenomenon results from a change in the direction of chip flow across the blade's surface. Significantly, at 140 rpm, an increase in cutting force led to the formation of shorter chips. The properties of aluminium alloys led to the generation of continuous chips, irrespective of variations in cutting speed or rake angle, as illustrated in Fig. 1.

Determination of properties during the machining process

Fig. 2 illustrates the serration height observed during the chip study at various cutting rates. The height rises as the spinning speed diminishes. At elevated rotating velocities, a continuous chip is produced with curls. Throughout the procedure, the tool tip engages with the work material, undergoes compression, and attains a plastic state. A longer serration length is noticed when mild steel is rotated at

¹ Dogra M., Sharma V.S., Dureja J.S. Effect of tool geometry variation on finish turning – A Review. *Journal of Engineering Science and Technology Review*, 2011, vol. 4, no. 1, pp. 1–13. DOI: [10.25103/jestr.041.01](https://doi.org/10.25103/jestr.041.01).

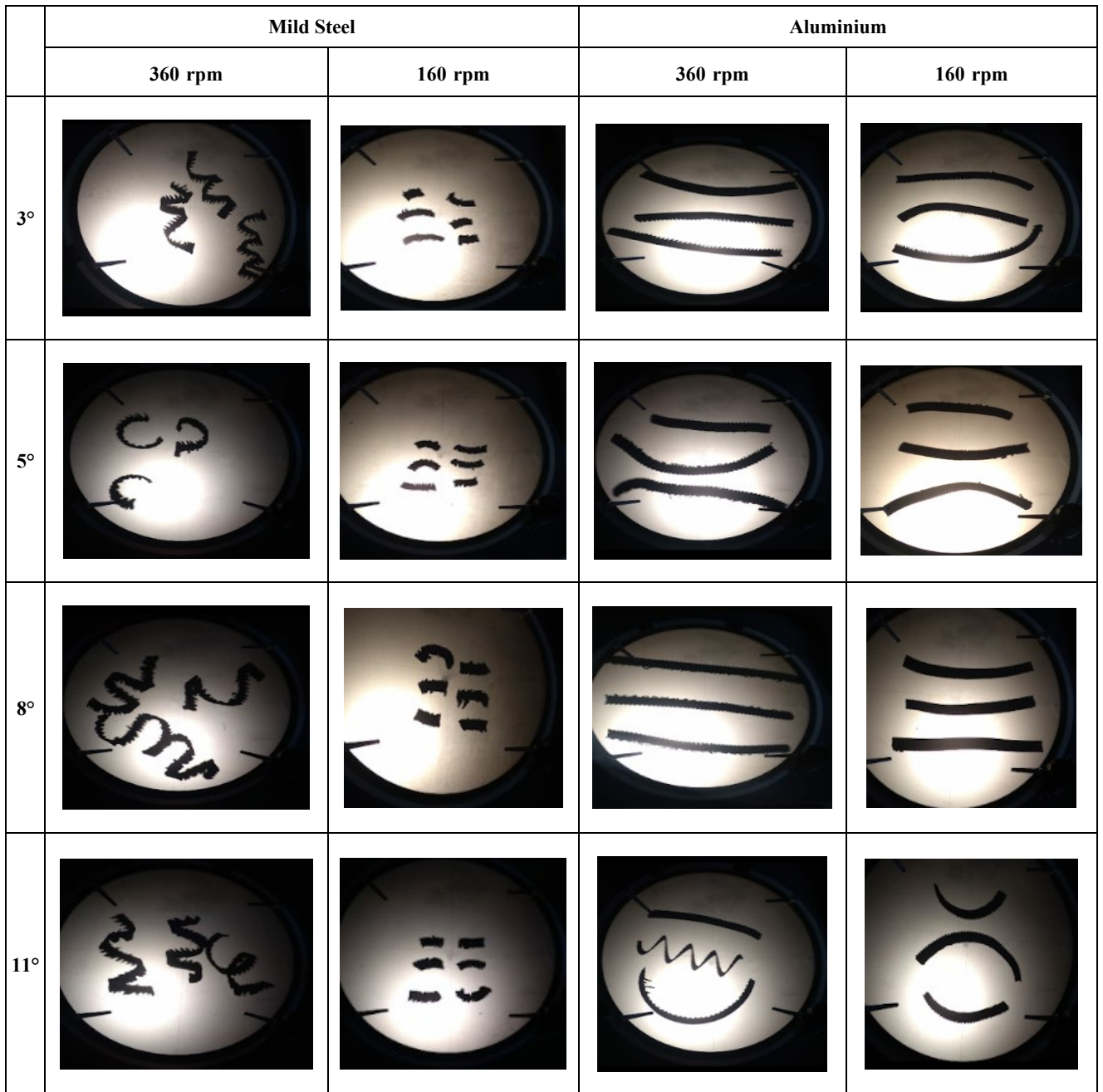


Fig. 1. Chip formation for the different materials at different rake angles and rotational speeds
Рис. 1. Образование стружки для различных материалов при различных углах наклона и скоростях вращения

a reduced speed. In aluminium alloys, a constant material removal thickness produces an elongated fragment with a reduced serration length.

Fig. 2 b illustrates the roughness values of the machined surface. For mild steel, these values diminished with an increase in cutting speed. The results indicate that its value is inversely related to the cutting temperature. Elevated cutting temperatures promote the thermal softness of the material, hence allowing for the facile extraction of the metal from the alloy. Moreover, an escalation in cutting speed amplifies surface-level vibrations and thermal generation. This leads to the creation of a coarse surface, which may also occur due to the disruption of the chip between

the tool tip and the pliable workpiece. In the machining process, an increase in the rake angle results in a reduction of cutting force due to diminished contact at the tool tip interface. Fig. 3 a illustrates that the fragment length grows until a rake angle of 5°, after which it diminishes. The temperature at the tool tip contact is measured using a pyrometer and illustrated in Fig. 3 b. Here the temperature increases with a higher rake angle and the chosen material. This may arise from the higher frictional force.

Table 1 delineates the experimental data for various process parameters, including rotational speed, cutting force, rake angle, and surface roughness, along with their corresponding output variables.

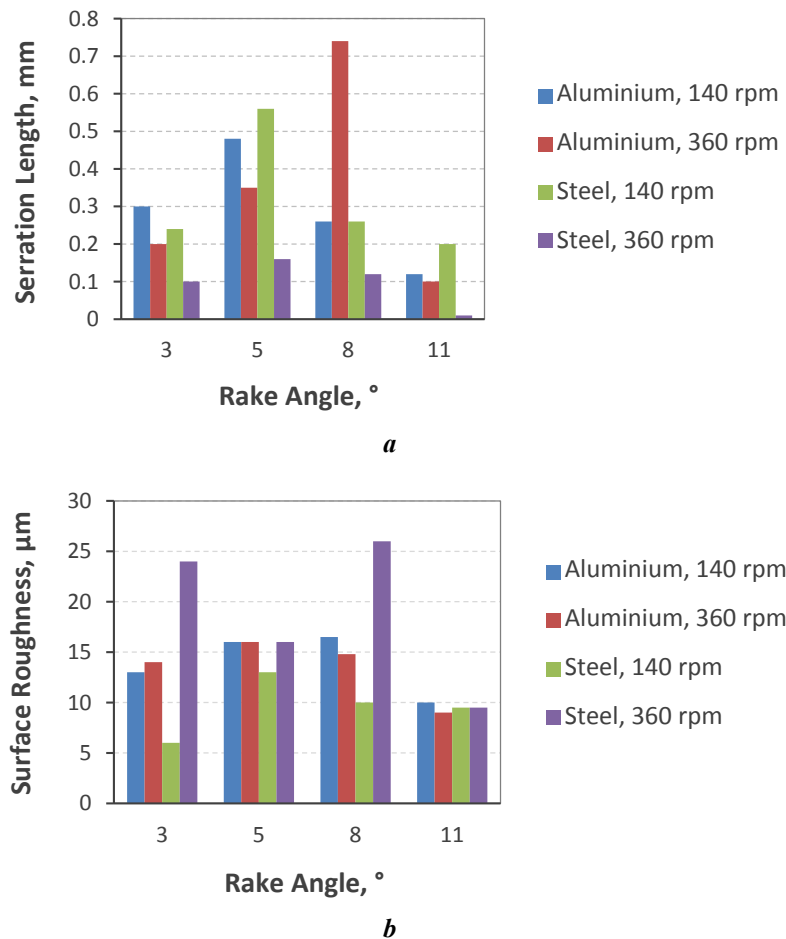


Fig. 2. Determination of some mechanical properties during the machining process
Рис. 2. Определение некоторых механических свойств во время процесса обработки

Table 2 shows the correlation values obtained from the analysis in the R software. The relationships between the different independent variables, and temperature are analysed using these coefficients. In this instance, surface roughness and cutting force have strong positive correlations with temperature. This acknowledges that an increase in surface roughness, and cutting force correlates with a rise in temperature throughout the machining process. These variables significantly influence the thermal behaviour of the process. The rake angle exhibits a moderate correlation with surface roughness. It exerts a minimal influence on the other variables in the study. The temperature had the most positive correlation with surface area and cutting force among the examined parameters. This indicates that the surface characteristics and cutting force produced during machining are directly correlated, with the resultant temperature. The correlation analysis revealed substantial correlations between these variables and the recorded temperature. Moreover, surface roughness and cutting force exhibited a negative correlation with the rake angle, as demonstrated in Table 2.

Multiple regression analysis showed that the cutting force, surface roughness, rake angle, and cutting speed significantly influenced the temperature generated at the contact during the studies. Tables 3 and 4 present the machin-

ing parameter values for aluminium and steel, respectively. For the provided data, the following response models are proposed for aluminium and steel:

Linear Regression for Steel

$$T = 199.64 - 0.05Fc - 0.1Ra + 6.482\gamma + 0.077SFM,$$

where T is temperature;
 Fc is cutting force;
 Ra is surface roughness;
 γ is rake angle;
 SFM is cutting speed.

Linear Regression for Aluminium

$$T = 116.41 - 0.02Fc - 0.05Ra + 2.66\gamma + 0.132SFM.$$

To enhance performance in machining, it is essential to comprehend the correlation between process parameters and temperature. The experimental results underscore the temperature sensitivity of cutting force, cutting speed, surface roughness, and rake angle. In both equations, the p -values for independent variables with interaction factors were below 0.05, signifying that these variables exerted a statistically significant positive effect on temperature. The use of interaction terms indicates that

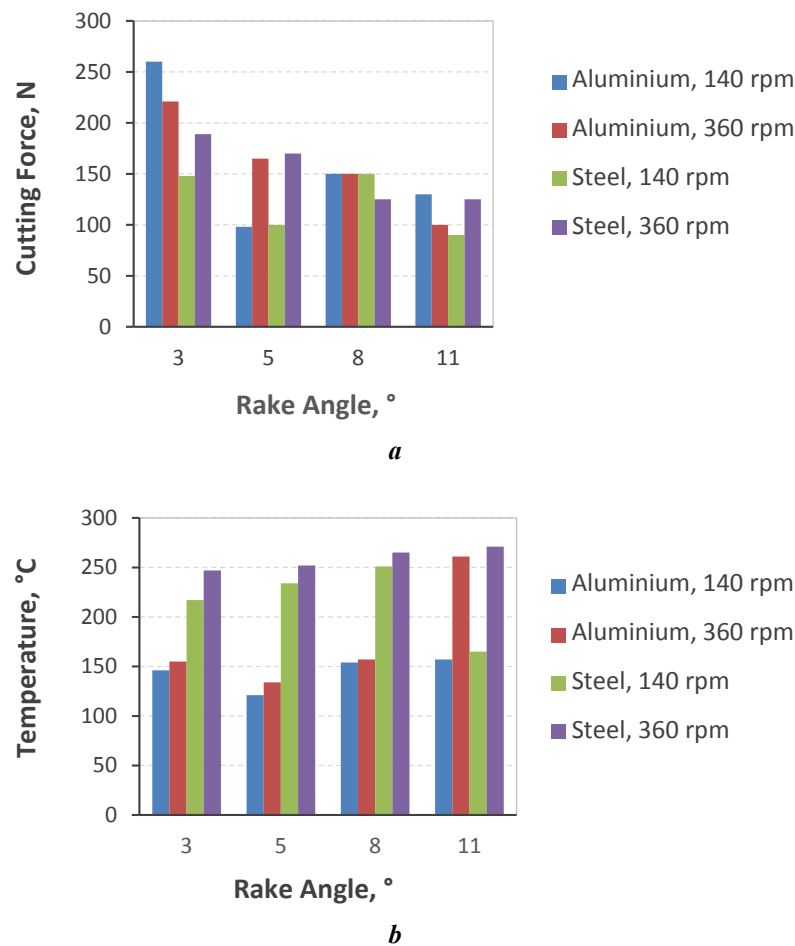


Fig. 3. Temperature distribution for various rake angle
Рис. 3. Распределение температуры для различных передних углов

the connection between temperature and the examined variables, is shaped by their interactions rather than being merely additive.

The *R*-squared values for both models were approximately 89 %, indicating their validity and goodness of fit. The elevated figures suggest that the models, grounded in the independent variables and their interactions, account for a substantial proportion of the temperature variance. The temperature regression analysis produced negligible residual values, signifying that the developed models effectively depict the relationship between the independent variables and temperature. The minimal residuals suggest that the models accurately approximate the actual temperature data.

Fig. 4 illustrates the actual and forecasted temperature measurements as depicted in R program. The graphical representation indicates that the temperature model was more precise than the stated process parameters. This confirms the efficacy of the developed models for forecasting temperature throughout the machining process.

The “plot3d” function from the “rgl” package is utilised to create a three-dimensional plot in R programming. The “plot3d” function is employed in this work to illustrate the correlation among force, cutting speed, and temperature for aluminium and steel alloys, as depicted in Fig. 5 a. From the figure, the cutting force diminishes

with an increase in cutting speed across different rake angles. As the cutting speed increases, the temperature escalates. From the Fig. 5 b, an increase in the temperature is observed due to the alloy’s hardness, which complicates its removal from the work surface. Furthermore, the tool tip conforms to the workpiece surface, elevating temperature. The effectiveness of the machining process is mostly influenced by the material of the workpiece and the configuration of the tool. Augmenting the rake angle improves the adhesion between the material surface and the rake surface of the instrument. This results in an increase in temperature, as illustrated in Fig. 6 a and 6 b. An increase in the hardness of the steel alloy resulted in a rise in temperature.

Fig. 7 illustrates the correlation between machined surface roughness, cutting speed, and temperature. As the rake angle is augmented, the surface irregularity initially escalates and subsequently diminishes. These observations were conducted for both alloys and two separate cutting rates. The machined surface value increased at a rake angle between 3° and 5°. The alteration in rake angle for aluminium elevated the roughness value from 14–15 µm to 17–18 µm at both cutting rates. This is mostly due to the establishment of lower temperatures at the tool tip contact. An increased rake angle results in the temperature shifting towards the centre of the workpiece,

Table 1. Tabulated values of process parameters for steel and aluminium
Таблица 1. Табличные значения параметров процесса для стали и алюминия

Material	Surface Roughness, μm	Cutting Force, N	Rake Angle, $^\circ$	Temperature, $^\circ\text{C}$	Speed, rpm	Peak Height, mm
Aluminium	13	260	3	136	140	0.3
	14	220	3	167	360	0.205
	17	100	5	141	140	0.48
	17	160	5	169	360	0.37
	17.5	150	8	143	140	0.27
	14.5	150	8	174	360	0.75
	10	125	11	151	140	0.13
	6.5	95	11	178	360	0.10
Steel	7	125	3	221	140	0.24
	24	190	3	243	360	0.12
	13	110	5	234	140	0.58
	17	170	5	253	360	0.17
	11	150	8	252	140	0.20
	27	120	8	257	360	0.13
	7	85	11	263	140	0.185
	7	125	11	289	360	0.015

Table 2. Correlation values for steel and aluminium under different process parameters
Таблица 2. Значения корреляции для стали и алюминия при различных параметрах процесса

	Steel			Aluminium		
	Roughness	Cutting Force	Rake Angle	Roughness	Cutting Force	Roughness
Roughness	1	–	–	1	–	–
Cutting Force	0.49	1	–	0.19	1	–
Rake Angle	–0.34	–0.57	1	–0.58	–0.72	1
Temperature	0.63	0.52	0.42	0.42	0.60	0.52
Cutting Speed	0.627	0.53	–	0.19	0.48	–

due to its elevated thermal conductivity. Throughout the machining process, the machined surface grows smoother, even with a slight increase in temperature. This diminishes surface roughness as fragments are readily removed from the workpiece. The roughness value diminished as the rake angle climbed to 8° and 11° ow-

ing to heat dissipation, through conduction and material softening.

For steel, a tougher material requires an increased cutting force to detach particles from the workpiece. Surface roughness escalates with an increase in rake angle, yet diminishes as built-up edge (BUE) or built-up layer (BUL)

Table 3. The process parameter values during the machining of aluminum and its corresponding values
Таблица 3. Параметры процесса при обработке алюминия и соответствующие им значения

Roughness, μm	Cutting Force, N	Rake Angle, $^\circ$	Cutting Speed, rpm	Temperature		Residuals
				Actual	Regression Value	
13	260	3	140	135	137.735	-0.02026
14	220	3	360	168	167.580	0.00250
17	100	5	140	146	146.275	-0.00188
17	160	5	360	172	174.115	-0.01230
17.5	150	8	140	152	153.2575	-0.00827
14.5	150	8	360	182	182.2825	-0.00155
10	125	11	140	162	161.700	0.001852
6.5	95	11	360	190	191.3225	-0.00696

Table 4. The process parameter values during the machining of steel and their corresponding values
Таблица 4. Параметры процесса при обработке стали и соответствующие им значения

Roughness, μm	Cutting Force, N	Rake Angle, $^\circ$	Cutting Speed, rpm	Temperature		Residuals
				Actual	Regression Value	
7	125	3	140	220	222.916	-0.013250
24	190	3	360	238	234.906	0.013000
13	110	5	140	235	236.030	-0.004380
17	170	5	360	254	249.570	0.017441
11	150	8	140	255	253.676	0.005192
27	120	8	360	268	270.516	-0.009390
7	85	11	140	270	276.772	-0.025080
7	125	11	360	290	291.712	-0.005900

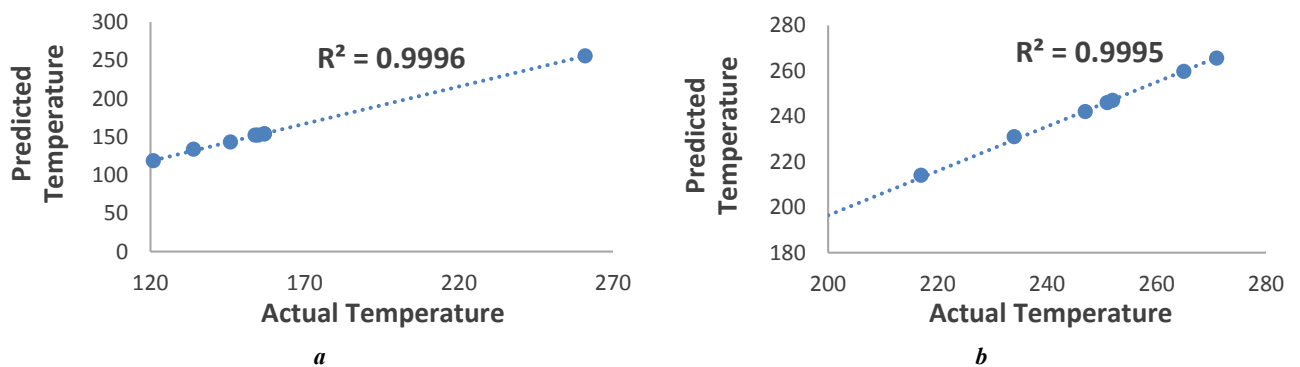


Fig. 4. Comparison of actual temperature and predicted temperature value for aluminum (a) and steel (b)
Рис. 4. Сравнение фактического и прогнозируемого значений температуры для алюминия (a) и стали (b)

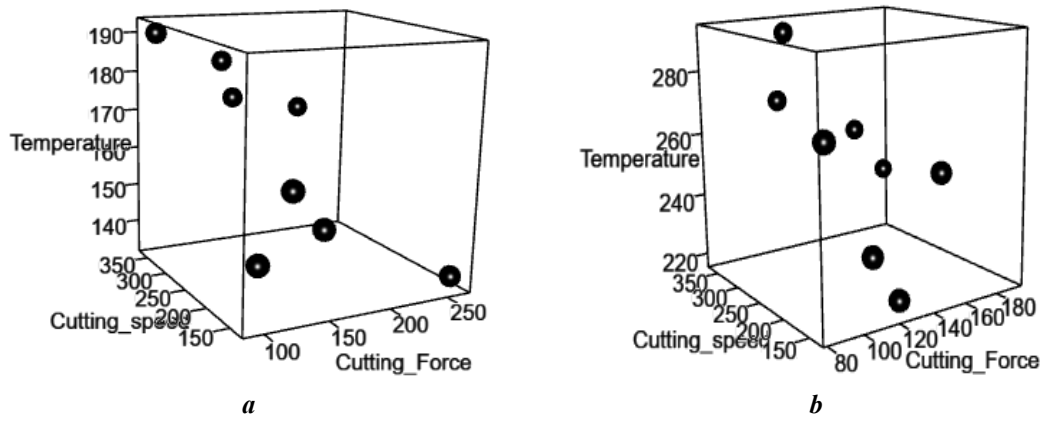


Fig. 5. Variation of cutting force and cutting speed with temperature for aluminium (a) and steel (b)
Рис. 5. Изменение силы и скорости резания в зависимости от температуры для алюминия (a) и стали (b)

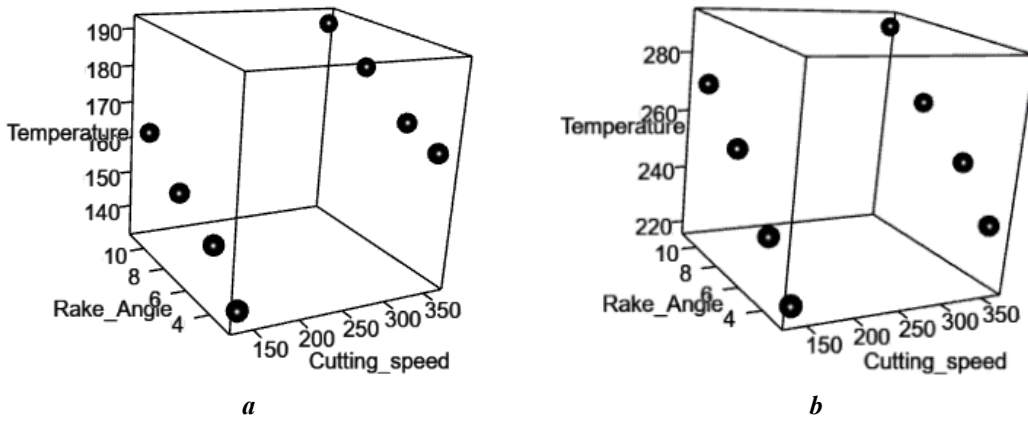


Fig. 6. Variation of rake angle and cutting speed with temperature for aluminium (a) and steel (b)
Рис. 6. Изменение переднего угла и скорости резания в зависимости от температуры для алюминия (a) и стали (b)

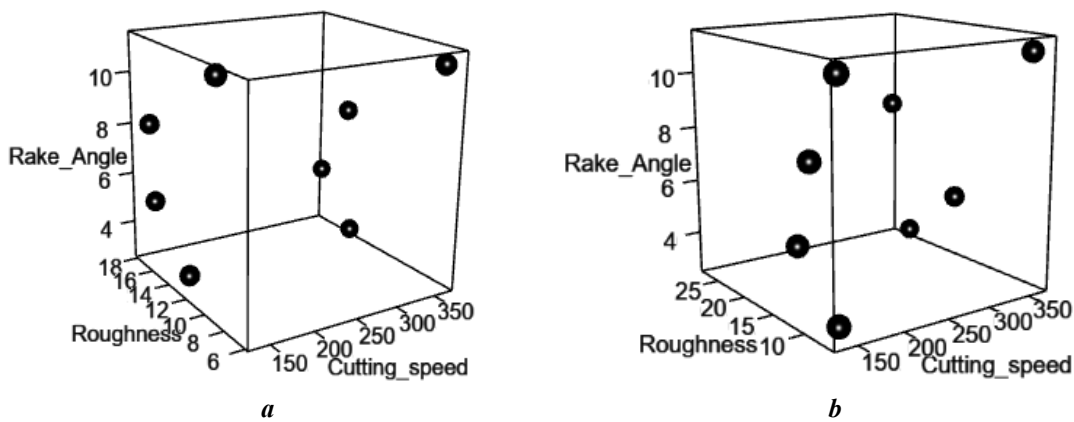


Fig. 7. Variation of roughness and cutting speed with rake angle for aluminium (a) and steel (b)
Рис. 7. Изменение шероховатости и скорости резания в зависимости от переднего угла для алюминия (a) и стали (b)

develops at the tool tip contact and the material undergoes softening. In comparison to aluminium, steel exhibits lower heat conductivity, and Fig. 8 a illustrates an elevation in cutting temperature. Surface roughness escalates with an increase in rake angle and cutting speed.

Random Forest is considered one of the most efficient categorisation approaches in machine learning. This methodology is used for a dataset comprising several process parameters of two distinct alloys. Notwithstanding the dataset's very limited size, the Random Forest algorithm effectively identified alterations in alloy properties depending on their processing features. From the dataset shown in Table 1, 70 % of the data points were allocated for the training set to facilitate precise model evaluation, while the remaining 30% were designated for validation.

The models' consistency was assessed using Fig. 8 a, which illustrated their performance throughout an increased number of decision trees. The graph indicated a positive correlation between the quantity of trees and model stability, suggesting that an increase in the number of trees enhanced the reliability of the classification results. All numerical results must be displayed in the section bearing the same title. Moreover, Fig. 8 b demonstrated the variables' reliance on material selections. Significantly, in comparison to steel and aluminium, the peak length exhibited a substantial association (about 55 % of the total) among the alloys. The maximum height was mostly influenced by the material's strength and composition throughout the turning process. Moreover, these material characteristics accounted for roughly 35 % of the temperature fluctuation during machining.

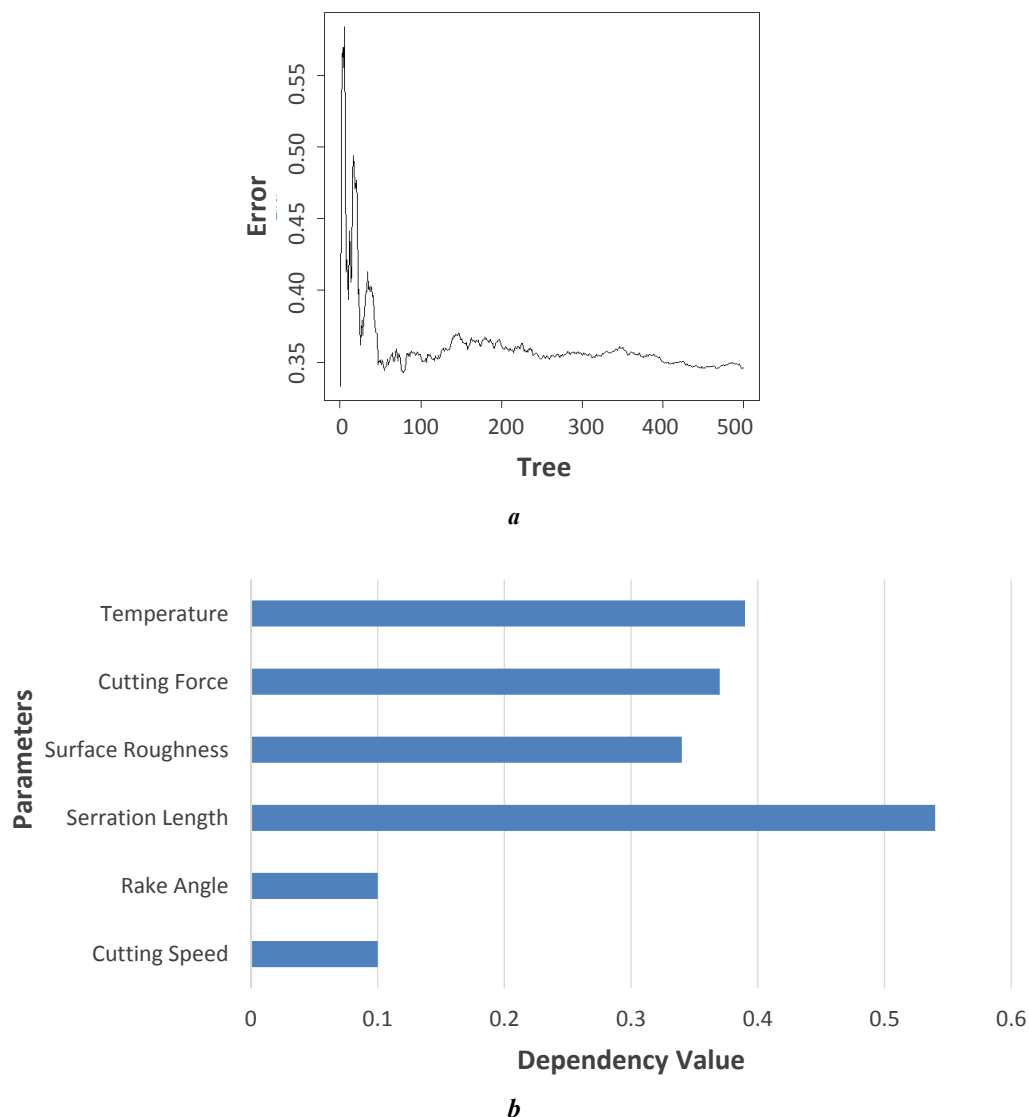


Fig. 8. Error plot during the Random Forest model iteration (a) and dependency plot between the variables for the material selection as output (b)

Рис. 8. Значимость параметров модели, полученная для случайного леса, по степени влияния на выходной параметр (a) и график зависимости между переменными для выбора материала в качестве выходных данных (b)

DISCUSSION

The chip formation provides insight into the workpiece quality and dictates machining stability. Continuous chips are generated when ductile materials are machined. This is mostly attributable to plastic deformation inside the work material. Inadequate cutting settings will lead to the generation of discontinuous chips when milling ductile and brittle materials. Substantial chip burrs are generated during milling under situations of elevated friction. This results from the frictional resistance and the formation of built-up edges at the tool tip's location. This study found that higher rotational speeds produced continuous chips in mild steel, while lower speeds yielded shorter chips [19]. This phenomenon can be elucidated by the inverse correlation between cutting speed and compressive stress, whereby an increase in cutting speed lowers compressive stress, facilitating the formation of continuous chips. Moreover, an increase in the rake angle resulted in a heightened serration elevation. This phenomenon is attributed to heightened segmentation and challenges in shear sliding, resulting in greater material being split off at each peak.

The alteration in rake angle also affected chip length, leading to a slight decrease in mild steel chips. This phenomena results from a change in the direction of chip flow across the blade's surface. Significantly, at 140 rpm, an augmentation in cutting force led to the formation of shorter chips. The properties of aluminium alloys led to the generation of continuous chips, irrespective of variations in cutting speed or rake angle. The morphological features of the fragments remained mostly unaltered despite modifications to these parameters.

The serration height was analysed in relation to varying cutting rates. The height rises as the spinning speed diminishes. At elevated rotating velocities, a continuous chip is produced with curls. Throughout the procedure, the tool tip encounters the work material, undergoes compression, and attains a plastic state. A longer serration length is noticed when mild steel is rotated at a reduced speed. This is mostly attributable to the increased stress that has arisen on the work surface. During machining, the material exhibits characteristics akin to those of a brittle substance. Augmenting the rake angle elevates the compressive stress [20]. In aluminium alloys, a constant material removal thickness yields an elongated fragment with a reduced serration length.

The surface roughness values of the machined area. For mild steel, these values diminished with an increase in cutting speed. The results indicate that its value is inversely related to the cutting temperature. Elevated cutting temperatures promote the thermal softness of the material, hence allowing for the facile extraction of the metal from the alloy [21]. The alloy's thermal softening at elevated temperatures is attributed to the ideal values of frictional energy, and shear plane energy [22]. The potential for elevated temperatures at the tool tip, facilitates the softening of the machined surface area. Demirpolat [23] and Martins [24] elucidate that an elevation in cutting speed diminishes the surface roughness of aluminium alloys, leading to reduced serration lengths. Moreover, an escalation in cutting speed amplifies surface-level vibrations and thermal generation. This leads

to the creation of a rough surface, potentially caused by the disruption of the chip between the tool tip and the pliable workpiece. Augmenting the tiny rake angle diminishes the contact point, hence progressively reducing the cutting force [25]. The generation of vibrations may lead to the development of a surface with an irregular texture. Increasing the rake angle to 11° enhances the surface finish [26].

In the machining process, an increase in rake angle results in a reduction of cutting force due to diminished contact at the tool tip interface [27; 28]. Fig. 3 a illustrates that the fragment length grows until a rake angle of 5° , after which it diminishes. The temperature at the tool tip contact is measured using a pyrometer and depicted in Fig. 3 b. Here the temperature increases with a larger rake angle and the chosen material. This may result from the heightened frictional force.

From the Table 2, the surface roughness and cutting force have strong positive correlations with temperature. This acknowledges that an increase in surface roughness and cutting force correlates with a rise in temperature throughout the machining process. These variables significantly influence the thermal behaviour of the process. The rake angle exhibits a moderate correlation with surface roughness. It exerts a minimal influence on the other variables in the study. The temperature had the most positive correlation with surface area and cutting force among the examined parameters. This indicates that the surface characteristics and cutting force produced during machining are directly correlated with the resultant temperature. The correlation analysis revealed substantial correlations between these variables and the recorded temperature. Additionally, surface roughness and cutting force exhibited a negative correlation with the rake angle.

Further, the cutting force diminishes as the cutting speed escalates over different rake angles as referred from Fig. 5 a. Here the reduction in cutting force is due to the diminished chip-tool interaction. As the cutting speed escalates, the temperature increases. As a result, the yield strength diminishes with the rise in cutting speed [29]. The strong thermal conductivity and low hardness of aluminium alloys, during machining enabled the efficient removal of material from the workpiece. In contrast to steel alloys, a considerable quantity of heat is dissipated across the chip area, leading to a reduction in temperature. BUE is generated at an increased cutting speed with steel. As observed from Fig. 5 b, at a lower cutting velocity, a rise in temperature is seen due to the alloy's hardness, which complicates its removal from the work surface. Furthermore, the tool tip conforms to the workpiece surface, elevating temperature. The effectiveness of the machining process is mostly influenced by the material of the workpiece, and the configuration of the tool.

Overall, the rake angle substantially influences the temperature produced at the tool's interface. The augmentation of thrust force resulted in a temperature elevation of both materials. The alteration of the rake profile leads to the development of the BUE and BUL beneath the chip surface in contact with the rake surface. This results in an increase in temperature, as illustrated in Figs. 6 a and 6 b.

With the increase in the cutting speed, the cutting temperature reduces and similar observations are made from [30], where it was observed that the BUE and BUL diminishes with an increase in cutting speed (depth of cut is 0.15 mm).

Fig. 7 illustrates the correlation between machined surface roughness, cutting speed, and temperature. Here the machined surface value increased at a rake angle of 3° to 5°. This is mostly due to the establishment of lower temperatures at the tool tip contact. An increased rake angle results in the temperature shifting towards the centre of the workpiece due to its elevated thermal conductivity. Throughout the machining process, the machined surface grows smoother, even with a slight increase in temperature. This diminishes surface roughness as fragments are readily removed from the workpiece. The roughness value diminished as the rake angle climbed to 8° and 11° owing to heat loss through conduction, and the softening of the materials. For steel, a tougher material requires an increased cutting force to detach particles from the workpiece. The surface roughness escalates with an increase in rake angle, although diminishes as BUE or BUL develops at the tool tip interface and the material undergoes softening. In comparison to aluminium, steel exhibits lower thermal conductivity, here a reduction in surface roughness is noticed finally.

CONCLUSIONS

The tool rake angle is one of the most important factors to access the machining parameters during a turning process. A variation in temperature at the tool tip contact can be attributed to the change in the rake angle, which also causes the surface roughness to change. In the current work, aluminium and steel alloys with comparable qualities are machined using the parameters that have been established for the procedure. The following are the findings and inferences that can be made from the work.

1. During the machining of mild steel specimen, a larger chip length is noticed with larger rotational speed. A smaller chip length is observed when the rotational speed is lower due to the reduction in the compressive stress, that occurs during machining. When working with soft aluminium alloys, continual lengthy chips are seen despite the difference in rotating speed.

2. The surface roughness of both alloys is increased with the increase in the cutting speed. The additional friction that has developed at the tool tip interface resulted in increased roughness.

3. The values of correlation observed between the variables have been determined to be satisfactory. In addition, the regression model has been constructed and has been successfully applied to the data from the trial.

4. The cutting force, cutting speed, rake angle, and surface roughness all have a significant impact on the temperature, that is generated at the interface between the tool and the workpiece.

5. The random forest model is started to comprehend the reliance on variables for the content that has been picked. During the machining process, it is understood that the material selection has a significant impact on the temperature,

cutting force, surface roughness, and chip shape that are produced.

REFERENCES

- Anand A., Behera A.K., Das S.R. An overview on economic machining of hardened steels by hard turning and its process variables. *Manufacturing Review*, 2019, vol. 6, pp. 1–9. DOI: [10.1051/mfreview/2019002](https://doi.org/10.1051/mfreview/2019002).
- Duc Pham Minh, Giang Le Hieu, Dai Mai Duc, Sy Do Tien. An experimental study on the effect of tool geometry on tool wear and surface roughness in hard turning. *Advances in Mechanical Engineering*, 2020, vol. 12, no. 9, pp. 1–11. DOI: [10.1177/1687814020959885](https://doi.org/10.1177/1687814020959885).
- Rao A.S. Effect of nose radius on the chip morphology, cutting force and tool wear during dry turning of Inconel 718. *Tribology – Materials Surfaces & Interfaces*, 2023, vol. 17, no. 1, pp. 62–71. DOI: [10.1080/17515831.2022.2160161](https://doi.org/10.1080/17515831.2022.2160161).
- Bellini C., Di Cocco V., Iacoviello F., Sorrentino L. Numerical model development to predict the process-induced residual stresses in fibre metal laminates. *Forces in Mechanics*, 2021, vol. 3, article number 100017. DOI: [10.1016/j.finmec.2021.100017](https://doi.org/10.1016/j.finmec.2021.100017).
- Mathivanan A., Swaminathan G., Sivaprakasam P., Suthan R., Jayaseelan V., Nagaraj M. DEFORM 3D Simulations and Taguchi Analysis in Dry Turning of 35CND16 Steel. *Advances in Materials Science and Engineering*, 2022, vol. 2022, no. 1, pp. 1–10. DOI: [10.1155/2022/7765343](https://doi.org/10.1155/2022/7765343).
- Mathivanan A., Sudeshkumar M., Ramadoss R., Ezilarasan C., Raju G., Jayaseelan V. Finite element simulation and regression modelling of machining attributes on turning AISI 304 stainless steel. *Manufacturing Review*, 2021, vol. 8, article number 24. DOI: [10.1051/mfreview/2021022](https://doi.org/10.1051/mfreview/2021022).
- Li Bin. A review of tool wear estimation using theoretical analysis and numerical simulation technologies. *International Journal of Refractory Metals and Hard Materials*, 2012, vol. 35, pp. 143–151. DOI: [10.1016/j.ijrmhm.2012.05.006](https://doi.org/10.1016/j.ijrmhm.2012.05.006).
- Outeiro J.K., Umbrello D., M'Saoubi R., Jawahir I.S. Evaluation of Present Numerical models for Predicting Metal Cutting Performance and Residual Stresses. *Machining Science and Technology*, 2015, vol. 19, no. 2, pp. 183–216. DOI: [10.1080/10910344.2015.1018537](https://doi.org/10.1080/10910344.2015.1018537).
- Zheng Jin, Zhang Yaoman, Qiao Hanying. Milling Mechanism and Chattering Stability of Nickel-Based Superalloy Inconel 718. *Materials*, 2023, vol. 16, article number 5748. DOI: [10.3390/ma16175748](https://doi.org/10.3390/ma16175748).
- Xiang Huimin, Xing Yan, Dai Fu-zhi et al. High-entropy ceramics: Present status, challenges, and a look forward. *Journal of Advanced Ceramics*, 2021, vol. 10, no. 3, pp. 385–441. DOI: [10.1007/s40145-021-0477-y](https://doi.org/10.1007/s40145-021-0477-y).
- Zhou Guo, Xu Chao, Wang Xiaohao, Feng Pingfa, Zhang Min. Determination of tool tip steady-state temperature in dry turning process based on artificial neural network. *Journal of Manufacturing Processes*, 2022, vol. 79, pp. 600–613. DOI: [10.1016/j.jmapro.2022.05.021](https://doi.org/10.1016/j.jmapro.2022.05.021).
- Shailesh R.A. Surface finish and cutting efficiency in gingelly oil during machining: regression analysis.

- Frontier Materials & Technologies*, 2024, no. 2, pp. 101–111. DOI: [10.18323/2782-4039-2024-2-68-9](https://doi.org/10.18323/2782-4039-2024-2-68-9).
13. Li Guo, Lu Wanqiu, Huang Shuchun, Zhang Xingyu, Ding Shuiting. Analysis and prediction of residual stresses based on cutting temperature and cutting force in rough turning of Ti–6Al–4V. *Heliyon*, 2022, vol. 8, no. 11, article number e11661. DOI: [10.1016/j.heliyon.2022.e11661](https://doi.org/10.1016/j.heliyon.2022.e11661).
 14. Hegab H., Salem A., Rahnamayan S., Kishawy H.A. Analysis, modelling, and multi-objective optimisation of machining Inconel 718 with nano-additives based minimum quantity coolant. *Applied Soft Computing*, 2021, vol. 108, article number 107416. DOI: [10.1016/j.asoc.2021.107416](https://doi.org/10.1016/j.asoc.2021.107416).
 15. Mhlanga D. Artificial Intelligence and Machine Learning for Energy Consumption and Production in Emerging Markets: A Review. *Energies*, 2023, vol. 16, no. 2, article number 745. DOI: [10.3390/en16020745](https://doi.org/10.3390/en16020745).
 16. Cai Wei, Li Yanqi, Li Li, Lai Kee-hung, Jia Shun, Xie Jun, Zhang Yuanhui, Hu Luoke. Energy saving and high efficiency production oriented forward-and-reverse multidirectional turning: Energy modelling and application. *Energy*, 2022, vol. 252, article number 123981. DOI: [10.1016/j.energy.2022.123981](https://doi.org/10.1016/j.energy.2022.123981).
 17. Li Kuan-Ming, Liang Steven Y. Modelling of cutting forces in near dry machining under tool wear effect. *International Journal of Machine Tools and Manufacture*, 2007, vol. 47, no. 7-8, pp. 1292–1301. DOI: [10.1016/j.ijmachtools.2006.08.017](https://doi.org/10.1016/j.ijmachtools.2006.08.017).
 18. Ko Jeong Hoon. Time-domain prediction of milling stability according to cross edge radius and flank edge profiles. *International Journal of Machine Tools and Manufacture*, 2015, vol. 89, pp. 74–85. DOI: [10.1016/j.ijmachtools.2014.11.004](https://doi.org/10.1016/j.ijmachtools.2014.11.004).
 19. Trujillo Vilches F.J., Hurtado L.S., Fernández F.M., Gamboa C.B. Analysis of the Chip Geometry in Dry Machining of Aeronautical Aluminium Alloys. *Applied Sciences*, 2017, vol. 7, no. 2, article number 132. DOI: [10.3390/app7020132](https://doi.org/10.3390/app7020132).
 20. Machado A.R., Da Silva L.R.R., De Souza F.C.R., Davis R., Pereira L.C., Sales W.F., De Rossi W., Ezugwu E.O. State of the art of tool texturing in machining. *Journal of Materials Processing Technology*, 2021, vol. 293, article number 117096. DOI: [10.1016/j.jmatprotec.2021.117096](https://doi.org/10.1016/j.jmatprotec.2021.117096).
 21. Radhika A., Shailesh Rao A., Yogesh K.B. Evaluating machining performance of AISI 1014 steel using gingelly oil as cutting fluid. *Australian Journal of Mechanical Engineering*, 2021, vol. 19, no. 4, pp. 445–456. DOI: [10.1080/14484846.2019.1636517](https://doi.org/10.1080/14484846.2019.1636517).
 22. Agari S.R. Wear and surface characteristics on tool performance with CVD coating of Al₂O₃/TiCN inserts during machining of Inconel 718 alloys. *Archive of Mechanical Engineering*, 2021, vol. 69, no. 1, pp. 59–75. DOI: [10.24425/ame.2021.139647](https://doi.org/10.24425/ame.2021.139647).
 23. Demirpolat H., Binali R., Patange A.D., Pardeshi S.S., Gnanasekaran S. Comparison of Tool Wear, Surface Roughness, Cutting Forces, Tool Tip Temperature, and Chip Shape during Sustainable Turning of Bearing Steel. *Materials*, 2023, vol. 16, no. 12, article number 4408. DOI: [10.3390/ma16124408](https://doi.org/10.3390/ma16124408).
 24. Martins P.S., Carneiro J.R.G., Ba E.C.T., Vieira V.F. Study on roughness and form errors linked with tool wear in the drilling process of an Al–Si alloy under high cutting speed using coated diamond-like carbon high-speed steel drill bits. *Journal of Manufacturing Processes*, 2021, vol. 62, pp. 711–719. DOI: [10.1016/j.jmapro.2021.01.006](https://doi.org/10.1016/j.jmapro.2021.01.006).
 25. Zhuang Gullin, Liu Hanzhong, Zong Wenjun. Research on the Method of Reducing Dynamic Cutting Force in Aspheric Machining. *Micromachines*, 2023, vol. 14, no. 5, article number 960. DOI: [10.3390/mi14050960](https://doi.org/10.3390/mi14050960).
 26. Ellersiek L., Menze C., Sauer F., Denkena B., Möhring H.-Ch., Schulze V. Evaluation of methods for measuring tool-chip contact length in wet machining using different approaches (microtextured tool, in-situ visualisation and restricted contact tool). *Production Engineering*, 2022, vol. 16, no. 5, pp. 635–646. DOI: [10.1007/s11740-022-01127-w](https://doi.org/10.1007/s11740-022-01127-w).
 27. Vukelic D., Simunovic K., Ivanov V., Sokac M., Kocovic V., Santosi V., Santosi Z., Simunovic G. Modelling of Flank and Crater Wear during Dry Turning of AISI 316L Stainless Steel as a Function of Tool Geometry Using the Response Surface Design. *Tehnicki Vjesnik – Technical Gazette*, 2024, vol. 31, no. 4, pp. 1376–1384. DOI: [10.17559/tv-20231226001235](https://doi.org/10.17559/tv-20231226001235).
 28. Younas M., Khan M., Jaffery S.H.I., Khan Z., Khan N. Investigation of tool wear and energy consumption in machining Ti6Al4V alloy with uncoated tools. *The International Journal of Advanced Manufacturing Technology*, 2024, vol. 132, no. 7-8, pp. 3785–3799. DOI: [10.1007/s00170-024-13548-1](https://doi.org/10.1007/s00170-024-13548-1).
 29. Çiftçi I. Machining of austenitic stainless steels using CVD multi-layer coated cemented carbide tools. *Tribology International*, 2006, vol. 39, no. 6, pp. 565–569. DOI: [10.1016/j.triboint.2005.05.005](https://doi.org/10.1016/j.triboint.2005.05.005).
 30. Gokkaya H., Taşkesen A. The effects of cutting speed and feed rate on BUE-BUL formation, cutting forces and surface roughness when machining AA6351 (T6) alloy. *Journal of Mechanical Engineering*, 2008, vol. 54, no. 7-8, pp. 521–530.

СПИСОК ЛИТЕРАТУРЫ

1. Anand A., Behera A.K., Das S.R. An overview on economic machining of hardened steels by hard turning and its process variables // *Manufacturing Review*. 2019. Vol. 6. P. 1–9. DOI: [10.1051/mfreview/2019002](https://doi.org/10.1051/mfreview/2019002).
2. Duc Pham Minh, Giang Le Hieu, Dai Mai Duc, Sy Do Tien. An experimental study on the effect of tool geometry on tool wear and surface roughness in hard turning // *Advances in Mechanical Engineering*. 2020. Vol. 12. № 9. P. 1–11. DOI: [10.1177/1687814020959885](https://doi.org/10.1177/1687814020959885).
3. Rao A.S. Effect of nose radius on the chip morphology, cutting force and tool wear during dry turning of Inconel 718 // *Tribology – Materials Surfaces & Interfaces*. 2023. Vol. 17. № 1. P. 62–71. DOI: [10.1080/17515831.2022.2160161](https://doi.org/10.1080/17515831.2022.2160161).
4. Bellini C., Di Cocco V., Iacoviello F., Sorrentino L. Numerical model development to predict the process-induced residual stresses in fibre metal laminates // *Forces in Mechanics*. 2021. Vol. 3. Article number 100017. DOI: [10.1016/j.finmec.2021.100017](https://doi.org/10.1016/j.finmec.2021.100017).
5. Mathivanan A., Swaminathan G., Sivaprakasam P., Suthan R., Jayaseelan V., Nagaraj M. DEFORM 3D

- Simulations and Taguchi Analysis in Dry Turning of 35CND16 Steel // *Advances in Materials Science and Engineering*. 2022. Vol. 2022. № 1. P. 1–10. DOI: [10.1155/2022/7765343](https://doi.org/10.1155/2022/7765343).
6. Mathivanan A., Sudeshkumar M., Ramadoss R., Ezilarasan C., Raju G., Jayaseelan V. Finite element simulation and regression modeling of machining attributes on turning AISI 304 stainless steel // *Manufacturing Review*. 2021. Vol. 8. Article number 24. DOI: [10.1051/mfreview/2021022](https://doi.org/10.1051/mfreview/2021022).
 7. Li Bin. A review of tool wear estimation using theoretical analysis and numerical simulation technologies // *International Journal of Refractory Metals and Hard Materials*. 2012. Vol. 35. P. 143–151. DOI: [10.1016/j.ijrmhm.2012.05.006](https://doi.org/10.1016/j.ijrmhm.2012.05.006).
 8. Outeiro J.K., Umbrello D., M'Saoubi R., Jawahir I.S. Evaluation of Present Numerical models for Predicting Metal Cutting Performance and Residual Stresses // *Machining Science and Technology*. 2015. Vol. 19. № 2. P. 183–216. DOI: [10.1080/10910344.2015.1018537](https://doi.org/10.1080/10910344.2015.1018537).
 9. Zheng Jin, Zhang Yaoman, Qiao Hanying. Milling Mechanism and Chattering Stability of Nickel-Based Superalloy Inconel 718 // *Materials*. 2023. Vol. 16. Article number 5748. DOI: [10.3390/ma16175748](https://doi.org/10.3390/ma16175748).
 10. Xiang Huimin, Xing Yan, Dai Fu-zhi et al. High-entropy ceramics: Present status, challenges, and a look forward // *Journal of Advanced Ceramics*. 2021. Vol. 10. № 3. P. 385–441. DOI: [10.1007/s40145-021-0477-y](https://doi.org/10.1007/s40145-021-0477-y).
 11. Zhou Guo, Xu Chao, Wang Xiaohao, Feng Pingfa, Zhang Min. Determination of tool tip steady-state temperature in dry turning process based on artificial neural network // *Journal of Manufacturing Processes*. 2022. Vol. 79. P. 600–613. DOI: [10.1016/j.jmapro.2022.05.021](https://doi.org/10.1016/j.jmapro.2022.05.021).
 12. Шайлеш Р.А. Качество обработки поверхности и эффективность резания в кунжутном масле во время механической обработки: регрессионный анализ // *Frontier Materials & Technologies*. 2024. № 2. С. 101–111. DOI: [10.18323/2782-4039-2024-2-68-9](https://doi.org/10.18323/2782-4039-2024-2-68-9).
 13. Li Guo, Lu Wanqiu, Huang Shuchun, Zhang Xingyu, Ding Shuiting. Analysis and prediction of residual stresses based on cutting temperature and cutting force in rough turning of Ti–6Al–4V // *Heliyon*. 2022. Vol. 8. № 11. Article number e11661. DOI: [10.1016/j.heliyon.2022.e11661](https://doi.org/10.1016/j.heliyon.2022.e11661).
 14. Hegab H., Salem A., Rahnamayan S., Kishawy H.A. Analysis, modeling, and multi-objective optimization of machining Inconel 718 with nano-additives based minimum quantity coolant // *Applied Soft Computing*. 2021. Vol. 108. Article number 107416. DOI: [10.1016/j.asoc.2021.107416](https://doi.org/10.1016/j.asoc.2021.107416).
 15. Mhlanga D. Artificial Intelligence and Machine Learning for Energy Consumption and Production in Emerging Markets: A Review // *Energies*. 2023. Vol. 16. № 2. Article number 745. DOI: [10.3390/en16020745](https://doi.org/10.3390/en16020745).
 16. Cai Wei, Li Yanqi, Li Li, Lai Kee-hung, Jia Shun, Xie Jun, Zhang Yuanhui, Hu Luo. Energy saving and high efficiency production oriented forward-and-reverse multidirectional turning: Energy modeling and application // *Energy*. 2022. Vol. 252. Article number 123981. DOI: [10.1016/j.energy.2022.123981](https://doi.org/10.1016/j.energy.2022.123981).
 17. Li Kuan-Ming, Liang Steven Y. Modelling of cutting forces in near dry machining under tool wear effect // *International Journal of Machine Tools and Manufacture*. 2007. Vol. 47. № 7-8. P. 1292–1301. DOI: [10.1016/j.ijmachtools.2006.08.017](https://doi.org/10.1016/j.ijmachtools.2006.08.017).
 18. Ko Jeong Hoon. Time-domain prediction of milling stability according to cross edge radius and flank edge profiles // *International Journal of Machine Tools and Manufacture*. 2015. Vol. 89. P. 74–85. DOI: [10.1016/j.ijmachtools.2014.11.004](https://doi.org/10.1016/j.ijmachtools.2014.11.004).
 19. Trujillo Vilches F.J., Hurtado L.S., Fernández F.M., Gamboa C.B. Analysis of the Chip Geometry in Dry Machining of Aeronautical Aluminum Alloys // *Applied Sciences*. 2017. Vol. 7. № 2. Article number 132. DOI: [10.3390/app7020132](https://doi.org/10.3390/app7020132).
 20. Machado A.R., Da Silva L.R.R., De Souza F.C.R., Davis R., Pereira L.C., Sales W.F., De Rossi W., Ezugwu E.O. State of the art of tool texturing in machining // *Journal of Materials Processing Technology*. 2021. Vol. 293. Article number 117096. DOI: [10.1016/j.jmatprotec.2021.117096](https://doi.org/10.1016/j.jmatprotec.2021.117096).
 21. Radhika A., Shailesh Rao A., Yogesh K.B. Evaluating machining performance of AISI 1014 steel using gingelly oil as cutting fluid // *Australian Journal of Mechanical Engineering*. 2021. Vol. 19. № 4. P. 445–456. DOI: [10.1080/14484846.2019.1636517](https://doi.org/10.1080/14484846.2019.1636517).
 22. Agari S.R. Wear and surface characteristics on tool performance with CVD coating of Al₂O₃/TiCN inserts during machining of Inconel 718 alloys // *Archive of Mechanical Engineering*. 2021. Vol. 69. № 1. P. 59–75. DOI: [10.24425/ame.2021.139647](https://doi.org/10.24425/ame.2021.139647).
 23. Demirpolat H., Binali R., Patange A.D., Pardeshi S.S., Gnanasekaran S. Comparison of Tool Wear, Surface Roughness, Cutting Forces, Tool Tip Temperature, and Chip Shape during Sustainable Turning of Bearing Steel // *Materials*. 2023. Vol. 16. № 12. Article number 4408. DOI: [10.3390/ma16124408](https://doi.org/10.3390/ma16124408).
 24. Martins P.S., Carneiro J.R.G., Ba E.C.T., Vieira V.F. Study on roughness and form errors linked with tool wear in the drilling process of an Al–Si alloy under high cutting speed using coated diamond-like carbon high-speed steel drill bits // *Journal of Manufacturing Processes*. 2021. Vol. 62. P. 711–719. DOI: [10.1016/j.jmapro.2021.01.006](https://doi.org/10.1016/j.jmapro.2021.01.006).
 25. Zhuang Gullin, Liu Hanzhong, Zong Wenjun. Research on the Method of Reducing Dynamic Cutting Force in Aspheric Machining // *Micromachines*. 2023. Vol. 14. № 5. Article number 960. DOI: [10.3390/mi14050960](https://doi.org/10.3390/mi14050960).
 26. Ellersiek L., Menze C., Sauer F., Denkena B., Möhring H.-Ch., Schulze V. Evaluation of methods for measuring tool-chip contact length in wet machining using different approaches (microtextured tool, in-situ visualization and restricted contact tool) // *Production Engineering*. 2022. Vol. 16. № 5. P. 635–646. DOI: [10.1007/s11740-022-01127-w](https://doi.org/10.1007/s11740-022-01127-w).
 27. Vukelic D., Simunovic K., Ivanov V., Sokac M., Kocovic V., Santosi V., Santosi Z., Simunovic G. Modelling of Flank and Crater Wear during Dry Turning of AISI 316L Stainless Steel as a Function of Tool Geometry Using the Response Surface Design // *Tehnicki Vjesnik – Technical Gazette*. 2024. Vol. 31. № 4. P. 1376–1384. DOI: [10.17559/tv-20231226001235](https://doi.org/10.17559/tv-20231226001235).
 28. Younas M., Khan M., Jaffery S.H.I., Khan Z., Khan N. Investigation of tool wear and energy consumption in machining Ti6Al4V alloy with uncoated tools // *The In-*

- ternational Journal of Advanced Manufacturing Technology. 2024. Vol. 132. № 7-8. P. 3785–3799. DOI: [10.1007/s00170-024-13548-1](https://doi.org/10.1007/s00170-024-13548-1).
29. Çiftçi I. Machining of austenitic stainless steels using CVD multi-layer coated cemented carbide tools // Tribology International. 2006. Vol. 39. № 6. P. 565–569. DOI: [10.1016/j.triboint.2005.05.005](https://doi.org/10.1016/j.triboint.2005.05.005).
30. Gokkaya H., Taşkesen A. The effects of cutting speed and feed rate on BUE-BUL formation, cutting forces and surface roughness when machining AA6351 (T6) alloy // Journal of Mechanical Engineering. 2008. Vol. 54. № 7-8. P. 521–530.

Оценка влияния состава сплава на параметры обработки и качество поверхности посредством комплексного анализа

Шайлеш Рао Азари^{*1}, кандидат наук, профессор, факультет машиностроения

*Рао Шрилата*², кандидат наук, профессор

Технологический институт Нитт Минкии, Бангалор (Индия)

*E-mail: shailesh.rao@nmit.ac.in

¹ORCID: <https://orcid.org/0000-0001-6190-9857>

²ORCID: <https://orcid.org/0000-0003-3691-8713>

Поступила в редакцию 25.04.2024

Пересмотрена 18.06.2024

Принята к публикации 05.11.2024

Аннотация: Изучалось влияние состава сплавов (мягкой стали и алюминия) на несколько параметров обработки, таких как температура, сила резания, шероховатость поверхности и морфология стружки. Значительные изменения этих параметров были обнаружены путем модификации сплавов при поддержании постоянных условий процесса. В мягкой стали скорость вращения влияла на морфологию стружки, при этом повышенные скорости приводили к образованию непрерывной стружки, а пониженные скорости – к образованию более короткой стружки. Увеличенный передний угол влияет на свойства стружки, что приводит к небольшому уменьшению ее длины. При заданной скорости вращения на длину стружки влияла сила резания. Алюминиевые сплавы, напротив, производили непрерывные фрагменты стружки независимо от скорости резания или переднего угла. Были выбраны коэффициенты корреляции переменных, разработана эффективная регрессионная модель и применена к экспериментальным данным. Модель случайного леса показывает, что выбор материала существенно влияет на температуру, силу резания, шероховатость поверхности и морфологию стружки во время обработки. Получены данные о корреляции между передним углом инструмента и другими параметрами обработки, выявлены факторы, влияющие на качество поверхности. Результаты способствуют лучшему пониманию свойств обработанной поверхности, что облегчает оптимизацию операций обработки для различных материалов.

Ключевые слова: токарная обработка; передний угол; морфология стружки; прогнозное моделирование.

Для цитирования: Шайлеш Рао А., Рао Ш. Оценка влияния состава сплава на параметры обработки и качество поверхности посредством комплексного анализа // Frontier Materials & Technologies. 2024. № 4. С. 97–110. DOI: 10.18323/2782-4039-2024-4-70-9.

Predictive fatigue life modelling for aluminum alloys winder high temperature and shot peening interact

Allawi H. Alwin^{1,3}, PhD (Mechanical Engineering),
Laboratory of Electro-Mechanic Systems (LASEM)

Hatem Ksibi^{2,4}, Professor, permanent member of the Materials, Environment and Energy Laboratory,
Faculty of Sciences of Gafsa

¹National School of Engineers of Sfax (ENIS), Sfax (Tunisia)

²Sfax Preparatory Engineering Institute (IPEIS), Sfax (Tunisia)

*E-mail: hatem.ksibi@ipeis.rnu.tn

³ORCID: <https://orcid.org/0009-0001-1015-2476>

⁴ORCID: <https://orcid.org/0000-0003-4144-9958>

Received 18.04.2024

Revised 22.05.2024

Accepted 11.09.2024

Abstract: Enhancing the surface quality of shells subjected to high stress is a major task. A variety of procedures are employed for dealing with this issue. Shot peening is particularly common for aluminium alloys made. In fact, the main method for assessing the surface's durability under consideration is fatigue testing using standard specimens over several cycles. This paper investigates the performance of aluminium alloys under high-temperature exposure, examining their behaviour with and without shot peening-induced hardening. In fact, the study focuses on the fatigue behaviour of aluminium alloys 2024-T4 and 2024-T361 at 250 °C. Experiments on standard-sized specimens were conducted at both room temperature and 250 °C to evaluate how temperature affects fatigue life. The findings were consistent with previously published data, providing useful insights into the behaviour of these alloys at extreme temperatures. Additionally, a mathematical model was developed, integrating the Stress – Number of cycles curve, loading sequence, temperature, and surface hardness from shot peening. This model was compared with Miner's rule to assess its predictive accuracy. The results show that the new model provides more accurate predictions of fatigue life than Miner's rule, thereby improving the reliability and safety of components in high-temperature applications. By offering precise fatigue life predictions, this research aids in the design and development of more durable aluminium alloy components, ensuring optimal performance and safety in challenging operating environments.

Keywords: shot peening; predictive fatigue life; aluminium alloys; AA2024-T4; AA2024-T361; high temperature exposure; variable loading.

For citation: Alwin A.H., Ksibi H. Predictive fatigue life modeling for aluminium alloys winder high temperature and shot peening interact. *Frontier Materials & Technologies*, 2024, no. 4, pp. 111–122. DOI: 10.18323/2782-4039-2024-4-70-10.

INTRODUCTION

For highly stressed aluminium alloy components such as plates and hulls, shot peening (SP) becomes an essential procedure to improve their durability [1]. SP is a process that induces compressive residual stresses, and hardens the outer layer of a material by bombarding its surface with high-speed spherical particles. Al-Obaid previously introduced the statistical and dynamical aspects of this process [2]. More recently, Hou et al. characterised the resulting surface features, using optical and scanning electron microscopy [3].

By pre-stressing the material and strengthening it against surface damage, this hardening helps to prevent fatigue fractures from forming and spreading while it is in use. SP, thus, is essential to guaranteeing the dependability and durability of aluminium alloy structures, that are exposed to harsh operating environments, including those found in automotive, aircraft, and marine settings.

The concept of variable fatigue, also known as cumulative damage, originated in 1924 when Palmgren intro-

duced the concept of linearly varying damage [4]. This theory later became known as Miner's rule, commonly known as the Miner–Palmgren rule [5]. The Miner–Palmgren rule has been widely used in fatigue analysis on a variety of materials and remains a fundamental concept in the field.

According to this assumption, fatigue damage accumulates linearly until failure is reached, which occurs when the stress cycle ratio equals unity. In simpler terms, it posits that the fatigue life of a material can be estimated by summing the damage caused by different stress cycles. Each stress cycle leads to a specific amount of damage, and once the cumulative damage attains a value of one, the material is considered to have reached its fatigue limit, with the likelihood of failure becoming significant.

Several cumulative damage theories exist for metallic materials, with Miner's theory being one of the most important [6; 7]. Miner's cumulative damage theory is widely

used to assess the fatigue life of materials subjected to cyclic loading. This theory is fundamental in engineering and structural design for ensuring the reliability and safety of components.

$$(D)Damage = \sum \frac{n_i}{N_i} = 100\% = 1, \quad (1)$$

where D is defined as fatigue and is equal to 1, when failure is occurred;

n_i is the applied number of cycles;

N_i is the number of cycles to failure as determined from the Stress – Number of Cycles curve ($S-N$ curve). The $S-N$ curve depicts the relationship between cyclic stress amplitude (S), and the number of cycles to failure (N) for a given material, and is commonly employed to estimate fatigue life under cyclic loading conditions.

Mahdi et al. examined AA7001-T6 at creep-fatigue interaction test at room temperature, 150, 280 and 330 °C [8]. It was revealed that the mechanical properties reduced by 37.2, 30 and 24 % for ultimate tensile strength (UTS), yield strength (YS), and Young's modulus (E) respectively. The UTS and YS increased by 5.5 and 5.3 %, respectively, while fatigue strength improved by 12.3 % after 10^7 cycles [9]. The endurance fatigue limit was also reduced from 208 to 184 MPa at 330 °C. A significant reduction was observed in mechanical and fatigue properties at high temperature for AA7001-T6. Mazlan et al. observed the same finding during his investigation of AA2024T351 specimens [10].

In previous studies, Alwin et al. tested AA2024-T4 samples to tensile and fatigue stress during a 10-minute SP procedure [9; 11]. They discovered that adding compressive residual stresses considerably increased fatigue strength and longevity.

Al-Rubaie proposed a theoretical model for the fatigue behaviour of 2024-T3 alloy, drawing on earlier work in the field, particularly the Walker equivalent stress model [12]. The application of this solution to the presented model showed successfully, estimation of fatigue variable loading life under room temperature.

Alalkawi et al. tested AA2024, to study the effect of high temperature (200–250 °C) on fatigue behaviour [13]. They concluded that mechanical properties reduced by a factor of 1.6 to 2.4 while fatigue strength reduced by 1.8 reduction factor.

Therefore, Alalkawi et al. explored the impact of hardening treatments on the cumulative fatigue performance of AA2024 through two block loading tests (120–180 MPa) – one involving low-high stress levels and the other high-low stress levels, both conducted at room temperature [13; 14]. The findings indicated a significant enhancement in cumulative fatigue life attributed to the surface hardening achieved through SP.

Mahdi et al. tested AA7001-T6 under fatigue rotating bending with high temperature (330 °C) and SP + high temperature (SP+330 °C) [8]. They used Miner's rule for variable fatigue loading and it was observed that this rule provided conservative for some samples and non-conservative for the others.

The Miner–Palmgren rule has been improved and adjusted to better suit certain materials and loading conditions in fatigue analysis [7–10]. These developments have resulted in a variety of changes and improvements, including their use as an effective mechanical surface treatment, as noted by Maleki et al. [15].

Fatigue models for alloys like AA2024 are essential for predicting fatigue life under a variety of stress circumstances. Hector and De Waele [16], Fatemi and Yang [17], and Li et al. have all developed well-known models in this field [18]. Therefore, Hector and De Waele's approach integrates experimental data and theoretical principles to estimate fatigue life using characteristics including stress amplitude, loading frequency, and material microstructure [16]. Hence, Fatemi and Yang's widely utilised model takes into account the impacts of average stress, and stress amplitude on fatigue life. This model uses experimental data and analytical approaches to estimate fatigue life under various loading circumstances [17]. Finally, Li et al. AA2024 finite element model correctly predicts fatigue life by integrating numerous material parameters, such as residual stress, strengthening, and loading conditions [18].

Other models for calculating a part's lifetime are available in the literature, including those of Marco and Starkey [19], Zhao et al. [20], and Hwang and Han [21], all from the late 20th century. When these models are applied to regularly used materials as AA2024, they encounter uncertainties. Indeed, Marco and Starkey (1954) investigated uniaxial stresses that were assessed and compounded with numerous harmonic components [19]. Recently, Zhao et al. investigated cumulative damage patterns during fatigue in 2022, based on load interaction and strength degradation [20]. They showed that their suggested cumulative damage model was more consistent with experimental fatigue data, but only at higher cycle loads [21].

Here, we propose to use the grinding spray method in the case of aluminium alloys, especially the alloys of AA2024-T4 and AA2024-T361. This research intends to improve aircraft safety, by creating exact predictive fatigue life models for aluminium alloys, namely AA2024, under high-temperature and SP circumstances. The effectiveness of AA2024-T4 and AA2024-T361 is assessed by comparing them to previously reported data. Analysing various fatigue prediction approaches against experimental data yields, useful insights, refines models, and improves aircraft structural safety.

The study aims to understand the performance of the aluminium alloys AA2024-T4 and AA2024-T361 at high, with and without shot peening-induced hardening. It seeks to understand whether elevated temperatures and shot peening impact the mechanical characteristics and fatigue life of these alloys, offering insights for improving their durability and reliability in high-temperature applications.

METHODS

The experimental phase began with selecting specimens and analysing their chemical composition, which is crucial for ensuring accurate and reliable subsequent testing and analysis.

In fact, we have chosen to focus on two specific aluminium alloys: AA2024-T4 and AA2024-T361. These alloys share the same base composition but undergo different tempering treatments, resulting in distinct mechanical properties. Examining both variants allows for a more comprehensive understanding of the influence of tempering on material behaviour.

The current model primarily utilises the $S-N$ curve and related assumptions, emphasising both the slope (α) and the fatigue endurance limit. It also incorporates the effects of sequential loading at two distinct stress levels: low (σ_L) and high (σ_H).

Furthermore, in this experimental study, we used a SCHENCK PUNU apparatus (SCHENCK USA CORP.), which can perform SP at both room and high temperature (Fig. 1 a). For high-temperature SP, we also utilised a furnace insulated with ka-wool (Fig. 1 b).

The COSQC-Baghdad laboratory carefully examined the alloys through chemical analysis to make sure they satisfied the strict Iraqi Specification Quality (ISQ) 1473/1989 requirements using the state-of-the-art spectrometer ARC-MET 8000 (Verichek Technical Services, USA) for this analytical procedure. Table 1 contains the

measured chemical composition, as well as the data of the relevant standards. Mechanical properties of the AA2024-T4 and AA2024-T361 alloys are given in Table 2.

The current study is focused on investigating fatigue behaviour under variable loading conditions. Therefore, we examine four distinct cases under the test conditions outlined in Table 3. We mention that R^2 assess the goodness of fit of a statistical model, particularly in linear regression analysis. In this context, we denote variable D_v as the damage due to variable amplitude fatigue, and n_i is the applied cycles under i^{th} constant-amplitude loading level.

Fatigue analysis is based on experimental data collected during continuous fatigue testing. 18 fatigue samples (Fig. 2) were studied at three stress levels – 323 MPa (0.7 UTS), 277 MPa (0.6 UTS), and 231 MPa (0.5 UTS), with three specimens tested per stress level. The average results were collected immediately from the fatigue test rig. It is therefore necessary to plot the $S-N$ curves, and obtain the equations of the $S-N$ curve for the above cases. The details of $S-N$ curve or Basquin equations are listed in Table 4.



a



b

Fig. 1. Fatigue testing (SCHENCK PUNU):

a – at room temperature; **b** – at high temperature using a furnace

Рис. 1. Машина для усталостных испытаний (SCHENCK PUNU):

a – при комнатной температуре; **b** – при высокой температуре с использованием печи

Table 1. Chemical analysis of AA2024-T4 and AA2024-T361 measured, wt. %
Таблица 1. Результаты химического анализа сплавов AA2024-T4 и AA2024-T361, мас. %

Element	AA204-T4 experimental measurements	AA204-T361 experimental measurements	Nominal chemical composition AA2024-T4 [24]	Nominal chemical composition AA2024-T361 [24]
Cu	4.10	4.6	3.8 to 4.9	3.8 to 4.9
Fe	0.38	0.5	0.5	0 to 0.5
Si	0.25	0.5	0.5	0 to 0.5
Mn	0.48	0.7	0.3 to 0.9	0.3 to 0.9
Mg	0.42	1.7	1.2 to 1.8	1.2 to 1.8
Zn	0.12	0.25	0.25	0 to 0.25
Cr	0.05	0.045	0.15	0 to 0.1
Al	Balance	Balance	90.9 to 93.0	90.7 to 94.7

Table 2. Mechanical properties of aluminum alloys AA2024-T4 and AA2024-T361
Таблица 2. Механические свойства алюминиевых сплавов AA2024-T4 и AA2024-T361

Mechanical properties	AA2024-T4	AA2024-T361
Ultimate tensile strength, MPa	470	487
Tensile yield strength	325	345
Elongation at break, %	12	11
Modulus of elasticity, MPa	720	710
Hardness, Rockwell B	72	71
Poisson's Ratio	0.33	0.32

Table 3. Selection of test conditions [10]
Таблица 3. Условия испытаний [10]

Setups	Empirical model
Case (1), 250 °C, AA2024-T4	$\sigma_f=2719 N_f^{-0.2053}, R^2=0.969$
Case (2), SP+250 °C, AA2024-T4	$\sigma_f=2243 N_f^{-0.1896}, R^2=0.970$
Case (3), 250 °C, AA2024-T361	$\sigma_f=2665 N_f^{-0.2005}, R^2=0.996$
Case (4), SP+250 °C, AA2024-T361	$\sigma_f=2709 N_f^{-0.1972}, R^2=0.924$

Note. SP is shot peening.

Примечание. SP – дробеструйное упрочнение.

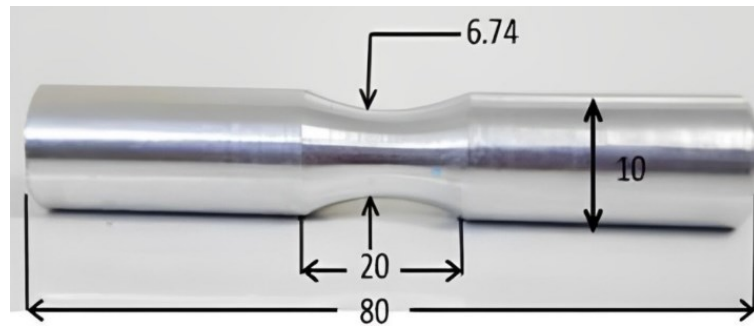


Fig. 2. Fatigue sample dimensions in mm as per DIN 50113 standard specifications
 Рис. 2. Размеры образца в мм в соответствии с DIN 50113

The Miner’s rule stipulates that failure happens when the cumulative fatigue damage reaches its limit. For the two blocks in question, this implies that failure occurs precisely at the point when:

$$\left[\frac{n_1}{N_{f1}} + \frac{n_2}{N_{f2}} \right] = 100\% = 1. \quad (2)$$

If more than two blocks are applied, this equation is generalised to write:

$$\sum \frac{n_i}{N_F} = 1. \quad (3)$$

It should be mentioned that the experiments with variable loading on flat samples of an AA2024-T3 sheet showed that the damage $\sum \frac{n}{N_F}$ values varying from 0.61 to 1.45, but on the average close to 1.0 as mentioned by Mahdi et al. [8]. In high-temperature environments, the limitations of this rule should be carefully considered to provide a more

accurate assessment of fatigue life under variable loading conditions. Elevated temperatures can significantly affect material properties, leading to changes in the behaviour of materials under cyclic loading.

In this study, we conducted tests on 24 round-shaped specimens stress ratio of $R=-1$. For each case, 6 samples were tested: three for low-high two-block loading and three for high-low two-block loading with variable loading conditions. The study focused on determining the average fatigue life for these specimens.

The safe proposed model (SPM): any fatigue damage D_v under variable loading requires a definition. It appears that the D_v concept should include the sequence effect, mechanical properties and the tested $S-N$ curve for the given case.

RESULTS

The reliable fatigue model for shot-peened aluminium alloys, as developed by Alwin et al. [10], utilises Miner’s rule, assuming that the $S-N$ curve accounts for 100 % of the fatigue damage. However, this assumption is somewhat unrealistic because the $S-N$ curve does not

Table 4. $S-N$ curve equations with correlation factor (R^2) for the four cases
 Таблица 4. Уравнения $S-N$ кривых с коэффициентом корреляции (R^2) для четырех режимов

Case No	Symbol	Description
1	250 °C	Cumulative fatigue testes at two stress levels, low-high and high-low for aluminum alloy AA2024T4 under 250 °C
2	SP+250 °C	Cumulative fatigue testes at two stress levels, low-high and high-low for the same alloy under SP and high temperature
3	250 °C	Cumulative fatigue testes at two stress levels, low-high and high-low for aluminum alloy AA2024-T361 at 250 °C
4	SP+250 °C	Cumulative fatigue testes at tow stress levels, low-high and high-low for the same alloy under SP and high temperature

Note. SP is shot peening.

Примечание. SP – дробеструйное упрочнение.

represent a constant damage line. This relationship highlights that fatigue damage is complex and cannot be fully captured by a single damage parameter, especially at high temperatures. For the SP process, only normal impingement was considered to allow for a direct comparison with earlier results.

The optimisation procedure by Miao et al. [22] assumes that individual shots act independently, ignoring interactions between them. This simplifies the analysis and focuses on key parameters. However, it may overlook cumulative effects that could impact the SP process's overall outcome.

The material was subjected to SP during 10 min, which is sufficient for significant increase in durability. The increased durability demonstrates SP's significant benefits in improving material fatigue resistance. Stress decreases dramatically as the number of cycles increases; however, the reduction is more noticeable at higher temperatures, as seen in Fig. 3. The number of cycles decreases from around 105,000 to 80,000 as the temperature rises from ambient to 200 °C, with an even higher reduction recorded at 250 °C. The *S*-curve presented, in conjunction with fatigue life formulas and *R*² values in Table 3, provides a better understanding of fatigue resistance. This analysis helps to optimise the performance of the alloys and processes, resulting in a significant extension of their operational lifespan.

The integration of non-linear models, a single damage parameter has failed to produce an improved Miner's rule, that can offer dependable predictions across a wide range of scenarios. Despite attempts to incorporate non-linear damage functions, the inherent limitations of the Miner's rule remain unresolved. This brings us to the critical question of how to precisely define fatigue damage *D_v*. It represents the cumulative damage that occurs in the considered alloy due to a cyclic loading.

The present work presents a new definition of *D_v* which depends on the following concepts:

- the mechanical properties such as ultimate tensile strength called σ_{UTS} and yield strength σ_y ;
- the *S*-*N* curve, i.e. the slope of the curve α and endurance fatigue limit σ_e , obtained from *S*-*N* curve equation at 10⁷ cycles for the given case;
- sequence loading effect, low stress σ_L and high stress σ_H .

Based on the above concepts *D_v* can be calculated from the equation:

for low-high loading sequence:

$$D_v = \left[\frac{\sigma_{UTS} - \sigma_L}{\sigma_{UTS} - \sigma_H} \right] \left(\frac{\sigma_b}{\sigma_H} \right)^\alpha ; \tag{4}$$

for high-low loading sequence:

$$D_v = \left[\frac{\sigma_{UTS} - \sigma_L}{\sigma_{UTS} - \sigma_H} \right] \left(\frac{\sigma_u}{\sigma_u} \right)^\alpha . \tag{5}$$

Following the work of Miller et al. [23], the fatigue life under variable loading can be predicted by the formula:

for high-low loading:

$$N_{fv} = \frac{\left[\frac{\sigma_{UTS} - \sigma_L}{\sigma_{UTS} - \sigma_H} \right] \left(\frac{\sigma_u}{\sigma_u} \right)^\alpha (\sigma_{UTS} - \sigma_L)^{1-\frac{1}{\alpha}}}{A^{\frac{1}{\alpha}} \left(\sigma_H^{1-\frac{1}{\alpha}} - \sigma_L^{1-\frac{1}{\alpha}} \right)} ; \tag{6}$$

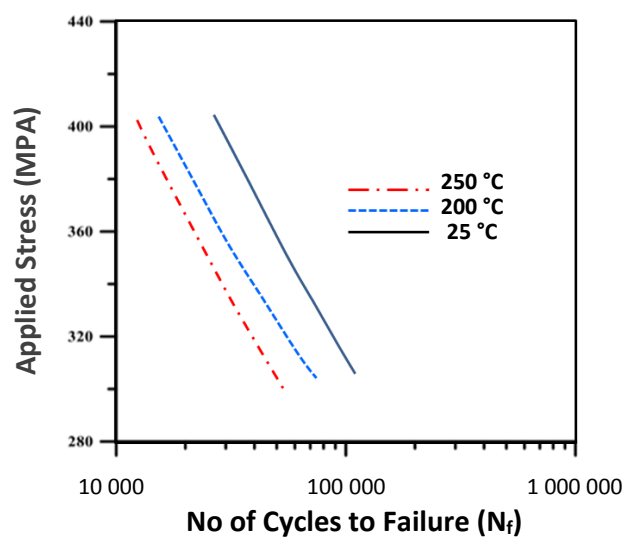


Fig. 3. Constant *S*-*N* curves at three temperatures (room temperature, 200 °C, 250 °C)

Рис. 3. Постоянные кривые усталости (*S*-*N* кривые) при трех температурах (комнатная температура, 200 °C, 250 °C)

for low-high loading:

$$N_{fv} = \frac{\left[\frac{\sigma_{UTS} - \sigma_L}{\sigma_{UTS} - \sigma_H} \right] \left(\frac{\sigma_u}{\sigma_u} \right)^\alpha (\sigma_H - \sigma_L)^{1-\frac{1}{\alpha}}}{A^{\frac{1}{\alpha}} \left(\sigma_H^{1-\frac{1}{\alpha}} - \sigma_L^{1-\frac{1}{\alpha}} \right)} \quad (7)$$

Experimental loading tests (high-low) and (low-high) were carried out for both alloys AA2024-T4 and AA2024-T361 at various temperatures, with or without SP, using the previously described apparatus. The observed maximum number of cycles, the mean number of cycles, and the predicted number of cycles based on the SPM are all listed in Table 5.

The analysis, which draws upon the experimental results presented in Table 5 and visualised through corresponding histograms, is illustrated in Fig. 4.

It is evident from the results that the SPM consistently predicts fatigue lives that fall within the safe range, indicating durations shorter than those observed in experimental testing. Indeed, Fig. 5, 6 depict comparisons between

these fatigue predictions, providing a clear distinction of how the model's predictions align with or deviate from the experimental data. The given representation offers a valuable insight into the performance and reliability of the SP model in estimating fatigue life for the examined aluminium alloys.

Fig. 5, 6 show a significant difference between the standard Miner's rule technique and the experimental results achieved with identical samples. The Miner's rule consistently yields predictions that exceed the actual fatigue life, primarily because it fails to account for crucial factors such as temperature variations and the impact of SP, which are considered by the safe model.

DISCUSSION

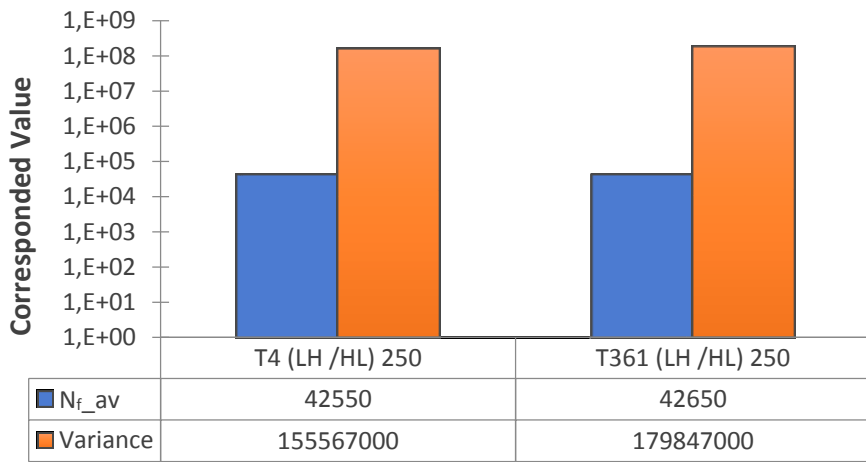
Based on data columned in Table 5, a comprehensive fatigue life assessment can be highlighted by comparing the experimentally obtained cumulative fatigue life with the predictions from the SPM. Indeed, the specification of the AA2024 alloy, whether T4 or T361, is a significant factor in fatigue performance. It appears that the SPM model fits better with the AA2024-T361 alloy than

Table 5. Cumulative fatigue life: experimental results and safe model prediction
Таблица 5. Совокупная усталостная долговечность: экспериментальные результаты и модельное прогнозирование

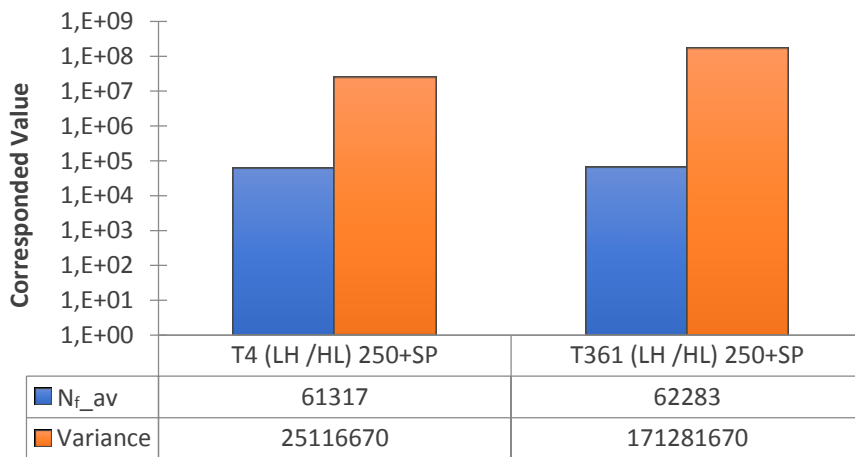
Loading sequence	Alloy	Specimen number	Experimental number of cycles N_{f_exp}	Mean number of cycles N_{f_av} [10]	Number of cycles modelling N_{f_model}
Low-high 250 °C	AA2024-T4	1	38,800	50,800	40,712
		2	51,000		
		3	62,600		
High-low 250 °C		4	41,800	34,300	28,151
		5	29,600		
		6	31,500		
Low-high SP+250 °C	AA2024-T4	7	48,200	69,267	35,352
		8	71,600		
		9	88,000		
High-low SP+250 °C		10	60,500	53,367	25,765
		11	49,600		
		12	50,000		
Low-high 250 °C	AA2024-T361	13	42,800	48,867	47,636
		14	66,000		
		15	37,800		
High-low 250 °C		16	48,200	36,433	34,360
		17	32,400		
		18	28,700		
Low-high SP+250 °C	AA2024-T361	19	53,000	68,767	61,885
		20	84,500		
		21	68,800		
High-low SP+250 °C		22	62,600	55,800	46,143
		23	56,800		
		24	48,000		

Note. SP is shot peening.

Примечание. SP – дробеструйное упрочнение.



a



b

Fig. 4. Cumulative fatigue life: a comparative study of AA2024-T4 and AA2024-T361 alloys (average $N_{f_{av}}$ and variance analysis)

Рис. 4. Совокупная усталостная долговечность: сравнительный анализ сплавов AA2024-T4 и AA2024-T361 (усредненный анализ $N_{f_{av}}$ и вариационный анализ)

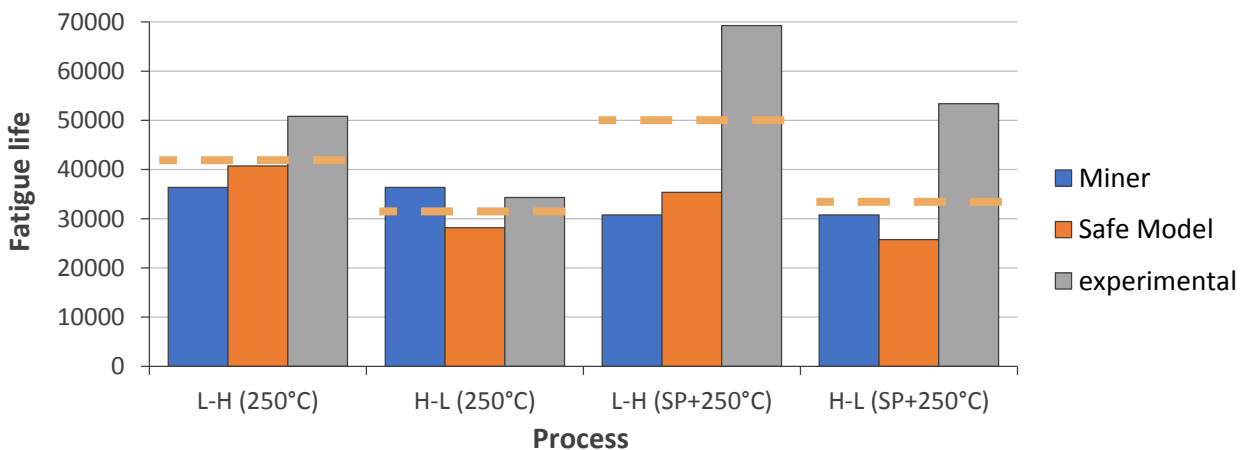


Fig. 5. Comparison between experimental and model prediction AA2024-T4.

The orange dashed line consistently matches both the safe model predictions and the experimental fatigue life values in every shot peening case (shot peening scenario)

Рис. 5. Сравнение экспериментальных результатов и результатов моделирования для сплава AA2024-T4. Оранжевая пунктирная линия соответствует модели безопасного прогнозирования и значениям экспериментальной усталостной долговечности для каждого режима дробеструйного упрочнения

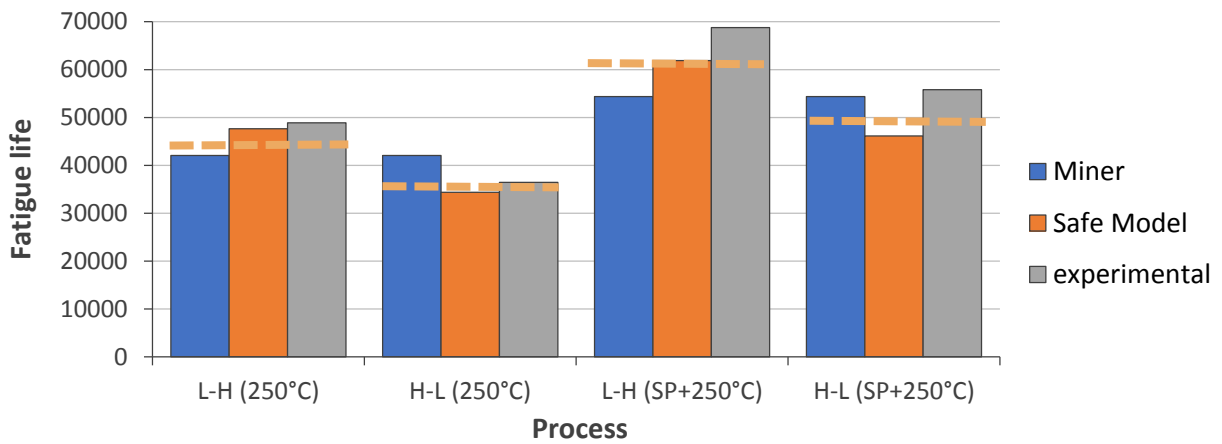


Fig. 6. Comparison of three methods for fatigue prediction for AA2024-T361.

The orange dashed line consistently matches both the safe model predictions and the experimental fatigue life values in every shot peening case (shot peening scenario)

Рис. 6. Сравнение трех методов усталостного прогнозирования для сплава AA2024-T361.

Оранжевая пунктирная линия соответствует модели безопасного прогнозирования и значениям экспериментальной усталостной долговечности для каждого режима дробеструйного упрочнения

with AA2024-T4. Furthermore, it proves to be effective in a SP scenario at high temperatures (250 °C).

Furthermore, the Miner's rule provides only an approximate estimate of fatigue life, with significant errors due to different limitations, as indicated by the histograms in Fig. 5 and 6 for alloys AA2024-T4 and AA2024-T361. First, the rule assumes that stress cycles below the fatigue limit are insignificant. Second, it fails to account for the effects of treatments such as SP and environmental factors such as temperature. Finally, the rule undervalues the significance of loading sequences that alternate between low and high stress levels. In contrast to Miner's rule, we've included the average value, shown by the orange dashed line, to show how close it is to the safe model, see Fig. 5, 6. The histogram illustrates the maximum number of cycles for the low-high and high-low scenarios at 250 °C, both with and without SP. In every SP case, the orange dashed line consistently aligns with the safe model predictions and the experimental fatigue life values. In fact, this observation is particularly evident for the AA2024-T361 alloy compared to the AA2024-T4 alloy.

Indeed, a complex interaction of important variables is the cause of the Miner theory's inaccuracies in fatigue life prediction. First off, a major flaw in the hypothesis is its disregard for fracture initiation, particularly in the early stages of the brief fatigue crack phase. Understanding the initiation dynamics requires an understanding of this phase, which spans approximately 80 % of the fatigue life as the applied stress approaches the fatigue limit. The absence of this important detail leads to a significant underestimate of the total cumulative harm [22], suggesting a key weakness in the theory's prediction power.

The fatigue performance of the two suggested aluminium alloys, AA2024-T4 and AA2024-T361, was assessed by comparing their service life (measured in

terms of cycles). The analysis focused on two key metrics: the mean number of cycles to failure ($N_{f,av}$) and the variance in fatigue life for each procedure. In fact, results indicated that AA2024-T361 demonstrated a significantly longer fatigue life than AA2024-T4, as depicted in Fig. 4. This superior performance of AA2024-T361 can be attributed to its specific damage processes, which may include enhanced resistance to crack initiation and propagation due to its microstructural characteristics or alloying elements [3; 18]. Additionally, the SP treatment, known for inducing compressive residual stresses, may have further improved the fatigue resistance of AA2024-T361 by delaying the onset of fatigue cracks. These findings suggest that AA2024-T361 is better suited for applications where extended fatigue life under high-temperature conditions is critical, offering valuable insights for selecting materials in engineering designs that require durability and reliability.

CONCLUSIONS

The study investigated the cumulative fatigue behaviour of AA2024-T4 and AA2024-T361 alloys at 250 °C, evaluating both isolated scenarios at temperature $T=250$ °C, and a combined shot peening (SP) treatment at the same temperature (SP+250 °C), all at a stress ratio $R=-1$. The results revealed that applying cumulative varied loads resulted in a significant decrease in fatigue life, particularly at high temperatures; however, SP demonstrated a significant improvement in fatigue resistance. Furthermore, classic approaches for estimating fatigue life, such as the linear damage rule or Miner's theory, or models derived from them, have shown limitations in terms of providing unreliable and inaccurate predictions.

As a result, a novel fatigue life prediction model has been developed that incorporates loading sequence data obtained from the $S-N$ curve, as well as pertinent mechanical

parameters. This model provides a conservative but robust way to estimating fatigue life under various stress situations, whether encountered at increased temperatures or in combination with SP treatment at elevated temperatures. A comparison of the mean number of possible cycles and variance for the various experimental settings, stated previously, demonstrates the accuracy of the provided model, although at elevated temperatures with SP for AA2024-T361 against AA2024-T4.

REFERENCES

- Ahcene A.S., Bey K., Mzad H. Mechanical Fatigue Test of Aluminum Composite Panel (ACP) with Aramid Nida-Core Under Cyclic Bending. *Strojnický časopis - Journal of Mechanical Engineering*, 2020, vol. 70, no. 2, pp. 1–10. DOI: [10.2478/scjme-2020-0015](https://doi.org/10.2478/scjme-2020-0015).
- Al-Obaid Y.F. Shot peening mechanics: experimental and theoretical analysis. *Mechanics of Materials*, 1995, vol. 19, no. 2-3, pp. 251–260. DOI: [10.1016/0167-6636\(94\)00036-g](https://doi.org/10.1016/0167-6636(94)00036-g).
- Hou Hua, Dong Ruifeng, Tan Yuxin, Li Chenhui, Zhang Xiaoyang, Wu Li, Zhu Bin, Zhao Yuhong. Microstructural characteristics and enhanced mechanical properties of 2024 aluminum alloy resulting from shot-peening treatment. *Materials Characterization*, 2023, vol. 206, part A, article number 113412. DOI: [10.1016/j.matchar.2023.113412](https://doi.org/10.1016/j.matchar.2023.113412).
- Palmgren A.G. Die Lebensdauer von Kugellagern. *Zeitschrift des Vereines Deutscher Ingenieure (ZVDI)*, 1924, vol. 14, pp. 339–341.
- Susmel L. The Modified Wöhler Curve Method calibrated by using standard fatigue curves and applied in conjunction with the Theory of Critical Distances to estimate fatigue lifetime of aluminum weldments. *International Journal of Fatigue*, 2009, vol. 31, no. 1, pp. 197–212. DOI: [10.1016/j.ijfatigue.2008.04.004](https://doi.org/10.1016/j.ijfatigue.2008.04.004).
- Miner M.A. Cumulative damage in fatigue. *Journal of Applied Mechanics*, 1945, vol. 12, no. 3, pp. A159–A164. DOI: [10.1115/1.4009458](https://doi.org/10.1115/1.4009458).
- Blasón S., Correia J.A.F.O., Jesus A.M.P., Calcada R.A.B., Fernandez-Canteli A. A probabilistic analysis of Miner's law for different loading conditions. *Structural Engineering and Mechanics*, 2016, vol. 60, no. 1, pp. 71–90. DOI: [10.12989/sem.2016.60.1.071](https://doi.org/10.12989/sem.2016.60.1.071).
- Mahdi H.S., Faris S.T., Abed R.M., Alalkawi H.M., Nasir R. Cumulative fatigue life estimation under combined shot peening and elevated temperature for AA7001-T6. *Diyala Journal of Engineering Sciences*, 2023, vol. 16, no. 2, pp. 50–59. DOI: [10.24237/djes.2023.16204](https://doi.org/10.24237/djes.2023.16204).
- Alwin A.H., Ksibi H., Driss Z., Alalkawi H.J.M. Fatigue variable loading under combined high temperature and shot peening treatment for AA2024-T4 and AA2024-T361. *Strojnický časopis - Journal of Mechanical Engineering*, 2023, vol. 73, no. 1, pp. 1–12. DOI: [10.2478/scjme-2023-0001](https://doi.org/10.2478/scjme-2023-0001).
- Mazlan S., Yidris N., Kooloor S.S.R., Petru M. Experimental and numerical analysis of fatigue life of aluminum Al 2024-T351 at elevated temperature. *Metals*, 2020, vol. 10, no. 12, article number 1581. DOI: [10.3390/met10121581](https://doi.org/10.3390/met10121581).
- Alwin A.H.A., Ksibi H., Driss Z., Alalkawi H.J.M. Optimization of the Shot Peening Time (SPT) in Terms of Mechanical Properties and Fatigue Life of AA2024-T4. *AIP Conference Proceedings*, 2024, vol. 3002, no. 1, article number 070048. DOI: [10.1063/5.0206464](https://doi.org/10.1063/5.0206464).
- Al-Rubaie K.S. A general model for stress-life fatigue prediction. *Materialwissenschaft Und Werkstofftechnik*, 2008, vol. 39, no. 6, pp. 400–406. DOI: [10.1002/mawe.200800282](https://doi.org/10.1002/mawe.200800282).
- Alkawi H.J.M., Mohammed Q.K., Al-Nuami W.S. The effect of shot peening and residual stresses on cumulative fatigue damage. *Engineering and Technology Journal*, 2010, vol. 28, no. 15, pp. 5055–5070. DOI: [10.30684/etj.28.15.14](https://doi.org/10.30684/etj.28.15.14).
- Kondo Y. Fatigue under variable amplitude loading. *Comprehensive Structural Integrity*, 2003, vol. 4, pp. 253–279. DOI: [10.1016/b0-08-043749-4/04029-5](https://doi.org/10.1016/b0-08-043749-4/04029-5).
- Maleki E., Bagherifard S., Unal O., Bandini M., Farrahi G.H., Guagliano M. Introducing gradient severe shot peening as a novel mechanical surface treatment. *Scientific Reports*, 2021, vol. 11, no. 1, article number 22035. DOI: [10.1038/s41598-021-01152-2](https://doi.org/10.1038/s41598-021-01152-2).
- Hectors K., De Waele W. Cumulative Damage and Life Prediction Models for High-Cycle Fatigue of Metals: A Review. *Metals*, 2021, vol. 11, no. 2, article number 204. DOI: [10.3390/met11020204](https://doi.org/10.3390/met11020204).
- Fatemi A., Yang L. Cumulative fatigue damage and life prediction theories: a survey of the state of the art for homogeneous materials. *International Journal of Fatigue*, 1998, vol. 20, no. 1, pp. 9–34. DOI: [10.1016/s0142-1123\(97\)00081-9](https://doi.org/10.1016/s0142-1123(97)00081-9).
- Li Guowei, Dong Zhicheng, Luo Tianhao, Huang Heyuan. Study on the influence of shot peening strengthening before shot peen forming on 2024-T351 aluminum alloy fatigue crack growth rate. *Scientific Reports*, 2023, vol. 13, no. 1, article number 5313. DOI: [10.1038/s41598-023-32616-2](https://doi.org/10.1038/s41598-023-32616-2).
- Starkey W.L., Marco S.M. Effect of Complex Stress-Time Cycles on the Fatigue Properties of Metals. *Transactions of ASME*, 1957, vol. 79, no. 6, pp. 1329–1336. DOI: [10.1115/1.4013318](https://doi.org/10.1115/1.4013318).
- Zhao Gongwei, Liu Yating, Ye Nanhai. An improved fatigue accumulation damage model based on load interaction and strength degradation. *International Journal of Fatigue*, 2022, vol. 156, article number 106636. DOI: [10.1016/j.ijfatigue.2021.106636](https://doi.org/10.1016/j.ijfatigue.2021.106636).
- Hwang W., Han K.S. Cumulative Damage Models and Multi-Stress Fatigue Life Prediction. *Journal of Composite Materials*, 1986, vol. 20, no. 2, pp. 125–153. DOI: [10.1177/002199838602000202](https://doi.org/10.1177/002199838602000202).
- Hong Yan Miao, Lévesque M., Gosselin F.P. Shot peen forming pattern optimization to achieve cylindrical and saddle target shapes: The inverse problem. *CIRP Journal of Manufacturing Science and Technology*, 2022, vol. 36, pp. 67–77. DOI: [10.1016/j.cirpj.2021.11.003](https://doi.org/10.1016/j.cirpj.2021.11.003).
- Miller K.J., Mohamed H.J., de los Rios E.R. Fatigue damage accumulation above and below the fatigue limit. *The Behavior of Short Fatigue Cracks. (EGF 1)*. London, Mechanical Engineering Publications, 1986, pp. 491–511.

24. Holt J.M.T., ed. *Structural Alloys Handbook*. West Lafayette, CINDAS/Purdue University Publ., 1996. 580 p.

СПИСОК ЛИТЕРАТУРЫ

- Ahcene A.S., Bey K., Mzad H. Mechanical Fatigue Test of Aluminum Composite Panel (ACP) with Aramid Nida-Core Under Cyclic Bending // *Strojnícky časopis - Journal of Mechanical Engineering*. 2020. Vol. 70. № 2. P. 1–10. DOI: [10.2478/scjme-2020-0015](https://doi.org/10.2478/scjme-2020-0015).
- Al-Obaid Y.F. Shot peening mechanics: experimental and theoretical analysis // *Mechanics of Materials*. 1995. Vol. 19. № 2-3. P. 251–260. DOI: [10.1016/0167-6636\(94\)00036-g](https://doi.org/10.1016/0167-6636(94)00036-g).
- Hou Hua, Dong Ruifeng, Tan Yuxin, Li Chenhui, Zhang Xiaoyang, Wu Li, Zhu Bin, Zhao Yuhong. Microstructural characteristics and enhanced mechanical properties of 2024 aluminum alloy resulting from shot-peening treatment // *Materials Characterization*. 2023. Vol. 206. Part A. Article number 113412. DOI: [10.1016/j.matchar.2023.113412](https://doi.org/10.1016/j.matchar.2023.113412).
- Palmgren A.G. Die Lebensdauer von Kugellagern. Life Length of Roller Bearings or Durability of Ball Bearings // *Zeitschrift des Vereines Deutscher Ingenieure (ZVDI)*. 1924. Vol. 14. P. 339–341.
- Susmel L. The Modified Wöhler Curve Method calibrated by using standard fatigue curves and applied in conjunction with the Theory of Critical Distances to estimate fatigue lifetime of aluminum weldments // *International Journal of Fatigue*. 2009. Vol. 31. № 1. P. 197–212. DOI: [10.1016/j.ijfatigue.2008.04.004](https://doi.org/10.1016/j.ijfatigue.2008.04.004).
- Miner M.A. Cumulative damage in fatigue // *Journal of Applied Mechanics*. 1945. Vol. 12. № 3. P. A159–A164. DOI: [10.1115/1.4009458](https://doi.org/10.1115/1.4009458).
- Blasón S., Correia J.A.F.O., Jesus A.M.P., Calçada R.A.B., Fernandez-Canteli A. A probabilistic analysis of Miner's law for different loading conditions // *Structural Engineering and Mechanics*. 2016. Vol. 60. № 1. P. 71–90. DOI: [10.12989/sem.2016.60.1.071](https://doi.org/10.12989/sem.2016.60.1.071).
- Mahdi H.S., Faris S.T., Abed R.M., Alalkawi H.M., Nasir R. Cumulative fatigue life estimation under combined shot peening and elevated temperature for AA7001-T6 // *Diyala Journal of Engineering Sciences*. 2023. Vol. 16. № 2. P. 50–59. DOI: [10.24237/djes.2023.16204](https://doi.org/10.24237/djes.2023.16204).
- Alwin A.H., Ksibi H., Driss Z., Alalkawi H.J.M. Fatigue variable loading under combined high temperature and shot peening treatment for AA2024-T4 and AA2024-T361 // *Strojnícky časopis - Journal of Mechanical Engineering*. 2023. Vol. 73. № 1. P. 1–12. DOI: [10.2478/scjme-2023-0001](https://doi.org/10.2478/scjme-2023-0001).
- Mazlan S., Yidris N., Koloor S.S.R., Petru M. Experimental and numerical analysis of fatigue life of aluminum Al 2024-T351 at elevated temperature // *Metals*. 2020. Vol. 10. № 12. Article number 1581. DOI: [10.3390/met10121581](https://doi.org/10.3390/met10121581).
- Alwin A.H.A., Ksibi H., Driss Z., Alalkawi H.J.M. Optimization of the Shot Peening Time (SPT) in Terms of Mechanical Properties and Fatigue Life of AA2024-T4 // *AIP Conference Proceedings*. 2024. Vol. 3002. № 1. Article number 070048. DOI: [10.1063/5.0206464](https://doi.org/10.1063/5.0206464).
- Al-Rubaie K.S. A general model for stress-life fatigue prediction // *Materialwissenschaft Und Werkstofftechnik*. 2008. Vol. 39. № 6. P. 400–406. DOI: [10.1002/mawe.200800282](https://doi.org/10.1002/mawe.200800282).
- Alkawi H.J.M., Mohammed Q.K., Al-Nuami W.S. The effect of shot peening and residual stresses on cumulative fatigue damage // *Engineering and Technology Journal*. 2010. Vol. 28. № 15. P. 5055–5070. DOI: [10.30684/etj.28.15.14](https://doi.org/10.30684/etj.28.15.14).
- Kondo Y. Fatigue under variable amplitude loading // *Comprehensive Structural Integrity*. 2003. Vol. 4. P. 253–279. DOI: [10.1016/b0-08-043749-4/04029-5](https://doi.org/10.1016/b0-08-043749-4/04029-5).
- Maleki E., Bagherifard S., Unal O., Bandini M., Farahi G.H., Guagliano M. Introducing gradient severe shot peening as a novel mechanical surface treatment // *Scientific Reports*. 2021. Vol. 11. № 1. Article number 22035. DOI: [10.1038/s41598-021-01152-2](https://doi.org/10.1038/s41598-021-01152-2).
- Hectors K., De Waele W. Cumulative Damage and Life Prediction Models for High-Cycle Fatigue of Metals: A Review // *Metals*. 2021. Vol. 11. № 2. Article number 204. DOI: [10.3390/met11020204](https://doi.org/10.3390/met11020204).
- Fatemi A., Yang L. Cumulative fatigue damage and life prediction theories: a survey of the state of the art for homogeneous materials // *International Journal of Fatigue*. 1998. Vol. 20. № 1. P. 9–34. DOI: [10.1016/s0142-1123\(97\)00081-9](https://doi.org/10.1016/s0142-1123(97)00081-9).
- Li Guowei, Dong Zhicheng, Luo Tianhao, Huang Heyuan. Study on the influence of shot peening strengthening before shot peen forming on 2024-T351 aluminum alloy fatigue crack growth rate // *Scientific Reports*. 2023. Vol. 13. № 1. Article number 5313. DOI: [10.1038/s41598-023-32616-2](https://doi.org/10.1038/s41598-023-32616-2).
- Starkey W.L., Marco S.M. Effect of Complex Stress-Time Cycles on the Fatigue Properties of Metals // *Transactions of ASME*. 1957. Vol. 79. № 6. P. 1329–1336. DOI: [10.1115/1.4013318](https://doi.org/10.1115/1.4013318).
- Zhao Gongwei, Liu Yating, Ye Nanhai. An improved fatigue accumulation damage model based on load interaction and strength degradation // *International Journal of Fatigue*. 2022. Vol. 156. Article number 106636. DOI: [10.1016/j.ijfatigue.2021.106636](https://doi.org/10.1016/j.ijfatigue.2021.106636).
- Hwang W., Han K.S. Cumulative Damage Models and Multi-Stress Fatigue Life Prediction // *Journal of Composite Materials*. 1986. Vol. 20. № 2. P. 125–153. DOI: [10.1177/002199838602000202](https://doi.org/10.1177/002199838602000202).
- Hong Yan Miao, Lévesque M., Gosselin F.P. Shot peen forming pattern optimization to achieve cylindrical and saddle target shapes: The inverse problem // *CIRP Journal of Manufacturing Science and Technology*. 2022. Vol. 36. P. 67–77. DOI: [10.1016/j.cirpj.2021.11.003](https://doi.org/10.1016/j.cirpj.2021.11.003).
- Miller K.J., Mohamed H.J., de los Rios E.R. Fatigue damage accumulation above and below the fatigue limit // *The Behavior of Short Fatigue Cracks. (EGF 1)*. London: Mechanical Engineering Publications, 1986. P. 491–511.
- Structural Alloys Handbook* / ed. J.M.T. Holt. West Lafayette: CINDAS/Purdue University, 1996. 580 p.

Прогнозное моделирование усталостной долговечности алюминиевых сплавов при повышенных температурах после воздействия дробеструйного упрочнения

Элвин Аллави Х.^{1,3}, кандидат технических наук, лаборатория электромеханических систем (LASEM)
Ксиби Хатем^{2,4}, профессор, постоянный член лаборатории материалов, окружающей среды и энергии,
факультет естественных наук Гафсы

¹Инженерный колледж в Сфаксе (ENIS), Сфакс (Тунис)

²Подготовительный инженерный институт в Сфаксе (IPEIS), Сфакс (Тунис)

*E-mail: hatem.ksibi@ipeis.rnu.tn

³ORCID: <https://orcid.org/0009-0001-1015-2476>

⁴ORCID: <https://orcid.org/0000-0003-4144-9958>

Поступила в редакцию 18.04.2024

Пересмотрена 22.05.2024

Принята к публикации 11.09.2024

Аннотация: Повышение качества поверхности оболочек из алюминиевых сплавов, подвергающихся высоким нагрузкам, остается актуальной задачей, для решения которой используются различные методы. Для алюминиевых сплавов наибольшее распространение получило дробеструйное упрочнение. В статье исследуются усталостные характеристики алюминиевых сплавов 2024-T4 и 2024-T361 после дробеструйного упрочнения и без него при комнатной и повышенной температуре (250 °C). Полученные результаты хорошо согласуются с ранее опубликованными данными, предоставляя полезную информацию о поведении этих сплавов при повышенных температурах. Была разработана математическая модель, объединяющая кривую усталости «напряжение – количество циклов до разрушения», амплитуду нагрузки, температуру и твердость поверхности, подвергнутой дробеструйному упрочнению. Полученные с использованием этой модели результаты были сравнены с гипотезой Майнера для оценки усталостной долговечности. Было установлено, что новая модель обеспечивает более точные прогнозы усталостной долговечности, чем гипотеза Майнера, тем самым повышая надежность и безопасность разработанных на ее основе компонентов при высокотемпературных условиях эксплуатации.

Ключевые слова: дробеструйное упрочнение; прогнозная усталостная долговечность; алюминиевые сплавы; AA2024-T4; AA2024-T361; высокотемпературное воздействие; переменное нагружение.

Для цитирования: Элвин А.Х., Ксиби Х. Прогнозное моделирование усталостной долговечности алюминиевых сплавов при повышенных температурах после воздействия дробеструйного упрочнения // Frontier Materials & Technologies. 2024. № 4. С. 111–122. DOI: 10.18323/2782-4039-2024-4-70-10.

OUR AUTHORS

Alwin Allawi H., PhD (Mechanical Engineering),
Laboratory of Electro-Mechanic Systems (LASEM).
Address: National School of Engineers of Sfax (ENIS),
3038, Tunisia, Sfax, Route de la Soukra km 4.
E-mail: tuqa1990@rocketmail.com

Begun Marina Eduardovna, student, technician
of the Research Institute of Advanced Technologies.
Address: Togliatti State University,
445020, Russia, Togliatti, Belorusskaya Street, 14.
E-mail: mariana.begun@gmail.com

Bogdanov Valery Mikhailovich, postgraduate student.
Address: Peter the Great St. Petersburg Polytechnic University,
195251, Russia, St. Petersburg, Politekhnikeskaya Street, 29.
E-mail: bogdanov.vm@edu.spbstu.ru

Botkin Aleksandr Vasilyevich, Doctor of Sciences (Engineering),
professor of Chair of Materials Science and Physics of Metals.
Address: Ufa University of Science and Technology,
450076, Russia, Ufa, Zaki Validi Street, 32.
E-mail: botkinav@yandex.ru

Gladkovsky Sergey Viktorovich, Doctor of Sciences (Engineering),
chief researcher, Head of the Laboratory of Deformation and Destruction.
Address: Institute of Engineering Science of the Ural Branch of RAS,
620049, Russia, Yekaterinburg, Komsomolskaya Street, 34.
E-mail: gsv@imach.uran.ru

Gusakova Sofya Viktorovna, PhD (Physics and Mathematics),
leading engineer of radiation and vacuum equipment in the Scientific Research Service Sector.
Address: Belarusian State University,
220006, Republic of Belarus, Minsk, Bobruiskaya Street, 5a.
E-mail: ita@vitebsk.by

Ilyukhin Dmitriy Igorevich, engineer of the 1st category.
Address: National Research University “Moscow Power Engineering Institute”,
111250, Russia, Moscow, Krasnokazarmennaya Street, 14, build. 1.
E-mail: IliukhinDI@mpei.ru

Kachalin Gennady Viktorovich, PhD (Engineering), leading researcher.
Address: National Research University “Moscow Power Engineering Institute”,
111250, Russia, Moscow, Krasnokazarmennaya Street, 14, build. 1.
E-mail: KachalinGV@mpei.ru

Kasyanenko Vladislav Aleksandrovich, engineer of the 1st category.
Address: National Research University “Moscow Power Engineering Institute”,
111250, Russia, Moscow, Krasnokazarmennaya Street, 14, build. 1.
E-mail: KasyanenkoVA@mpei.ru

Khudododova Gandzhina Dastambuevna, junior researcher
of the Research Institute of Physics of Advanced Materials.
Address: Ufa University of Science and Technology,
450076, Russia, Ufa, Zaki Validi Street, 32.
E-mail: khudododova.gd@gmail.com

Kostin Gleb Vyacheslavovich, student
of Chair “Nanotechnology, Materials Science and Mechanics”.
Address: Togliatti State University,
445020, Russia, Togliatti, Belorusskaya Street, 14.
E-mail: gleb.kostin2000@mail.ru

Ksibi Hatem, Professor, permanent member
of the Materials, Environment and Energy Laboratory, Faculty of Sciences of Gafsa.
Address: Sfax Preparatory Engineering Institute (IPEIS),
3072, Tunisia, Sfax, Rue Riadh.
E-mail: hatem.ksibi@ipeis.rnu.tn

Lomach Marina Sergeevna, junior researcher.
Address: Institute of Technical Acoustics of the National Academy of Sciences of Belarus,
210009, Republic of Belarus, Vitebsk, General Lyudnikov Prospekt, 13.
E-mail: ita@vitebsk.by

Lutsko Valery Fedorovich, senior researcher.
Address: Institute of Technical Acoustics of the National Academy of Sciences of Belarus,
210009, Republic of Belarus, Vitebsk, General Lyudnikov Prospekt, 13.
E-mail: ita@vitebsk.by

Mednikov Aleksey Feliksovich, PhD (Engineering), leading researcher.
Address: National Research University “Moscow Power Engineering Institute”,
111250, Russia, Moscow, Krasnokazarmennaya Street, 14, build. 1.
E-mail: MednikovAlF@mpei.ru

Medvedev Konstantin Sergeevich, leading engineer.
Address: National Research University “Moscow Power Engineering Institute”,
111250, Russia, Moscow, Krasnokazarmennaya Street, 14, build. 1.
E-mail: MedvedevKS@mpei.ru

Merson Dmitry Lvovich, Doctor of Sciences (Physics and Mathematics), Professor,
Director of the Research Institute of Advanced Technologies.
Address: Togliatti State University,
445020, Russia, Togliatti, Belorusskaya Street, 14.
E-mail: D.Merson@tltsu.ru

Merson Evgeny Dmitrievich, PhD (Physics and Mathematics),
senior researcher of the Research Institute of Advanced Technologies.
Address: Togliatti State University,
445020, Russia, Togliatti, Belorusskaya Street, 14.
E-mail: mersoned@gmail.com

Myagkikh Pavel Nikolaevich, PhD (Engineering),
junior researcher of the Research Institute of Advanced Technologies.
Address: Togliatti State University,
445020, Russia, Togliatti, Belorusskaya Street, 14.
E-mail: p.myagkikh@tltsu.ru

Naurzalinov Alibek Serpaevich, technician
of Chair “Technologies and Systems for Automated Design of Metallurgical Processes” (1101).
Address: Moscow Aviation Institute (National Research University),
125993, Russia, Moscow, Volokolamskoe Shosse, 4.
E-mail: alibeek@mail.ru

Pashkov Igor Nikolaevich, Doctor of Sciences (Engineering),
professor of Chair “Technologies and Systems for Automated Design of Metallurgical Processes” (1101).
Address: Moscow Aviation Institute (National Research University),
125993, Russia, Moscow, Volokolamskoe Shosse, 4.
E-mail: pashkov_prof@mail.ru

Patselov Aleksandr Mikhailovich, PhD (Physics and Mathematics),
senior researcher at the High Pressure Physics Laboratory.
Address: M.N. Mikheev Institute of Metal Physics of the Ural Branch of RAS,
620108, Russia, Yekaterinburg, Sofya Kovalevskaya Street, 18.
E-mail: patselov@imp.uran.ru

Pilyugin Vitaly Prokofyevich, PhD (Physics and Mathematics), leading researcher, Head of the High Pressure Physics Laboratory.
Address: M.N. Mikheev Institute of Metal Physics of the Ural Branch of RAS, 620108, Russia, Yekaterinburg, Sofya Kovalevskaya Street, 18.
E-mail: pilyugin@imp.uran.ru

Poluyanov Vitaly Aleksandrovich, PhD (Engineering), junior researcher of the Research Institute of Advanced Technologies.
Address: Togliatti State University, 445020, Russia, Togliatti, Belorusskaya Street, 14.
E-mail: vitaliy.poluyanov@gmail.com

Rao Srilatha, PhD, Professor.
Address: Nitte Meenakshi Institute of Technology, 560064, India, Bangalore, Yelahanka, P.B. No. 6429.
E-mail: srilatha.rao.p@nmit.ac.in

Rubanik Vasily Vasilyevich, Doctor of Sciences (Engineering), Professor, Head of the Laboratory of Physics of Metals, Corresponding Member of the National Academy of Sciences of Belarus.
Address: Institute of Technical Acoustics of the National Academy of Sciences of Belarus, 210009, Republic of Belarus, Vitebsk, General Lyudnikov Prospekt, 13.
E-mail: ita@vitebsk.by

Rubanik Vasily Vasilyevich Jr., Doctor of Sciences (Engineering), Professor, Director.
Address: Institute of Technical Acoustics of the National Academy of Sciences of Belarus, 210009, Republic of Belarus, Vitebsk, General Lyudnikov Prospekt, 13.
E-mail: ita@vitebsk.by

Shailesh Rao Agari, PhD, Professor, Department of Mechanical Engineering.
Address: Nitte Meenakshi Institute of Technology, 560064, India, Bangalore, Yelahanka, P.B. No. 6429.
E-mail: shailesh.rao@nmit.ac.in

Svyatkin Aleksey Vladimirovich, PhD (Engineering), assistant professor of Chair “Nanotechnology, Materials Science and Mechanics”.
Address: Togliatti State University, 445020, Russia, Togliatti, Belorusskaya Street, 14.
E-mail: astgl@mail.ru

Tkhabisimov Aleksandr Borisovich, PhD (Engineering), senior researcher.
Address: National Research University “Moscow Power Engineering Institute”, 111250, Russia, Moscow, Krasnokazarmennaya Street, 14, build. 1.
E-mail: TkhabisimovAB@mpei.ru

Valiev Ruslan Zufarovich, Doctor of Sciences (Physics and Mathematics), Professor, Director of the Research Institute of Physics of Advanced Materials.
Address: Ufa University of Science and Technology, 450076, Russia, Ufa, Zaki Validi Street, 32.
E-mail: valiev.rz@ugatu.su

Veselova Valeria Evgenievna, PhD (Engineering), researcher at the Laboratory of Deformation and Destruction.
Address: Institute of Engineering Science of the Ural Branch of RAS, 620049, Russia, Yekaterinburg, Komsomolskaya Street, 34.
E-mail: veselova@imach.uran.ru

Volkova Elena Pavlovna, junior researcher of the Research Institute of Physics of Advanced Materials.
Address: Ufa University of Science and Technology, 450076, Russia, Ufa, Zaki Validi Street, 32.
E-mail: epvolkova@mail.ru

AUTHORS

Zhukov Evgeny Yurievich, engineer

of Chair “Technologies and Systems for Automated Design of Metallurgical Processes” (1101).

Address: Moscow Aviation Institute (National Research University),
125993, Russia, Moscow, Volokolamskoe Shosse, 4.

E-mail: jezzacome@gmail.com

Zilova Olga Sergeevna, PhD (Engineering),

leading researcher.

Address: National Research University “Moscow Power Engineering Institute”,
111250, Russia, Moscow, Krasnokazarmennaya Street, 14, build. 1.

E-mail: ZilovaOS@mpei.ru

НАШИ АВТОРЫ

Бегун Марина Эдуардовна, студент, техник
НИИ прогрессивных технологий.
Адрес: Тольяттинский государственный университет,
445020, Россия, г. Тольятти, ул. Белорусская, 14.
E-mail: mariana.begun@gmail.com

Богданов Валерий Михайлович, аспирант.
Адрес: Санкт-Петербургский политехнический университет Петра Великого,
195251, Россия, г. Санкт-Петербург, ул. Политехническая, 29.
E-mail: bogdanov.vm@edu.spbstu.ru

Боткин Александр Васильевич, доктор технических наук,
профессор кафедры материаловедения и физики металлов.
Адрес: Уфимский университет науки и технологий,
450076, Россия, г. Уфа, ул. Заки Валиди, 32.
E-mail: botkinav@yandex.ru

Валиев Руслан Зуфарович, доктор физико-математических наук, профессор,
директор Научно-исследовательского института физики перспективных материалов.
Адрес: Уфимский университет науки и технологий,
450076, Россия, г. Уфа, ул. Заки Валиди, 32.
E-mail: valiev.rz@ugatu.su

Веселова Валерия Евгеньевна, кандидат технических наук,
научный сотрудник лаборатории деформирования и разрушения.
Адрес: Институт машиноведения имени Э.С. Горкунова Уральского отделения РАН,
620049, Россия, г. Екатеринбург, ул. Комсомольская, 34.
E-mail: veselova@imach.uran.ru

Волкова Елена Павловна, младший научный сотрудник
Научно-исследовательского института физики перспективных материалов.
Адрес: Уфимский университет науки и технологий,
450076, Россия, г. Уфа, ул. Заки Валиди, 32.
E-mail: epvolkova@mail.ru

Гладковский Сергей Викторович, доктор технических наук,
главный научный сотрудник, заведующий лабораторией деформирования и разрушения.
Адрес: Институт машиноведения имени Э.С. Горкунова Уральского отделения РАН,
620049, Россия, г. Екатеринбург, ул. Комсомольская, 34.
E-mail: gsv@imach.uran.ru

Гусакова Софья Викторовна, кандидат физико-математических наук,
ведущий инженер радиационной и вакуумной аппаратуры
сектора обслуживания научных исследований.
Адрес: Белорусский государственный университет,
220006, Республика Беларусь, г. Минск, ул. Бобруйская, 5а.
E-mail: ita@vitebsk.by

Жуков Евгений Юрьевич, инженер кафедры 1101
«Технологии и системы автоматизированного проектирования металлургических процессов».
Адрес: Московский авиационный институт (национальный исследовательский университет),
125993, Россия, г. Москва, Волоколамское шоссе, 4.
E-mail: jezzacome@gmail.com

Зилова Ольга Сергеевна, кандидат технических наук,
ведущий научный сотрудник.
Адрес: Национальный исследовательский университет «МЭИ»,
111250, Россия, г. Москва, ул. Красноказарменная, 14, стр. 1.
E-mail: ZilovaOS@mpei.ru

Илюхин Дмитрий Игоревич, инженер 1 категории.
Адрес: Национальный исследовательский университет «МЭИ»,
111250, Россия, г. Москва, ул. Красноказарменная, 14, стр. 1.
E-mail: IliukhinDI@mpei.ru

Касьяненко Владислав Александрович, инженер 1 категории.
Адрес: Национальный исследовательский университет «МЭИ»,
111250, Россия, г. Москва, ул. Красноказарменная, 14, стр. 1.
E-mail: KasyanenkoVA@mpei.ru

Качалин Геннадий Викторович, кандидат технических наук,
ведущий научный сотрудник.
Адрес: Национальный исследовательский университет «МЭИ»,
111250, Россия, г. Москва, ул. Красноказарменная, 14, стр. 1.
E-mail: KachalinGV@mpei.ru

Костин Глеб Вячеславович, студент
кафедры «Нанотехнологии, материаловедение и механика».
Адрес: Тольяттинский государственный университет,
445020, Россия, г. Тольятти, ул. Белорусская, 14.
E-mail: gleb.kostin2000@mail.ru

Ксиби Хатем, профессор, постоянный член лаборатории
материалов, окружающей среды и энергии, факультет естественных наук Гафсы.
Адрес: Подготовительный инженерный институт в Сфаксе (IPEIS),
3072, Тунис, г. Сфакс, Рю Риад.
E-mail: hatem.ksibi@ipeis.rnu.tn

Ломач Марина Сергеевна, младший научный сотрудник.
Адрес: Институт технической акустики Национальной академии наук Беларуси,
210009, Республика Беларусь, г. Витебск, пр-т Генерала Людникова, 13.
E-mail: ita@vitebsk.by

Луцко Валерий Федорович, старший научный сотрудник.
Адрес: Институт технической акустики Национальной академии наук Беларуси,
210009, Республика Беларусь, г. Витебск, пр-т Генерала Людникова, 13.
E-mail: ita@vitebsk.by

Медведев Константин Сергеевич, ведущий инженер.
Адрес: Национальный исследовательский университет «МЭИ»,
111250, Россия, г. Москва, ул. Красноказарменная, 14, стр. 1.
E-mail: MedvedevKS@mpei.ru

Медников Алексей Феликсович, кандидат технических наук,
ведущий научный сотрудник.
Адрес: Национальный исследовательский университет «МЭИ»,
111250, Россия, г. Москва, ул. Красноказарменная, 14, стр. 1.
E-mail: MednikovAlF@mpei.ru

Мерсон Дмитрий Львович, доктор физико-математических наук, профессор,
директор НИИ прогрессивных технологий.
Адрес: Тольяттинский государственный университет,
445020, Россия, г. Тольятти, ул. Белорусская, 14.
E-mail: D.Merson@tltsu.ru

Мерсон Евгений Дмитриевич, кандидат физико-математических наук,
старший научный сотрудник НИИ прогрессивных технологий.
Адрес: Тольяттинский государственный университет,
445020, Россия, г. Тольятти, ул. Белорусская, 14.
E-mail: mersoned@gmail.com

Мягких Павел Николаевич, кандидат технических наук,
младший научный сотрудник НИИ прогрессивных технологий.
Адрес: Тольяттинский государственный университет,
445020, Россия, г. Тольятти, ул. Белорусская, 14.
E-mail: p.myagkikh@tltsu.ru

Наурзалинов Алибек Серпаевич, техник кафедры 1101
«Технологии и системы автоматизированного проектирования металлургических процессов».
Адрес: Московский авиационный институт (национальный исследовательский университет),
125993, Россия, г. Москва, Волоколамское шоссе, 4.
E-mail: alibeeek@mail.ru

Пацелов Александр Михайлович, кандидат физико-математических наук,
старший научный сотрудник лаборатории физики высоких давлений.
Адрес: Институт физики металлов имени М.Н. Михеева Уральского отделения РАН,
620108, Россия, г. Екатеринбург, ул. Софьи Ковалевской, 18.
E-mail: patselov@imp.uran.ru

Пашков Игорь Николаевич, доктор технических наук,
профессор кафедры 1101
«Технологии и системы автоматизированного проектирования металлургических процессов».
Адрес: Московский авиационный институт (национальный исследовательский университет),
125993, Россия, г. Москва, Волоколамское шоссе, 4.
E-mail: pashkov_prof@mail.ru

Пилюгин Виталий Прокофьевич, кандидат физико-математических наук,
ведущий научный сотрудник, заведующий лабораторией физики высоких давлений.
Адрес: Институт физики металлов имени М.Н. Михеева Уральского отделения РАН,
620108, Россия, г. Екатеринбург, ул. Софьи Ковалевской, 18.
E-mail: pilyugin@imp.uran.ru

Полуянов Виталий Александрович, кандидат технических наук,
младший научный сотрудник НИИ прогрессивных технологий.
Адрес: Тольяттинский государственный университет,
445020, Россия, г. Тольятти, ул. Белорусская, 14.
E-mail: vitaliy.poluyanov@gmail.com

Рао Шрилата, кандидат наук, профессор.
Адрес: Технологический институт Нитт Минкши,
560064, Индия, г. Бангалор, Йелаханка, п. я. 6429.
E-mail: srilatha.rao.p@nmit.ac.in

Рубаник Василий Васильевич, доктор технических наук, профессор,
заведующий лабораторией физики металлов,
член-корреспондент Национальной академии наук Беларуси.
Адрес: Институт технической акустики Национальной академии наук Беларуси,
210009, Республика Беларусь, г. Витебск, пр-т Генерала Людникова, 13.
E-mail: ita@vitebsk.by

Рубаник Василий Васильевич мл., доктор технических наук, профессор, директор.
Адрес: Институт технической акустики Национальной академии наук Беларуси,
210009, Республика Беларусь, г. Витебск, пр-т Генерала Людникова, 13.
E-mail: ita@vitebsk.by

Святкин Алексей Владимирович, кандидат технических наук,
доцент кафедры «Нанотехнологии, материаловедение и механика».
Адрес: Тольяттинский государственный университет,
445020, Россия, г. Тольятти, ул. Белорусская, 14.
E-mail: astgl@mail.ru

АВТОРЫ

Тхабисимов Александр Борисович, кандидат технических наук,
старший научный сотрудник.

Адрес: Национальный исследовательский университет «МЭИ»,
111250, Россия, г. Москва, ул. Красноказарменная, 14, стр. 1.

E-mail: TkhabisimovAB@mpei.ru

Худододова Ганджина Дастамбуевна, младший научный сотрудник
Научно-исследовательского института физики перспективных материалов.

Адрес: Уфимский университет науки и технологий,
450076, Россия, г. Уфа, ул. Заки Валиди, 32.

E-mail: khudododova.gd@gmail.com

Шайлеш Рао Агари, кандидат наук, профессор,
факультет машиностроения.

Адрес: Технологический институт Нитт Минкши,
560064, Индия, г. Бангалор, Йелаханка, п. я. 6429.

E-mail: shailesh.rao@nmit.ac.in

Элвин Аллави Х., кандидат технических наук,
лаборатория электромеханических систем (LASEM).

Адрес: Инженерный колледж в Сфаксе (ENIS),
3038, Тунис, г. Сфакс, Рут де ла Сукра, 4 км.

E-mail: tuqa1990@rocketmail.com

On the cover: Surface morphology of a thermal barrier coating based on zirconium dioxide partially stabilized by yttrium oxide, formed using an uncooled target at a power of 9 kW. Author of the photo: A.A. Burmistrov, leading engineer of “Wear Resistance” Research Center (National Research University “Moscow Power Engineering Institute”, Moscow, Russia).

На обложке: Морфология поверхности термобарьерного покрытия на основе диоксида циркония, частично стабилизированного оксидом иттрия, сформированного с использованием неохлаждаемой мишени при мощности 9 кВт. Автор фото: А.А. Бурмистров, ведущий инженер Научного центра «Износостойкость» (Национальный исследовательский университет «МЭИ», Москва, Россия).